

From laser cooled molecules to novel quantum matter

Qi Sun

Submitted in partial fulfillment of the
requirements for the degree of
Doctor of Philosophy
under the Executive Committee
of the Graduate School of Arts and Sciences

COLUMBIA UNIVERSITY

2025

© 2025

Qi Sun

All Rights Reserved

Abstract

From laser cooled molecules to novel quantum matter

Qi Sun

Recent achievements in quantum-state control of atoms and molecules have demonstrated their potential for quantum information science, ultracold chemistry, and precision measurements. Meanwhile, the fact that only a third of all the elements have been optically trapped indicates a huge room for exploration. Among the optically untrapped elements, hydrogen stands out due to its simplicity, offering a uniquely ideal platform for rigorous comparisons between theoretical predictions and experimental results. Calcium monohydride is favorable for laser cooling, and has a unique double-well potential that is proposed to enable controlled photodissociation. In this thesis, I will present our experimental efforts and theoretical studies aimed at trapping and photodissociating CaH and CaD molecules to generate ultracold hydrogen and deuterium clouds. These investigations pave the way for a universal platform to produce exotic ultracold atomic gases, with profound implications for fundamental science and advancements in quantum technology.

Table of Contents

List of Tables	viii
List of Figures	xii
Acknowledgments	xxv
Dedication	xxix
Chapter 1: Introduction	1
1.1 Cold and Ultracold Molecules	1
1.1.1 Quantum Simulation and Computing	2
1.1.2 Cold and Ultracold Chemistry	2
1.1.3 Precision Measurements	3
1.2 Trapping More Atomic Species	4
1.2.1 Hydrogen Spectroscopy	5
1.3 Molecules as a Pathway to Exotic Atomic Gases	8
1.3.1 How to Get Cold Molecules	8
1.3.2 How Can We Dissociate Them	10
1.3.3 Can the Product Atoms Stay Cold after Dissociation	11
1.4 Structure of This Thesis	12

Chapter 2: Basic Information about CaH	14
2.1 Molecular Structure	14
2.1.1 Electronic and Spin-orbit Levels	15
2.1.2 Vibrational and Rotational Levels	15
2.1.3 Spin-rotation Coupling	17
2.1.4 Hyperfine Structure	18
2.1.5 Hund's Case a and b	18
2.2 Summary of CaH	19
2.2.1 Physical Properties	20
2.2.2 Spectroscopy Relevant	20
2.2.3 Optical Cycling Properties	20
Chapter 3: Experimental Hardware, and Why We Build It This Way	26
3.1 Cryogenic System	27
3.1.1 PTR, Cryostat, and Shields	27
3.1.2 Buffer Gas Cell	28
3.1.3 Target for ablation	33
3.2 Laser System	37
3.2.1 MOT Lasers	37
3.2.2 Slowing Lights	39
3.2.3 Cooling Lights	40
3.3 Laser Locking Systems	40
3.3.1 Wavemeter Sealing	40

3.3.2	Galvo-Based Fiber Switch	41
3.4	Vacuum System	43
3.4.1	Vacuum Lifetime	44
3.4.2	Baking	44
3.4.3	Painting	46
3.5	Misc	47
3.5.1	Magnetic Lens	47
3.5.2	Acousto-Optic Modulator (AOM)	61
3.5.3	Electro-Optic Modulator (EOM)	62
Chapter 4: Endothermic Reaction in a Cryogenic Buffer Gas Cell		63
4.1	Introduction: Motivation and Surprises	63
4.2	Experimental Implementation	65
4.3	Results	66
4.3.1	Ca + H ₂ Chemical Reaction in a CBGB Source	66
4.3.2	Reaction Network Model	68
4.3.3	H ₂ as a Buffer Gas Coolant	69
4.3.4	Collisional Cross Sections	71
4.4	Conclusion	72
4.5	Further Details	74
4.5.1	Rotational Temperature	74
4.5.2	QCT Simulations	75
4.5.3	Ablation Plume Temperature Measurement	77

4.5.4 Extraction of Collisional Cross Sections	78
 Chapter 5: Study of Predissociation	80
5.1 Relevant Background Information	80
5.2 What is Predissociation and Why Do We Study It	82
5.3 Theoretical Modeling of CaH	82
5.3.1 Calculation of Franck-Condon Factors	84
5.3.2 $B^2\Sigma^+$ Predissociation Estimate	85
5.4 $B^2\Sigma^+$ Predissociation Measurement	86
5.4.1 Experimental Setup	86
5.4.2 $B^2\Sigma^+ (\nu' = 0)$ Measurement Method	88
5.4.3 $B^2\Sigma^+ (\nu' = 1)$ Measurement Method	90
5.4.4 Predissociation Measurement Analysis	91
5.4.5 $A^2\Pi_{1/2}$ Predissociation Estimate	94
5.5 Discussion	95
5.5.1 Other Possible Loss Channels	95
5.5.2 Examples of Measurement Stages	97
5.5.3 Bootstrap Method in Data Analysis	100
 Chapter 6: Laser Cooling and Slowing	106
6.1 Fun Fact: An Experimentalist Should Be Brave	106
6.2 Summary of CaH Laser Cooling Experiment	106
6.2.1 Introduction	107
6.2.2 Experimental Setup	109

6.2.3	Vibrational Branching Ratio Measurement	111
6.2.4	Scattering Rate Measurement	115
6.2.5	Magnetically Assisted Sisyphus Cooling	118
6.2.6	CaH Laser Cooling Experiment Conclusion	121
6.2.7	Laser Configuration	121
6.2.8	Molecular Beam Flux Estimation	122
6.2.9	VBR Measurement	123
6.2.10	OBE and MC Simulations	125
6.3	Summary of CaD Laser Cooling Experiment	127
6.3.1	Introduction	128
6.3.2	Methods	130
6.3.3	Experimental setup	130
6.3.4	Results	132
6.3.5	Conclusion of CaD Laser Cooling Experiment	135
6.3.6	Synthesis of CaD ₂	135
6.3.7	Characterization of Molecular Yield	137
6.3.8	Vibrational Branching Ratios	138
6.3.9	Laser Configuration	139
6.3.10	Beam Temperature Estimation	140
6.3.11	Doppler Cooling	140
6.4	Recent Progress with Laser Slowing CaH	140
	Chapter 7: Optical Bloch Equation (OBE) Solver	149

7.1	Why Solve OBE	149
7.2	OBE Theory	149
7.2.1	Liouville–von Neumann Master Equation	150
7.2.2	Dissipator	151
7.2.3	Hamiltonian	152
7.2.4	Rabi Rate	153
7.2.5	Unitary Transformation	156
7.2.6	Example: 3+1 System	157
7.3	Dark States in Toy Models	160
7.3.1	What is a Dark State	160
7.3.2	Examples of Dark States	160
7.3.3	Adding B field to Destabilize Dark States	162
7.4	3+1 Toy Model	164
7.5	3+3 and 5+3 Toy Model	165
7.6	CaH System	167
7.6.1	Case 1: X-A Dark State Remixed Experiment	167
7.6.2	Case 2: Sisyphus Cooling Experiment	174
Chapter 8:	Future Outlook: 3D MOT, Dissociation, and H Detection	176
8.1	3D MOT	176
8.2	Ultracold Chemistry	177
8.3	Controlled Dissociation Pathways for Ultracold Atom Production	181
8.4	Detection of Atomic Fragments after Controlled Dissociation	184

8.4.1	Calcium Detection	184
8.4.2	Hydrogen Detection via Photoionization and Ion Imaging	184
8.4.3	Future Outlook and Integration	185
References		203
Appendix A:	Indirect Measurement of Beam Forward Velocity	204
A.1	Ghosting Effect in BGF	207

List of Tables

2.1	Spectroscopic constants of CaH in units of GHz (instead of cm^{-1} for convenience)	21
2.2	Some important state energies of CaH. Ω , v, N, J stand for total angular momentum, vibrational number, rotational number, spin-rotation angular momentum, respectively. Parity 1 refers to the overall parity in terms of optical transition. An E1 transition is only possible if the two states have opposite parity 1 values. Parity 2 refers to the parity that is commonly used for diatomic molecule spectroscopic purpose. Labels are for spectroscopic purpose. Es are the state energies. The errors of Es are 100MHz for $X^2\Sigma^+$, $A^2\Pi_{1/2}$ and $B^2\Sigma^+$ states (Ref. [27]), 1GHz for $E^2\Pi_{1/2}$ states (Ref. [28]). Hyperfine splittings are ignored due to finite errors.	22
2.3	Some transition frequencies for CaH. Values are measured with Highfinesse WS7 wavemeter with 60 MHz absolute error, calibrated with a strontium 689nm transition.	23
2.4	FCFs and VBRs for the measured transitions of CaH. The experimental radiative lifetime for the A state was obtained from Ref. [31] and for the B state from Ref. [32]. The excited state vibrational quantum number is always $v' = 0$. The $A(v' = 0) \leftarrow X(v'' = 0)$ excitation wavelength at 695.13 nm, the $B(v' = 0) \leftarrow X(v'' = 0)$ excitation wavelength at 635.12 nm, and the $B(v' = 0) \leftarrow X(v'' = 1)$ excitation wavelength at 690.37 nm were determined experimentally. The other transition wavelengths are derived using measured vibrational energies given in Ref. [27]. The calculated FCFs are obtained from [33] for the $A \rightarrow X$ decay and from [34] for the $B \rightarrow X$ decay. Error bars for the measured FCFs and VBRs are statistical standard errors.	25
3.1	An incomplete list of lasers deployed for CaH / CaD experiments. To explain the acronym, HB: home-built; Mol: molecules including CaH and CaD; RP: repump; ECDL: external cavity diode laser.	38
4.1	Collisional cross sections (in units of 10^{-16} cm^2) for Ca and CaH with He, H ₂ , HD, and D ₂ . Table adopted from Ref. [83].	79

5.1	Calculated and measured values of FCFs for CaH. We show the experimental FCFs taken from [106] for comparison. A' is the same active space as the $B^2\Sigma^+$ state in this work, shifting the potential to the left by $0.0375 a_0$. Table adopted from Ref. [89].	84
5.2	Calculated and measured values of FCFs for CaH. We show the experimental FCFs taken from [106] for comparison. Note that the active space was optimized for the B state for this work, which leads to a disagreement for the A state. Table adopted from Ref. [89].	85
5.3	Here we present the frequencies of all the transitions we used in this experiment. The $A^2\Pi_{1/2}$ and $B^2\Sigma^+$ states that we used have unresolved hyperfine splittings. All frequencies presented here have 10 MHz statistical uncertainty and 60 MHz systematic uncertainty due to the wavemeter used for measurement. Table adopted from Ref. [89].	89
5.4	Experimental stages for $B(v' = 0)$ state predissociation measurement. In the second column, we use $M_{v'-v''}^N$ notation to describe the laser information. M can be either A or B , representing the electronic excited state. N can be S , I , or C , representing state preparation region, interaction region, and cleanup region, respectively. In the third column, we express the normalized ground state molecule population at different stages with respect to that of the unperturbed stage using unknown variables and calculated VBRs. We use five variables here, including n_1 , κ , F_{B0a} , d_A and d_B , representing $X(v'' = 1)$ state natural population, cleanup efficiency of laser B_{1-0}^C , $B(v' = 0)$ state predissociation probability, depletion efficiency of laser A_{0-0}^I and depletion efficiency of laser B_{0-0}^I , respectively. We denote the VBR normalization factors as $\mathcal{F}_{A_0} \equiv \sum_{i \in Z^+} F_{A0i}$, $\mathcal{F}_{B_0} \equiv F_{B0a} + \sum_{i \in Z^*, i \neq 1} F_{B0i}$, and $\mathcal{F}_{B_1} \equiv F_{B0a} + \sum_{i \in Z^+} F_{B0i}$. A more complete table of vibrational population distribution can be found in appendix Table 5.5.2. Table adopted from Ref. [89].	90
5.5	Method I of $B^2\Sigma^+$ ($v' = 1$) state predissociation measurement. Notations are the similar with what are used in table 5.4, so here we will only discuss the differences. In the third column, the variables include a , n_1 , κ , F_{B1a} and d_B , representing state preparation (from $X(v'' = 0)$ to $X(v'' = 1)$) efficiency, $X(v'' = 1)$ state natural population, cleanup efficiency of laser A_{1-0}^C , $B(v' = 1)$ state predissociation probability, depletion efficiency of laser B_{1-1}^I , respectively. We denote the VBR normalization factors as $\mathcal{F}_{A_1} \equiv \sum_{i \in Z^*, i \neq 1} F_{A0i}$, $\mathcal{F}_{A_2} \equiv \sum_{i \in Z^+} F_{A1i}$ and $\mathcal{F}_{B_2} \equiv F_{B1a} + \sum_{i \in Z^*, i \neq 1} F_{B1i}$. A more complete table of vibrational population distribution downstream can be found in appendix Table 5.5.2. Table adopted from Ref. [89].	91

- 5.6 Method II of $B^2\Sigma^+$ ($v' = 1$) state predissociation measurement. In the third column, we introduce seven variables, that include a , n_1 , κ_1 , κ_2 , F_{B1a} , d_A and d_B , representing state preparation (from $X(v'' = 0)$ to $X(v'' = 1)$) efficiency, $X(v'' = 1)$ state natural population, cleanup efficiency of laser A_{1-0}^C , cleanup efficiency of laser A_{1-2}^C , $B(v' = 1)$ state predissociation probability, depletion efficiency of laser A_{1-1}^I , depletion efficiency of laser B_{1-1}^I , respectively. We denote the VBR normalization factors as $\mathcal{F}_{A_2} \equiv \sum_{i \in Z^+} F_{A1i}$, $\mathcal{F}_{A_3} \equiv \sum_{i \in Z^*, i \neq 1} F_{A1i}$, $\mathcal{F}_{A_4} \equiv \sum_{i \in Z^*, i \neq 2} F_{A1i}$, and $\mathcal{F}_{B_2} \equiv F_{B1a} + \sum_{i \in Z^*, i \neq 1} F_{B1i}$. A more complete table of vibrational population distribution downstream can be found in appendix Table 5.5.2. Table adopted from Ref. [89]. 92
- 5.7 Spin-orbit matrices accounting for mixing of vibrational states of the A and B states. The Π_x and Π_y basis states split under SOC to produce $\Pi_{1/2}$ and $\Pi_{3/2}$ states. Bottom, mixing between $A^2\Pi_{1/2}$ ($v' = 1$), $B^2\Sigma^+$ ($v' = 1$) and $B^2\Sigma^+$ ($v' = 0$). The Franck-Condon factor f is introduced to account for the off-diagonal vibrational wavefunction overlap. The diagonal terms represent the energies of the unperturbed states in units of cm^{-1} . Table adopted from Ref. [89]. 93
- 5.8 Complete stage information for $B^2\Sigma^+$ state predissociation measurement. Key information is presented in the main text and in Tables 5.4 5.5 and 5.6. For $B(v' = 0)$, we use five variables, including n_1 , κ , F_{B0a} , d_A and d_B , representing $X(v'' = 1)$ state natural population, cleanup efficiency of laser B_{1-0}^C , $B(v' = 0)$ state predissociation probability, depletion efficiency of laser A_{0-0}^I and depletion efficiency of laser B_{0-0}^I , respectively. For $B(v' = 1)$ method I, five variables are used, including a , n_1 , κ , F_{B1a} and d_B , representing state preparation (from $X(v'' = 0)$ to $X(v'' = 1)$) efficiency, $X(v'' = 1)$ state natural population, cleanup efficiency of laser A_{1-0}^C , $B(v' = 1)$ state predissociation probability, depletion efficiency of laser B_{1-1}^I , respectively. For $B(v' = 1)$ method II we use seven variables, that include a , n_1 , κ_1 , κ_2 , F_{B1a} , d_A and d_B , representing state preparation (from $X(v'' = 0)$ to $X(v'' = 1)$) efficiency, $X(v'' = 1)$ state natural population, cleanup efficiency of laser A_{1-0}^C , cleanup efficiency of laser A_{1-2}^C , $B(v' = 1)$ state predissociation probability, depletion efficiency of laser A_{1-1}^I , depletion efficiency of laser B_{1-1}^I , respectively. We denote the VBR normalization factors as $\mathcal{F}_{A_0} \equiv \sum_{i \in Z^+} F_{A0i}$, $\mathcal{F}_{A_1} \equiv \sum_{i \in Z^*, i \neq 1} F_{A0i}$, $\mathcal{F}_{A_2} \equiv \sum_{i \in Z^+} F_{A1i}$, $\mathcal{F}_{A_3} \equiv \sum_{i \in Z^*, i \neq 1} F_{A1i}$, $\mathcal{F}_{A_4} \equiv \sum_{i \in Z^*, i \neq 2} F_{A1i}$, $\mathcal{F}_{B_0} \equiv F_{B0a} + \sum_{i \in Z^*, i \neq 1} F_{B0i}$, $\mathcal{F}_{B_1} \equiv F_{B0a} + \sum_{i \in Z^+} F_{B0i}$, and $\mathcal{F}_{B_2} \equiv F_{B1a} + \sum_{i \in Z^*, i \neq 1} F_{B1i}$ 101

6.1 FCFs and VBRs for the measured transitions of CaH. The experimental radiative lifetime for the <i>A</i> state was obtained from Ref. [31] and for the <i>B</i> state from Ref. [32]. The excited state vibrational quantum number is always $\nu' = 0$. The $A(\nu' = 0) \leftarrow X(\nu'' = 0)$ excitation wavelength at 695.13 nm, the $B(\nu' = 0) \leftarrow X(\nu'' = 0)$ excitation wavelength at 635.12 nm, and the $B(\nu' = 0) \leftarrow X(\nu'' = 1)$ excitation wavelength at 690.37 nm were determined experimentally. The other transition wavelengths are derived using measured vibrational energies given in Ref. [27]. The calculated FCFs are obtained from [33] for the $A \rightarrow X$ decay and from [34] for the $B \rightarrow X$ decay. Error bars for the measured FCFs and VBRs are statistical standard errors. Table adopted from Ref. [30].	114
6.2 Measured parameter values that are used to calculate VBRs and FCFs for CaH given in Sec. 6.2.3. Table adopted from Ref. [30].	124
6.3 List of all dichroic filters used in the VBR and FCF measurements for CaH given in Sec. 6.2.3. All filters are purchased from Semrock, except FL635-10 which is purchased from Thorlabs. Table adopted from Ref. [30].	125
6.4 Measured CaH VBRs [106] and calculated CaH and CaD VBRs [203]. The calculated VBRs for CaH are in good agreement with our own calculations [89]. Table adopted from Ref. [88].	138
6.5 CaD transition frequencies used in this work. The uncertainties are \sim 10 MHz statistical and \sim 60 MHz systematic from the wavemeter. Table adopted from Ref. [88].	139

List of Figures

1.1	Elements (neutral atomic species) that have been laser cooled till 2016 are marked in blue. This thesis is about exploring the pathway to yield exotic atomic gases from molecules, using hydrogen as an example. Figure adopted from Ref. [14].	5
2.1	Potential energy curves (PEC, sometimes called potential energy surfaces, PES) of CaH. This indicates the PEC for most of the states relevant to our work with CaH and CaD, including $X^2\Sigma^+$, $A^2\Pi_{1/2}$, $B^2\Sigma^+$, $E^2\Pi_{1/2}$, etc. Figure adopted from Ref. [25].	16
2.2	Some of the lowest energy states in CaH, with quantum numbers labelled and energies, including energy differences in MHz. A reasonable error estimate for the energies is about 0.05MHz. The numbers are derived from Ref. [29].	24
3.1	What our experiment looks like on one of the optical tables.	27
3.2	The evolution of different cells. (a) The latest buffer gas cell. The base is similar to the design used in CaOH experiment from Doyle's lab at Harvard. We installed the second stage without additional cooling. Operating without a front mesh seems to work best in our case. (b) A different angle of the cell when it's taken out. It was still single stage when the picture was taken. (c) Buffer gas cell at early stage of the experiment. The key dimensions are basically the same, but the newer generation is more modular so it's easier to work with.	28
3.3	A schematic showing beam forward velocity vs. Reynolds number (flow rate). The lower bound is $1.2v_{0,s}$, where $v_{0,s}$ is the thermal velocity of CaH. At 6 K, $1.2v_{0,s} = 70$ m/s and $1.4v_{0,b} = 250$ m/s. Figure adopted from Ref. [35].	30

3.4 Zone of freezing. This data was taken in the way that, a calcium 423nm laser was shooting into the cell from the downstream of the beamline, and used a Thorlabs CMOS camera with imaging optics to detect the fluorescence from Calcium at different spatial location. We also vary the laser detuning to address different velocity classes in different sequences. The blue curve is closest to the cell aperture, and one can see the calcium forward velocity distribution seems slowest. While traveling till the green curve, which is 13cm away from the cell, the forward velocity has been altered to peak around 250m/s.	33
3.5 Interesting observations with targets. (a) two interesting things on a used CaH ₂ target. The white powder comes from exposing CaH ₂ in the air, very likely CaCO ₃ . The black coating is not well understood, and it can significantly reduce the signal over time. (b) the left target is CaD ₂ , and the right one is CaH ₂ solid. Both are fabricated from chemical reactions in the lab. (c) The calcium metal pieces that are more commonly used in the later stage of the experiment. (d) Left piece is compressed CaH ₂ pill and broken into two parts, and right piece is a regular CaH ₂ granule. (e) There can be some other significant coating on the surfaces of calcium pieces after running the experiments for a while, and the coating is still not well understood. We see black coatings and yellow coatings but this picture only shows yellow coatings.	34
3.6 Frequency engineering scheme to achieve full frequency control over both MOT and slowing light using a single laser source. Techniques such as the 1 GHz EOM will be discussed later in this section.	39
3.7 AOM ladder schematic for creating all frequency components needed for MOT light.	40
3.8 Laser alignment schematic for the slowing laser setup, including the main cycling laser and vibrational repumpers up to $v = 3$	41
3.9 Wavemeter sealing setup. We used a Thorlabs bare fiber, epoxied through a KF blank with a drilled center hole, and a set of vacuum nipples to construct the sealed enclosure. To reduce vibration-induced readout fluctuations, sorbothane pads were placed between the wavemeter and the chamber walls. This setup worked well. We no longer observe large, sudden drifts in the measured frequencies across all lasers. However, we still see a slow, regular frequency shift of about 10–20 MHz per month, which we believe is due to gradual temperature changes in the lab. Overall, we are satisfied with this improvement, but continuous calibration with an absolute frequency reference is a must. We previously used the 689 nm laser from our neighboring strontium dimer experiment, to calibrate the wavemeter, but it seems it is necessary to have a stable frequency source ourselves, aka potassium vapor cell.	42
3.10 The first iteration of the Galvo-based fiber switch.	43

3.11 Baking of the vacuum chamber (MOT section). (a) External bake. (b) In-situ bake. This brought the pressure below 10^{-10} Torr, beyond the detection range of both our ion gauge and residual gas analyzer (RGA).	46
3.12 Black painting on the interior of the vacuum chamber. (a) Main MOT chamber after painting. (b) In-vacuum RF MOT coils after painting.	47
3.13 Magnetization direction and shape of magnets	49
3.14 B in yz plain at $x=0$, and valley on the potential	50
3.15 B along x when $\rho = 0.25r_1$, and Hsin-I's S(x) function fitting result	51
3.16 another fitting function, and Sigmoid fitting function when $\rho = 0.5r_1$	51
3.17 stability of fitting parameter "d" in space. This plot gives the average $d = 3.1\text{mm}$, at $r_1 = 1.3\text{cm}$, $ll = 4.0\text{cm}$. The right figure is the direction of magnetic field in space	52
3.18 Simulation setup. Above is experiment geometry, below is python simulation parameter	54
3.19 trajectory without mag lens, and signal without mag lens	55
3.20 Parameter scanning results. (a)-(c) are the trajectory of molecules with different r_1 , noticing changes of focal length. (d)-(e) represent the normalized signal dependence on r_1 ll and dm , respectively.	56
3.21 Focal length scan	57
3.22 (a) At a given d_4 , we can vary r_1 and ll to achieve the similar shape of enhancement factor vs. forward velocity. And it was predicted in fig3.21. By tuning r_1 and ll we can compensate the effect caused by velocity. (b) Different detection position gives different enhancement factor.	58
3.23 The geometry designed to optimize for 100m/s and 150m/s at $d_4 = 1\text{m}$. The first number in the label is inner radius, the second is length.	59

3.24 Measured forward-velocity distributions of BaH molecules for a range of beam-aperture diameters and buffer-gas are slightly less reliable due to a mild sensitivity on specific data cuts flow rates. Velocity distributions above 250 m/s (dashed lines) made to reject fluorescence noise from ablation light. The small-scale structure at low velocities is an artifact of deconvolution. (a) Velocity distributions for three beam-aperture diameters. The inset shows a conservatively estimated cumulative population of molecules as a function of forward velocity under 100 m/s. The 5 mm aperture is optimal, although a slight enhancement of very slow molecules at rates of 11 ± 2 sccm were used. (b) Velocity distributions for four 50 m/s is observed for the 3 mm aperture. For this data set, He flow He flow rates and a 7 mm cell aperture, with the inset as in part (a). There is an enhancement of slow molecules at lower flow rates. Figure adopted from Ref. [43].	60
4.1 The enthalpies of several reactions that are being used or proposed to produce ultracold molecules through ablation induced buffer gas cooling. Within each table, the first row is the chemicals interested, the first column is the donor gas. The values are enthalpies of reaction. Orange box represent it's exothermic, while Blue box represent the reaction is the endothermic. From what can be clearly seeing reactions to form hydrides are all deeply endothermic reactions.	65
4.2 Horizontal cross section of the cryogenic buffer gas cell. Hot Ca atoms are generated via laser ablation of a solid target and subsequently react with H ₂ molecules that flow in at ~ 150 K. Additionally, ⁴ He flows in at ~ 6 K for efficient buffer gas cooling. The Ca atoms and the product molecules are probed through laser absorption, with optical access ~ 2 cm downstream from the target. Figure adopted from Ref. [83].	66
4.3 Chemical reaction in a cryogenic buffer gas cell. Time-averaged CaH density measurements (0-1 ms after ablation) as a function of Ca density, for 10 SCCM of H ₂ (red points) and 20 SCCM of H ₂ (blue points). The lines denote theoretical results at the same conditions, showing qualitative agreement. The inset shows reaction efficiency, defined as the ratio of CaH and Ca densities. A notable decrease in reaction efficiency is observed experimentally at higher Ca densities, whereas the theoretical model does not capture this trend, showing the need for further refinement. Experimental data points include 1- σ statistical errors. Figure adopted from Ref. [83].	67
4.4 Significant improvement of the use of $Ca + H_2 \rightarrow CaH + H$ reaction compared to the old way of forming CaH through ablation on CaH ₂ solid samples (as well as deuterium related experiments). The 20 times longer time constant comes from the better crystal structure of a calcium compared to CaH ₂ , making it less brittle. I do not have a good intuition to clearly explain why it improves the yield, but we know this reaction can happen fast despite its endothermic nature. What we know for sure is, the endothermic nature is still limiting CaH yield.	68

4.5 Time-averaged densities (0-1 ms after ablation) of Ca and CaH (or CaD) under different gas flow configurations. Reactant gases H ₂ , HD, or D ₂ are supplied at 20 SCCM, with He (if used) added at 8.8 SCCM. Ablation energy is 19 mJ per pulse. Green, yellow, and red bars represent results for H ₂ , HD, and D ₂ , respectively, while black-framed bars show the yields with He added. The dashed lines indicate the detection limits. Figure adopted from Ref. [83].	70
4.6 (a) Sample Ca density trace as a function of time after the ablation pulse. The blue curve is the original data, the orange line highlights the data used for fitting, and the green dashed line indicates the fitted result. This data is obtained with 8.8 SCCM He flow. (b) Measured collisional cross sections of He, H ₂ , HD, and D ₂ with Ca and CaH. Figure adopted from Ref. [83].	72
4.7 (a) Relative in-cell absorption for X ² Σ ⁺ (N = 0) and X ² Σ ⁺ (N = 2) states with respect to X ² Σ ⁺ (N = 1), versus ablation energy. Absorption for X ² Σ ⁺ (N = 3) and higher ro-vibronic states is below the detection limit and therefore neglected. Solid lines are fitted quadratic functions to guide the eyes. (b) Fitted rotational temperature versus ablation energy. Temperatures are extracted from a least-squares fit according to Eq. (4.4), as shown in inset (c). Figure adopted from Ref. [83].	74
4.8 Temperature-dependent rates for the (a) vibrational quenching of H ₂ and (b) vibrational excitation of H ₂ , where the subscripts denote the initial and final vibrational states of H ₂ , and (c) formation of CaH from the collision between Ca and H ₂ , where the subscripts denote the initial vibrational state of H ₂ . Figure adopted from Ref. [83].	76
4.9 (a) Ca absorption spectra at different ablation energies. The data is fitted with the Gaussian function. (b) The Ca plume temperature versus ablation energy. The gray shaded area represents the theoretical temperature that optimally matches with experimental results in the main panel of Fig. 4.3. Figure adopted from Ref. [83].	77

5.1	CaH molecular properties relevant to this work. (a) Potential energy surfaces (PES) for the 4 lowest electronic states - $X^2\Sigma^+$, $A^2\Pi$, $B^2\Sigma^+$ and $D^2\Sigma^+$. Spin-orbit interaction is not included here. The x-axis is the internuclear separation r in bohr radii (a_0) and the y-axis is energy in cm^{-1} ($1 \text{ cm}^{-1} \approx 30 \text{ GHz}$). The energy origin is chosen as the $\text{Ca}(^1S)+\text{H}(^2S)$ continuum threshold (v_{th}). Superimposed are the wavefunctions (bottom to top) for the $X(v'' = 0)$ absolute ground state, $X(v'' = 15)$ lowest energy bound state and $B(v' = 4)$ excited state. (b) Experimental layout used for this work. A buffer gas cooled molecular beam emanates from the cryogenic cell and encounters four spatially separated regions. The state preparation (S), interaction (I), clean-up (C) and detection (D) regions. Each region is composed of multipassed lasers described in the text. (c) Relevant vibrational branching ratios (squiggly arrows) calculated for the $B^2\Sigma^+$ state. Measured predissociation probabilities for the $B(v' = 0)$ and $B(v' = 1)$ are denoted by dashed lines. Figure adopted from Ref. [89].	81
5.2	Graphical illustration of ratio extractions process of $B^2\Sigma^+$ ($v' = 0$) predissociation measurement. We run the group of stages sequentially with a reference stage interlaced between other stages, and collect LIF with EMCCD. We integrate the images along both axes to obtain the signals, which we then used to calculate ratios. By repeating the whole sequence N times, we collect N sets of five ratios. In this figure, we first show an example sequence of one-shot camera images of the stages. We present the integrated signal along one axis, and use colored traces for science stages and black traces for reference stages. The horizontal lines represent the baseline in the plots. Lastly, we show the histograms of the five ratios individually. The vertical dashed line represents the mean of the ratios. The difference in distribution widths indicates that we are dominated by source fluctuation and detection noise. Figure adopted from Ref. [89].	104
5.3	Predissociation measurement results. Red squares are the theoretical calculation results from the non-radiative decay rates for different vibrational states of $B^2\Sigma^+$. The blue circles are the experimental results, where errorbars represent 95% confidence interval. Figure adopted from Ref. [89].	105

- 6.1 Experimental setup and molecular structure. (a) Experiment diagram (not to scale). CaH molecules and Ca atoms are produced via ablation of a solid target of CaH₂. The ejected molecules thermalize to the ~ 6 K ⁴He buffer gas and are extracted through a 3 mm diameter aperture. An additional 5 mm aperture is placed just before the molecular beam enters the interaction region to limit the transverse velocity distribution. The cooling chamber consists of 12 cm of optical access followed by a cleanup region and a detection region. (b) A sample image of molecules in the beam taken with the EMCCD camera. Photons are collected for 7 ms during imaging. Arrow indicates the direction of the molecular beam. (c) The main cooling line used in this work is the $A^2\Pi_{1/2}(\nu' = 0, J' = 1/2) \leftarrow X^2\Sigma^+(\nu'' = 0, N'' = 1)$ transition at 695 nm. We detect the molecular beam using the $B^2\Sigma^+(\nu' = 0, N' = 0) \leftarrow X^2\Sigma^+(\nu'' = 0, N'' = 1)$ transition using 2.6 W/cm² of 635 nm light. We employ laser light at 690 nm to repump molecules that decay to the $\nu'' = 1$ vibrational state in X by addressing the $B^2\Sigma^+(\nu' = 0, N' = 0) \leftarrow X^2\Sigma^+(\nu'' = 1, N'' = 1)$ transition. By closing this leak, we create a quasi-closed transition capable of cycling ~ 200 photons sufficient to exert a measurable Sisyphus force. (d) The 1.86 GHz spin-rotation splitting and the 54 MHz (101 MHz) hyperfine structure of the $J = 1/2$ ($J = 3/2$) states in the ground X manifold. The details of the laser setup can be found in Appendix 6.2.7. 109
- 6.2 Measurement of the VBRs for CaH molecules. (a) An example of PMT traces used to calculate the VBRs. These two time traces correspond to background-subtracted fluorescence from the decay to $X(\nu'' = 0)$ for PMTs P_1 (orange, dashed) and P_2 (blue, solid) while the $B^2\Sigma^+(\nu' = 0) \leftarrow X^2\Sigma^+(\nu'' = 0)$ transition is excited. Due to a different operating configuration, the molecular beam velocity is ~ 400 m/s for this data. The inset denotes how the ratio of integrated signals, R_0 , is computed. We perform a one-parameter fit of the dashed trace to the solid trace. The result of the fit produces the orange points that can be seen to overlap temporally with the blue trace. (b,c) The resulting VBRs from the measured ratio $R_{\nu''}$, obtained by evaluating Eq. (6.4), for the A and B states. Each point represents an average of at least 200 shots with background subtraction, while the higher vibrational decays require ~ 700 shots for an appreciable signal-to-noise ratio due to the low probability of decaying to these excited states. Error bars are statistical standard errors. Figure adopted from Ref. [30]. 113
- 6.3 Scattering rate measurement. The fraction of molecules remaining in the $X(\nu'' = 0)$ state when cycling on the $A(\nu' = 0) \leftarrow X(\nu'' = 0)$ transition (orange circles) and the fraction remaining in $X(\nu'' = 0) + X(\nu'' = 1)$ states when cycling simultaneously on the $A(\nu' = 0) \leftarrow X(\nu'' = 0)$ and the $B(\nu' = 0) \leftarrow X(\nu'' = 1)$ transitions (blue squares) are measured as a function of the interaction time. Lines are fits to exponential decay curves with finite offsets. The offset is due to detected molecules that are only weakly addressed in the interaction region. The exponential decay time constant τ from the fit is $5.5(3) \times 10^4$ s⁻¹ for the orange curve and $3.92(13) \times 10^3$ s⁻¹ for the blue curve. Figure adopted from Ref. [30]. 116

- 6.4 Magnetically assisted Sisyphus effect in CaH. (a) Molecular beam profiles obtained for an unperturbed beam (green), Sisyphus cooled beam (purple) at $\delta = +20$ MHz, and Sisyphus heated beam (blue) at $\delta = -20$ MHz. The y-axis is normalized to the unperturbed beam maximum and no other scale factors are used. Lines are fits to a 1D Gaussian function to obtain the $1/e$ cloud radius σ . The increase in on-axis molecule number seen in the cooling configuration is a clear signature of Sisyphus cooling. Statistical error for each point is represented by the bar on top right and is depicted separately for clarity. (b) Change in σ as a function of detuning, where $\Delta\sigma > 0$ implies heating and vice versa. The detuning is applied globally to each spin-rotation and hyperfine addressing lasers. The data was taken at an intensity of 200 mW/cm 2 . The band represents the result of OBE and MC simulations for our experimental system. (c) Change in beam size $\Delta\sigma$ as a function of laser intensity. Detuning has been fixed at $\delta = +20$ MHz. We do not saturate the Sisyphus cooling effect even at the largest available laser intensity (~ 300 mW/cm 2). The simulations shown as a band suggest that an intensity of >600 mW/cm 2 is required for saturation. (d) Change in beam size $\Delta\sigma$ as a function of magnetic field strength. Detuning is $\delta = +20$ MHz and intensity is 200 mW/cm 2 . Maximum cooling is seen for $B \approx 1$ G. Note that the scattering rate is maximized at $B \approx 3$ G. The Sisyphus effect is expected to be nulled at $B = 0$, but due to the presence of the Earth's magnetic field and the low laser intensity we do not resolve the dip. The simulation shows the same behavior. The bands shown in simulations encompass the spatial variation in laser intensity we expect in the experiment. Each point is a result of 200 repetitions of the experiment, and the experimental error bars are standard errors of Gaussian fitting. Figure adopted from Ref. [30]. 142
- 6.5 Laser configuration for Sisyphus cooling. (a) schematic of the Sisyphus cooling process in the $F' = 0 \leftarrow F'' = 1$ configuration. The standing wave formed by the overlap of the blue detuned, linearly polarized laser beam leads to a Stark-shifted potential hill. As a molecule (blue sphere) travels up this potential hill, it loses energy and is optically pumped to the excited state at the top of the hill. The spontaneous decay brings the molecule back to the dark ground state. Precession around an external magnetic field (\vec{B}) mixes the ground sublevels and brings the molecule back into the bright state to continue the process. (b) schematic of the interaction region. Blue arrow denotes molecular beam direction. Two separate laser beams are used to form independent standing waves. The first laser beam (1) containing both $A \leftarrow X(v'' = 0)$ and $B \leftarrow X(v'' = 1)$ frequencies enters the interaction region near the end and is retroreflected such that the spacing between adjacent passes gradually decreases. After 16 passes, the adjacent passes have sufficient overlap to form a standing wave. The second laser beam (2) only addresses $A \leftarrow X(v'' = 0)$ and can be added to obtain higher average intensities. (c) arrangement of ECDLs and ILAs used to generate the cooling and repump light and their combination. Some components such as mirrors and waveplates are omitted for simplicity. Note that the method of combination leads to an equal split of the cooling light into two fibers (1) and (2). Figure adopted from Ref. [30]. 143

- 6.6 (a) Schematic of the experiment viewed from above. CaD molecules are generated in a \sim 6 K CBGB source. The molecular beam is collimated by a 2.5-mm diameter aperture and enters the interaction region where it is addressed by the main cooling laser, copropagating with the ($v = 1$) repump laser. The laser beam is expanded to (10.8 mm \times 5.4 mm) $1/e^2$ diameter and retro-reflected to form a standing wave. The molecules then enter the clean-up region where only the ($v = 1$) repump laser is applied in a multipass configuration and are finally detected in the ($v = 0$) state. (b) Level structure of the main cycling transition $A^2\Pi_{1/2}(v' = 0, J' = 1/2, +) \leftarrow X^2\Sigma^+(v'' = 0, N'' = 1, -)$. The hyperfine splittings are adapted from Ref. [201]. (c) In-beam spectroscopy of the transition. The inset shows signal enhancement with rotational closure. Figure adopted from Ref. [88]. 144
- 6.7 Molecular beam profile with Sisyphus cooling and heating. (a-c) Beam images under unperturbed, Sisyphus cooling at +40 MHz, and Sisyphus heating at -40 MHz configurations, respectively. (d) Integrated 1D profile. Sisyphus cooling narrows the width of the center of the molecular beam (blue), while Sisyphus heating expels molecules away from the center (red). Unperturbed beam is shown as gray. Solid lines show the fits to the beam profile. Figure adopted from Ref. [88]. 144
- 6.8 Parameter scans of the Sisyphus effect. (a) Peak height change as a function of the main laser detuning, taken with magnetic field $|\vec{B}| = 1.7$ G and at 45° with respect to laser polarization. (b) Sisyphus cooling (blue circles) and heating (red squares) as a function of the main laser intensity, taken at ± 40 MHz detuning and the same magnetic field configuration as in (a). Saturation is not observed. The gray lines are guides to the eye for the unperturbed scenario (horizontal) and zero detuning (vertical in (a)). (c) Sisyphus cooling (blue circles) and heating (red squares) as a function of applied magnetic field, taken at ± 40 MHz detuning and maximum laser intensity. A sharp decrease in the strength of Sisyphus effect is observed when $|\vec{B}| \approx 0$. Error bars represent the 95% confidence intervals. Figure adopted from Ref. [88]. 145

- 6.9 Synthesis of CaD₂. (a) Illustration of the home-built setup used for the synthesis. The main reactor is a standard CF 2.75", 5" long 304 stainless steel nipple. The base is wrapped with heating tape connected to a variac via a temperature controller (Extech 48VFL). A standard J-type thermocouple attached to the base is used for temperature stabilization. A high-pressure gauge (MG1-100-A-9V-R) is placed close to the top of the reactor. All connections henceforth are VCR type. The reactor connects to a scroll pump and a Convectron gauge (MKS 275) via a tee. The other end of the tee connects to a D₂ cylinder using a long flexible hose. The regulator on the cylinder allows for control of the charging pressure, while the valves shown are used to direct the flow. (b) Pressure measured on the high-pressure gauge as a function of time at 450 °C. The reactor contains 3 g of Ca pieces. From an exponential fit, we obtain a reaction rate of $k = 0.11 \text{ min}^{-1}$. (c) Powder X-ray diffraction study of the resulting sample. Red lines are the known CaD₂ peaks. Almost all measured peaks match with the known CaD₂ values except for the peak at $2\theta = 37^\circ$. This peak could be attributed to CaO or Ca(OH)₂, possibly resulting from short contact with air. The results suggest very high conversion efficiency from Ca to CaD₂. Figure adopted from Ref. [88]. 146
- 6.10 Doppler cooling and heating as a function of laser detuning, A change in the molecular beam width demonstrate Doppler cooling (negative) and heating (positive). Error bars represent the 95% confidence intervals. Figure adopted from Ref. [88]. . 147
- 6.11 Two-photon background-free velocity detection of CaH. (a) Relevant level structure. CaH molecules are excited on the $A \leftarrow X$ transition at 695 nm and subsequently the $E \leftarrow A$ transition at 1668 nm. The photons emitted from E to X thus provide background-free detection at 490 nm. (b) Background-free spectroscopy of the $E^2\Pi_{1/2}(J' = 3/2, -) \leftarrow A^2\Pi_{1/2}(J = 3/2, +)$ transition. (c) Sample CaH velocity measurement. The $A \leftarrow X$ is applied transversely while the $E \leftarrow A$ laser is applied 45° relative to the molecular beam as a velocity sensitive probe. A PMT collects the 490 nm photons with temporal information. The white line marks the earliest possible arrival time for each velocity class. 147
- 6.12 White-light slowing of CaH molecules. (a) PMT signal of slowed molecules subtracted from unperturbed molecules at various velocities. An accumulation of lower-velocity molecules (highlighted red region) appears with slowing. (b) Time-integrated signal as a function of molecular velocity. Excess molecules below a typical MOT capture velocity (~10 m/s) are observed. 148
- 7.1 Excited state population versus B field, θ and Rabi rate in a 3+1 system. Different figures represent excited state population results at different total Rabi rate (equivalent to laser intensity). B field and Rabi rate are in unit of Γ , θ is in degree. 165

7.2	An example study of dependence on angle θ in a 3+1 system. This plot is generated for $B=0.45$, $\Omega=3$. Rabi matrix strength is the sum of total excitation to the ground state reflected in the hamiltonian. One can notice at 0 degree and 90 degree there is always some states being in dark, and around 55-65 degree the Rabi matrix is more balanced.	166
7.3	Excited state population versus B field, θ and Rabi rate in a 3+3 system. Different figures represent excited state population results at different total Rabi rate (equivalent to laser intensity). B field and Rabi rate are in unit of Γ , θ is in degree.	167
7.4	Excited state population versus B field, θ and Rabi rate in a 5+3 system. Different figures represent excited state population results at different total Rabi rate (equivalent to laser intensity). B field and Rabi rate are in unit of Γ , θ is in degree.	168
7.5	CaH optical cycling dependence on laser polarization angle and B field strength. (a) X axis is the angle of the waveplate that controls the X-A laser polarization angle with respect to applied B field. A θ degree change with the waveplate indicates a 2θ degree change with the laser polarization angle. Y axis is the normalized remaining population when we are doing the depletion experiment (deplete CaH from $v=0$ state to higher vibrational states through optical cycling in X-A 0-0 transition). A high remaining population indicates slow optical cycling, whereas a low population indicates fast cycling. (b) X axis is the strength of applied B field in unit of Gauss.	169
7.6	CaH system Hamiltonian diagonal terms in sequence. (a) before unitary transformation. (b) after transformation.	171
7.7	CaH system Hamiltonian off-diagonal terms top right corner part, and the bottom left corner matrix elements are the complex conjugate of the top right corner. There are no coupling between the ground states so the top left corner is mostly zeros. (a) before unitary transformation. (b) after transformation.	171
7.8	Two methods of calculating Rabi rate from laser power and gaussian beam size. . .	172
7.9	OBE result1: sweep B field strength and angle at different laser power conditions.	173

7.10 OBE result2: (a-d) change different B field strength, while varying J=3/2 two hyperfine laser power (Rabi rate) and monitor the excited state population. The conditions are: two SR components parallel to each other, group detuning = 0, θ = 60 degree (since we know this is when we have maximum scattering rate), J=1/2 laser power is fixed (30mW, $\Omega \approx 7\Gamma$ for F=0 and $\Omega \approx 4\Gamma$ for F=1). (e-h) change different B field strength, while varying J=1/2 two hyperfine laser power (Rabi rate) and monitor the excited state population. Here, group detuning = 0, θ = 60 degree, J=3/2 laser power is fixed (30mW). (i-j) Set all transitions to have the same Rabi rate, we can sweep this Rabi rate with B field strength and see the correspondance. (k-l) Study of how group detuning affects the excited state population with B field and θ	174
8.1 Simulation and calibration done for the RF MOT coil in DC configuration. (a) COMSOL simulated B field gradient under 1A of current. (b) the spatial direction of the field. (c) experimentally calibrated x direction (on plane) gradient to be 2.42Gs / cm / A. (d) calibrated z direction (on axis) gradient to be 4.83Gs / cm / A.	178
8.2 Thermal simulation and RF electronic driving circuits. (a) thermo simulation, using console for the initial version of MOT coil. The final version has similar thermal performance. (b) bottom view of the painted MOT coils. (c) RF driving circuits design. The tuneup capacitor is CVUN-1500AC/4-BEAA, and the LC residence circuit is made to be tunable at least 800 kHz to 1200 kHz. For wider frequencies one needs to replace the static capacitor. The impedance matching coils is approximately 5 to 30 rounds ratio, and the event for impedes is approximately 50 ohms. However, the RF amplifiers that we used are purchased from the eBay, and they don't seem to have 50 ohms impedance, leading to a not very ideal energy transfer. However, with a realization in (d), we are able to drive maximum at 12 A amplitude at 1MHz as shown in (e).	179
8.3 Proposed state-controlled photodissociation of CaH molecules [89]. (a) Calculated molecular potentials for CaH in its ground ($X^2\Sigma^+$) and first three excited (A , B and D) states. The lowest bound state of $A^2\Pi$ lies above the Ca+H dissociation continuum placed at 0 cm^{-1} . This implies that a molecule can spontaneously break apart into its constituent atoms when optically excited. The green curves are wavefunctions in the lowest $X(v = 0)$, threshold $X(v = v_{\text{th}})$, and $B(v = 4)$ states. The double-well structure of $B^2\Sigma$ suggests a two-photon molecule dissociation pathway, using laser light at 513 and 1745 nm. (b) Relative transition strengths between $B(v')$ and $X(v)$ vibrational levels, highlighting the ‘diagonal’ nature for low v' and a bifurcation at higher v' . The latter property suggests strong coupling of $v' \sim 4$ to both the absolute ground state of the molecule and the threshold states near dissociation. (c) Expected Rabi frequencies for the controlled dissociation process, with the $v' = 4$ level highlighted as an optimal choice.	182

A.1 Left is calcium $^1S_0 \rightarrow ^1P_1$ transition at 423nm in a beam configuration, right is the FVD measurement result using methods in the text.	205
A.2 Left plot is the diagram of CaH two photon background-free detection method. The $E^2\Pi_{1/2}$ to $X^2\Sigma^+$ decay photon is different from all laser sources in this system, leading to high SNR in the spectrum (middle plot) and FVD measurement (right plot).	207
A.3 Study of CaH ghosting effect. (a) For the $ X, N = 1, J = 3/2\rangle$ laser, we turn off EOM and park it at F=2 states, and perform FVD measurement. (b) we turn on EOM and park it in between F=1 and F=2, which is our regular detection method. (c) 1668 nm laser spectrum in velocity insensitive fashion when $ X, N = 1, J = 3/2\rangle$ laser is at different configurations. (d) 1668 nm laser spectrum in velocity insensitive fashion when $ X, N = 1, J = 3/2\rangle$ laser EOM is tuned. The legends 0, 150, 340 is proportional to the EOM modulation depth, where 0 means turned off, 340 means modulation depth is 1. (e) N=3 laser effect on the 1668 nm laser spectrum. (f) J=3/2 laser spectrum and its dependence on A-E laser.	209

Acknowledgements

During one's academic journey, it is not the grades that matter most, it is about what one learns throughout the journey. Fortunately enough, I learned a great deal of things during my PhD career, making this perhaps the most meaningful part of my thesis.

First of all, I would like to thank my PhD advisor, Professor Tanya Zelevinsky. She has played an important role in many of the most important decisions I made during my PhD time. I have always appreciated that her office door was open whenever we needed guidance. Her responses to my questions would always reveal themselves to be remarkably insightful. It takes great wisdom to offer such thoughtful and effective guidance, and I feel fortunate to have learned from her.

I would also like to thank Professor Debayan Mitra, the strongest postdoc and best mentor in this world, who spent three unforgettable years mentoring me. I can never forget all the laughter and joy shared over a few rounds of Voodoo Rangers, or his favorite Main Lunch. His existence solved a long-term puzzle for me: is it possible for a human being to be a combination of so many admirable qualities: wise, gentle, humble and decisive.

When I first joined the lab, I was lucky enough to be shined and supported by many brilliant minds, and received the most proper training as a junior grad student. Ivan and Rees taught me every detail of the experiments, *Laser Cooling 101*. 2020 was supposed to be the year of low efficiency, yet with relentless help from them, it became my most efficient year in learning. Chih-Hsi resurrected my long-gone dream as pianist with the Winter Wind of Chopin. Discussion between Konrad and Rees was always fun to watch. Kon, the man who knows everything, taught me many interesting ideas outside of the scope of my own research. Sebastian had the wildest dreams, and he was as cool as the name of his dog: Musashi. Emily was always the sunshine to the lab, and to me, even more.

Time flew by. By the time I realized it, I was already the oldest student in the lab. And I'm proud to say I was always surrounded by a group of great people who shine in different aspects. Jinyu / Jimmy / Oscar worked with me the longest, which means he needed to endure all my quirkiness longer than anyone else. I'm super happy and grateful to witness his growth and development over the past years, and there is no doubt that he can become an amazing professor, who cares about others' feelings, and remembers all his students' birthdays with his eidetic memories. A special thank-you note is for Brandon and Aaron, who offered me the most precious gift in my first two years, friendship. You may not know but it really matters a lot to me. The weirdest part is, till today I still don't understand why Brandy calls me "mom". Jianhui left us for Chicago so early but he is always open to share insights when we need him. Perry, Wenwei, Jingjing and Gisung joined us later and brought new energies and possibilities to the lab and their experiments. The future of the CaH experiment will lie on the shoulder of Ben, who is very warm and confident, and has everything needed to lead and bring the experiment to the next level. With more patience and time, I'm sure he will become a great scientist and leader, as well as photographer and film maker. I'm also grateful for a group of amazing undergraduate students that interned in my experiment, including Tianli, Shuhan, Issac, Alex, Andrei, Carson, Christine, Misha, Shuqi, Jintai, Antoine. I learned a lot from them and from this process. What cheers me up is that most of them will continue as graduate students in physics, at least I didn't discourage them haha.

For many people pursuing academia, publishing papers often means collaborating out of necessity. For me, it has felt quite different. I was fortunate to work with collaborators like Jesus, Rian, Claire, Anastassia, and Lan, who made every project feel less like work and more like spending time with friends. I learned a great deal from each of them, and I am truly grateful for their insight and support. A special thank you goes to Professor Mitra, whose initiative helps to bring these collaborations to life.

Despite all the drama and deeply bureaucratic style, Columbia is a special place where many brilliant minds of the world accumulate, and I feel myself lucky to be in this community.

My cohort is the first group of people I fought numerous battles (on the problem sets) with, Zihao, Karen, Jooyun et al, I do appreciate their support and help in many ways. The AMO community at Columbia, although small, has left me with precious memories. There were numerous serious academic discussions, there could also be karaoke and drinking and chitchatting. Shout out to Aaron and Weijun, it's always fun to spend time with you.

My Poopein' Ballers (basketball team) are probably the group of people who hear me yelling the most in the world, and I really cherish my time with you guys, especially when I got to block your shots after your trash talks (Aaron this is for you!). Grateful to my dearest bball friends, Yuewen, Chengzhu, HK, Aaron, Emily, and many others. My roommate, Ye, who is a great mentor and friend, saved me many times from heading in the wrong direction. The group of people that I hung out with most during my PhD must be the Reading Club, where knowledge was shared, together with countless beers and snacks. Xiao, David, En-hung, Xiong, Jiajin, Yuewen, Ji, Rain, we are all different, yet somehow unite and attract each other. Wishing a bright future for everybody.

Lucky as I am, many of the helps and guidance I received are not only from Columbia. I am also deeply connected with New York, USTC, and 1205 from Shanxi Experimental Secondary School. Here I'd like to thank all the people that helped me when I was applying for an internship and full time job, and everyone in the USTC AAGNY executive boards, and my best friends from high school. Wei, Kun, Haojun, Xiangyu, words cannot explain the deep friendship between us, trust and faith are probably the best gift I've ever received. A special note is for my best friend since high school, Wei. I've lost count of how many times we have deep chats that made Rain jealous. We somehow always feel to be at the exact same pace in almost every moment of life, even though we may be on different continents. That kind of synchronization let me know there is a strong, long-coherent quantum entanglement between us. To Wei and all my friends, we are each fighting our own battles, but time with old friends can be a healing to the wounds. May we all get what we want.

Everything I have accomplished all traces back to my parents. My mother not only provided

me with healthy food, but also the wisdom of life and nature. When I got excited for looking smart in some occasions, I always know there is a long way to go from smart to wise. With every new experience, there is a growing admiration to my mother, the greatest teacher in this world, beloved by all of her students including me. The simplest yet most profound lesson she and my father taught me, which remains the most challenging in this world, is how to be a good person. There are parts that I learned, there are also parts for me to master. I hope to continue learning them as I move forward.

Lastly, to the love of my life, Miss Rain. By the time I write this, we have been together for nearly 11 years. I like one of the lyrics from your favorite song: when you meet the right one, every day is Valentine's day. It describes our time these years precisely, and that's how lucky I am. There are ups and downs in life, not to mention life as a poor PhD student in a foreign country, uncertain of his direction. You provide me the warmest support when I need most, and share my happiness as my best friend. You cheered me up millions of times when I was down, and showed me the beauty and color of the world. My life would not be complete without you, and I eagerly look forward to exploring the world with you, wherever it may lead.

The first principle is that you must not fool yourself — and you are the easiest person to fool.

- Richard Feynman

Chapter 1: Introduction

Humans have always sought to understand the world and harness its power. As early as the 13th century BCE, ancient Chinese philosophers proposed the concept of the five elements — Metal, Wood, Water, Fire, and Earth — to explain the nature and transformation of matter. Similarly, in the 5th century BCE, Democritus introduced the idea of *atomos*, an indivisible unit of matter. Over thousands of years, these early ideas have evolved into a detailed understanding of molecules, atoms, and even smaller particles like quarks and leptons. This progress has led to the development of the Standard Model, the most comprehensive and successful framework in physics to date. But humanity’s curiosity never ceases, which motivates brilliant minds throughout history to continue exploring the boundaries of the objective world. One would hope to use physics to advance human technology, thereby making the world a better place. On the other hand, the Standard Model has its own limitations and will not be the final chapter of physics, indicating the need for measurement with extreme precision and complexity to find the beyond Standard Model (BSM) physics.

1.1 Cold and Ultracold Molecules

In the pursuit of these goals, ultracold molecules have emerged as versatile tools. Their complex internal structures enable a wide range of studies. There are two common ways to create trapped molecules at ultracold temperatures. The first is by assembling pre-trapped-and-cooled atoms to form molecules, typically through Feshbach Resonances (e.g. NaCs, KRb, SrRb, FrAg) or photoassociation (e.g. Sr₂, NaCs). The second method is direct laser cooling of the buffer-gas-cooled molecules, which will be the focus of this thesis. This section introduces several recent advancements in achieving quantum control of molecules and highlights their applications in various domains, to show the level of control over molecules at the moment.

1.1.1 Quantum Simulation and Computing

Ultracold molecules offer an ideal playground for simulating complex quantum systems due to their large dipole moments and theoretically long coherence times. Polar molecules interact via long-range dipole-dipole forces, making them ideal for emulating Bose-Hubbard and Fermi-Hubbard models in different regimes which could potentially explain phenomena such as high-temperature superconductivity and topological phases. Recently, Will Lab at Columbia first figured out how to suppress inelastic collisions between diatomic molecules (NaCs) [1, 2], and successfully cooled them to below 10 nK and formed the first BEC of polar molecules [3]. Besides that, Bakr Lab at Princeton successfully used quantum gas microscopy to study ultracold polar molecules (NaRb) confined in a 2D optical lattice [4]. With single-site resolution, they observed spin correlation and dynamics through implemented XY spin-exchange model.

Moreover, these advantages allow molecules to act as promising qubits in quantum computing, leveraging their rotational and hyperfine states to encode quantum information and facilitate efficient two-qubit gates. Recently, Ni Lab at Harvard first demonstrated the implementation of an iSWAP gate between molecular qubits using individually trapped NaCs molecules in optical tweezers [5]. The qubits are encoded in hyperfine states, which are stable and largely insensitive to environmental noise, enabling long coherence time.

1.1.2 Cold and Ultracold Chemistry

Advancements in cooling techniques have enabled the cooling of molecules to ultracold temperatures below 1 uK, offering unprecedented control over molecular interactions and reactions. These temperatures allow the investigation of chemical dynamics in regimes where quantum effects dominate, such as coherences and resonances. For example, Ni lab's research on KRb molecules demonstrated the formation of long-lived intermediate complexes during cold molecular collisions [6], and observed nuclear spin coherence conservation in these thought-to-be-chaotic dynamic chemical reactions $2KRb \rightarrow K_2 + Rb_2$ [7]. Additionally, Feshbach Resonances is also observed experimentally in Ketterle lab at MIT where a narrow (25 mG) but pronounced reso-

nance is found to be able to tune the collisional properties in between two triplet ground state NaLi molecules [8].

1.1.3 Precision Measurements

Molecules provide fertile ground for testing fundamental physics. One of the best examples that exemplify the supremacy of AMO techniques is the measurement of the electron electric dipole moment (eEDM). eEDM, predicted by the Standard Model to be exceedingly small ($\approx 10^{-39} e \cdot cm$), might be a few orders of magnitude larger as predicted by many particle physics models such as SUSY, or M theory. Due to the fact that eEDM is typically measured through applying strong electric field and magnetic field to measure Larmor precession frequency differences when flipping the fields, the signal is basically proportional to the strength of electric field. Electrons can experience strong intrinsic electric fields within a polarized molecule, typically a few orders of magnitude higher than what can be achieved in labs using electrodes. Experiments using molecular ions such as HfF⁺ [9] (JILA collaboration) and neutral molecules like ThO [10] (ACME collaboration) have set stringent limits on the EDM, surpassing the sensitivity of high-energy colliders (e.g. LHC) in certain scenarios. Future advancements propose using polyatomic molecules in optical traps [11], which promise increased coherence times and enhanced measurement precision.

Molecules can also be used as the probes for dark matter searches. There are various dark matter candidate particles, such as the axons, ultralight dark matter (UDM), weakly interacting massive particles (WIMPs), sterile neutrinos etc. [12]. And coupling between Standard Model particles and UDM may cause time variations in fundamental constants, such as the proton-to-electron mass ratio. In polyatomic molecules, like SrOH, the presence of nearly degenerate vibrational energy levels with different characteristics can significantly amplify relative energy shifts in molecular spectra arising from $\partial_t \mu$, thereby reducing the experimental complexity needed for high-sensitivity measurements [13].

Techniques such as molecular lattice clock can take advantage of various electronic and ro-vibrational states to select the transition that is most narrow and easy accessible, and perform

spectroscopy measurement. A single species molecular clock can have theoretically infinite coherence time, thus guaranteeing a better clock than atomic clock in the long future. The juicy physics behind this idea is the possibility to make clocks of different isotopes. Due to the difference in neutron number, the gravity between nucleus within a molecule can affect the state energies, in the way that is sensitive to the exact expression of gravity. Yukawa force, or the fifth force, predicts the gravity potential is different from Newton’s expression. And by comparing different isotopes of molecular clocks, one can measure or exclude certain regime of fifth force expression. All these developments mentioned above could lead to groundbreaking discoveries in BSM physics.

1.2 Trapping More Atomic Species

Since the pioneering work on laser cooling and trapping by Steven Chu, William Phillips, and Claude Cohen-Tannoudji, scientists have achieved unprecedented control over atomic systems. The demonstration of Bose-Einstein condensation (BEC) by Eric Cornell, Carl Wieman, and Wolfgang Ketterle marked a milestone, bringing atomic temperatures to the ultracold regime and enabling the exploration of novel quantum phenomena. Today, ultracold atoms are integral to many groundbreaking applications. One of the best examples that exemplify human enjoying the benefits of AMO techniques is the use of optical clock, which could be used to improve the resolution of GPS systems. Nowadays, with more and more limits broken down, Sr atoms in optical lattices can form the most precise optical clocks, capable of resolving gravitational redshifts on the millimeter scale. Similarly, Rydberg atoms, with their large dipole moments, enable long-range interactions, positioning neutral atom arrays as strong contenders in the quantum computing race. Ultracold atoms have also been pivotal in studying new phases of matter, such as superfluidity and supersolidity, and in determining fundamental constants with high precision.

However, it is fair to say the periodic table’s full potential remains untapped. Of the 118 known elements, less than a third of them have had their stable isotopes in neutral atomic form successfully laser-cooled and trapped [14] as shown in Fig. 1.1 (note that there have been some laser cooled species since the publication of this paper in 2016, such as Titanium, but the big picture remains

the same). Many elements are excluded due to experimental challenges, such as deep ultraviolet transition requirements or the absence of a cycling transition. Hydrogen, the simplest and most abundant element in this universe, exemplifies these difficulties.

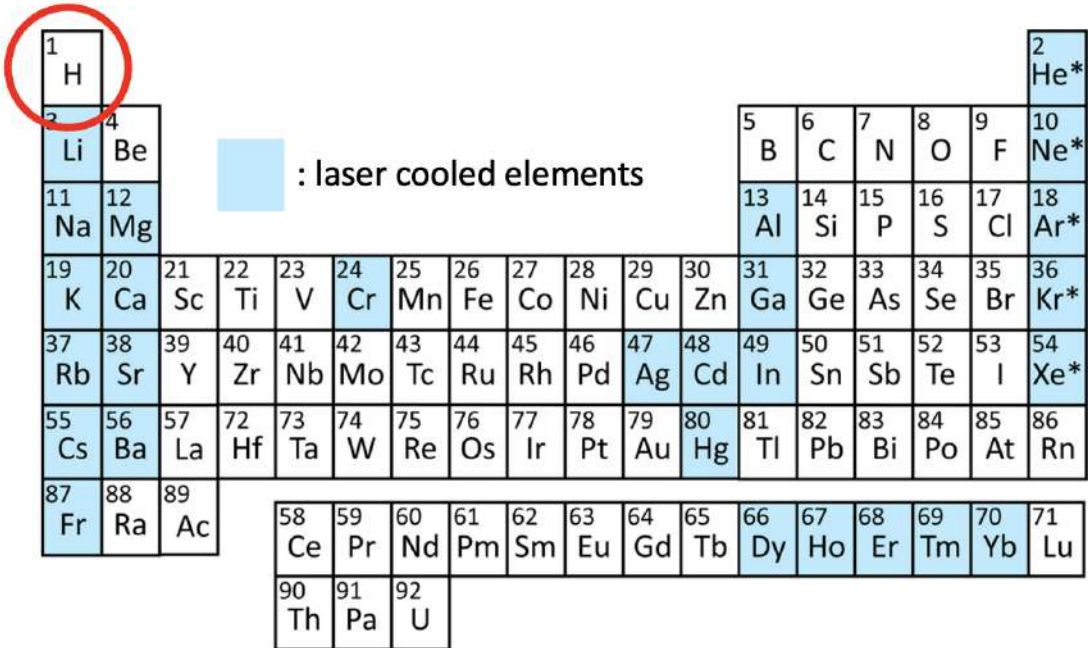


Figure 1.1: Elements (neutral atomic species) that have been laser cooled till 2016 are marked in blue. This thesis is about exploring the pathway to yield exotic atomic gases from molecules, using hydrogen as an example. Figure adopted from Ref. [14].

1.2.1 Hydrogen Spectroscopy

Hydrogen (${}^1\text{H}$), consisting of a single electron and a single proton, is the simplest and most thoroughly studied atom in physics. Owing to its structural simplicity and the lack of nuclear complexity, hydrogen provides a uniquely clean system for testing quantum electrodynamics (QED), determining fundamental constants, and probing possible physics beyond the Standard Model.

The energy levels of hydrogen can be expressed with exceptional theoretical precision. The bound-state energy of an electron in a hydrogen atom can be written as follows [15]:

$$E_n = hcR_\infty \left[-\frac{1}{n^2} + f_{n,l,j}(\alpha, \frac{m_e}{m_p}, \dots) + \delta_{0,l} \frac{C_{NS}}{n^3} r_p^2 \right], \quad (1.1)$$

where n , l , and j denote the principal quantum number, orbital angular momentum, and total angular momentum, respectively. The first term, $-\frac{1}{n^2}$, arises from the Coulomb potential and corresponds to the gross energy structure as described by the Bohr model. The second term, $f_{n,l,j}$, encapsulates higher-order corrections due to relativistic effects, reduced mass, fine and hyperfine structure, Lamb shifts, and QED loop corrections. It depends on several physical constants, most notably the fine-structure constant α and the electron-to-proton mass ratio m_e/m_p , both of which are independently measurable with high precision. The third term accounts for the finite size of the proton and only contributes to S-states ($l = 0$); it is proportional to the square of the proton's root-mean-square (RMS) charge radius r_p , with a coefficient C_{NS} that can also be theoretically calculated.

The prefactor hcR_∞ sets the energy scale, where the Rydberg constant R_∞ itself is expressible in terms of fundamental constants as

$$R_\infty = \frac{m_e e^4}{8\epsilon_0^2 h^3 c} = \frac{m_e c \alpha^2}{2h}.$$

A remarkable aspect of hydrogen spectroscopy is that the Lamb shift, which is a sensitive probe of QED, requires only a few input parameters for precise theoretical calculation. Among these, the proton charge radius r_p is the key limiting factor in theoretical uncertainty. While in principle r_p can be calculated from lattice QCD by modeling the proton's quark-gluon structure, such calculations remain challenging and uncertain. In practice, values of r_p are extracted from experimental data, such as elastic electron-proton scattering and high-precision hydrogen spectroscopy.

Proton Radius Puzzle One key motivation for my thesis work is the determination of the proton charge radius. Precise measurements of transitions such as 1S–2P (the Lamb shift) allow comparisons with QED theory, where the only uncertain parameter is r_p . This makes hydrogen spectroscopy a powerful tool to test lattice QCD predictions, search for new physics (e.g., violations of lepton universality), and refine fundamental constants such as the Rydberg constant.

The long-standing discrepancy between values of r_p extracted from regular hydrogen spec-

troscopy and those from muonic hydrogen experiments—commonly referred to as the proton radius puzzle—has brought renewed attention to hydrogen spectroscopy. The muonic hydrogen result ($0.84087(39)\text{fm}$), with its ~ 8 million times enhanced sensitivity to r_p due to the heavier mass of the muon, deviated from previous values (CODATA, $0.8775(51)\text{fm}$) by about 7 standard deviations [16]. This discrepancy prompted significant theoretical and experimental efforts to resolve the puzzle, including new hydrogen spectroscopy experiments, re-analysis of existing data, and improved electron-proton scattering measurements.

Ultracold Hydrogen for Spectroscopy Current hydrogen spectroscopy is performed using a fast beam of cold hydrogen, employing various techniques to reduce velocity, improve homogeneity, and lower the transverse temperature. This approach has enabled the highest precision hydrogen spectroscopy to date and has led to reduced uncertainty in proton radius measurements. However, it has several inherent disadvantages that limit its ultimate performance. One is the finite transverse temperature, which leads to significant Doppler broadening and second-order Doppler shifts, the dominant sources of error in the error budget [17]. Another issue is that the beam typically travels at relatively high velocities (200–1000 m/s), while the spectroscopic laser beam is only about 1 cm wide, limiting the interaction time to tens of microseconds.

To further push the frontier of precision, a promising direction is to perform hydrogen spectroscopy on ultracold, trapped hydrogen atoms. The advantages include narrow velocity distributions, reduced Doppler and transit-time broadening, longer interrogation times, and the possibility of single-atom control. These improvements could enable more precise measurements of transition frequencies, identifying Lamb shifts, and hyperfine splittings.

While laser cooling of hydrogen is technically challenging due to its deep UV transition (Lyman- α at 121.6 nm), alternative approaches such as buffer gas cooling followed by magnetic trapping [18] and moving optical lattices to decelerate hydrogen beams have been attempted [19]. The magnetic trapping method successfully achieved the first hydrogen BEC over 20 years ago. However, trapping buffer-gas-cooled hydrogen requires extremely large magnetic fields (typically generated

by superconducting coils, on the order of Teslas) to provide sufficient gradients. This results in a high average magnetic field across the ensemble, which poses calibration challenges and introduces systematic errors from Zeeman shifts, making it severe concerns for precision spectroscopy. To mitigate this, the field must be quenched or the atoms must be transported out of the magnetic trap. Unfortunately, that setup was eventually decommissioned before more research could be carried out.

The second method, pursued by Prof. Dylan Yost's group, has also made notable progress. Researchers have successfully applied a strong moving lattice to a hydrogen beam and slowed the atoms by 20 m/s. With continued upgrades and technical improvements, it is theoretically possible to decelerate them by up to 400 m/s and load them into an optical lattice.

As described above, creating an ultracold, optically trapped hydrogen gas for high-precision spectroscopy is technically challenging. This naturally leads to the question: is there another, perhaps better, way to achieve this? My answer is, *yes, my friend, yes*.

1.3 Molecules as a Pathway to Exotic Atomic Gases

As mentioned above, tremendous progress has been made in achieving quantum control of molecules, and many atomic species are still difficult to laser cool directly. It is natural to ask: is it possible to trap molecules first and then dissociate them to obtain cold, trapped atoms? This thesis is dedicated to answering that question in the context of hydrogen. But before diving into the details, let's break it down into smaller parts: How do we get cold molecules? How can we dissociate them? And can the resulting atoms stay cold after dissociation? I'll discuss these one by one.

1.3.1 How to Get Cold Molecules

There are generally two approaches to obtaining ultracold molecules today. The first is by assembling ultracold atoms. Atom species such as alkali atoms, alkaline earth atoms, and some lanthanide atoms have been laser cooled and trapped to ultracold temperatures. Molecules can then

be formed via photoassociation or magneto-association. This method has been very successful; researchers have produced molecules such as NaCs, NaK, KRb, NaLi, Sr₂, Li₂, etc. Its advantages include high molecular number and high phase-space density. However, a clear disadvantage is the limited choice of atoms. And for my purpose (using molecules to generate atoms) it isn't applicable obviously. Additionally, molecules formed this way typically lack optical cycling transitions, making further laser cooling difficult. That said, this class of molecules has demonstrated potential in areas like quantum simulation and computation.

The second approach is buffer gas cooling. Molecules are generated by chemical reactions or laser ablation and then immersed in a cold buffer gas environment, such as helium or argon. Collisions with the buffer gas cool both translational and ro-vibrational degrees of freedom. This method can produce a cold molecular beam, which can then be further slowed and trapped using different techniques.

Option 1: The most successful method here is direct laser slowing and trapping, which has been demonstrated with molecules like SrF, CaF, YO, CaOH, SrOH, and BaF. The basic idea is to treat molecules similarly to alkali atoms, using photons to remove entropy from the system. This method relies on the existence of a semi-closed optical cycling transition that allows the scattering of more than 10,000 photons. This thesis focuses on applying this method to calcium hydride (CaH). However, this method is not entirely general. One potential limitation is that if too many lasers are required to repump leakage states, the experiment becomes too complex and unappealing. The complex structure of molecules also introduces new challenges, such as photodissociation and predissociation. If you work with molecules containing ytterbium, for example, you might run into issues caused by inner-shell orbitals. So, this method isn't universally applicable.

Option 2: Another attractive method is to use electric fields to slow and confine molecules. Since most molecules (except homonuclear ones) have permanent dipole moments, spatially and temporally varying electric fields can be engineered to convert kinetic energy into Stark potential energy, which can be dissipated by switching off the field. Although this method typically yields low phase-space densities and can't reach the lowest temperatures, it can be applied to a broader

range of species. The dipole moment of CaH is around 2 Debye, making this method potentially viable for slowing CaH.

Other options: Researchers have also explored other methods for either general trapping or specialized for a certain class of molecules. For example, similar to a Stark decelerator, one can use an optical cavity to generate extremely strong light fields and leverage the AC Stark effect to directly trap buffer-gas-cooled molecules [20]. Another approach is the Zeeman-Sisyphus effect, which uses strong magnetic fields to convert kinetic energy into Zeeman energy, dissipated via optical cycling [18]. There are proposals to use the strong dipole moments of Rydberg atoms to slow and stop molecules [21], though it has yet to be realized.

As will be discussed later in this thesis, option 1 appears most suitable for CaH. Other methods may be used for future exploration but are beyond the scope of this thesis. The point is, we have a viable direction for slowing and trapping the CaH molecules, as the first step towards a more generalized machine.

1.3.2 How Can We Dissociate Them

We assume that the trapped molecules are in their ground electronic and vibrational states (not necessarily in the rotational ground state). A brute-force approach to dissociation would be to excite the molecule to a dissociative state, causing it to break apart and release a large amount of kinetic energy. We avoid this approach for the increased temperature on the product species, which can easily become hundreds of kelvin (sub-eV energy).

Instead, we aim for quantum-state-controlled and selective dissociation to minimize energy insertion. Researchers have demonstrated such controlled dissociation after first assembling molecules. For example, molecules formed via photoassociation or magneto-association can be dissociated by reversing the process, which is now fairly routine. However, to date, no one has attempted to dissociate directly cooled molecules in this way. We should assess the feasibility of different methods.

Can we do magneto-dissociation with CaH? Probably not. Calcium has a closed-shell electronic structure, making it difficult to tune magnetic fields to match the energy between the closed

and open channels. Calcium has two valence electrons and no nuclear spin, so its ground state has $s = 0$, $l = 0$, $J = 0$, resulting in weak magnetic responses. Its excited states may have non-zero spin, but the number of available states is far fewer than in alkali atoms. Therefore, it's hard to find overlapping energy trajectories in the B–E (magnetic field vs energy) diagram. While I haven't fully explored this, I suspect any Feshbach resonances in CaH would occur at extremely high magnetic fields, not easily achievable with standard coil setups.

A more promising route is photodissociation (PD). Let's first look at what has been done with Sr₂ molecules from our lab. Assuming molecules are prepared in the ground vibrational state, researchers use two lasers to adiabatically transfer the population into a weakly bound state (typically $v = -1$ in the ground potential) using Stimulated Raman Adiabatic Passage (STIRAP) [22]. We'll discuss STIRAP in more detail in later chapters. While it's possible to use a direct Raman process, STIRAP takes advantage of creating a dark state that avoids populating the intermediate state, thereby increasing transfer efficiency. Theoretically, more than 99% transfer efficiency is possible, though achieving this in practice requires very careful engineering. Nowadays, 90% efficiency is considered realistic. After preparing Sr₂ in the $v = -1$ state, researchers use either single- or two-photon PD to break the molecule apart. This requires identifying an excited state that overlaps well with both the bound state and the continuum, and then implementing a two-photon Raman transition to reach the dissociated atomic states.

Our plan with CaH is similar, with one difference: we aim to use STIRAP to directly transfer population from the ground vibrational state to an unbound excited state. This is theoretically feasible, and I'll go into more detail in later chapters.

1.3.3 Can the Product Atoms Stay Cold after Dissociation

Based on experience with Sr₂ (photodissociation) and NaCs (magneto-dissociation) at Columbia, atoms tend to heat up slightly after molecular dissociation. This is likely due to imperfections in laser intensity, frequency noise, or magnetic field fluctuations, which couple the system to continuum states with higher kinetic energy. However, the resulting heating appears manageable,

detectable but not too significant. Let's assume the heating effect is minimal.

That said, our case is unique due to the large mass difference between the two atomic species—Calcium (40 amu) and Hydrogen (1 amu). This mass ratio changes the dynamics. Assuming no external energy is introduced and the process is perfectly controlled, the product atoms (Ca and H) should inherit the velocity distribution of the parent molecule (CaH). According to the Maxwell-Boltzmann distribution,

$$f(v) = \left(\frac{m}{2\pi k_B T} \right)^{3/2} 4\pi v^2 \exp \left(-\frac{mv^2}{2k_B T} \right)$$

If the velocity distribution stays the same but the mass is 40 times smaller, the effective temperature (scaling with mass) will be reduced by a factor of 40. To some extent, this means we can achieve additional cooling of hydrogen atoms through molecular dissociation [23]. While heating effects exist, there is currently no theoretical or experimental evidence suggesting they disproportionately affect the lighter species. This makes it an open and intriguing question.

1.4 Structure of This Thesis

This thesis outlines the essential steps toward creating ultracold atoms from molecules, using CaH and CaD as case studies.

Chapter 2 provides foundational background on the CaH molecule. I introduce the nomenclature and core properties of CaH, including its molecular structure, spectroscopic constants, vibrational branching ratios, and other characteristics relevant to laser cooling.

Chapter 3 describes the experimental hardware, including the cryogenic setup, laser systems, vacuum system, and other critical components necessary for producing and manipulating cold molecular beams.

Chapter 4 explores the creation of a good molecular source. I investigate the use of endothermic reactions in a cryogenic buffer gas cell to generate a stable and intense beam of CaH. Surprising experimental results are discussed, along with the theoretical understanding that supports them.

Chapter 5 examines whether CaH is amenable to laser slowing in the presence of predissociation. Through a combination of experimental measurement and theoretical modeling, I assess the feasibility of scattering sufficient photons to enable a magneto-optical trap (MOT), provided that repumping states are chosen carefully.

Chapter 6 presents the laser cooling and slowing experiments performed on CaH and CaD. I describe the technical challenges, theoretical simulations, and experimental progress, demonstrating that a strong optical force can indeed be applied to these molecules.

Chapter 7 focuses on one of my theoretical contributions. I discuss my understanding and modeling of the optical Bloch equations as applied to CaH-type molecules, and how these insights guide the design of cooling strategies.

Finally, Chapter 8 outlines future directions, including the path toward realizing a three-dimensional MOT and the next steps for producing ultracold atomic gases via controlled molecular dissociation. I also discuss the implications of a recent theoretical collaboration and how its results inform our project.

Chapter 2: Basic Information about CaH

2.1 Molecular Structure

One of the most interesting aspects of working on a molecular experiment is that molecules are much more complex than atoms, due to their additional internal degrees of freedom. This complexity leads to a richer structure and a corresponding increase in the number of quantum numbers required to specify a state. Understanding these notations should be the first step in *Molecular Experiment 101*.

Fortunately, the Born-Oppenheimer approximation allows us to factor this complexity into manageable layers. It postulates that the electronic, vibrational, and rotational degrees of freedom of a diatomic molecule can be treated independently to zeroth order. Consequently, the total Hamiltonian can be written as:

$$H = H_e + H_{SO} + H_{vib} + H_{rot} + H_{SR} + H_{HFS} + H_{\Lambda d} \quad (2.1)$$

Here, H_e , H_{SO} , H_{vib} , H_{rot} , H_{SR} , H_{HFS} , $H_{\Lambda d}$ represent the electronic, spin-orbit, vibrational, rotational, spin-rotational, hyperfine, and Λ -doubling contributions, respectively.

If you are interested in a detailed and pedagogical breakdown of different terms and how these angular momenta couple in different Hund's cases, I recommend reading Sec. II of John Barry's thesis [24]. In my thesis, I only focus on CaH, without being general; although many alkaline earth monohydrides and monofluorides (such as CaF, SrF, and BaF) share quite similar structures, especially in the ground and low-lying excited states relevant for laser cooling. One notable exception is YO, which exhibits different Hund's cases.

2.1.1 Electronic and Spin-orbit Levels

It is conventional to label electronic states in diatomic molecules using letters. The ground state is always called X. Excited states are labeled with capital letters A, B, C, and so on by the order of discovery (yes it's not a typo). Although in principle, the letters follow the order of increasing energy. It is reasonable to make an analogy to atomic physics here: these letters are similar to the main quantum number n in alkali atoms, they represent the largest energy scale in a molecular system. Other than that, the second part of notation for electronic states typically takes the form:

$$^{2S+1}\Lambda_{\Omega}^{(+/-)} \quad (2.2)$$

Here, S is the total electronic spin ($1/2$ for CaH), Λ is the projection of the electronic orbital angular momentum on the internuclear axis ($\Sigma = 0$, $\Pi = 1$, $\Delta = 2$, etc.), and $\Omega = |\Lambda \pm \Sigma|$ is the projection of the total electronic angular momentum on the axis. The $+/-$ indicates reflection symmetry with respect to a plane containing the internuclear axis.

For CaH, the ground state is $X^2\Sigma^+$, with $\Lambda = 0$, and thus $\Omega = 1/2$. There are no other Ω values, so there is no spin-orbit splitting in the ground state. The first excited state used in laser cooling is typically $A^2\Pi_{1/2}$, where spin-orbit coupling splits the $\Lambda = 1$ level into $\Omega = 1/2$ and $\Omega = 3/2$ components. The spin-orbit coupling constant A (a spectroscopic constant) determines the separation between these levels, typically on the order of hundreds of cm^{-1} .

2.1.2 Vibrational and Rotational Levels

Each electronic state supports a ladder of vibrational levels, with spacings typically in the tens of THz. These vibrational levels come from the motion of the two nuclei within the molecule, which to zeroth order can be modeled as a quantum harmonic oscillator. However, real molecules are not perfectly harmonic: the bond can stretch and eventually break. A more realistic potential, or to say, a better approximation, that captures this behavior is the Morse potential, which accounts for the anharmonicity of the bond and gives a finite number of bound vibrational states.

Because of this anharmonicity, the spacing between vibrational levels gets slightly smaller as v increases. The energy levels are usually expressed as:

$$G(v) = \omega_e \left(v + \frac{1}{2} \right) - \omega_e \chi_e \left(v + \frac{1}{2} \right)^2 + \dots \quad (2.3)$$

Here, ω_e is the harmonic vibrational constant, and χ_e is the anharmonic correction factor. The first term gives the evenly spaced levels you'd expect from a harmonic oscillator, and the second term gives the leading-order correction from the Morse potential. For CaH, it can be seen from Fig. 2.2, $X^2\Sigma^+$, $A^2\Pi_{1/2}$ and $E^2\Pi_{1/2}$ states look more similar to Morse potential, but $B^2\Sigma^+$ states look very different, as they exhibit a unique double-well potential. This potential arises from two overlapping states that interact strongly with each other.

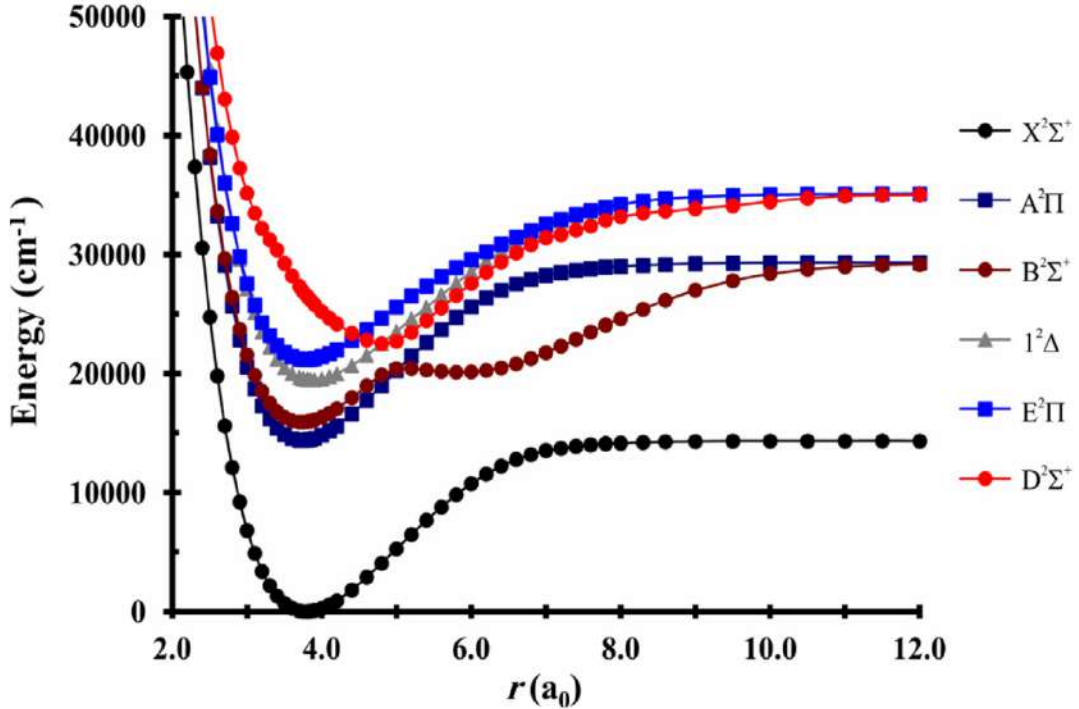


Figure 2.1: Potential energy curves (PEC, sometimes called potential energy surfaces, PES) of CaH. This indicates the PEC for most of the states relevant to our work with CaH and CaD, including $X^2\Sigma^+$, $A^2\Pi_{1/2}$, $B^2\Sigma^+$, $E^2\Pi_{1/2}$, etc. Figure adopted from Ref. [25].

It is worth mentioning that the transitions between different vibrational states are not governed by selection rules, so when molecules are in the excited states, such as $A^2\Pi_{1/2}$ $v=0$ states, when it

spontaneously decays, it may land in almost any vibrational level but with different probabilities. The probabilities are called vibrational branching ratios (VBR), and will be discussed later this section.

The rotational levels, built on top of each vibrational level, are spaced by ~ 100 GHz and are well described by the rigid rotor model:

$$F_v(N) = B_v N(N+1) - D_v N^2(N+1)^2 + \dots \quad (2.4)$$

Here, N is the rotational angular momentum excluding spin, with values of 0,1,2 and above. B_v is the rotational constant for vibrational level v , and D_v accounts for centrifugal distortion. It's worth noting that N is a good quantum number in Hund's case b (which applied to $X^2\Sigma^+$ and $B^2\Sigma^+$), but not a good quantum number in Hund's case a ($A^2\Pi_{1/2}$ and $E^2\Pi_{1/2}$).

It is important to know that there are selection rules governing rotational state transitions. This is because in Hund's case b, nearby rotational states will possess different parity, and electric dipole transitions have to rely on a change of parity (here, the parity refers to wavefunction parity). As an example, $N=0$ in the ground states can only be excited to $N=1$ in the excited states, $N=1$ in the ground states can be excited to $N=0$ & $N=2$ in the excited states, and $N=0$ in the excited states can only decay to $N=1$ in the ground state. Using that smartly, we can reduce the number of lasers in our experiment, by choosing the transitions from $N=1$ in the ground states to $N=0$ in the excited states, such that it decays back to the original state.

2.1.3 Spin-rotation Coupling

In a ${}^2\Sigma$ state, the spin and rotational angular momentum are weakly coupled. The Hamiltonian for spin-rotation interaction is:

$$H_{SR} = \gamma \vec{S} \cdot \vec{N} \quad (2.5)$$

This term splits each rotational level into two $J = N \pm 1/2$ components because $S = 1/2$. The

spin-rotation constant γ is typically ~ 2 GHz in the $X^2\Sigma^+$ manifolds in CaH.

2.1.4 Hyperfine Structure

For CaH and CaD, the hydrogen or deuterium nucleus carries nuclear spin $I = 1/2$ or 1, respectively. The hyperfine Hamiltonian is:

$$H_{HFS} = b \vec{I} \cdot \vec{S} + c (\vec{I} \cdot \vec{z})(\vec{S} \cdot \vec{z}) + C \vec{I} \cdot \vec{N} \quad (2.6)$$

Here, b , c and C are the hyperfine constant, dipole-dipole constant, and nuclear spin-rotation constants.

Hyperfine interactions further split the J levels into $F = |J \pm I|$ manifolds. For $I = 1/2$, each J state splits into two F states. The resulting energy splittings are on the order of tens of MHz. For CaD, the larger nuclear spin ($I = 1$) and quadrupole moment of deuterium leads to richer structure with three F levels per J .

This spin-rotation and hyperfine structure is crucial in designing laser cooling and detection schemes, as it determines the number of resolved transitions and required frequency components in the laser setup. One of the technical challenges is posed by the large spin-rotation spacing: whether a single laser can be used to address this large spin-rotation spacing (~ 2 GHz) and relatively minor hyperfine spacing (~ 100 MHz).

2.1.5 Hund's Case a and b

To make sense of how different angular momenta couple in molecules, especially when assigning quantum numbers or interpreting spectra, it's important to understand the Hund's case formalism. Among the several coupling schemes, Hund's case (a) and (b) are the two most relevant for CaH.

Hund's case (a) describes the situation where both the electronic orbital angular momentum Λ and spin angular momentum S are strongly coupled to the internuclear axis. In this case, their projections add to form $\Omega = \Lambda + \Sigma$, and the total angular momentum (excluding nuclear spin) is

$J = \Omega + R$, where R is the rotational angular momentum of the nuclei. This scheme applies well to states with non-zero Λ , like $^2\Pi$ or $^2\Delta$ states. For example, in CaH, the excited $A^2\Pi_{1/2}$ and $E^2\Pi_{1/2}$ states are described by Hund's case (a), because the orbital angular momentum $\Lambda = 1$ dominates the coupling. The good quantum numbers are therefore: $\Lambda, S, \Sigma, J, \Omega$.

On the other hand, in Hund's case (b), the orbital angular momentum is either zero or weakly coupled to the internuclear axis. Here, the total angular momentum J is formed by coupling the rotational angular momentum N (which includes the motion of the nuclei but not the electron spin) with the electronic spin S : $J = N + S$. This case is relevant for $^2\Sigma$ states, such as the CaH ground state $X^2\Sigma^+$ and excited state $B^2\Sigma^+$, where $\Lambda = 0$ and the spin-rotation interaction provides a relatively small perturbation. The good quantum numbers are therefore: Λ, N, S, J .

In practice, the real eigenstates of the system are often intermediate between these idealized cases, especially in low-lying rotational levels where spin-rotation and spin-orbit couplings are comparable. However, Hund's case (a) and (b) serve as very useful limits for labeling states and interpreting experimental spectra.

2.2 Summary of CaH

Before discussing our experiment to laser cool the calcium hydride molecule, It is critical to understand the basic properties of calcium hydride. Also, it takes a while to get used to the molecular state nomenclature for beginners. I may also cover some basic information about CaH_2 molecules because in the early phase of the experiment we typically used a CaH_2 solid target to create CaH molecules.

CaH is a small diatomic radical, consisting of a calcium atom bonded to a hydrogen atom. The calcium atom has two valence electrons, where one is used to form a covalent bond with hydrogen, and the other electron is shared as the valence electron and makes up the electronic states of the molecule. The valence electron's wavefunction is typically localized around the calcium nucleus.

2.2.1 Physical Properties

Melting point: CaH decomposes upon melting, typically above 1000°C. It's not a volatile species but it oxides easily. Normally in our experiments, we study the gas phase CaH. CaH₂ has a melting point of 816°C. Upon ablation, the temperature is typically in the order of a few thousands kelvin.

Color and crystal structure: In solid form, CaH appears as a white or grey powder. In the gas phase, the color is not relevant, but its optical transitions lie in the red to blue region of the spectrum. And the CaH₂ solid sample is crystallized, but it's relatively brittle, due to its ionic lattice and limited slip systems.

2.2.2 Spectroscopy Relevant

This section may have the highest information density in my thesis. We are, in some sense, spectroscopists, so spectroscopic properties of CaH matter a lot. Here is the summary of a few optical properties of CaH, including:

- The spectroscopic constants for most of the interested states of CaH are listed (in GHz for convenience) in Table 2.1.
- The state energies for most of the interested states of CaH are listed in Table 2.2.
- All the transitions that we have been measured with CaH (including some theoretical values if noted) in Table 2.3.
- Some $X^2\Sigma^+$ states HFS energies with high precision (from Ref. [26]) in Fig. 2.2.

2.2.3 Optical Cycling Properties

A state of CaH has 33ns lifetime, leading to 4.8MHz natural linewidth ($1/33\text{ns}/2\pi$). B state has 58ns lifetime, so the linewidth is 2.7MHz.

State	Parameter	v=0	v=1	v=2
X	T_v	0	37802.207	74336.617
	B_v	126.81	123.893	121.033
	γ_v	1.306	1.261	1.216
	$10^4 D_v$	55.512	55.467	55.458
A	T_v	432471.287	471044.445	509461.4
	A_v	2394.319	2391.532	2389.354
	B_v	129.334	126.189	122.944
	γ_v	12.811	12.571	12.367
	$10^4 D_v$	54.925	54.699	54.366
B	T_v	472269.334	509632.048	545143.214
	B_v	132.58	129.128	125.447
	γ_v	-21.927	-21.12	-18.162
	$10^4 D_v$	66.437	67.939	79.26
E	T_v	611396.039	646847.18	-
	A_v	717.728	754.537	-
	B_v	128.643	124.823	-
	γ_v	-4.581	-5.509	-
	$10^4 D_v$	67.59	67.477	-

Table 2.1: Spectroscopic constants of CaH in units of GHz (instead of cm^{-1} for convenience)

The vibrational branching ratio (VBR) and Frank-Condon factors (FCFs) are also measured experimentally, which will be illustrated in detail in Chapter 6, here we will briefly introduce them.

Physically, FCFs are the squared overlap integrals between vibrational wavefunctions in the excited and ground electronic states, so they capture how likely it is for the nuclei to remain in the same configuration during an electronic excitation or decay. The more similar the vibrational wavefunctions are between two levels, the higher the FCF.

In experiments, what really matters is the VBR, which tells us the fraction of spontaneous decays from a given excited vibrational level (say $v' = 0$ in the $A^2\Pi_{1/2}$ or $B^2\Sigma^+$ state) that land in a particular ground-state vibrational level v'' . VBRs are closely related to FCFs, but not identical. They also account for the ω^3 dependence of the spontaneous emission rate due to electric dipole radiation. The formula that connects the two is [30]:

State	Ω	v	N	J	parity 1	parity 2	label	E (GHz)	E (cm^{-1})
X	0.5	0	0	0.5	+	e	F1	0.000	0.0000
X	0.5	0	1	0.5	-	f	F2	252.218	8.4131
X	0.5	0	1	1.5	-	e	F1	254.177	8.4784
X	0.5	0	2	1.5	+	f	F2	758.480	25.3002
X	0.5	0	2	2.5	+	e	F1	761.743	25.4090
X	0.5	0	3	2.5	-	f	F2	1517.867	50.6306
X	0.5	0	3	3.5	-	e	F1	1522.433	50.7829
X	0.5	0	4	3.5	+	f	F2	2529.982	84.3911
X	0.5	0	4	4.5	+	e	F1	2535.845	84.5867
X	0.5	1	0	0.5	+	e	F1	37777.672	1260.1275
X	0.5	1	1	0.5	-	f	F2	38024.119	1268.3481
X	0.5	1	1	1.5	-	e	F1	38026.014	1268.4113
X	0.5	1	2	1.5	+	f	F2	38518.777	1284.8481
X	0.5	1	2	2.5	+	e	F1	38521.931	1284.9533
X	0.5	2	0	0.5	+	e	F1	74408.446	2481.9986
X	0.5	2	1	0.5	-	f	F2	74649.093	2490.0257
X	0.5	2	1	1.5	-	e	F1	74650.918	2490.0866
X	0.5	2	2	1.5	+	f	F2	75132.082	2506.1365
X	0.5	2	2	2.5	+	e	F1	75135.125	2506.2380
A	0.5	0	0	0.5	-	f	F1	431502.350	14393.3691
A	0.5	0	0	0.5	+	e	F1	431528.846	14394.2529
A	0.5	0	1	1.5	+	f	F1	431856.942	14405.1970
A	0.5	0	1	1.5	-	e	F1	431907.918	14406.8974
A	0.5	0	2	2.5	-	f	F1	432458.586	14425.2657
A	0.5	0	2	2.5	+	e	F1	432530.306	14427.6580
A	1.5	0	2	1.5	+	f	F2	434072.825	14479.1109
A	1.5	0	2	1.5	-	e	F2	434074.800	14479.1768
B	0.5	0	0	0.5	+	e	F1	472280.930	15753.5961
B	0.5	0	1	1.5	-	e	F1	472531.835	15761.9654
B	0.5	0	1	0.5	-	f	F2	472569.291	15763.2148
B	0.5	0	2	2.5	+	e	F1	473049.112	15779.2199
B	0.5	0	2	1.5	+	f	F2	473118.070	15781.5201
B	0.5	1	0	0.5	+	e	F1	509583.158	16997.8645
B	0.5	1	1	1.5	-	e	F1	509828.571	17006.0506
B	0.5	1	1	0.5	-	f	F2	509864.270	17007.2414
B	0.5	1	2	2.5	+	e	F1	510333.446	17022.8914
B	0.5	1	2	1.5	+	f	F2	510375.695	17024.3007
E	0.5	0	0	0.5	-	f	F1	611251.730	20389.1630
E	0.5	0	0	0.5	+	e	F1	611250.478	20389.1213
E	0.5	0	1	1.5	+	f	F1	611543.718	20398.9027
E	0.5	0	1	1.5	-	e	F1	611542.995	20398.8786
E	0.5	0	2	2.5	-	f	F1	612071.787	20416.5172
E	0.5	0	2	2.5	+	e	F1	612071.664	20416.5131
E	1.5	0	2	1.5	+	f	F2	612186.647	20420.3485

Table 2.2: Some important state energies of CaH. Ω , v, N, J stand for total angular momentum, vibrational number, rotational number, spin-rotation angular momentum, respectively. Parity 1 refers to the overall parity in terms of optical transition. An E1 transition is only possible if the two states have opposite parity 1 values. Parity 2 refers to the parity that is commonly used for diatomic molecule spectroscopic purpose. Labels are for spectroscopic purpose. Es are the state energies. The errors of Es are 100MHz for $X^2\Sigma^+$, $A^2\Pi_{1/2}$ and $B^2\Sigma^+$ states (Ref. [27]), 1GHz for $E^2\Pi_{1/2}$ states (Ref. [28]). Hyperfine splittings are ignored due to finite errors.

Ground state	Excited state	Frequency (THz)	Comment
X v=0 N=1 J=3/2 F=2	A v=0 J=1/2	431.274592.4 (2.0)	X-A v=0 cycling
X v=0 N=1 J=3/2 F=1	A v=0 J=1/2	431.274694.0 (2.0)	
X v=0 N=1 J=1/2 F=1	A v=0 J=1/2	431.276604.5 (2.0)	
X v=0 N=1 J=1/2 F=0	A v=0 J=1/2	431.276551.2 (2.0)	
X v=0 N=1 J=3/2 F=2	B v=0 N=0 J=1/2	472.026679	X-B v=0 cycling
X v=0 N=1 J=3/2 F=1	B v=0 N=0 J=1/2	472.026780	
X v=0 N=1 J=1/2 F=1	B v=0 N=0 J=1/2	472.028692	
X v=0 N=1 J=1/2 F=0	B v=0 N=0 J=1/2	472.028639	
X v=1 N=1 J=3/2 F=2	A v=1 J=1/2	432.342011(10)	X-A v=1 cycling
X v=1 N=1 J=3/2 F=1	A v=1 J=1/2	432.342120(10)	
X v=1 N=1 J=1/2 F=1	A v=1 J=1/2	432.343958(10)	
X v=1 N=1 J=1/2 F=0	A v=1 J=1/2	432.343902(10)	
X v=1 N=1 J=3/2 F=2	B v=1 N=0 J=1/2	471.557078	X-B v=1 cycling
X v=1 N=1 J=3/2 F=1	B v=1 N=0 J=1/2	471.557178	
X v=1 N=1 J=1/2 F=1	B v=1 N=0 J=1/2	471.559025	
X v=1 N=1 J=1/2 F=0	B v=1 N=0 J=1/2	471.558969	
X v=0 N=0 J=1/2 F=1	A v=0 J=1/2	431.50229	In cell data, HFS unresolved
X v=0 N=0 J=1/2 F=0	A v=0 J=1/2	431.50229	11.03.2021 retake
X v=0 N=2 J=5/2 F=3	A v=0 J=5/2	431.696788	In cell data, HFS unresolved
X v=0 N=2 J=5/2 F=2	A v=0 J=5/2	431.696788	Q1 line
X v=0 N=1 J=3/2 F=2	A v=0 J=5/2	431.602714	In cell data, HFS unresolved
X v=0 N=1 J=3/2 F=1	A v=0 J=5/2	431.602714	Q1 line
X v=0 N=0 J=1/2 F=1	B v=0 N=1 J=1/2	472.56924	Guess = 472.569291 THz
X v=0 N=0 J=1/2 F=0	B v=0 N=1 J=1/2	472.56940	Low signal, not accurate to +/- 10 MHz
X v=0 N=2 J=3/2 F=2	B v=0 N=1 J=1/2	471.810821	Guess = 471.810811 THz
X v=0 N=2 J=3/2 F=1	B v=0 N=1 J=1/2	471.810761	HFS determined through peak height
X v=0 N=1 J=1/2 F=0	A v=0 J=3/2	431.604611(15)	N=3 J=5/2 rotational pump
X v=0 N=1 J=1/2 F=1	A v=0 J=3/2	431.604664(15)	Guess = 431.604724
X v=0 N=1 J=3/2 F=1	A v=0 J=3/2	431.602751(15)	Guess = 431.602765
X v=0 N=1 J=3/2 F=2	A v=0 J=3/2	431.602651(15)	
X v=0 N=3 J=5/2 F=2	B v=0 N=2 J=3/2	471.600203(inf)	Guess = 471.600203
X v=0 N=3 J=5/2 F=3	B v=0 N=2 J=3/2	471.600123(inf)	
X v=0 N=3 J=5/2 F=2	A v=0 J=3/2	430.338953	Guess = 430.338962
X v=0 N=3 J=5/2 F=3	A v=0 J=3/2	430.339023	
A v=0 Ω=1/2 J=3/2	E v=0 J=3/2	179.6853805(5)	
X v=1 N=1 J=3/2 F=2	B v=0 N=0 J=1/2	434.25484	X(v=1)-B(v=0) Repump
X v=1 N=1 J=3/2 F=1	B v=0 N=0 J=1/2	434.254949	
X v=1 N=1 J=1/2 F=1	B v=0 N=0 J=1/2	434.256787	
X v=1 N=1 J=1/2 F=0	B v=0 N=0 J=1/2	434.256731	
X v=1 N=1 J=3/2 F=2	A v=0 J=1/2	393.502723	X(v=1)-A(v=0) Repump
X v=1 N=1 J=3/2 F=1	A v=0 J=1/2	393.502832	
X v=1 N=1 J=1/2 F=1	A v=0 J=1/2	393.50467	
X v=1 N=1 J=1/2 F=0	A v=0 J=1/2	393.504614	
X v=2 N=1 J=3/2 F=2	B v=1 N=0 J=1/2	434.932175(10)	X(v=2)-B(v=1) Repump
X v=2 N=1 J=3/2 F=1	B v=1 N=0 J=1/2	434.932285(10)	
X v=2 N=1 J=1/2 F=1	B v=1 N=0 J=1/2	434.934045(10)	
X v=2 N=1 J=1/2 F=0	B v=1 N=0 J=1/2	434.933995(10)	
X v=2 N=1 J=3/2 F=2	A v=1 J=1/2	395.717108	X(v=2)-A(v=1) Repump
X v=2 N=1 J=3/2 F=1	A v=1 J=1/2	395.717218	Calculated from X-B 11 cycling
X v=2 N=1 J=1/2 F=1	A v=1 J=1/2	395.718978	
X v=2 N=1 J=1/2 F=0	A v=1 J=1/2	395.718928	
X v=0 N=1 J=3/2 F=2	A v=1 J=1/2	470.113870(10)	X(v=0)-A(v=1) Off diag pumping
X v=0 N=1 J=3/2 F=1	A v=1 J=1/2	470.113971(10)	
X v=0 N=1 J=1/2 F=1	A v=1 J=1/2	470.115873(10)	
X v=0 N=1 J=1/2 F=0	A v=1 J=1/2	470.115819(10)	

Table 2.3: Some transition frequencies for CaH. Values are measured with Highfinesse WS7 wavemeter with 60 MHz absolute error, calibrated with a strontium 689nm transition.

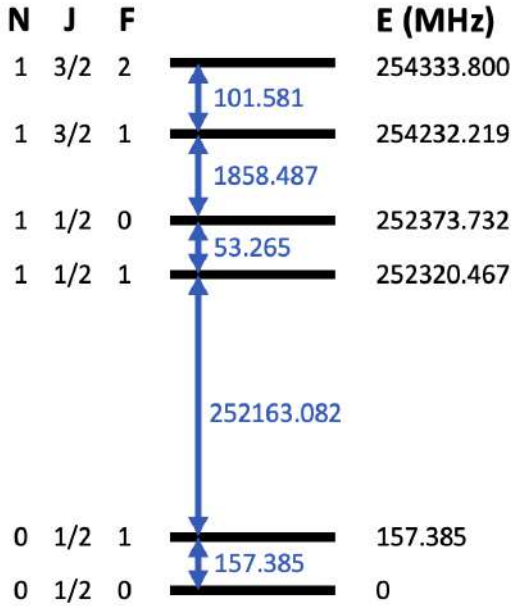


Figure 2.2: Some of the lowest energy states in CaH, with quantum numbers labelled and energies, including energy differences in MHz. A reasonable error estimate for the energies is about 0.05MHz. The numbers are derived from Ref. [29].

$$q_{0\nu''} = \frac{f_{0\nu''} \cdot \omega_{0\nu''}^3}{\sum_{\nu''} f_{0\nu''} \cdot \omega_{0\nu''}^3} \quad (2.7)$$

Here, $f_{0\nu''}$ is the Franck-Condon factor between $\nu' = 0$ and a specific ν'' , and $\omega_{0\nu''}$ is the transition frequency (in angular frequency units). So even if an FCF is small, a short enough wavelength can boost the VBR.

For laser cooling, VBRs are critical because they determine how many repump lasers we need to maintain optical cycling. Ideally, most decay goes back to the original ground-state vibrational level, so we can scatter many photons without population leaking into dark states. But if even a few percent of population decays into $\nu'' = 1$ or higher, we need to address those with additional repump transitions, otherwise the molecule falls out of the cycle. Our experimentally measured FCFs and VBRs for CaH are shown in Table 2.4. About how they are measured and what implications are from the measurement will be discussed in more detail in Chapter 6.

Transition	Lifetime τ (ns)	Vibrational Quanta (ν'')	Transition wavelength (nm)	FCF Theory ($f_{0\nu''}$)	FCF measured ($f_{0\nu''}$)	VBR theory ($q_{0\nu''}$)	VBR measured ($q_{0\nu''}$)
$A \rightarrow X$	33(3)	0	695.13	0.953	0.9572(43)	0.9645	0.9680(29)
		1	761.87	0.0439	0.0386(32)	0.0337	0.0296(24)
		2	840.07	2.74×10^{-3}	$4.2(3.2) \times 10^{-3}$	1.57×10^{-3}	$2.4(1.8) \times 10^{-3}$
		3	932.80	2.3×10^{-4}	-	9.6×10^{-5}	-
$B \rightarrow X$	58(2)	0	635.12	0.9856	0.9807(13)	0.988982	0.9853(11)
		1	690.37	0.0132	0.0173(13)	0.010313	0.0135(11)
		2	753.97	1.1×10^{-3}	$2.0(0.3) \times 10^{-3}$	6.60×10^{-4}	$1.2(0.2) \times 10^{-3}$
		3	827.84	1×10^{-4}	-	4.5×10^{-5}	-

Table 2.4: FCFs and VBRs for the measured transitions of CaH. The experimental radiative lifetime for the A state was obtained from Ref. [31] and for the B state from Ref. [32]. The excited state vibrational quantum number is always $\nu' = 0$. The $A(\nu' = 0) \leftarrow X(\nu'' = 0)$ excitation wavelength at 695.13 nm, the $B(\nu' = 0) \leftarrow X(\nu'' = 0)$ excitation wavelength at 635.12 nm, and the $B(\nu' = 0) \leftarrow X(\nu'' = 1)$ excitation wavelength at 690.37 nm were determined experimentally. The other transition wavelengths are derived using measured vibrational energies given in Ref. [27]. The calculated FCFs are obtained from [33] for the $A \rightarrow X$ decay and from [34] for the $B \rightarrow X$ decay. Error bars for the measured FCFs and VBRs are statistical standard errors.

Chapter 3: Experimental Hardware, and Why We Build It This Way

When humans are blessed with intelligence, the first thing they do is make a toy.

The study of physics relies on experiment. Numerous stories describe how the evolution of physical tools led to the development of "explanations". These explanations, after undergoing generalization and simplification, became theories. In the 20th century, there were many major advancements in technology, for example, lasers and cryogenic systems. With the help of these tools, we were able to construct the complex quantum machine discussed in this thesis.

Any complex system is composed of individual smaller modules, each with its own goal and specifications. Therefore, I will provide an overview of the system and discuss its important sub-modules individually.

As shown in Fig. 3.1, molecules are generated on the left side, from the center of the cryostat, within a copper cell. They undergo many collisions with the background buffer gas, helium at 4K, and then exit the cell and form a beam with an average velocity around 250 m/s. The molecules then interact with light fields, and are either cooled or slowed as they travel within the UHV system on the right side of the figure. The light field parameters (e.g., intensity and frequency) are controlled via a Cicero-based sequencer (initially, a LabVIEW-based one). The optical detection systems (PMT or EMCCD) typically collect fluorescence photons when molecules interact with light, and the data is sent to the Data Acquisition system (DAQ), which is stored on a local server using a Samba-based file system. The data is eventually analyzed using a code library, mostly written in Python.

I'm proud to say that I built, or made substantial contributions to, everything mentioned above.

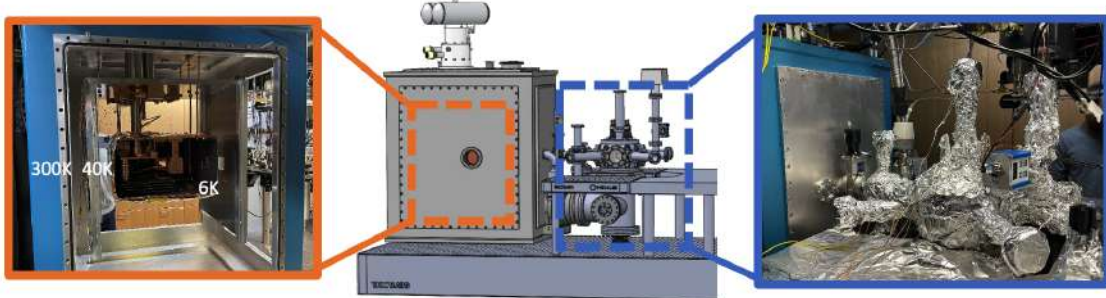


Figure 3.1: What our experiment looks like on one of the optical tables.

3.1 Cryogenic System

3.1.1 PTR, Cryostat, and Shields

We use a Cryomech PT415 pulsed tube refrigerator (PTR) to create the cryogenic environment. It has two cooling stages (not counting the room-temperature shield), which reach approximately 40 Kelvin and 4 Kelvin. The coldest temperature we have ever seen on the cold head was around 4.1 K, but during most of my PhD, the temperature was closer to 5 K, and the cell was typically around 6 K.

The reason we operate at such a "high" temperature (compared to most laser cooling experiments that run near 1–4 K) is because of the light mass of hydrogen. Since the hydrogen atom is much lighter than calcium, the rotational energy spacing of CaH is significantly larger, around 250 GHz, compared to ~20 GHz for many other laser-coolable molecules. As a result, if we operate at too low a temperature, such as 1–4 K, too many CaH molecules will fall into the lowest rotational state, reducing the population in the first excited rotational state ($N = 1$), which is typically targeted for optical cycling.

Assuming CaH fully thermalizes with the background helium gas, the temperature that maximizes the population in the $N = 1$ state is around 10 K. So why do we operate at 6 K instead of 10 K? It's because we need to balance molecular yield and beam velocity. Too high a temperature leads to high molecular velocity. This tradeoff will be discussed in the next subsection.

3.1.2 Buffer Gas Cell

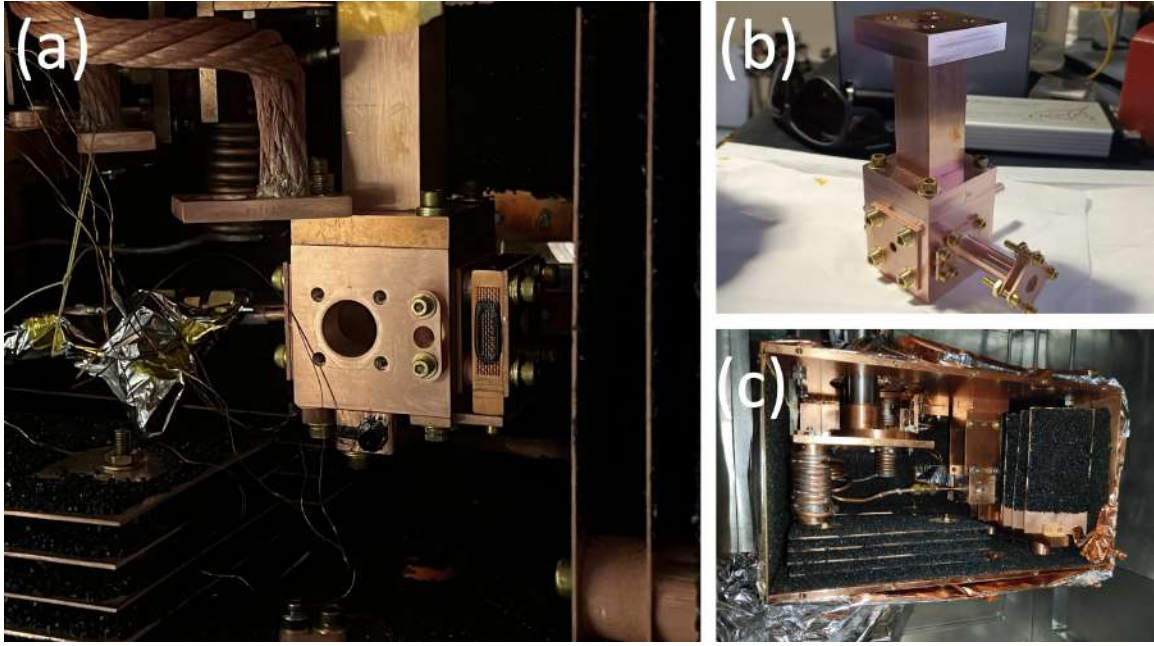


Figure 3.2: The evolution of different cells. (a) The latest buffer gas cell. The base is similar to the design used in CaOH experiment from Doyle’s lab at Harvard. We installed the second stage without additional cooling. Operating without a front mesh seems to work best in our case. (b) A different angle of the cell when it’s taken out. It was still single stage when the picture was taken. (c) Buffer gas cell at early stage of the experiment. The key dimensions are basically the same, but the newer generation is more modular so it’s easier to work with.

The buffer gas cells we used all share similar dimensions. The length is 2 inches, the inner diameter is 1 inch. If using a single-stage cell, the optimal aperture diameter is 5 mm. For the two-stage version, the inner and outer aperture diameters are 9 mm and 7 mm, respectively. These designs can be seen in Fig. 3.2.

But an important question is: why do we choose these specific dimensions? Could the system still work if the length were a bit longer or the diameter a bit wider? To answer that, we need to go back to some basic calculations and considerations for buffer gas cells.

The following discussion is mainly based on Ref. [35], and will also reference specific sections from the theses of John Barry [36], Geoffrey Iwata [37], and Louis Baum [38]. The goal is to briefly summarize the theory behind cryogenic buffer gas cooled beam (CBGB) techniques, and plug in our experimental parameters to see whether things still work out for CaH. Unless otherwise

specified, c refers to CaH, b refers to helium, and all quantities are in SI units.

Here are some parameters that matter for a simple buffer gas cooling model:

- Flow rate (F)
- Cell aperture diameter and area (d, A)
- Cell dimensions, including longitudinal length (in the direction of molecule propagation), cross section area, and the entire volume of the cell ($L, A_{\text{cell}}, V_{\text{cell}}$)
- Helium temperature (T)

Mean free path λ is the average distance a particle travels between two collisions. Assuming $\sigma_{cb} = \sigma_{bb} = 10^{-14} \text{ cm}^2$ and helium is the dominant species:

$$n_b = 3.2 \times 10^{21} \text{ m}^{-3} \quad (\text{calculated using } F = 2.2 \text{ SCCM}, d = 3 \text{ mm}, T = 6 \text{ K})$$

$$\lambda_c = \frac{1}{n_b \sigma_{cb} \sqrt{m_c/m_b + 1}} \approx \frac{3 \times 10^{17}}{n_b} = 94 \mu\text{m}$$

$$\lambda_b = \frac{1}{n_b \sigma_{bb} \sqrt{2}} \approx \frac{7 \times 10^{17}}{n_b} = 220 \mu\text{m}$$

Mean thermal velocity of helium from the Maxwell-Boltzmann distribution is:

$$\bar{v}_{\text{th}} = \sqrt{\frac{8k_B T_b}{\pi m_b}} = 178 \text{ m/s} \quad (\text{at } T = 6 \text{ K})$$

Fully supersonic velocity assuming adiabatic expansion:

$$v_{\text{sup}} = \sqrt{\frac{2\gamma k_B T}{(\gamma - 1)m}} = \sqrt{\frac{5k_B T}{m}} = 1.4\bar{v}_{\text{th}} = 250 \text{ m/s}$$

Emission rate at the aperture into a solid angle $d\omega$ at angle θ is given by:

$$dQ_{c(b)} = \frac{d\omega}{4\pi} n_{c(b)} v_{c(b)}^{\text{exit}} A \cos \theta$$

Integrating over all angles yields the total flow rate. Assuming uniform buffer gas density:

$$n_b = \frac{4F}{A\bar{v}_{\text{th}}} = 6.3 \times 10^{21} \text{ m}^{-3}$$

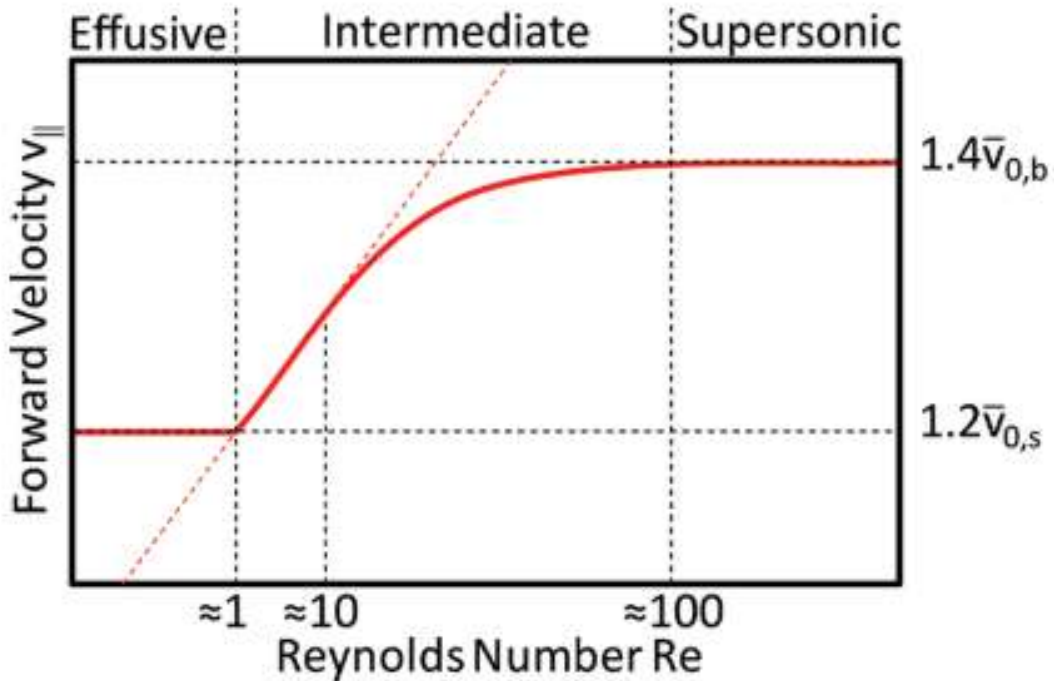


Figure 3.3: A schematic showing beam forward velocity vs. Reynolds number (flow rate). The lower bound is $1.2v_{0,s}$, where $v_{0,s}$ is the thermal velocity of CaH. At 6 K, $1.2v_{0,s} = 70$ m/s and $1.4v_{0,b} = 250$ m/s. Figure adopted from Ref. [35].

Reynolds number (Re) characterizes flow behavior. It's related to the Knudsen number and Mach number by the von Kármán relation:

$$\frac{1}{2} \text{Kn} \cdot Re \approx \text{Ma} \approx 1$$

So,

$$Re \approx 2\text{Kn}^{-1} = \frac{2d_{\text{aperture}}}{\lambda_b} = \frac{8\sqrt{2}dF\sigma_{bb}}{A\bar{v}_{\text{th}}}$$

For $d = 3$ mm and $F = 1 \times 10^{18} \text{ s}^{-1}$ (1 SCCM $\approx 4.5 \times 10^{17} \text{ s}^{-1}$), we get $Re \approx 27$.

There are three flow regimes:

- $Re < 1$: Effusive. Low velocity, high temperature, few collisions. Forward helium velocity is $1.2\bar{v}_{\text{th}}$.
- $Re > 100$: Supersonic (fully hydrodynamic). High velocity, low temperature, lots of collisions. Forward velocity is $1.4\bar{v}_{\text{th}}$.
- $1 < Re < 100$: Intermediate buffer gas cooling regime.

There are three processes with individual time constants that are worth paying attention to, namely, thermalization, diffusion, and extraction. They should be calculated in the following ways.

Thermalization

CaH temperature evolution under collisions with cold helium:

$$\frac{dT_c(N)}{dN} = -\frac{T_c(N) - T_b}{\kappa}, \quad \kappa = \frac{(m_c + m_b)^2}{2m_c m_b} = 6.2$$

Solving this equation, we have

$$T_c(N) = T_b + T_c(0) \exp(-N/\kappa)$$

After 60 collisions, we are able to cool CaH from 5000K to 6.2K. Given that the mean free path of CaH is 47 μm, the thermalization length is approximately 5.6 mm. The thermalization time is calculated by summing the time for each step (assuming helium temperature being constant) and using the most probable velocity to estimate the time required [37], which equals 20us. (A quick sanity check: mean velocity here is 500m/s, consider temperature initially as hot as 5000K, it seems fine.)

Diffusion

Diffusion time constant is derived from diffusion equation [37], while making Chapman-Enskog approximation, we can have an upper limit on the diffusion time/length. The time constant is set when mean-squared displacement is equal to cross section of the cell:

$$D = \frac{3\pi v_{th}}{32n_b\sigma_{cb}}$$

and the diffusion time is

$$\tau_{diff} = \frac{16A_{cell}n_b\sigma_{cb}}{9\pi v_{th}} = 12ms$$

which is typically between 1 and 10 ms.

Extraction

Extraction time is the time cost for the helium in the cell volume to be pumped out, and thus how much time it takes for CaH to be swept from the cell by helium.

$$\tau_{pump} = \frac{4V_{cell}}{v_{th}A_{aperture}} = 6ms$$

which is typically between 1 and 10 ms as well.

In general, we want $\gamma = \frac{\tau_{diff}}{\tau_{pump}} = \frac{\sigma_{cb}F}{L_{cell}v_{th}}$ to be high, to achieve a high extraction efficiency. However, they [35] mentioned that there are other factors affecting extraction efficiency that are not shown in the above calculation, for example aperture diameter (if too small could decrease efficiency while preserving γ). As a result, they suggest using aperture bigger than 3mm diameter.

Actual molecular beam velocity

According to our direct beam velocity measurement, the distribution typically peaks at 250(10) m/s, which is faster than the pure Reynold number consideration. This is due to a prominent effect

called "zone of freezing". It's very straightforward: when molecules exit the cell, the peak forward velocity is typically ~ 150 m/s, however, helium is traveling at ~ 250 m/s, so the helium is going to catch up on the molecules and experience forward direction collisions that significantly boost the forward velocity of the molecules, as shown in Fig. 3.4 with the help of high SNR of calcium.

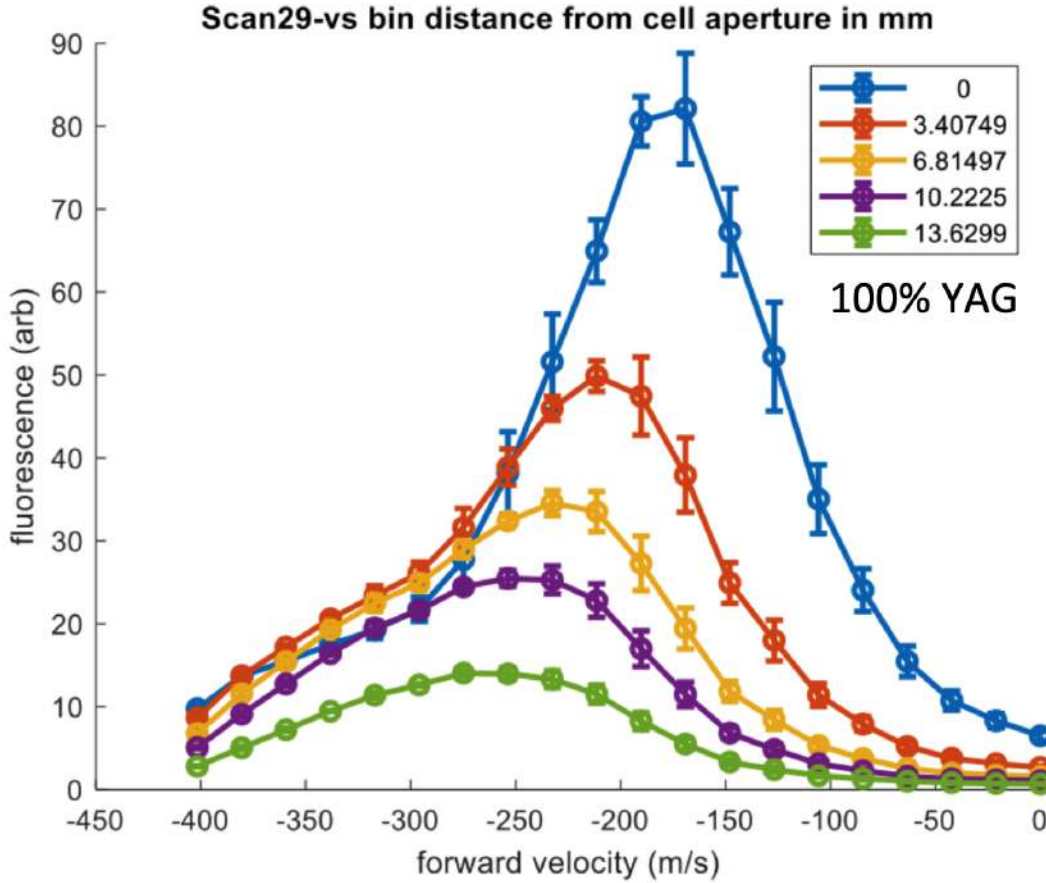


Figure 3.4: Zone of freezing. This data was taken in the way that, a calcium 423nm laser was shooting into the cell from the downstream of the beamline, and used a Thorlabs CMOS camera with imaging optics to detect the fluorescence from Calcium at different spatial location. We also vary the laser detuning to address different velocity classes in different sequences. The blue curve is closest to the cell aperture, and one can see the calcium forward velocity distribution seems slowest. While traveling till the green curve, which is 13cm away from the cell, the forward velocity has been altered to peak around 250m/s.

3.1.3 Target for ablation

There used to be four kinds of targets that we have tried in our buffer gas cell for creating CaH molecules. All targets are glued to the target holder with regular epoxy. Here we will describe

them individually. Spoiler alert, target type 4 is by far the best of all.

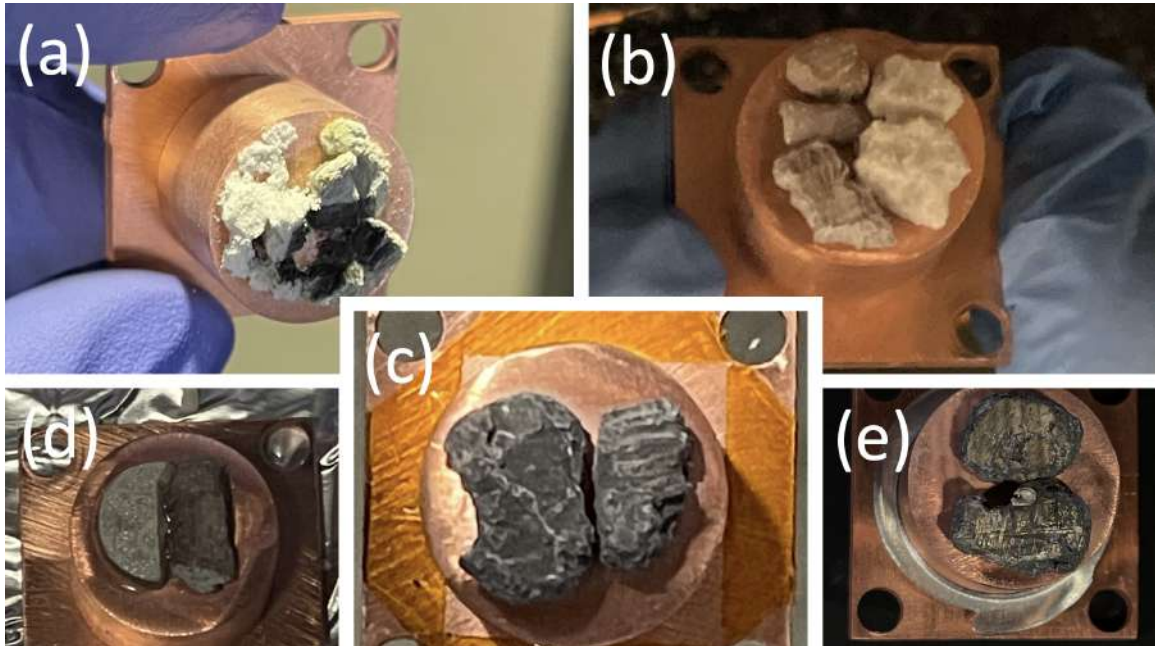


Figure 3.5: Interesting observations with targets. (a) two interesting things on a used CaH₂ target. The white powder comes from exposing CaH₂ in the air, very likely CaCO₃. The black coating is not well understood, and it can significantly reduce the signal over time. (b) the left target is CaD₂, and the right one is CaH₂ solid. Both are fabricated from chemical reactions in the lab. (c) The calcium metal pieces that are more commonly used in the later stage of the experiment. (d) Left piece is compressed CaH₂ pill and broken into two parts, and right piece is a regular CaH₂ granule. (e) There can be some other significant coating on the surfaces of calcium pieces after running the experiments for a while, and the coating is still not well understood. We see black coatings and yellow coatings but this picture only shows yellow coatings.

Target type 1 The first kind was granule samples from Sigma Aldrich. CaH yield is normal level (X-A absorption peak less than 10%), but different locations will have very different yield performance. The degradation rate of a given spot typically ranges from 200 to 500 shots. There are usually at least one spot from each sample that can last longer and capable of having higher yield. They degrade as well, but after ablating on other locations for a while, and coming back, it is possible to achieve nearly 80% of original max signal. The current theory is that those are small holes that can accumulate dust of CaH₂ and others from ablation on other spots.

Lifetime, and mysterious coating

It usually takes 1-1.5 months for one sample to completely run out of good ablation spots. Once taken out, one can observe an obvious layer of black coating on top of the sample, as shown in Fig. 3.5 (a). With one to two weeks of ablation, it is not enough to create this coating. We did not do thorough study with the coating, but we tend to believe that they are carbon that came from the glue. The reason is, Ca, CaO, CaCO₃, Ca(OH)₂, are all white-ish, Cu, CuO, CuH₂, CuCO₃, Cu(OH)₂ are also not black. Any leakage of ablation light to the glue can vaporize it, and deposit a layer of carbon which did not react with the environment, which is why we tend to think the coating is carbon. However, it is definitely quite important to figure out the formula of the coating, since it's significantly affecting the lifetime of a target.

Dust covering the cell

Another fact that affects the performance of the CBGB is the heavy coating on the cell wall. We usually observe a significant velocity boost a month after sample change, and this is basically the time it takes to cover the cell with dust. The dust would look gray-ish, we tend to believe that the white parts are all calcium based chemicals, while the black stuff are the same as coating on the target, probably carbon. To remove them, it is efficient to clean with Kimwipes soaked in methanol and apply finger pressure.

Target type 2 Because the signal from target 1 was unstable, we used to attempt to use hydraulic press to make the target (Instron 5984 in Carleton Lab at Columbia, 9 Tons force on 1cm dia, 20 mins ramp up followed by 20 mins of stay), as shown in Fig. 3.5 (d). It indeed solved the issue of inhomogeneity, but it did not significantly outperform target 1. The signal level was almost the same as average level of target 1, and there is no magic spot for us to exploit. The degradation time constant is maybe slightly longer than target 1, but it's around 500 shots level, not significantly better. And there was a couple of times where we experienced sudden loss of signal, and after opening the cell, we found that it was a layer of CaH₂ cracked and fell, leading to significant

dusting in the cell and inhomogeneous surfaces. I do not think it is worth the effort to make the target in this way because the reward is not significant enough.

Target type 3 Because we cannot buy CaD₂ samples from suppliers, we have to make our own targets. The way we generate the molecules is very simple: put calcium pieces and D₂ gas together at high temperature, they will react and form CaD₂. The exact procedure and more details are illustrated in the CaD laser cooling section (Sec. 6.3.6), and the schematic can be found in Fig. 6.9. Eventually, we can also use the same method to create CaH₂ target, which has the same performance as ones from Sigma Aldrich. However, it is worth noting that, CaD₂ sample somehow outperforms CaH₂ sample by many times. CaD yield is about three times higher than CaH yield using this method. One potential explanation is that due to the higher mass of deuterium compared to hydrogen, the rotational spacing is halved, so the optimal cryogenic temperature is lower for CaD, which is closer to our operational temperature.

Target type 4 For better signal and stability, we tried to use calcium and hydrogen reaction to create CaH, meaning the target this time is calcium metal pieces, which flowing hydrogen gas into the system. The improvement is significant: the signal was raised by about 2-3 times, and the signal stability was improved by almost 20 times. Because of the strong crystal structure / bonds of calcium, it is not as brittle as CaH₂. The reason why we get signal improvement is not very well understood. As will be discussed in later chapter (Chapter 4), this chemical reaction (Ca + H₂ → CaH + H) is highly endothermic. So in some sense, we understand how we got the durability, but we don't fully understand how we got the yield boost, so I guess it's lucky for us.

However, it is worth mentioning that there are still some major issues with this way of creating CaH molecules. The most important one is, even after this signal boost, we are still a few orders of magnitude lower yield than all the molecular species that have been laser trapped by far, as can be seen from the Table 3.1.3. This remains the primary limiting factor for the development of the project, as we consistently lack sufficient SNR for clear signal observation.

Molecule	Flux (num/sr/pulse)
CaH	1×10^{10}
SrF	2×10^{12}
ThO	3×10^{13}
CaF	$\approx 1 \times 10^{12}$
CaOH	$\approx 1 \times 10^{12}$

3.2 Laser System

Due to the complex nature of molecules, we use many different lasers in the lab. A list of the main ones is shown in Table 3.1, along with their purposes and typical usage. This list is not exhaustive. Many lasers that are currently unused or decommissioned are not included, lasers from Strontium and all injection locked amplifiers are not included either.

The roles of these lasers can be grouped into a few main categories. The most important application is for direct interaction with the molecules, such as for cooling, slowing, and magneto-optical trapping (MOT). Other lasers serve calibration purposes. For example, the potassium laser is used to calibrate our wavemeter, and the Ca/CaOH lasers are used to characterize beam velocity and system performance.

3.2.1 MOT Lasers

For the MOT lasers, we need a highly stable source with linewidth narrower than 1 MHz. To meet this requirement, we chose the Precilaser SFG system as our main laser. At the same time, this laser also serves the slowing stage. All MOT and slowing light needs to cover the ~ 2 GHz spin-rotation splitting of the CaH ground state.

To achieve a basic MOT, the laser frequencies and powers do not require fine tuning. However, for a fully optimized MOT in the future, individual control over both frequency and intensity will be necessary for all laser components.

To address the challenges mentioned above, I designed the frequency engineering scheme shown in Fig. 3.6.

A more detailed schematic of the AOM ladder used to generate all required MOT frequencies

Company & Partnum	Type	λ (nm)	Power	Purpose	Comment
HB, DL5146-101S	ECDL	405	60mW	Ca Rydberg	Thorlabs
HB, NDV4A16	ECDL	423	120mW	Ca detection	Nichia
HB, PLT5-488	ECDL	490	60mW	Mol X-E	Osram
Quantel, Anderson Laser	Nd:YAG	532	210mJ	2nd ablation laser	6ns pulse
M2, Equinox	DPSS	532	12W	Pump for Ti:Sa	Degrading
HB, HL63163DG	ECDL	626	30mW	CaOH detection	Thorlabs (0°C)
HB, L638P200	ECDL	635	150mW	Mol X-B	Thorlabs (17°C)
HB, HL6545MG	ECDL	657	100mW	Ca narrow line	Thorlabs (17°C)
HB, MSHG1420-0.5-40	SFG	690	2W	Mol X-B v1 RP	Precilaser + IPG
Precilaser, FL-SSFG-695-4-CW	SFG	695	3.5W	Mol X-A	1080nm & 1950nm
HB, HL69001DG	ECDL	695	200mW	Mol X-A	Ushio (45°C)
HB, LD-0760-0080-AR-2	ECDL	753	80mW	Mol v3 RP	Toptica
Toptica, TA-Pro-25758	TA	758	1.5W	Mol v2 RP	
Thorlabs, DBR767PN	DBR	767	23mW	K D2 line	
M2, 01-M2-S-EQ-PI	Ti:Sapph	705-1010	2W-6W	General	
Big Sky, UL620111	Nd:YAG	1064	30mJ	1st ablation laser	Idle
Sacher, TEC150	ECDL	1068	20mW	seed for IPG	
IPG, YAR-20-1064-LP-SF	FiberAmp	1068	20W	for SFG	
HB, TO0-174-161	ECDL	1665	120mW	Mol X-E detection	Seminex (-5°C)
Vexlum, VALO-SF-16681110	VECSEL	1668	800mW	Mol X-E detection	Degrading

Table 3.1: An incomplete list of lasers deployed for CaH / CaD experiments. To explain the acronym, HB: home-built; Mol: molecules including CaH and CaD; RP: repump; ECDL: external cavity diode laser.

is shown in Fig. 3.7.

Because we aim to implement an AC MOT, it is essential to synchronize the polarization of the MOT beams with the direction of the magnetic field gradient. Currently, we use a Pockels cell to rotate the polarization after all beams are combined. However, we have observed some thermal drift associated with the Pockels cell, which affects stability. In the future, we should consider switching to a system based on AOMs and PBSs for polarization control, which may offer improved long-term reliability. A detailed schematic of this alternative setup can be found in Yicheng Bao’s thesis.

The overall efficiency of the AOM ladder setup is around 15%. Sometimes this output is not sufficient to achieve strong trapping forces. To address this, at the time of writing, we use light from the Precilaser seed to injection-lock four slave lasers. The injection-locked amplifiers (ILAs) use Ushio 690nm diodes (Part number: HL69001DG, 200mW, purchased from WorldStarTech), and the ILA system performs well, typically yielding a higher output power of approximately 30

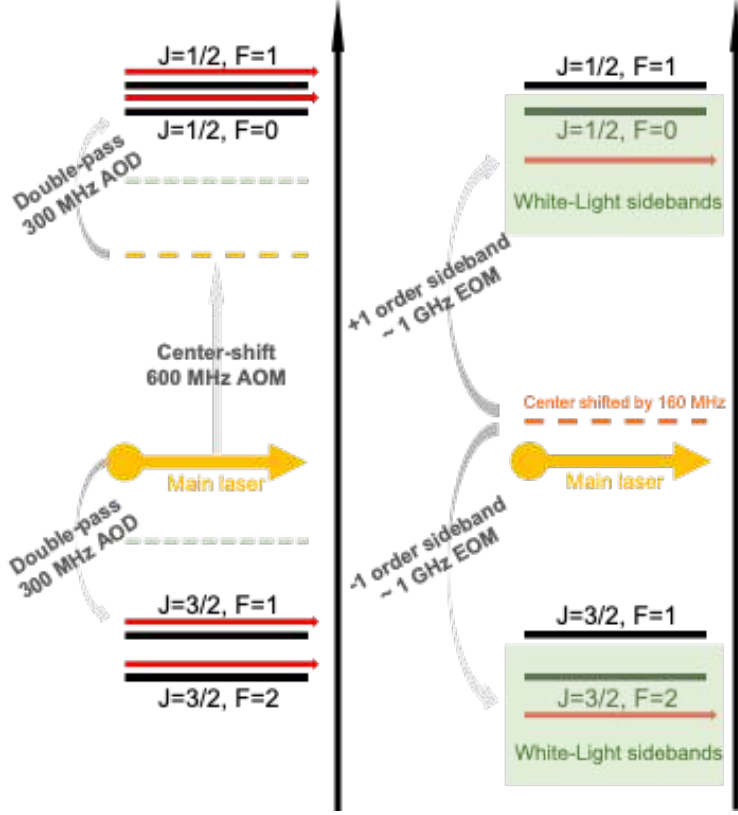


Figure 3.6: Frequency engineering scheme to achieve full frequency control over both MOT and slowing light using a single laser source. Techniques such as the 1 GHz EOM will be discussed later in this section.

mW per beam path.

3.2.2 Slowing Lights

We plan to use white light slowing to decelerate CaH molecules, while keeping the option open to switch to chirp slowing if needed. Thanks to the high output power from the Precilaser, we have enough laser power available for the slowing stage.

The slowing light needs to be modulated using a series of AOMs and EOMs to achieve broad enough spectral coverage to address all relevant ground-state transitions. This includes the hyperfine splittings (50–100 MHz) and the spin-rotation splitting (~2 GHz). To make things more complicated, the same level of frequency modulation must also be applied to all vibrational repumpers.

Based on our calculations, we need to address vibrational levels up to $v = 3$ in the ground elec-

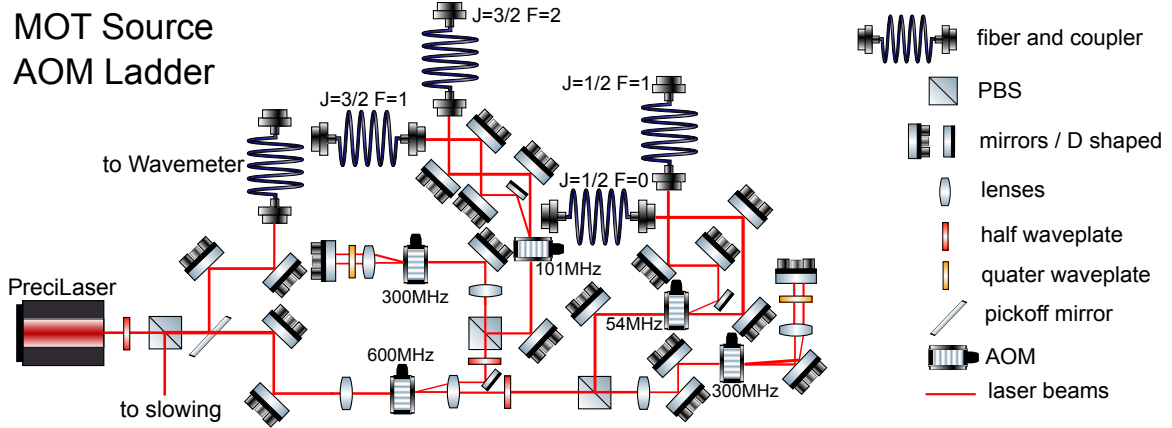


Figure 3.7: AOM ladder schematic for creating all frequency components needed for MOT light.

tronic state in order to scatter a sufficient number of photons to slow the molecules from their initial velocity (around 250 m/s) down to laser-trappable speeds (around 10 m/s). A detailed schematic of the slowing laser setup is shown in Fig. 3.8.

3.2.3 Cooling Lights

In our laser cooling experiments, we have used two types of laser sources. Before 2023, we used home-built ECDLs to seed injection-locked amplifiers (ILAs), though the power was relatively low. After 2023, we transitioned to using the Precilaser, which provides significantly higher output power.

Although the ECDLs typically exhibit frequency fluctuations of ± 2 MHz, they still provide a sufficient signal-to-noise ratio (SNR) to observe strong cooling signals. The higher power and stability of the Precilaser further improved our ability to apply stronger cooling and enabled the study of molecular slowing.

3.3 Laser Locking Systems

3.3.1 Wavemeter Sealing

Most of our molecular transitions have natural linewidths of just a few MHz, and these are further broadened by Doppler effects and power broadening. Because of this, we rely on the

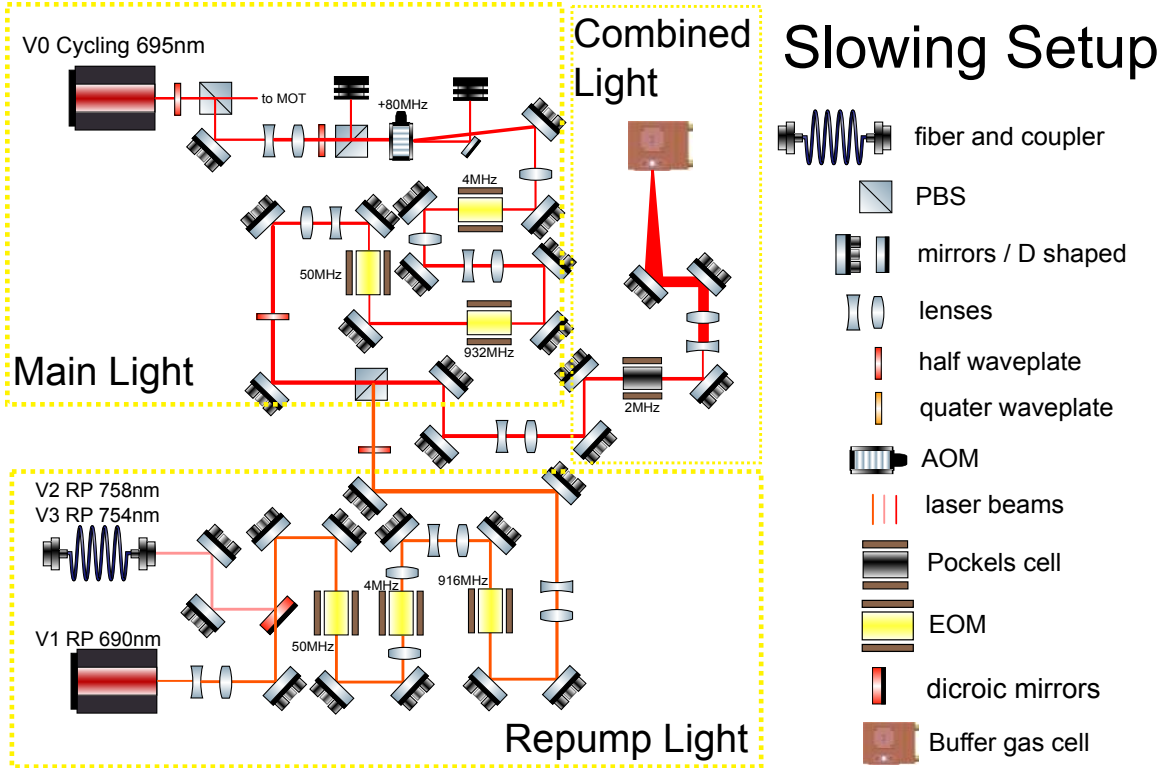


Figure 3.8: Laser alignment schematic for the slowing laser setup, including the main cycling laser and vibrational repumpers up to $v = 3$.

HighFinesse WS7 wavemeter as our primary frequency locking reference. This wavemeter has a resolution of 1 MHz and an absolute accuracy of about 60 MHz, which is good enough for most of our purposes.

However, we noticed that the wavemeter readings are significantly affected by room pressure and temperature. On stormy days, we observed all laser readings oscillating in phase with each other, clearly indicating a wavemeter drift. To mitigate this, we decided to place the wavemeter inside a sealed chamber constructed from vacuum components. We did not actively pump or control the pressure inside the chamber, but simply sealed it off. The setup is shown in Fig. 3.9.

3.3.2 Galvo-Based Fiber Switch

The HighFinesse wavemeter comes with an 8-port fiber switch, but in our setup, we typically need to lock around 12 to 16 lasers at the same time. To work around this limitation, we developed a method to bypass the restriction of the built-in fiber switch.

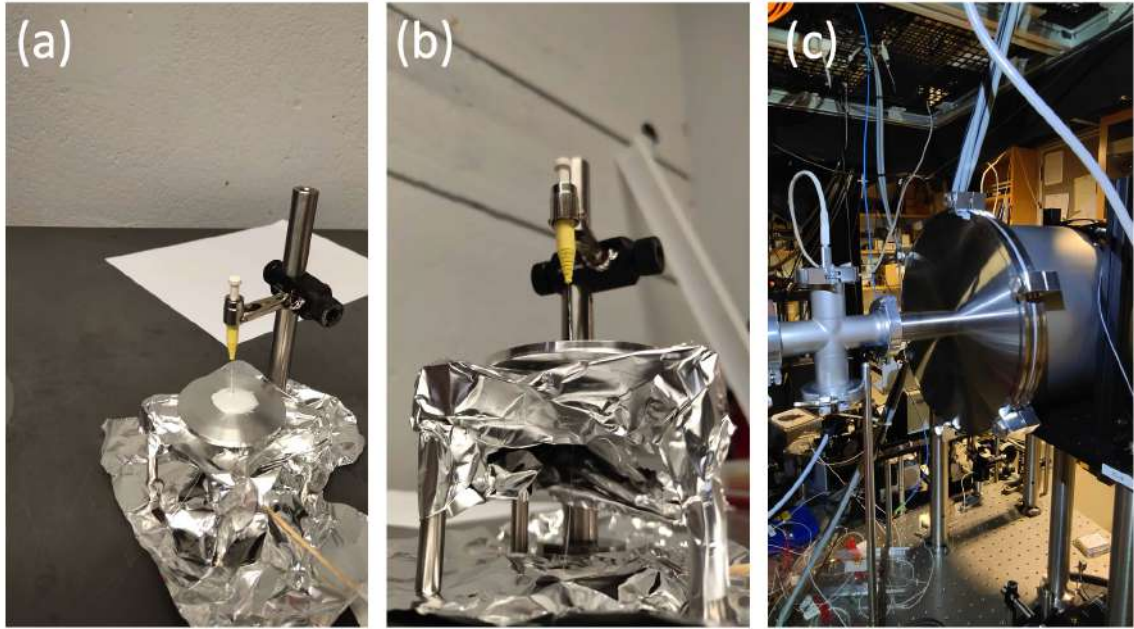


Figure 3.9: Wavemeter sealing setup. We used a Thorlabs bare fiber, epoxied through a KF blank with a drilled center hole, and a set of vacuum nipples to construct the sealed enclosure. To reduce vibration-induced readout fluctuations, sorbothane pads were placed between the wavemeter and the chamber walls. This setup worked well. We no longer observe large, sudden drifts in the measured frequencies across all lasers. However, we still see a slow, regular frequency shift of about 10–20 MHz per month, which we believe is due to gradual temperature changes in the lab. Overall, we are satisfied with this improvement, but continuous calibration with an absolute frequency reference is a must. We previously used the 689 nm laser from our neighboring strontium dimer experiment, to calibrate the wavemeter, but it seems it is necessary to have a stable frequency source ourselves, aka potassium vapor cell.

The basic idea is as follows: on an optical table, we set up 16 (or any other required number of) fiber ports for the lasers to be locked. All these beams are directed toward a pair of Galvo mirrors (Thorlabs GVS002). A Galvo mirror allows for precise and repeatable angular adjustments based on an input analog voltage. By programming the Galvo mirrors appropriately, we can steer each laser beam into a single fiber, which then sends the light into the wavemeter one at a time.

The first version of the control system was built using an Arduino Due along with some home-built voltage summation and multiplication circuits. This setup is shown in Fig. 3.10. We used the DAC outputs from the Arduino, but they introduced significant noise in the control signal. This was visible as strong fluctuations in the intensity readings from the wavemeter. After investigating the issue, we learned that the onboard DAC of the Arduino was not ideal for low-noise applications.

To improve performance, we replaced it with an external DAC card from Analog Devices, which significantly reduced the noise.

The second iteration of the system, including software control, was adapted from a setup in Doyle's lab at Harvard. That version was led by Debayan and is now the current operating model in our lab.

Interestingly, the communication protocol between the wavemeter and its original fiber switch is quite simple. To decode it, we opened the cable and measured the voltages on each line while operating the wavemeter in switching mode. Once we identified the channel logic, we used that information in the Arduino to synchronize the Galvo control with the channel switching sequence.

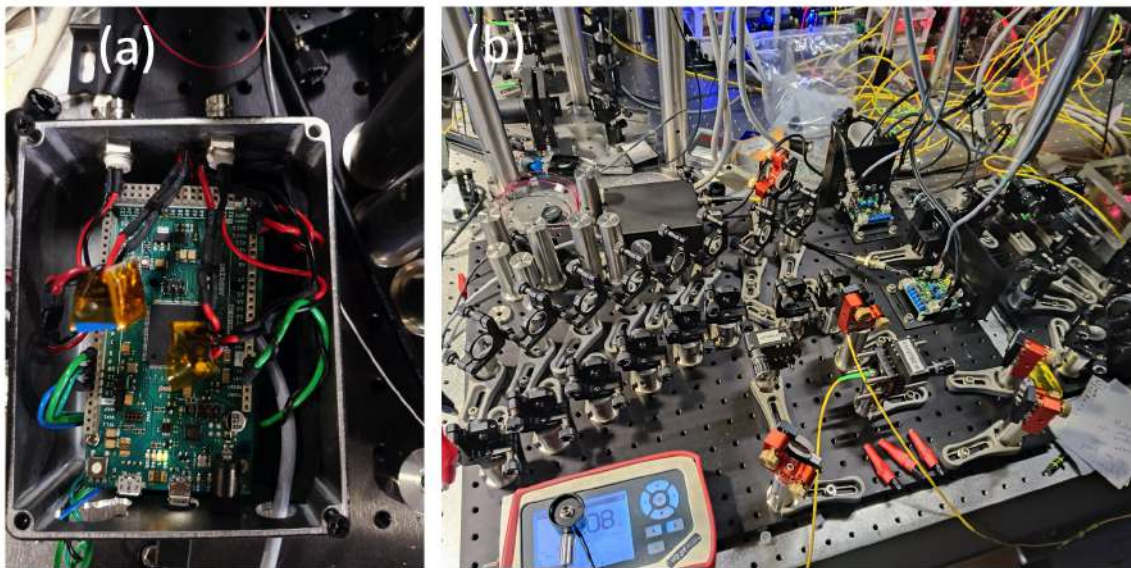


Figure 3.10: The first iteration of the Galvo-based fiber switch.

3.4 Vacuum System

When molecules are traveling or laser-trapped, they must be in an ultra-high vacuum (UHV) environment. Otherwise, they will collide with background gas and gain energy, which leads to heating. Since we constantly flow helium into the system as buffer gas for the CBGB, we do not expect our chamber vacuum pressure to reach the same level as in many ultracold atomic experiments. Instead, our goals are as follows: when the chamber is not connected to the cryostat,

the pressure should be around or lower than 10^{-9} Torr. When it is connected and helium is flowing, the pressure should remain below 10^{-8} Torr.

3.4.1 Vacuum Lifetime

Here we present a simple back-of-the-envelope model to estimate the vacuum-limited lifetime of a MOT:

- CaH–He cross section: $\sigma = 77 \times 10^{-20} \text{ m}^2$
- Helium pressure: $P = 1 \times 10^{-7} \text{ Torr} = 3.3 \times 10^{-5} \text{ Pa}$ (worst-case estimate)
- Helium density: $n = \frac{P}{k_B T} = 3.2 \times 10^{15} \text{ m}^{-3}$
- Helium average thermal velocity at room temperature: $v = \sqrt{\frac{8k_B T}{\pi m}} = 1260 \text{ m/s}$

The time constant for CaH–He collisions is:

$$\tau = \frac{1}{nv\sigma} \approx 300 \text{ ms}$$

In typical molecular MOTs, the dominant loss mechanism is optical cycling loss, which usually limits the lifetime to a few tens of milliseconds. So even if the helium pressure reaches 10^{-7} Torr, vacuum loss will not be the main limitation for observing a MOT. This is even more true for slowing and cooling stages. That is why we do not need ultra-high vacuum conditions as stringent as those in atomic experiments.

3.4.2 Baking

Even though the calculation above suggests that vacuum may not be a strict limitation, it is still good practice to aim for the best vacuum possible. Oils, including human grease, trap gases and slowly release them inside a UHV system. Special care must be taken to clean all objects before they enter the vacuum. It is worth noting that human skin is naturally covered in oils, so

when working with UHV components, it is strongly recommended to wear disposable gloves and long-sleeve clothing.

To achieve a good vacuum, the following cleaning and baking steps are typically followed:

- Assume every object is dirty by default. For heavily contaminated parts, wash with soap and Citranox acid cleaner to remove surface oils, dust, and oxides. This step can be skipped if the part is clean when purchased.
- Wash all surfaces using organic solvents to remove remaining oils and dust. Sonication is highly effective. Start with acetone, a strong solvent that removes most surface oils. However, be cautious with delicate components. For example, some coated mirrors, some plastics, and charcoals should not be immersed in acetone. Also, acetone can damage some materials if used for too long. According to lab mates working on strontium experiments, prolonged acetone exposure caused brass screws to oxidize. If safe to use, sonicate in acetone for multiple 10-minute rounds, replacing the solvent when it looks dirty.
- After acetone, rinse with isopropanol (iso) to remove any acetone residue. Iso is another strong solvent that evaporates quickly and helps carry away remaining contaminants. Usually, one 10-minute sonication in iso is sufficient.
- Finally, rinse with methanol. Methanol is a weaker solvent but evaporates even faster than iso. This final rinse helps to remove any lingering residues. After this, the part should be ready for baking.
- **Baking:** No matter how polished a surface appears, it has microscopic roughness that traps gas molecules. In UHV, these trapped gases slowly desorb and degrade the vacuum. Baking accelerates this outgassing by raising the surface temperature. For stainless steel, baking above 300°C is effective. If the system includes glass viewports, the temperature should be limited according to the manufacturer's rating, typically between 100°C and 150°C. Turbo pumps (backed by scroll pumps) must be active during the entire bake. For large components, we typically bake twice: once externally and again in situ, as shown in Fig. 3.11.

Without baking, we have observed pressure levels as high as 10^{-7} Torr due to increased outgassing.

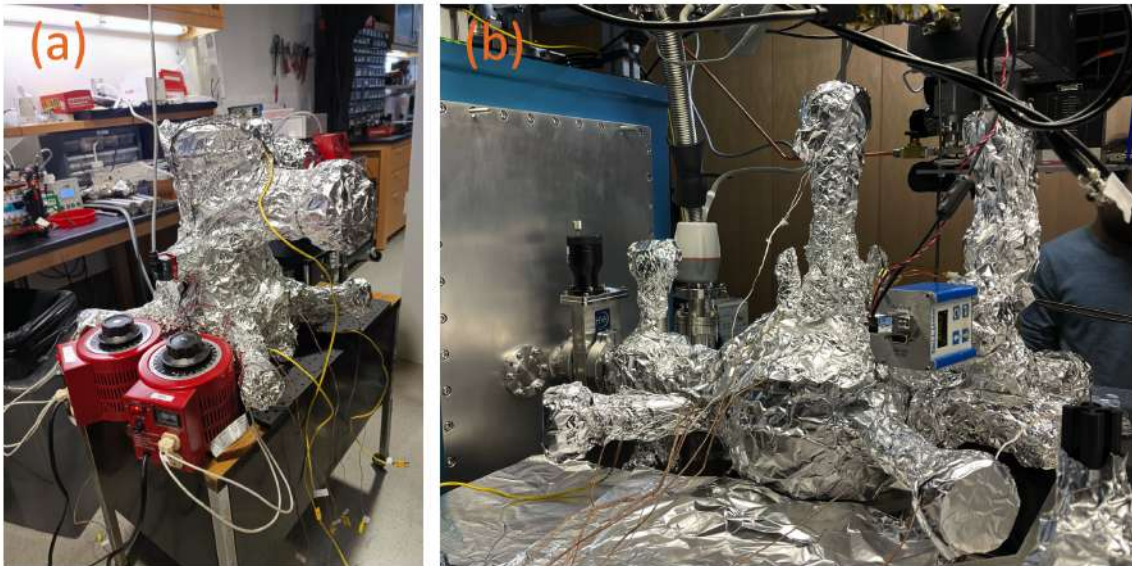


Figure 3.11: Baking of the vacuum chamber (MOT section). (a) External bake. (b) In-situ bake. This brought the pressure below 10^{-10} Torr, beyond the detection range of both our ion gauge and residual gas analyzer (RGA).

During baking, it is highly recommended to use a residual gas analyzer (RGA) and multiple vacuum gauges to monitor pressure continuously. The RGA identifies dominant gas species in the chamber. Before baking, water and nitrogen are usually dominant. After baking, these species are significantly reduced, along with the pressure floor. However, helium may still remain in the system, as it is notoriously difficult to pump out. By recording pressure over time, one can estimate how long it will take to reach the desired vacuum level.

3.4.3 Painting

Compared to ultracold atomic experiments, molecular experiments suffer from both lower signal strength and lower scattering rates. This makes laser absorption techniques impractical for detecting molecules in a beam. Instead, we rely on laser-induced fluorescence (LIF), which requires detecting weak photon signals using sensitive detectors like PMTs and EMCCDs.

In this case, scattered background light can easily overwhelm the signal if not carefully controlled. The interior of the vacuum chamber must be painted black to reduce reflections. If left untreated, the shiny stainless steel surfaces would scatter too much light, making LIF detection extremely challenging.

The paint we use is MH2200 black optical absorber, which has worked well in our system. More details on the painting procedure can be found in Jinyu Dai's upcoming thesis. Some example images are shown in Fig. 3.12.

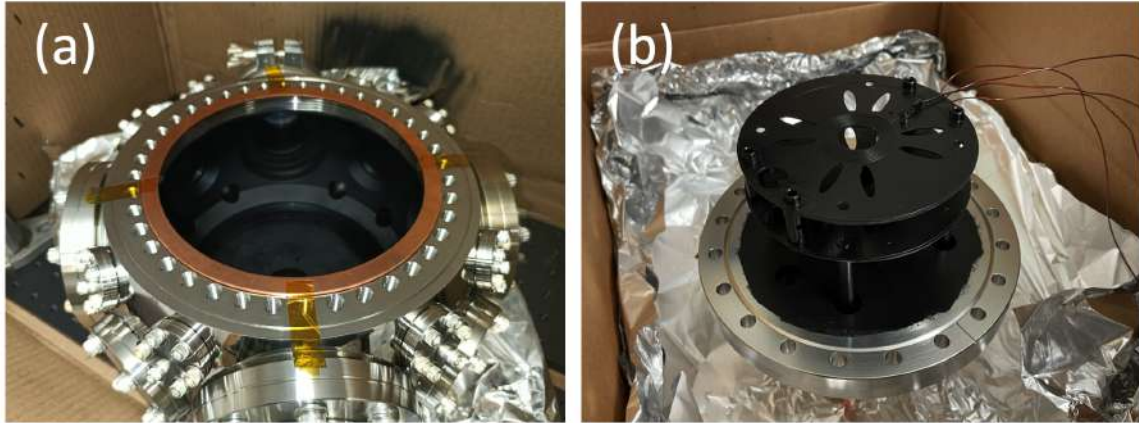


Figure 3.12: Black painting on the interior of the vacuum chamber. (a) Main MOT chamber after painting. (b) In-vacuum RF MOT coils after painting.

3.5 Misc

3.5.1 Magnetic Lens

Purpose The goal is to create a magnetic field that focuses weak-field seeking CaH molecules as they pass through, increasing the number that reach the detection region and enhancing signal strength. The desired potential is approximately quadratic in the transverse direction, producing a restoring force toward the center. The lens is built from twelve Neodymium (N52) permanent magnets with remanence $B_r = 1.45$ T. The magnets, casing, and assembly were provided by Magnet Sales & Service Limited.

Forces and Potential CaH molecules can be treated as magnetic dipoles. The dipole potential in a magnetic field is given by

$$V_{\text{dip}} = -\vec{\mu} \cdot \vec{B}.$$

The corresponding force is

$$\vec{F}_{\text{mag}} = -\nabla V_{\text{dip}} = \nabla(\vec{\mu} \cdot \vec{B}).$$

As in the Stern-Gerlach experiment, transverse spin components rapidly precess and average out. We therefore approximate $\vec{\mu}$ as aligned (anti-parallel) with \vec{B} , giving

$$\vec{F}_{\text{mag}} = -\nabla(|\mu B|), \quad V_{\text{dip}} = |\mu B|.$$

Shape of expected field We use 12 magnets, six arcs magnetized across the circumference, three magnetized with the north pole on the outside face, and three magnetized with the south pole on the outside face. The magnitude of the magnetic field, due to the hexapole design, is $|\vec{B}(\rho, \phi, z)| = B\rho^2 S(z)$, where $S(z)$ is the correction term for finite length. Here we use the cylindrical coordinate system, which should not be confused with the Cartesian coordinate system coming later. It gives the potential

$$\begin{aligned} V_{\text{dip}} &= |\mu B| \\ &= \mu B_0 \rho^2 S(z) \end{aligned} \tag{3.1}$$

where B_0 is magnetic flux density curvature (constant), and the force will be

$$\begin{aligned} \vec{F} &= -\nabla V \\ &= -\hat{\rho} \cdot 2\mu B_0 \rho S(z) - \hat{z} \cdot \mu B_0 \rho^2 S'(z) \end{aligned} \tag{3.2}$$

The last term is too small compared to the first term and can be ignored, which reduces the force expression to

$$\vec{F}(x, y, z) = -\hat{x} \cdot 2\mu B_0 x S(z) - \hat{y} \cdot 2\mu B_0 y S(z).$$

Simulation

Magnetic field simulation based on Mathematica We used the package "Radia" under Mathematica environment to simulate the magnetic field generated by the 12 permanent magnets at given geometry parameters adopted from the python program. The direction of magnetization is shown in figure 3.13, and the shape of magnets used in simulation is in figure 3.5.1.

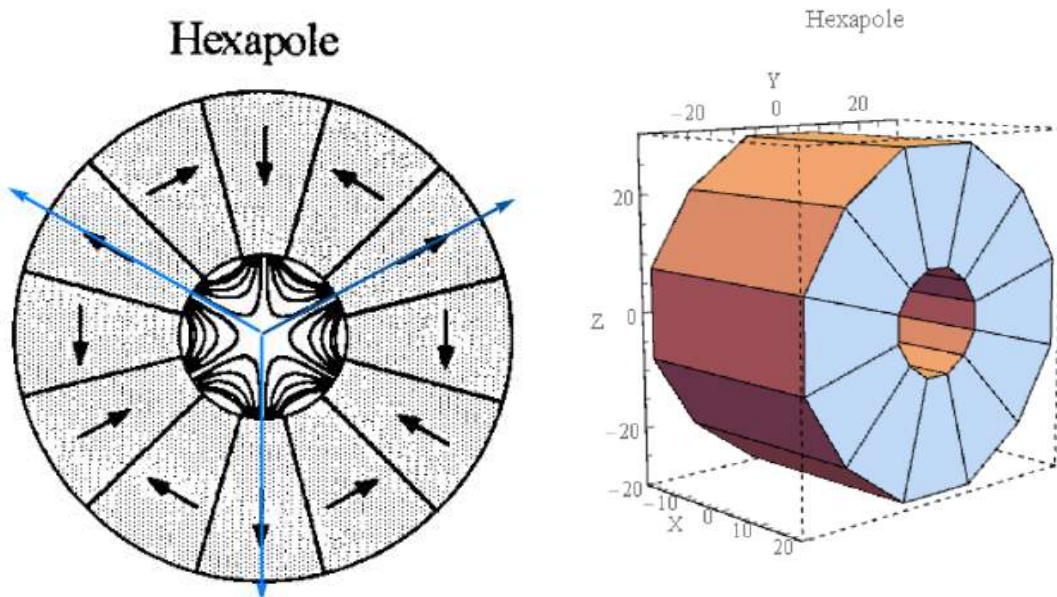


Figure 3.13: Magnetization direction and shape of magnets

Quadratic function approximation Given the geometry parameters, which is determined by molecular trajectory simulation on Python, we are able to use Mathematica to calculate the magnetic field in space.

According to PhysRevA.54.5067, the magnitude of \mathbf{B} follows a quadratic function:

$$|\vec{B}| = B_3(\rho/\rho_1)^2 = \frac{3}{2}B_r[1 - (\rho_1/\rho_2)^3]G_{12,3}(\rho/\rho_1)^2,$$

where ρ_1 and ρ_2 are the inner and outer radius respectively, B_r is the remanence of magnet, $G_{12,3}$ is geometry factor.

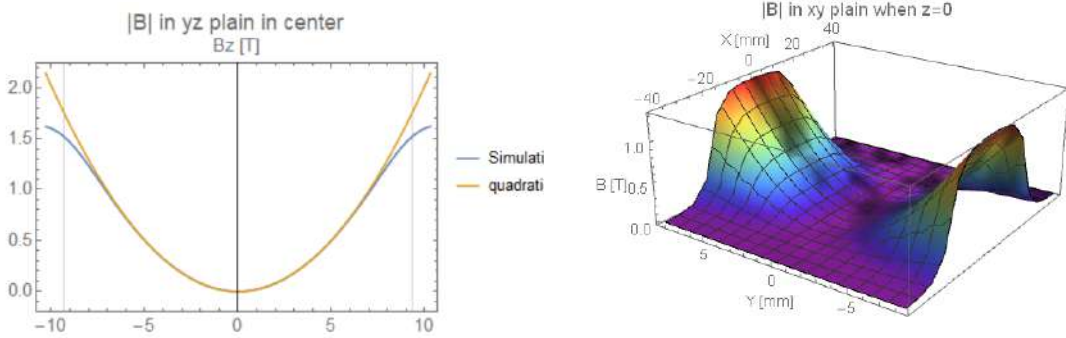


Figure 3.14: B in yz plain at x=0, and valley on the potential

The blue line in figure 3.14 is the quadratic function using the parameter from [39], so in some sense we have proven this approximation is acceptable. To picture it in a more vivid way, fig 3.5.1 it shows the magnitude of B in xy plain where z=0. Here we don't consider the dependence of μ (or g) on B.

Finding the fitting function $S(x)$ Along the x direction, the field is not constant due to the finite length of magnets. And we can see that from fig 3.15. After normalization we should get expression of $S(x)$ from eqn.3.1. According to Hsin-I Lu's thesis [40] (page 80) and [41], $S(x) = 1/(1+x^2/d^2)^2$. However, the fitting result doesn't look good, as shown in fig 3.5.1. And the function used in [42], $S(x) = \frac{1}{(1+(x/a)^4)^2}$ also isn't satisfying enough, shown in fig 3.16. We can see the reason why these functions are not working properly is they are not increasing/decreasing fast enough. Eventually, after some attempts, I took the idea of Sigmoid Function (widely used in Neural Networks), and “guessed” that it should have the form of $S(x) = \frac{1+e^{-l|x|/d}}{1+e^{(|x|-l/2)/d}}$, with one fitting parameter “d”. The fitting result in Fig. 3.5.1 appears to be quite accurate, suggesting it is a reasonable approximation of the field decay at present.

But there are some questions with it. First, "d" might not have a physical meaning, due to the fact that the first order derivative of the fitting function is discontinuous at x=0. The good news is, in the python simulation, we don't need to know that. Second, “d” varies with a bunch of parameters, for example, fig 3.17 shows the dependence of d on angle and distance (not normalized and poor fitting on the edge/center due to digital inaccuracy). To deal with it, we use an average value

of approximately 2.9 mm for d and put that into the python program. It remains a pretty good approximation in almost all regions.

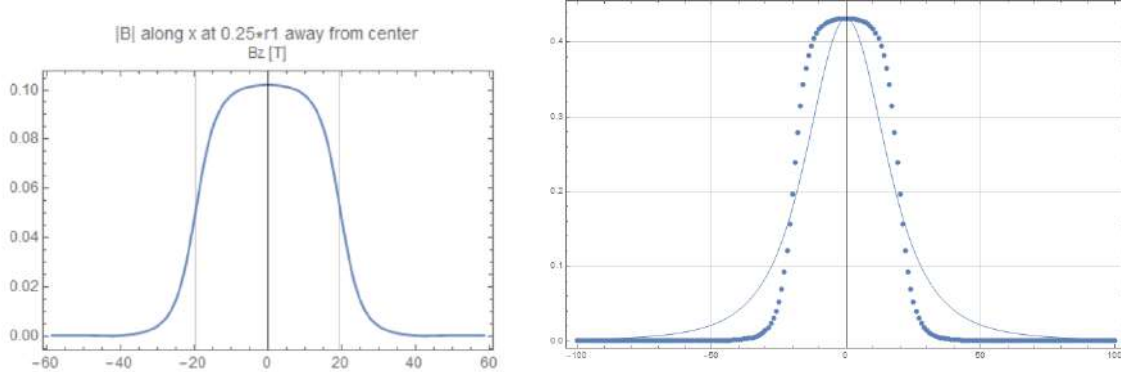


Figure 3.15: B along x when $\rho = 0.25r_1$, and Hsin-I's $S(x)$ function fitting result

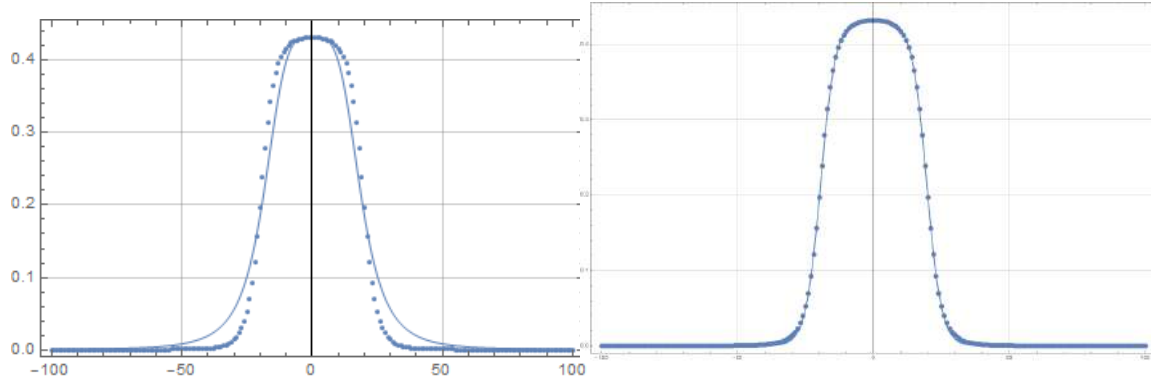


Figure 3.16: another fitting function, and Sigmoid fitting function when $\rho = 0.5r_1$

Some flaws There are some flaws on the digital solution by "Radia" package, one key point is the boundary instability. Here, we have adjacent magnets with different magnetization directions, which will make the field near the joint region behave weird. In fig 3.5.1, the external region is cut-off, but it should not affect the simulation accuracy in other regions. Another flaw is the limited significant figures, evident in the nonzero field at the geometric center. It should be zero due to the geometrically symmetric design; but the simulation gives a pretty small but nonzero value.

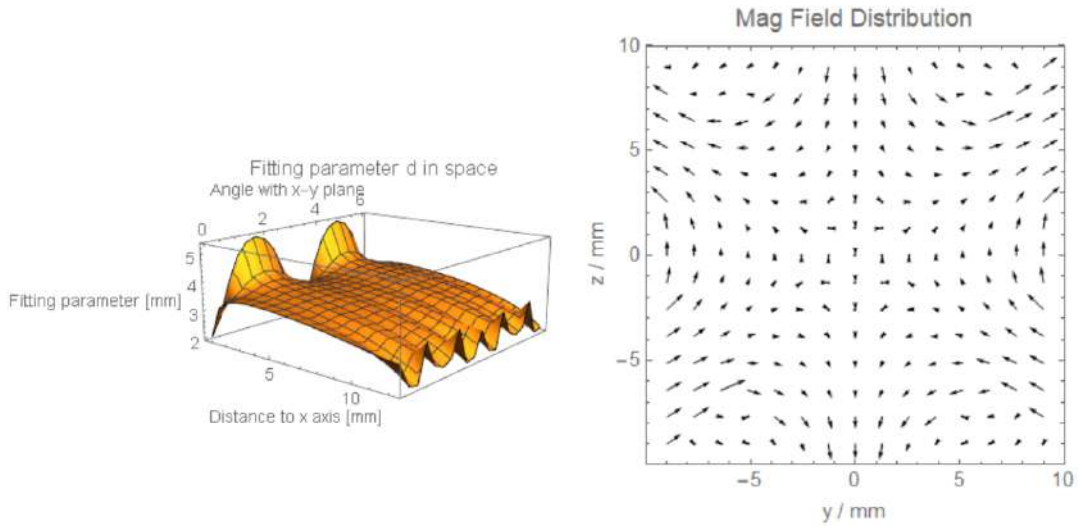


Figure 3.17: stability of fitting parameter "d" in space. This plot gives the average $d = 3.1\text{mm}$, at $r_1 = 1.3\text{cm}$, $l_l = 4.0\text{cm}$. The right figure is the direction of magnetic field in space

Molecular trajectory simulation based on Python

Parameters and variables All discussion here is based on program version4.1.

The important variables and parameters associated with magnetic lens is shown in the table below.

<i>parameters name</i>	<i>value</i>	<i>comment</i>
ro	0.005	the cryochamber diameter (m)
vxx	180	forward velocity (m/s)
B_r	1.45	remanence of magnet (T)
G_12_3	np.sin((3+1)*pi/12)/((3+1)*pi/12)	geometry factor
B_3	$3/2 * Br * (1 - (r1/r2)^{**3}) * G_{12_3}$	$ B = B_0 r^2 = B_3 r^2 / r_1^2$
ooke	$- mu_B * g * 2 * B_3 / r1^{**2}$	$F_x = ooke \cdot x = -2\mu_B g B_0 x$
<i>variables name</i>	<i>optimal point</i>	<i>comment</i>
r1	0.0093 → 0.010	inner radius (m)
r2	0.0300	outer radius (m)
ll	0.0390 → 0.040	magnets length (m)
dm	0.2000	distance from source to mag lens (m)

In this table, the optimal point change is from version 3.1 to version 4.1; the difference comes from changing d1 and d4. d1 difference comes from the geometry measurement I did recently. See fig 3.20 for more information about dependence on d4.

We switch to Cartesian coordinate, where x is the dominant velocity direction. The program simulates the following process (also in fig 3.18). Molecules are emitted from the cryochamber (diameter ro), propagating (dw), skimmed by the wall (diameter rw), propagating (dm-dw-ll/2), feeling the leaked field (length ll/2), converged and skimmed by the mag lens (ll, r1), feeling the other part of leaked field, propagating till collimator (d1 = 0.481m), skimmed by the collimator (radius rc = 0.005m), propagating to detection region (d4, area=0.005m*0.02m).

Logic of program + some details State 1: Initializing. The molecules are evenly distributed in y and z in space and skimmed by a circle with diameter ro. They are assigned with velocity following Maxwell-Boltzmann speed distribution. Then skimmed by another collimator (the stainless steel

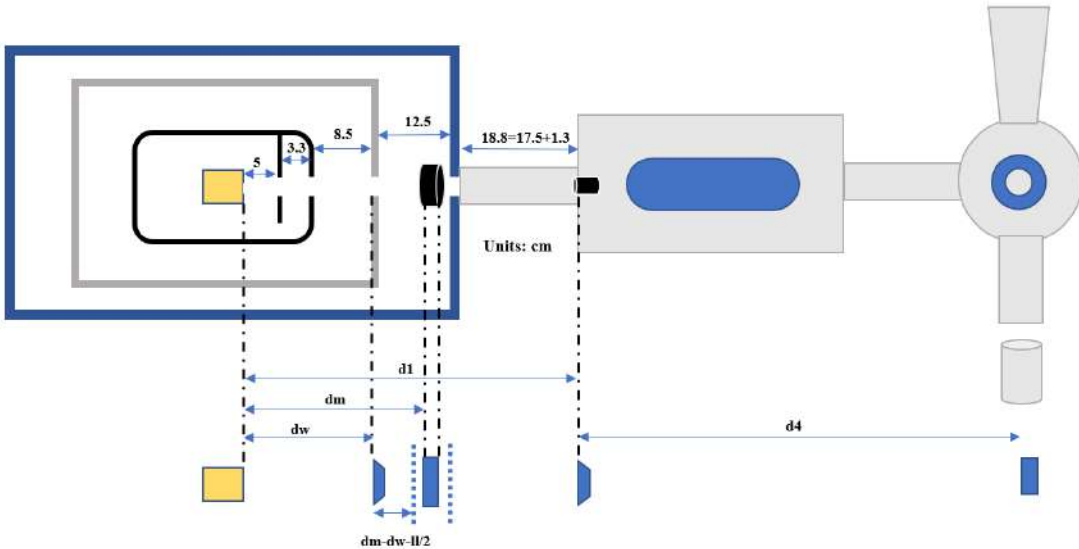


Figure 3.18: Simulation setup. Above is experiment geometry, below is python simulation parameter

wall).

State 2: Passing through lens. This process consists of two parts, outside the lens and inside the lens, but the algorithm is the same. Calculate the quadratic function $B(r)$, and read g-factor from CaH. We do interpolation on $g(B)$ using $B(r)$. Using the fitting function $S(x)$ to get the overall magnetic field. Then we use Leap-Frog method to calculate molecular motion. We check for possible skimming all the way.

State 3: Propagating to the collimator and getting skimmed, then to the laser region (which is turned off), and eventually arriving at detection region.

Simulation result We analyze velocity and distribution after all important nodes, and we can get the trajectory of molecules in space, and their distribution in the detection region. We then use the number of molecules in that region to represent the signal strength.

First we run the case where there is no mag lens. And when there are $1e6$ molecules coming out, the signal ≈ 270 when $d4=0.45m$, and signal ≈ 150 when $d4=1.0m$. From the trace plot in fig 3.19, we can see strong dispersion after lens.

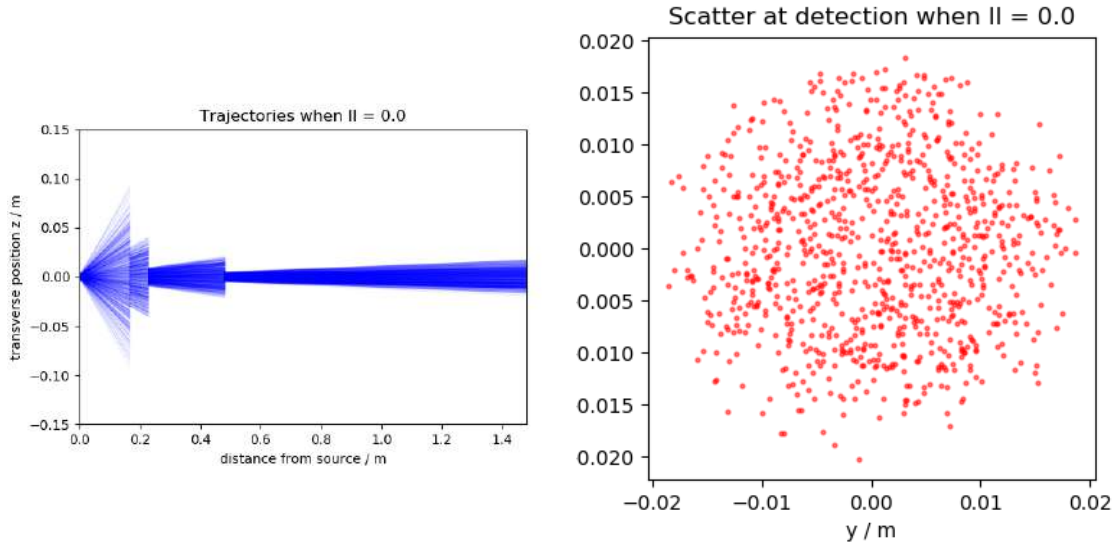


Figure 3.19: trajectory without mag lens, and signal without mag lens

Second we set B_r (remanence), ll (magnets length), dm (distance between chamber and lens) as constant, and scan r_1 (inner radius), we can find a peak. Use this peak value so that we can fix r_1 temporarily, and scan ll . Then do the same to dm . r_1 and ll converge pretty fast in parameter space. The results are shown in fig 3.20.

The signal strength ratio for different d_4 is about 4600 (0.45m) : 1230 (1.0m) : 330 (2.0m) \approx 14 : 3.7 : 1.

Another interesting topic is the focal length of the magnetic lens. According to [40], the analytical expression of f is

$$f = \frac{Mv^2}{\mu \delta_r^2 B_0 L},$$

Here, $\delta_r^2 B_0$ means $2B_0$ in the previous table. I scan r_1 and ll , and get some theoretical f using above equation, shown in fig 3.21. We can try some data, and compare them with the theory ones, e.g. we can choose from fig 3.20 (a) and (b). By observation, (a) gives $u=0.248\text{m}$, $v=0.15\text{m}$. Using thin

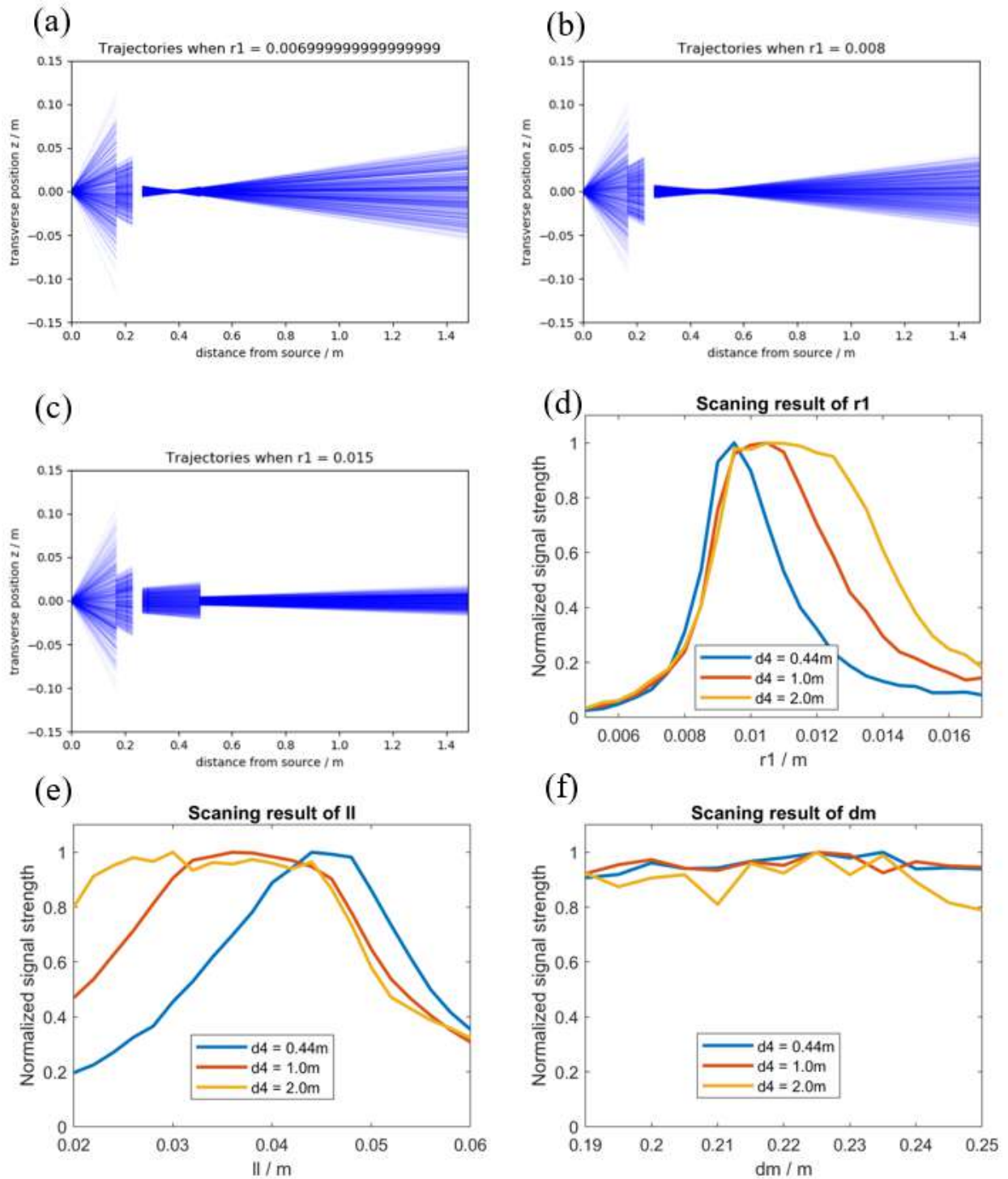


Figure 3.20: Parameter scanning results. (a)-(c) are the trajectory of molecules with different r_1 , noticing changes of focal length. (d)-(e) represent the normalized signal dependence on r_1 ll and dm , respectively.

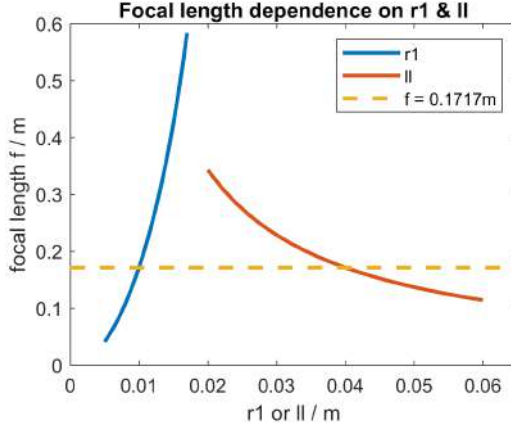


Figure 3.21: Focal length scan

lens equation,

$$\frac{1}{f} = \frac{1}{u} + \frac{1}{v},$$

we can get the estimate $f=0.0935\text{m}$. And the theoretical parameters give $f=0.0821\text{m}$. We can do the same to (b), and $f=0.1137$, while theory gives $f=0.1079$. So we can safely say that the lens focal length can be roughly calculated in the above way. The ideal geometry dimension we chose, gives $v=0.5581\text{m}$.

More questions related with simulation Now we are confident about analytical expression of focal length, which is $f = \frac{Mv^2}{\mu\delta_r^2 B_0 L}$, here are some other questions.

The forward velocity can influence the effective focal length by changing the time needed to pass the lens. For CaH molecules, so far we do not have TOF data to support the forward velocity distribution, but we can make simply estimation using BaH data, which was presented in [43], fig 3.24. In our current setup, the aperture is 5mm, so maybe we can assume the forward velocity of **CaH** is mainly in the range of 100m/s to 200m/s. Thus, we need to investigate the optimal geometry dimension for different velocities.

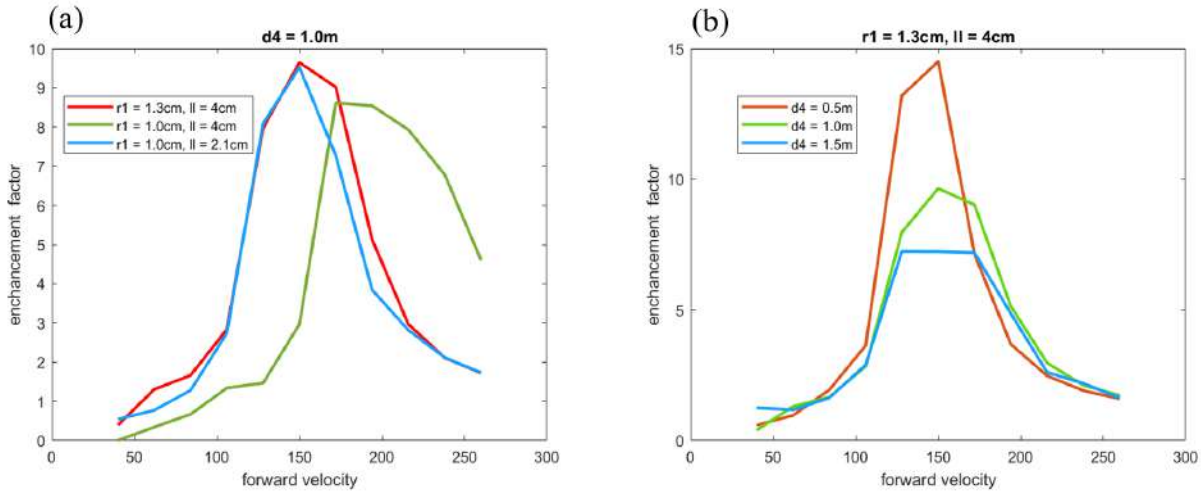


Figure 3.22: (a) At a given d_4 , we can vary r_1 and l_l to achieve the similar shape of enhancement factor vs. forward velocity. And it was predicted in fig3.21. By tuning r_1 and l_l we can compensate the effect caused by velocity. (b) Different detection position gives different enhancement factor.

		Forward velocity	120m/s	180m/s	240m/s
$d_4 = 0.5\text{m}$	r_1 / cm	1.5	1.0	0.8	
	l_l / cm	4.3	4.0	4.5	
$d_4 = 1.0\text{m}$	r_1 / cm	1.5	1.0	0.85	
	l_l / cm	4.3	3.6	4.1	
$d_4 = 1.5\text{m}$	r_1 / cm	1.5	1.0	0.9	
	l_l / cm	4.0	3.5	4.6	

We can know that at a certain d_4 (detection position unchanged), if we increase (/decrease) forward velocity, we are increasing (/decreasing) the focal length. To move the focal point back to the original place, we should decrease or increase r_1 , respectively. The change of l_l seems insensitive. This trend can also be discovered in fig 3.22 (a), where we manage to keep the shape by changing r_1 and l_l individually.

The general process for designing an effective lens system 1, varying r_1 and l_l individually under the expected peak velocity using program version 4.1, and we can get peak signal strength

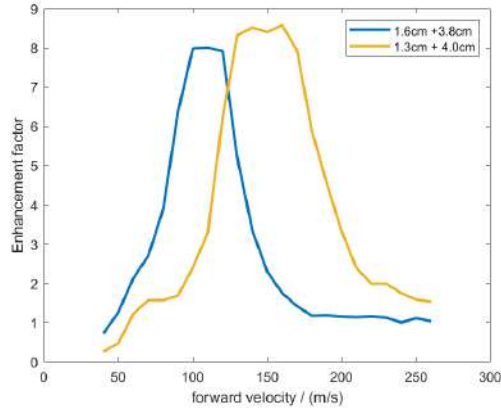


Figure 3.23: The geometry designed to optimize for 100m/s and 150m/s at $d_4 = 1\text{m}$. The first number in the label is inner radius, the second is length.

settings; 2, put the optimal settings generated by step one into the velocity scan, using program version 4.1.1. The result agrees with each other due to focal length equation.

By following above steps, if we want the peak at around **150m/s**, the configuration is: **r1 = 1.3cm, ll = 4.0cm**. If we want the peak at around **100m/s**, it's: **r1 = 1.6cm, ll = 3.8cm**. And the enhancement factor is given in fig.3.23.

Position of detection region / focusing point Our ultimate goal is to load the molecules to a MOT, so it's reasonable to assume d_4 in the range of 0.5m to 1.5m. For a given lens geometry, we see different response when we vary d_4 , from fig 3.22 (b).

Also, the detection region, since our purpose has switched to loading MOT, is now changed to a small circle with radius 5mm. However, this appears to be a minor change, as the signal strength does not vary significantly.

Orders related

CAD design The CAD model was initially created by intern Tianli Wang, and I completed it. The expected geometry dimension should follow the simulation.

Material choices For magnets, according to K&J Magnetics, the remanence of N42 magnets is 13.0-13.2 KGs, and the remanence of N52 is 14.5-14.8 KGs. In the simulation I used 14.5 KGs as

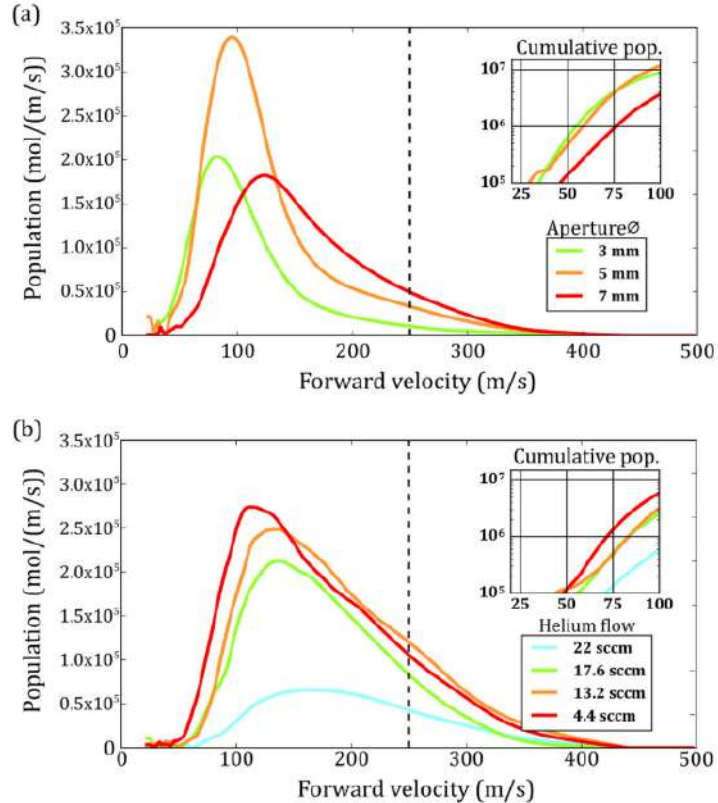


Figure 3.24: Measured forward-velocity distributions of BaH molecules for a range of beam-aperture diameters and buffer-gas are slightly less reliable due to a mild sensitivity on specific data cuts flow rates. Velocity distributions above 250 m/s (dashed lines) made to reject fluorescence noise from ablation light. The small-scale structure at low velocities is an artifact of deconvolution. (a) Velocity distributions for three beam-aperture diameters. The inset shows a conservatively estimated cumulative population of molecules as a function of forward velocity under 100 m/s. The 5 mm aperture is optimal, although a slight enhancement of very slow molecules at rates of 11 ± 2 sccm were used. (b) Velocity distributions for four 50 m/s is observed for the 3 mm aperture. For this data set, He flow He flow rates and a 7 mm cell aperture, with the inset as in part (a). There is an enhancement of slow molecules at lower flow rates. Figure adopted from Ref. [43].

Br.

For Inner ring, we want it to be strong enough to withstand the strong compressive and attractive forces between the magnets, so we are considering stainless steel, brass, and titanium. According to K&J Magnetics, magnetic stainless steel (like a 400 series) might change the field inside the halbach array. After talking to Magnet Sales & Service, we decided to use 300 stainless steel for inner ring. The outer case will be made of aluminum.

3.5.2 Acousto-Optic Modulator (AOM)

In modern molecular physics experiments, precise control over laser frequency, intensity, and timing is essential. Two key devices used to achieve such control are the acousto-optic modulator (AOM) and the electro-optic modulator (EOM). These devices are critical in implementing laser frequency shifting, amplitude modulation, and generating sidebands for addressing multiple molecular transitions. I will begin with the AOM.

AOM is based on the acousto-optic effect, where sound waves propagating through an optically transparent medium (crystal) create a periodic modulation of the refractive index. This modulation acts like a diffraction grating for light. The device consists of a non-linear crystal (commonly made from TeO_2 , fused silica, quartz, or germanium) through which an RF-driven piezo vibrates and generates an oscillating compression wave, phonons (quantized sound waves).

When a laser beam passes through the crystal, photons interact with the phonons in the medium. A photon absorbing a phonon experiences a frequency shift equal to the RF drive frequency. This process also causes a change in the photon's propagation direction. The frequency-shifted beam appears in the first-order diffracted direction, with either a positive or negative frequency offset depending on the geometry. Bragg's law governs the phase-matching condition for efficient diffraction. With good alignment and optimized everything, the diffraction efficiency into the first order can exceed 99%.

In our lab, we typically use AOMs from reliable companies such as IntraAction and Gooch & Housego, which are known for high stability and clean beam profiles. Other manufacturers

like Isomet, AA, and Brimrose are also used, although performance can vary depending on the application.

3.5.3 Electro-Optic Modulator (EOM)

The EOM relies on the electro-optic effect, where an applied electric field alters the refractive index of a nonlinear crystal. Materials like lithium niobate (LiNbO_3), beta-barium borate (BBO), and lithium tantalate (LiTaO_3) are commonly used. A typical EOM consists of a crystal sandwiched between electrodes, where an externally applied voltage induces a phase shift in the transmitted light. Higher voltage corresponds to a greater phase shift.

When a sinusoidal voltage is applied, it modulates the optical phase, creating sidebands at integer multiples of the modulation frequency. So sometimes people want only +/- 1st order frequency sidebands, then one can drive it with a simple LC circuit. But to drive to, for example, +/- 50th order, one needs careful engineering. This is expected for Jinyu Dai's thesis. For details of how to build an EOM in house, I strongly recommend reading Eric Norgarrd's thesis [44]. EOM is particularly useful in applications where multiple frequency components are needed simultaneously, such as driving transitions between different hyperfine states or even spin-rotation states for slowing light.

Chapter 4: Endothermic Reaction in a Cryogenic Buffer Gas Cell

4.1 Introduction: Motivation and Surprises

Chemical reactions at low densities and low relative energies are characterized by the limited number of available reactive trajectories. Such reactions occur in astrophysical environments and may be responsible for the production of hydrocarbons in the early universe [45, 46]. Studies of rate coefficients for single-collision events in controlled laboratory environments can shed light on phenomena such as quantum interference between reaction pathways [47, 48] and the role of entanglement in reactions [49]. Techniques such as cold molecular beams [50, 51], supersonic jets [52, 53, 54], Stark deceleration [55, 56], centrifuge deceleration [57], ion trapping [58, 59, 60, 61, 62], optical lattice trapping [63], and optical tweezers [64] have enabled extreme reaction regimes unrealizable with traditional techniques and have exposed new quantum phenomena [65].

However, there is an intermediate regime in the chemical reaction landscape where densities and temperatures straddle the line between quantum and classical [66]. Here, the motional states of the reactants can be treated classically but the quantum nature of their internal states cannot be neglected. This regime is manifested in cryogenic buffer gas beam (CBGB) sources [67, 68]. Typical gas densities in a CBGB source can be of the order of 10^{15} cm^{-3} and equilibrium temperatures of the order of 4 K. But laser ablation, which is typically used to create the molecules of interest, can produce transient temperatures as high as 10^4 K [69]. Hence this configuration allows scattering processes that extend from multiple partial waves [70, 71] to simple hard-sphere scattering [72]. CBGB sources are experimentally versatile since different gaseous reactants can be introduced with ease. Therefore, a CBGB source is an ideal playground to study chemistry over a large parameter range. Not only from the perspective of chemistry, but one would hope for a different way to produce CaH in a CBGB source other than YAG ablating on CaH₂ solid samples,

which produces CaH signal unstably and weakly.

Three physical and chemical processes occur in a CBGB source. The first one consists of elastic collisions between the cold buffer gas and particles of interest, leading to translational cooling. The second one is inelastic collisions that reduce the internal temperature, or ro-vibrational cooling. The third one is chemical reactions that actually produce the particles of interest. The combination of the first two processes is buffer gas cooling, which has been a very successful technique for producing cold beams of atoms and molecules in their ro-vibrational ground states [68]. The third, reactive process has attracted renewed attention since many new molecular species have been successfully produced in CBGBs. These molecules range from diatomics such as CaF [73], YbF [74] and AlF [75, 76], to triatomics such as CaOH [77], YbOH [78] and SrOH [79], to polyatomics such as CaOCH₃ [80] and CaOC₆H₅ [81]. The typical protocol to produce a molecule of type *MX* is to laser ablate a metal target (*M* = Ca, Sr, Yb, ...) and allow the resulting hot plume to react with a donor gas (*RX* = SF₆, H₂O, CH₃OH, ...).

Typical reactions in CBGB sources are either barrierless or have low barriers that can be overcome with thermal or optical excitation, as can be seen from Fig 4.1. For example, Ca and SF₆ exothermically react to produce CaF [82], while the reaction between Ca and H₂O to produce CaOH requires exciting the Ca atom to the metastable 3P_1 state to overcome the ~ 1.3 eV barrier [77]. In contrast, the reaction between Ca and H₂ has a barrier of ~ 2.7 eV. Temperatures as high as $\sim 3 \times 10^4$ K would be required to overcome this barrier thermally, which is not readily accessible with laser ablation. One might expect such a reaction to produce a very low yield. In this work, we study the reaction of Ca atoms with H₂, D₂, and HD isotopologues, both with and without helium as a buffer gas. Counterintuitively, we find that the reaction is far more efficient than could be expected from a simple thermodynamic estimate, pointing to the critical role of the reaction dynamics over pure energetic considerations. Furthermore, we find that H₂, but not D₂ or HD, can serve as a buffer gas and thermalize the resulting CaH molecules to their ro-vibrational ground state. To explain these results, we model the reactant dynamics using rates obtained from quasi-classical trajectory simulations (QCT). Our calculations elucidate the general trends observed in

the experiment and provide an order-of-magnitude estimate of reaction rates.

				CaH / CaD	
				H ₂ / D ₂	653THz
				CH ₄	654THz
H ₂ O ₂	-387THz	-411THz	-846THz		
H ₂ O	314THz	290THz	-145THz		
CH ₃ OH	193THz	169THz	-266THz	H ₂ O ₂	483THz

	CaF	SrF	AlF	BaF	MgF	YbF
SF ₆	-362THz	-387THz	-677THz	-459THz	-435THz	-605THz
NF ₃	-652THz	-677THz	-967THz	-750THz	-725THz	-895THz

Figure 4.1: The enthalpies of several reactions that are being used or proposed to produce ultracold molecules through ablation induced buffer gas cooling. Within each table, the first row is the chemicals interested, the first column is the donor gas. The values are enthalpies of reaction. Orange box represent it's exothermic, while Blue box represent the reaction is the endothermic. From what can be clearly seeing reactions to form hydrides are all deeply endothermic reactions.

4.2 Experimental Implementation

Figure 4.2 illustrates the experimental setup. A copper cell with inner dimensions of 25.4 mm in diameter and 50.8 mm in length is thermally anchored to a pulse tube refrigerator cold plate at ~6 K. A Ca metal target is attached to the cell. We employ a pulsed Nd:YAG laser at 532 nm, focused onto the Ca target with a beam diameter of ~100 μ m, to ablate the target with an energy of up to ~30 mJ per pulse, pulse duration of ~10 ns, and repetition rate of ~1 Hz, creating a hot plume of Ca atoms. We simultaneously flow multiple species of gas into the cell for chemical reactions and thermalization. A thermally isolated fill line held at ~150 K is attached to the cell to flow H₂, D₂ and HD. He gas is pre-cooled to ~6 K and diffused so the distribution inside the

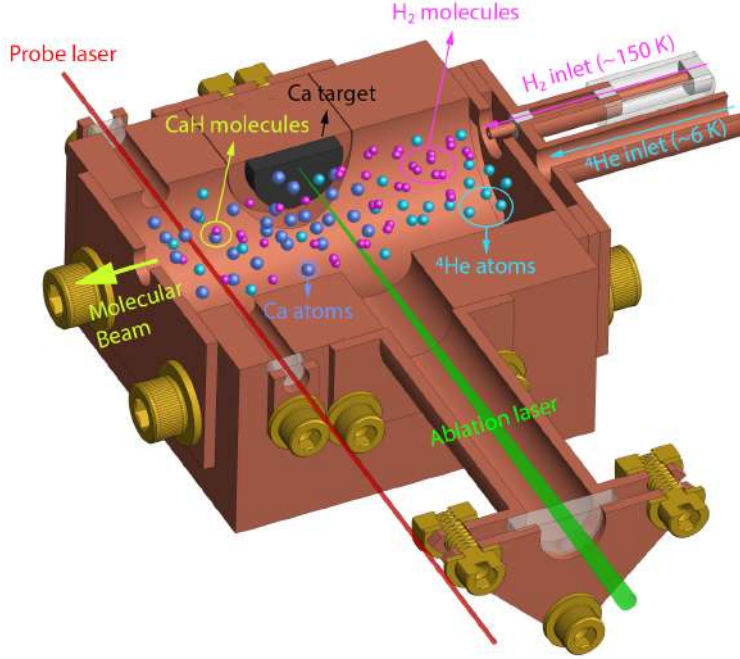


Figure 4.2: Horizontal cross section of the cryogenic buffer gas cell. Hot Ca atoms are generated via laser ablation of a solid target and subsequently react with H₂ molecules that flow in at ~150 K. Additionally, ⁴He flows in at ~6 K for efficient buffer gas cooling. The Ca atoms and the product molecules are probed through laser absorption, with optical access ~2 cm downstream from the target. Figure adopted from Ref. [83].

cell is homogeneous for more effective cooling. We probe the atoms and molecules of interest through laser absorption, via optical access ~2 cm downstream from the target. Specifically, we probe Ca atoms on the 4s4p $^3P_1 \leftarrow 4s^2 \ ^1S_0$ transition at 657 nm and CaH molecules on the $A^2\Pi_{1/2}(\nu' = 0, J' = 3/2, +) \leftarrow X^2\Sigma^+(\nu'' = 0, N'' = 1, J'' = 1/2, -)$ transition at 695 nm. We convert the CaH molecular density in the $X^2\Sigma^+(\nu = 0, N = 1, J = 1/2, -)$ state to cover all ro-vibrational states up to ($\nu = 0, N = 2$), accounting for all the cold molecules generated (Sec. 4.5.1).

4.3 Results

4.3.1 Ca + H₂ Chemical Reaction in a CBGB Source

Due to its endothermic nature, the Ca + H₂ chemical reaction is expected to be barely within reach in a CBGB source. However, we observe substantial production ($\sim 3\text{-}10 \times 10^{10}$ molecules /

steradian / pulse) of CaH molecules due to unique properties of cryogenic H₂ which can be found in Fig. 4.4, as explained below. We carefully calibrate the internal state distribution at various ablation energies up to the highest occupied state ($\nu = 0, N = 2$) (Sec. 4.5.1). We conclude the total CaH density in these internal states represents the entire CaH yield. The reaction occurs starting from the H₂ flow of a few standard cubic centimeters per minute (1 SCCM $\approx 4.5 \times 10^{17}$ molecules per second), and saturates at several tens of SCCM. This process is \sim 2-3 orders of magnitude more efficient than the exothermic reactions with other hydrogen isotopologues that we investigated; we further find that H₂ can serve as buffer gas without the need to flow He (Section 4.3.3).

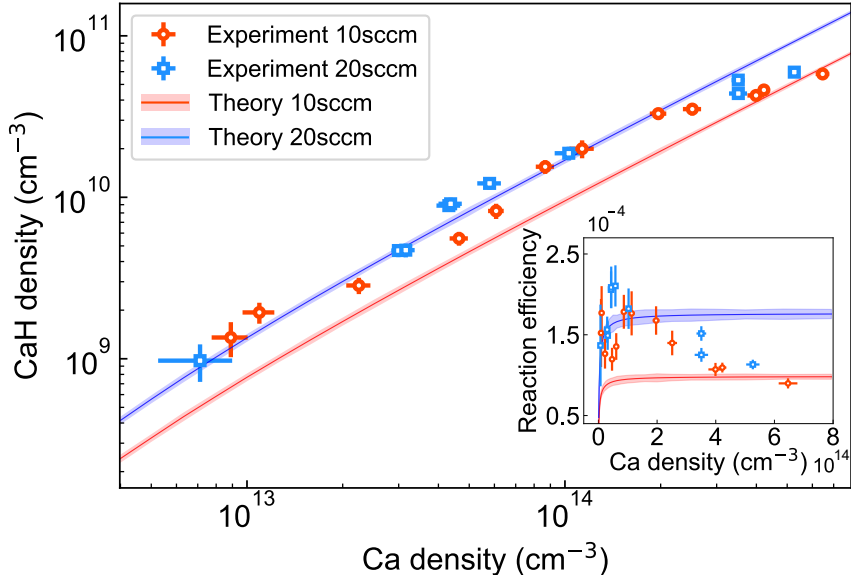


Figure 4.3: Chemical reaction in a cryogenic buffer gas cell. Time-averaged CaH density measurements (0-1 ms after ablation) as a function of Ca density, for 10 SCCM of H₂ (red points) and 20 SCCM of H₂ (blue points). The lines denote theoretical results at the same conditions, showing qualitative agreement. The inset shows reaction efficiency, defined as the ratio of CaH and Ca densities. A notable decrease in reaction efficiency is observed experimentally at higher Ca densities, whereas the theoretical model does not capture this trend, showing the need for further refinement. Experimental data points include 1- σ statistical errors. Figure adopted from Ref. [83].

Figure 4.3 shows the total measured CaH density as a function of the initial Ca density. The Ca density is varied by adjusting the ablation energy, which can also alter the ablation plume temperature. We develop a chemical reaction network model (lines in Fig. 4.3), utilizing the rates

from QCT calculations (Sec. 4.5.2). We find that a constant plume temperature with respect to Ca density provides the best fit to the data. This assumption is tested by measuring the plume temperature without gas flow (Sec. 4.5.3). We find a maximum 45(10)% increase with ablation energy, supporting the constant temperature assumption.

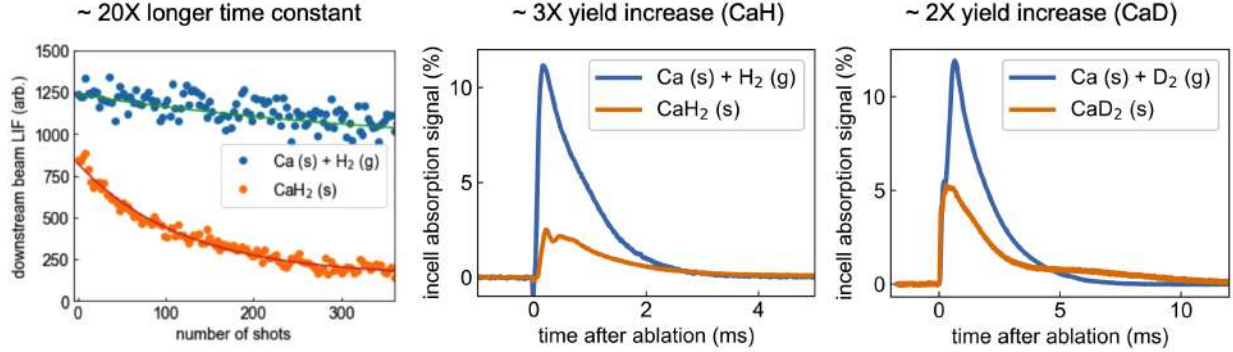


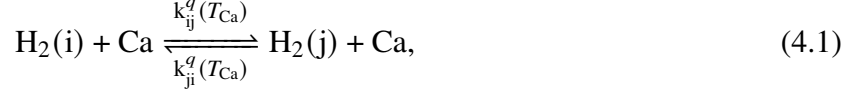
Figure 4.4: Significant improvement of the use of $\text{Ca} + \text{H}_2 \rightarrow \text{CaH} + \text{H}$ reaction compared to the old way of forming CaH through ablation on CaH_2 solid samples (as well as deuterium related experiments). The 20 times longer time constant comes from the better crystal structure of a calcium compared to CaH_2 , making it less brittle. I do not have a good intuition to clearly explain why it improves the yield, but we know this reaction can happen fast despite its endothermic nature. What we know for sure is, the endothermic nature is still limiting CaH yield.

While the data is in reasonable agreement with the reaction model predictions, some discrepancies arise at high Ca densities. As shown in the inset of Fig. 4.3, the reaction efficiency, or the fraction of Ca atoms converted to CaH molecules, falls toward higher densities. In contrast, in the reaction model the reaction efficiency saturates at high densities. This may be because the model does not include diffusion dynamics or non-equilibrium processes. One possibility is that the cooling is accelerated at higher densities, lowering the final CaH yield.

4.3.2 Reaction Network Model

The reaction model considers collisions between the ablated Ca atoms and H_2 molecules, allowing for vibrational excitation of H_2 and formation of CaH. We find that the vibrational state of H_2 affects the reaction while the rotational state does not. Thus we assume H_2 to be in the rotational ground state.

The cold H₂ gas in the CBGB source is assumed to be in the ground vibrational state initially. The model includes inelastic vibrational transitions of H₂ due to collisions with Ca in the cell,



where $i = (0, 1)$, $j = (1, 2)$, $i \neq j$ represent the vibrational level of the molecule. The formation of CaH is described as



where $i = (0, 1, 2)$ represents the vibrational level of H₂. Each collision has an associated temperature-dependent rate which is calculated via the QCT method (Sec. 4.5.2), $k_{ij}^q(T_{\text{Ca}})$ for the vibrational excitation of H₂ and $k_i^r(T_{\text{Ca}})$ for the formation of CaH.

We use a deterministic approach to study the evolution of these reactions in a closed system at thermal equilibrium by solving the set of differential equations associated with Eqs. (4.1) and (4.2). The temperature of the reaction is given by the translational temperature of Ca, or T_{Ca} , which falls via collisions with the H₂ and He buffer gases according to

$$\frac{dT_{\text{Ca}}}{dt} = -\frac{R_{\text{H}_2}(T_{\text{Ca},0} - T_{\text{H}_2})}{\kappa_{\text{H}_2}} - \frac{R_{\text{He}}(T_{\text{Ca},0} - T_{\text{He}})}{\kappa_{\text{He}}}. \quad (4.3)$$

The elastic collision rate between Ca and buffer gas (BG = He, H₂) is given by $R_{\text{BG}} = n_{\text{BG}}\sigma_{\text{BG}}^{\text{el}}\bar{v}_{\text{BG}}$, where n_{BG} , $\sigma_{\text{BG}}^{\text{el}}$, and \bar{v}_{BG} are the BG density, elastic cross section between Ca and BG, and average relative velocity between Ca and BG, respectively. $T_{\text{Ca},0}$ is the initial kinetic temperature of Ca, and $\kappa_{\text{BG}} \equiv (m_{\text{Ca}} + m_{\text{BG}})^2/(2m_{\text{Ca}}m_{\text{BG}})$. More details of the reaction network model and QCT methods can be found in Sec. 4.5.2 and Ref. [84].

4.3.3 H₂ as a Buffer Gas Coolant

We observe a pronounced discrepancy in the experimental production of CaH or CaD depending on whether H₂, HD, or D₂ is used as the reactant gas. With H₂, substantial yields of thermalized

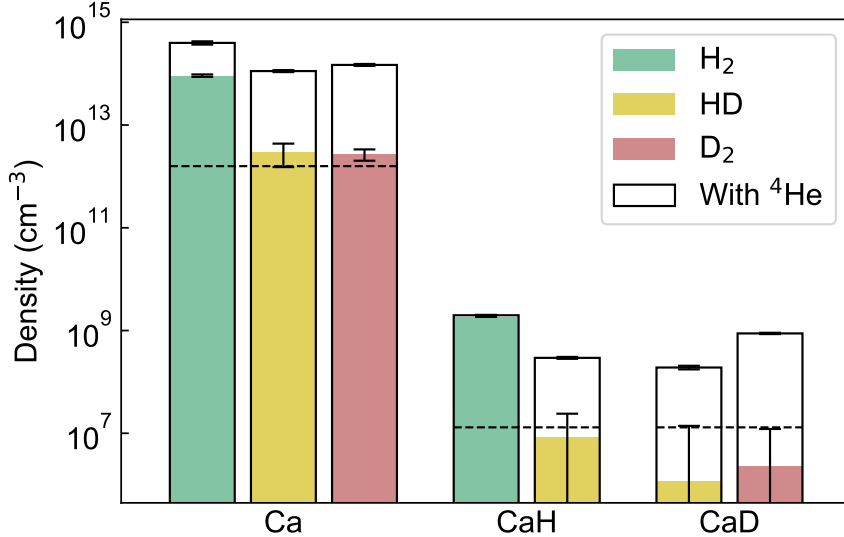


Figure 4.5: Time-averaged densities (0-1 ms after ablation) of Ca and CaH (or CaD) under different gas flow configurations. Reactant gases H₂, HD, or D₂ are supplied at 20 SCCM, with He (if used) added at 8.8 SCCM. Ablation energy is 19 mJ per pulse. Green, yellow, and red bars represent results for H₂, HD, and D₂, respectively, while black-framed bars show the yields with He added. The dashed lines indicate the detection limits. Figure adopted from Ref. [83].

Ca atoms and CaH molecules are detected, even in the absence of He as a buffer gas (Fig. 4.5, green). In contrast, using HD or D₂ under similar conditions results in significantly lower yields of thermalized Ca atoms, with molecular production falling below our detection limits (Fig. 4.5, yellow and red). These findings highlight the unique advantages of H₂ as a reactant and cooling medium in CBGB systems.

This phenomenon can be explained by the exceptionally high saturated vapor pressure of H₂ at cryogenic temperatures. For instance, the vapor pressure of H₂ at 6 K is ~ 1.5 mTorr, a few orders of magnitude higher than for HD (4.0×10^{-2} mTorr) and D₂ (1.5×10^{-3} mTorr) [85, 86]. This high vapor pressure allows a sufficient density of H₂ molecules to remain in the gas phase, enabling several productive collisions with Ca atoms before adhering to the cell walls or exiting the cell, and thus facilitating efficient chemical reactions and thermalization. In contrast, the lower vapor pressures of HD and D₂ result in rapid conversion to a condensed phase, leaving an insufficient gas-phase density to sustain a reaction with Ca. Additionally, the QCT simulations indicate an order of magnitude decrease in the formation of CaD in the presence of D₂ when compared with

CaH formation in the presence of H₂. This can be attributed to the increased mass of D₂ compared with H₂ [84].

Introducing cryogenic He into the system enhances the yields of both thermalized Ca atoms and CaH molecules across all reactants (black-framed bars in Fig. 3). This effect is likely due to He's high efficiency in gas mixture thermalization and providing hydrodynamic entrainment [68], which helps maintain a more stable and homogeneous environment in the cryogenic cell that is conducive to Ca and CaH detection. Adding He into the system therefore mitigates the limitations imposed by the lower vapor pressures of HD and D₂. Note that the CaH molecular yield does not increase as much as the thermalized Ca yield in the presence of He. This could be attributed to a faster drop of the Ca atom temperature in the presence of cryogenic He which in turn reduces the chemical reaction efficiency.

4.3.4 Collisional Cross Sections

Elastic collisions play a pivotal role in the thermalization process of CBGB systems. Larger elastic cross sections correspond to higher collision rates, facilitating rapid thermal equilibration of translational degrees of freedom. Inert gases such as He and Ne are often favored as buffer gas choices due to their relatively large elastic collisional cross sections with a variety of molecular species, on the order of 10^{-14} cm². Due to our observations of a strong H₂ buffer gas cooling effect, here we study the elastic cross sections of H₂, HD, and D₂ with Ca and CaH.

We employ a method adapted from Ref. [68], where we monitor the exponential decays of in-cell signals over time to derive the elastic collisional cross section. Details of the method can be found in Sec. 4.5.4. The data is presented in Fig. 4.6.

In order to reduce measurement errors, we select multiple ablation spot and flow rate combinations, and take statistical averages of the results. Given the low densities of Ca and CaH (or CaD) when using the HD and D₂ gases, we average these measurements more extensively. Noticeable shifts in the background signal were observed during measurements involving H₂, HD, and D₂, likely due to sublimation of ice deposits on the cell windows. This was accounted for by including

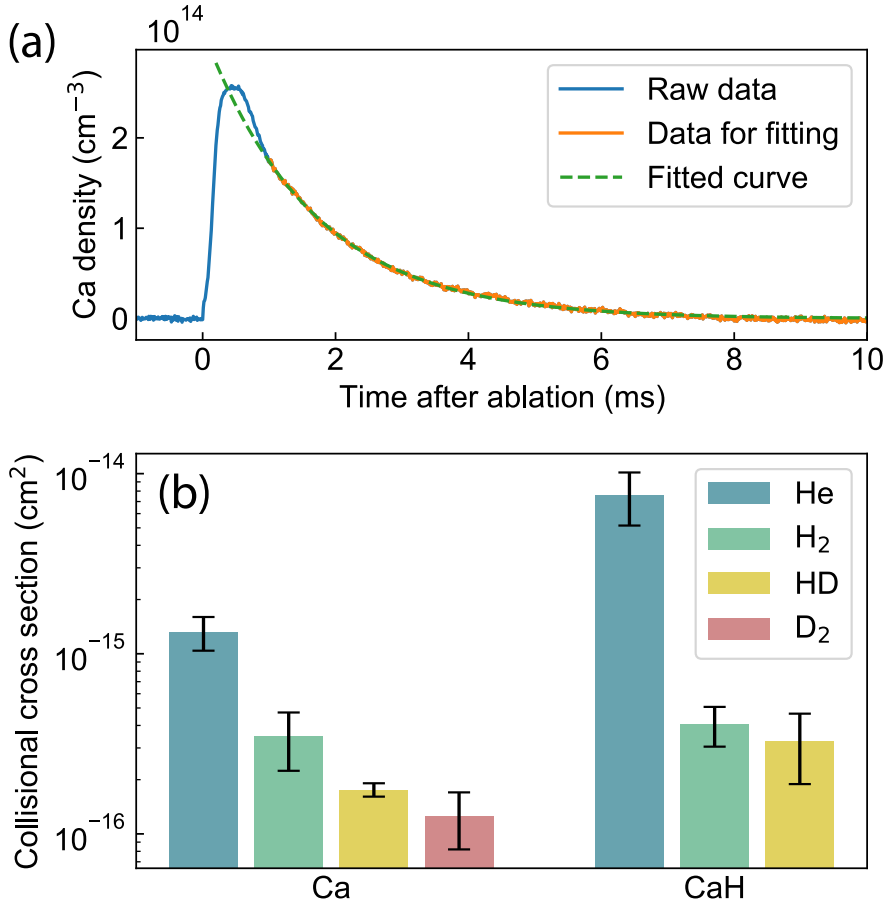


Figure 4.6: (a) Sample Ca density trace as a function of time after the ablation pulse. The blue curve is the original data, the orange line highlights the data used for fitting, and the green dashed line indicates the fitted result. This data is obtained with 8.8 SCCM He flow. (b) Measured collisional cross sections of He, H₂, HD, and D₂ with Ca and CaH. Figure adopted from Ref. [83].

a constant offset in the exponential fit. Ultimately, we have measured the elastic cross section of H₂ with CaH to be $4.1(1.0) \times 10^{-16}$ cm². This is high enough for efficient translational cooling in a regular buffer gas cell. We have also measured the ro-vibrational temperature of CaH with a H₂ buffer gas (Sec. 4.5.1) which provided evidence for efficient cooling with H₂.

4.4 Conclusion

We have observed and quantified the remarkable chemical and thermal properties of H₂ molecules as a reactant and buffer gas in CBGB sources. Our study of the chemical production of CaH molecules demonstrates several notable phenomena that broaden the scope of cryogenic chemistry

studies. This work also demonstrates a reliable method for generating cold CaH molecules in their ro-vibrational ground states, which shows a \sim 5-fold improvement over previous approaches [30, 87, 88], and holds significant promise for producing ultracold trapped clouds of CaH and ultimately H atoms for quantum chemistry experiments and high-precision spectroscopy [89].

The successful production of CaH molecules despite the significant reaction barrier (\sim 2.7 eV) demonstrates the effectiveness of H₂ as both a reactant and a cooling agent. This observation challenges the conventional thermodynamic assumptions associated with endothermic reactions in CBGB setups. The ability of H₂ to simultaneously facilitate chemical reactions and act as a buffer gas coolant highlights a dual functionality that has not been previously explored in depth.

The isotopic comparison reveals that H₂ outperforms D₂ and HD in both chemical reactivity and buffer gas cooling efficiency. This disparity can be attributed to the higher saturated vapor pressure and lower melting point of H₂ at cryogenic temperatures, as well as larger collisional cross-sections. These properties ensure a more robust supply of cold H₂ molecules in the gas phase.

We have simulated the reaction dynamics in a CBGB source using a reaction network model supplied with reaction rates from QCT simulations. This reaction model predicts the dependence of the reaction rate on the vibrational state of H₂ and successfully captures several qualitative trends observed in our experiments. This includes the influence of translational temperature on reaction dynamics and the isotopic differences. However, the inability of the model to accurately predict the reaction efficiency trend in the high density regime points to the need for more refined theoretical approaches such as including additional quantum mechanical effects.

This study advances the understanding of cryogenic chemical reactions and highlights the potential of H₂ as a versatile tool in CBGB systems. By combining experimental observations with computational modeling, we provide a comprehensive picture of the unique properties of H₂ and its isotopologues, paving the way for future explorations in this field.

4.5 Further Details

4.5.1 Rotational Temperature

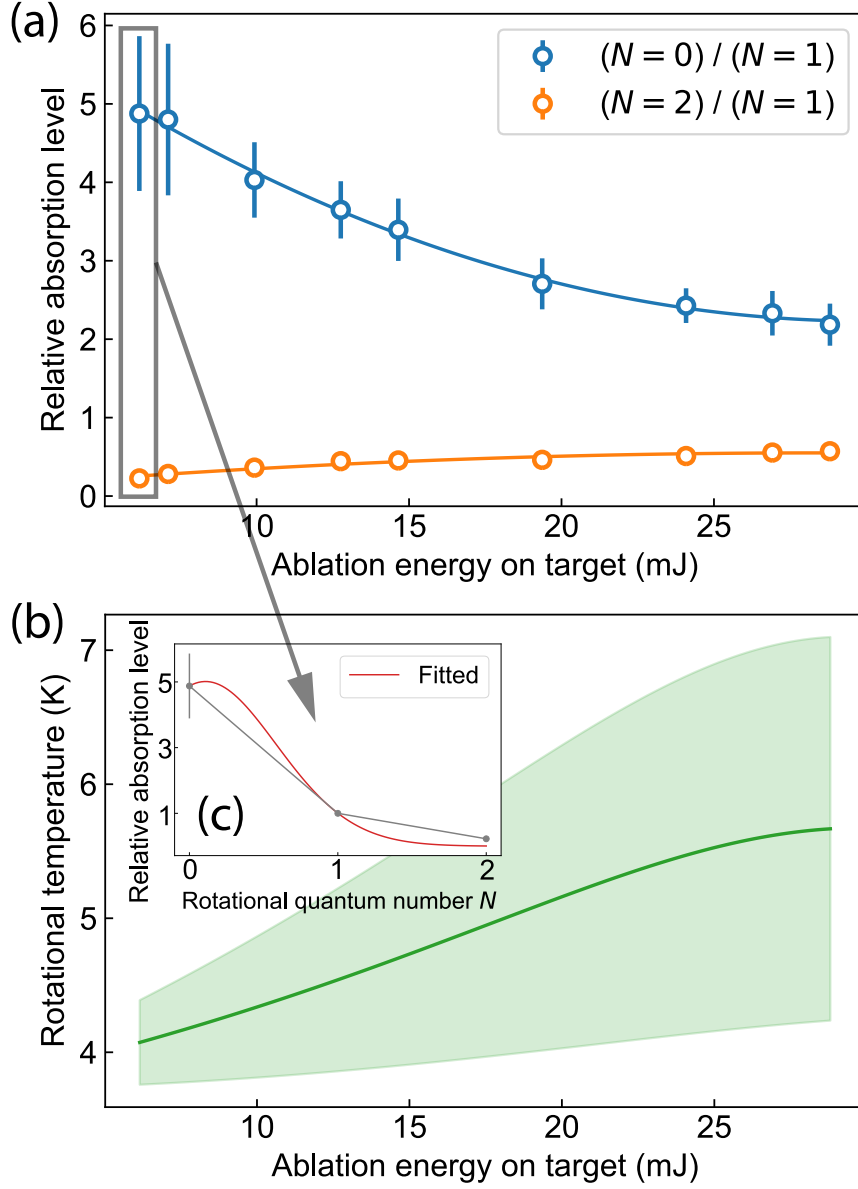


Figure 4.7: (a) Relative in-cell absorption for $X^2\Sigma^+(N = 0)$ and $X^2\Sigma^+(N = 2)$ states with respect to $X^2\Sigma^+(N = 1)$, versus ablation energy. Absorption for $X^2\Sigma^+(N = 3)$ and higher ro-vibronic states is below the detection limit and therefore neglected. Solid lines are fitted quadratic functions to guide the eyes. (b) Fitted rotational temperature versus ablation energy. Temperatures are extracted from a least-squares fit according to Eq. (4.4), as shown in inset (c). Figure adopted from Ref. [83].

We measure the rotational temperature of the molecules by comparing the relative populations in different rotational states. Figure 4.7(a) shows the measured relative absorption of $X^2\Sigma^+(N = 0)$ and $X^2\Sigma^+(N = 2)$ states with respect to $X^2\Sigma^+(N = 1)$ for varying ablation energies. The transitions involved in these measurements are $A^2\Pi_{1/2}(v' = 0, J' = 1/2, -) \leftarrow X^2\Sigma^+(v'' = 0, N'' = 0, J'' = 1/2, +)$, $A^2\Pi_{1/2}(v' = 0, J' = 3/2, +) \leftarrow X^2\Sigma^+(v'' = 0, N'' = 1, J'' = 3/2, -)$, and $A^2\Pi_{1/2}(v' = 0, J' = 5/2, -) \leftarrow X^2\Sigma^+(v'' = 0, N'' = 2, J'' = 5/2, +)$, for the states with $N = 0, 1$, and 2 , respectively. We fit the relative absorption values to extract the corresponding rotational temperature via the expression

$$P \propto S \times d \times e^{-BN(N+1)/k_B T}, \quad (4.4)$$

where P , S , d , and B denote the absorption, the Hönl-London factor, the degeneracy of the hyperfine states, and the ground-state rotational constant, respectively, and k_B is the Boltzmann constant. The fitted rotational temperature as a function of ablation energy is shown in Fig. 4.7(b), with the inset (c) showing a sample fit. With the knowledge of the rotational temperature, we can use the population in the $X^2\Sigma^+(N = 1)$ state to predict the population in all occupied rotational states. We find that the rotational states higher than $X^2\Sigma^+(N = 2)$ can be neglected here since their population is very small with buffer gas cooling down to ~ 6 K.

4.5.2 QCT Simulations

We use the quasi-classical trajectory method (QCT) [90, 91] via the PyQCAMS [92] software to calculate the energy-dependent cross sections relevant to the reaction network in Eqs. (4.1-4.2). The particle motion is treated classically, such that their trajectories are found using Hamilton's equations of motion. The internal states are treated according to the Bohr-Sommerfeld quantization rule, which quantizes the classical action into discrete energy levels. Thus, we gain insight into the state-to-state cross sections of relevant processes, such as the vibrational excitation or quenching of H₂, or a reaction leading to CaH formation, at variable collision energies. For an appropriate

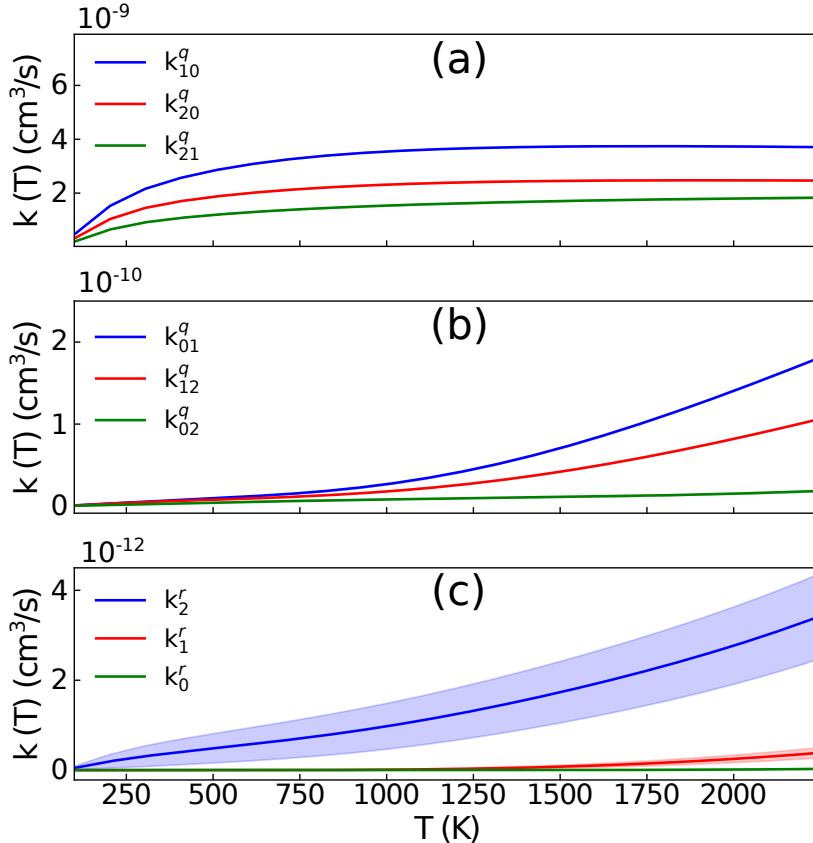


Figure 4.8: Temperature-dependent rates for the (a) vibrational quenching of H_2 and (b) vibrational excitation of H_2 , where the subscripts denote the initial and final vibrational states of H_2 , and (c) formation of CaH from the collision between Ca and H_2 , where the subscripts denote the initial vibrational state of H_2 . Figure adopted from Ref. [83].

Maxwell-Boltzmann distribution of energies, we then calculate the temperature-dependent rates of these processes by integrating the cross sections over the energy range. For example, after calculating the energy-dependent cross section $\sigma_{ij}^q(E)$ of a vibrational excitation of H_2 from state i to state j through collisions with Ca , the temperature-dependent rate is given by

$$k_{ij}^q(T) = \frac{2}{(k_B T)^{3/2}} \int \sigma_{ij}^q(E) v(E) \sqrt{\frac{E}{\pi}} e^{-E/k_B T} dE, \quad (4.5)$$

where $v(E) = \left(\frac{2E}{\mu}\right)^{1/2}$ represents the relative velocity between Ca and H_2 , with the reduced mass $\mu = m_{\text{Ca}}m_{\text{H}_2}/(m_{\text{Ca}} + m_{\text{H}_2})$. The same procedure is performed to calculate the temperature-dependent rate for reactive collisions leading to CaH formation, $k_i^r(T)$, for a given initial vibra-

tional state i of H_2 . Figure 4.8 presents the temperature-dependent rates that were used in our reaction model.

4.5.3 Ablation Plume Temperature Measurement

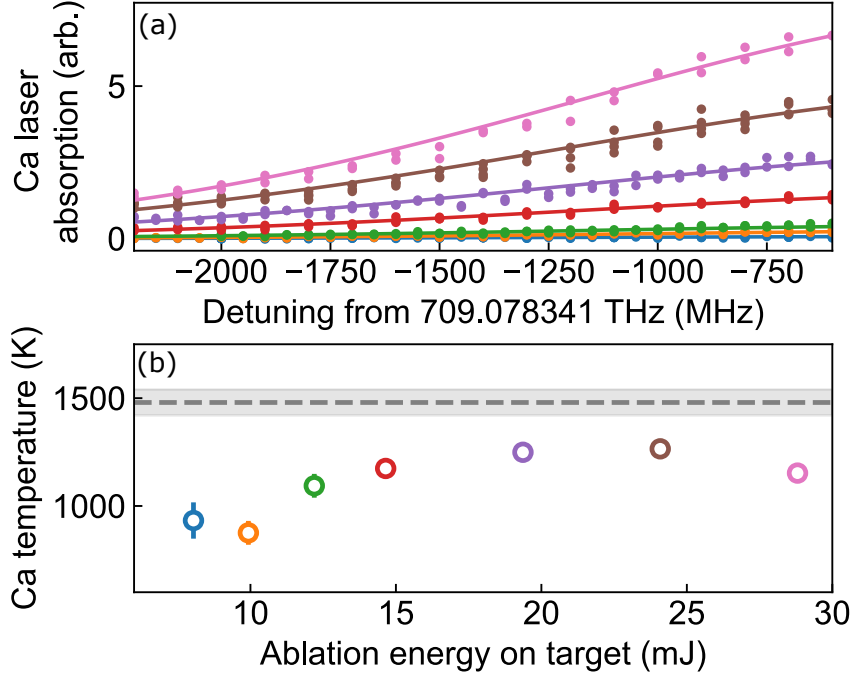


Figure 4.9: (a) Ca absorption spectra at different ablation energies. The data is fitted with the Gaussian function. (b) The Ca plume temperature versus ablation energy. The gray shaded area represents the theoretical temperature that optimally matches with experimental results in the main panel of Fig. 4.3. Figure adopted from Ref. [83].

We have measured the dependence of the ablation plume temperature on the ablation energy when there is no gas flow in the system, as shown in Fig. 4.9. The temperature of the ablation plume is determined by analyzing the measured absorption linewidth of the $\text{Ca } 4s4p \ ^1P_1 \leftarrow 4s^2 \ ^1S_0$ transition at 423 nm. While the Ca yield remains stable during the measurement, we sweep the frequency of the 423 nm laser through the cell and observe a Gaussian-shaped absorption spectrum. Its linewidth is influenced by various line-broadening mechanisms which we carefully consider to identify the dominant contributor.

The natural linewidth of the transition is ~ 30 MHz. Collisional broadening is negligible here due to the low density of the buffer gas in the cell, and power broadening is minimal due to the low

intensity of the probe laser light. Consequently, the dominant broadening mechanism is attributed to the Doppler effect. The measured linewidth of ~ 1 GHz is significantly larger than any of the other broadening contributions, allowing us to directly translate the linewidth to temperature.

It is important to note that the measured temperature represents a lower bound on the actual translational temperature of the ablation plume. In non-equilibrium systems such as the CBGB source, the translational temperature is anisotropic: the temperature along the direction of ablation is typically higher than the temperature perpendicular to it [93]. Based on our QCT simulations, a temperature of 1480(60) K provides the best fits to the experimental data. We therefore estimate this value to be near the average plume temperature in our system. Future experiments with more optical access could enable measurements along multiple spatial directions to provide a more precise characterization of the plume's anisotropic temperature distribution.

4.5.4 Extraction of Collisional Cross Sections

Here we describe the determination of the elastic collisional cross sections. These measurements are based on the method in Ref. [68]. We assume that particles either stick to the cell walls or exit through the cell aperture via a diffusion process when the density of buffer gas is low. By monitoring the decay of the signal over time, we estimate the diffusion time constant and consequently derive the elastic collisional cross section.

The diffusion time constant is extracted by fitting an exponentially decaying function to the later part of the absorption time trace as illustrated in Fig. ??(a). The elastic collisional cross section is then

$$\sigma = \frac{9\pi v_{BG}\tau}{16A_{cell}n_{BG}}, \quad (4.6)$$

where $v_{BG} = \sqrt{8k_B T_0 / \pi m_{BG}}$ is the expected speed of the buffer gas which follows the standard Maxwell-Boltzmann distribution, τ is the fitted diffusion time constant, A_{cell} is the cross-sectional cell area of ~ 5 cm², and n_{BG} is the density of the buffer gas. The density is set by controlling the flow as $n_{BG} = 4f_{BG}/v_{BG}A_{aperture}$, where f_{BG} is the flow rate of the buffer gas into the system and $A_{aperture}$ is the aperture size of the buffer gas cell of ~ 0.25 cm².

	He	H ₂	HD	D ₂
Ca	13.2(2.8)	3.5(1.2)	1.8(0.2)	1.3(0.4)
CaH	77(25)	4.1(1.0)	3.3(1.4)	–

Table 4.1: Collisional cross sections (in units of 10^{-16} cm^2) for Ca and CaH with He, H₂, HD, and D₂. Table adopted from Ref. [83].

To reduce systematic errors, we chose 3 different ablation spots and 2 different gas flow rates, and averaged the results to obtain the cross section values and the measurement error estimates. The results are presented in Table 4.1.

Chapter 5: Study of Predissociation

For a majority of my PhD, we talked about the feasibility of optical slowing CaH. And the word that was discussed most is predissociation. It is an unwanted phenomenon, and detailed characterization, aka the result of this study, is critical to the future of this experiment and determines the feasibility of optical deceleration. To introduce predissociation in a sentence: whenever we excite the molecules to excited states, predissociation is the possibility that the molecule just breaks apart and get lost completely. I will introduce the background of this measurement, the experimental method and result, and theoretical characterization performed by our collaborator, Claire, Anastassia, Daniel from UCLA, and Lan from JHU.

5.1 Relevant Background Information

Rapid and repeated photon scattering is not only an efficient method of removing entropy from an atom or a molecule via photon recoils [94], but it also enables high fidelity single quantum state preparation and measurement needed for quantum information protocols [95, 96]. Optical cycling between the ground state and a low lying electronic excited state has led to recent progress with laser cooled molecules, such as tweezer arrays of CaF [97], a three-dimensional lattice of YO [98], magneto-optical trapping (MOT) of CaOH [77] and one-dimensional Sisyphus cooling of CaOCH₃ [80].

The primary challenge of direct laser cooling is the enormous photon budget necessary for bringing a cryogenically precooled molecular beam to within the MOT capture velocity [99, 100]. For example, typical molecular beams emanating from a cryogenic buffer gas beam (CBGB) source travel at mean forward velocities of ≈ 200 m/s [68]. The recoil velocity per photon is ≈ 20 mm/sec. Hence upwards of 10,000 photon scatters are needed to bring the molecular beam to a standstill.

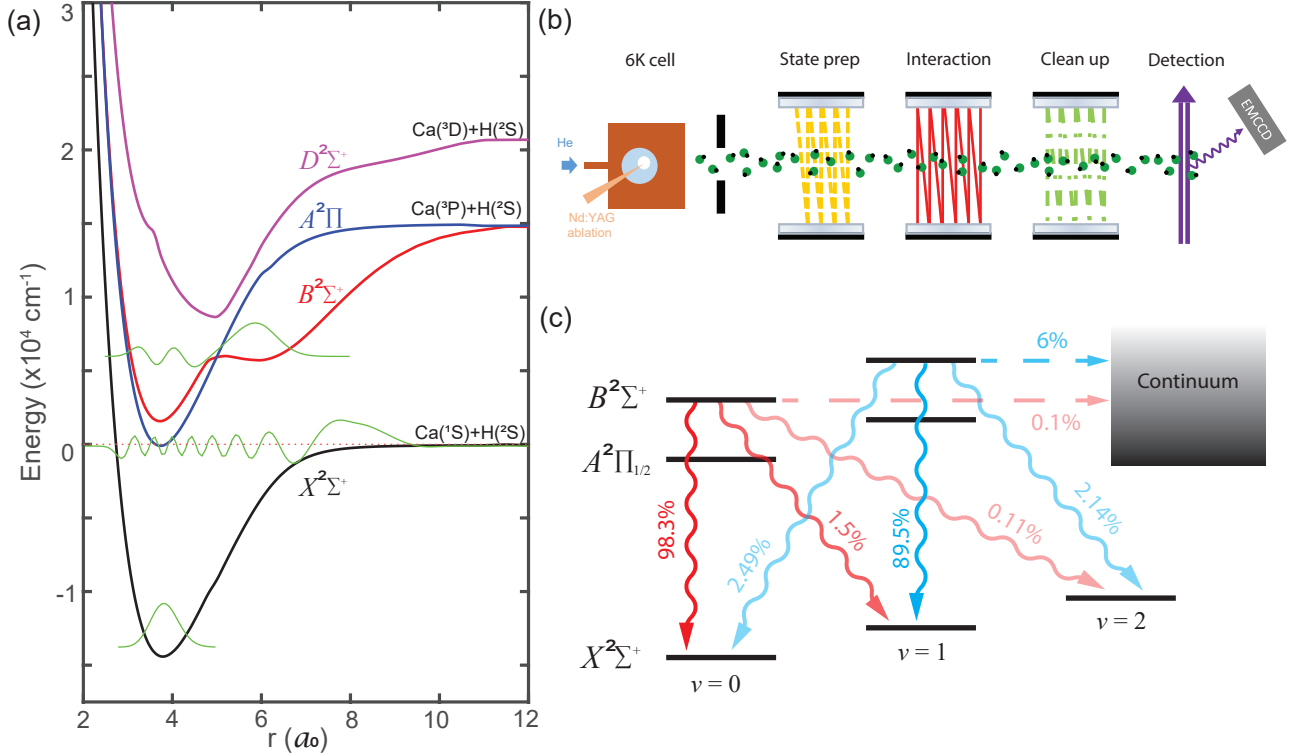


Figure 5.1: CaH molecular properties relevant to this work. (a) Potential energy surfaces (PES) for the 4 lowest electronic states - $X^2\Sigma^+$, $A^2\Pi$, $B^2\Sigma^+$ and $D^2\Sigma^+$. Spin-orbit interaction is not included here. The x-axis is the internuclear separation r in bohr radii (a_0) and the y-axis is energy in cm^{-1} ($1 \text{ cm}^{-1} \approx 30 \text{ GHz}$). The energy origin is chosen as the $\text{Ca}(^1\text{S})+\text{H}(^2\text{S})$ continuum threshold (v_{th}). Superimposed are the wavefunctions (bottom to top) for the $X(v'' = 0)$ absolute ground state, $X(v'' = 15)$ lowest energy bound state and $B(v' = 4)$ excited state. (b) Experimental layout used for this work. A buffer gas cooled molecular beam emanates from the cryogenic cell and encounters four spatially separated regions. The state preparation (S), interaction (I), clean-up (C) and detection (D) regions. Each region is composed of multipassed lasers described in the text. (c) Relevant vibrational branching ratios (squiggly arrows) calculated for the $B^2\Sigma^+$ state. Measured predissociation probabilities for the $B(v' = 0)$ and $B(v' = 1)$ are denoted by dashed lines. Figure adopted from Ref. [89].

In addition, these photons need to be scattered at a rate faster than 10^6 s^{-1} to accomplish slowing within a $\approx 1 \text{ m}$ distance. Satisfying all these criteria simultaneously can be challenging for molecules with complex internal structures. Indeed, alternative slowing schemes such as travelling wave Stark deceleration [101], electro-optic Sisyphus effect [102], centrifuge deceleration [103] and Zeeman-Sisyphus slowing [104] have been demonstrated for atoms, diatomic and polyatomic molecules. These alternate schemes leverage the state dependent electric and magnetic field dependencies to remove entropy with minimal photon scatters. However, quantum state resolved

detection still requires optical cycling.

5.2 What is Predissociation and Why Do We Study It

Although calcium monohydride (CaH) was amongst the earliest candidates proposed for laser cooling [105], not much experimental progress was made in that regard until recently [106]. One of the reasons is the unique electronic structure of CaH [33]. In CaH, the lowest energy excited state $A^2\Pi_{1/2}$ lies roughly 556 cm^{-1} above the $\text{Ca}(^1S)+\text{H}(^2S)$ dissociation threshold of the ground $X^2\Sigma^+$ manifold (Fig. 5.1(a)). So a molecule in the excited state can, in principle, decay into the continuum via a radiationless transition. This phenomenon is known as predissociation [107, 108]. This decay pathway is different from vibrational branching in that a predissociated molecule can not be optically repumped back into the bound state because of the significant physical separation and relative velocity of the dissociated fragments. Hence the predissociation probability (P_{pd}) sets a limit on the number of photons one can scatter with laser cooling.

Despite the fact that the $A^2\Pi_{1/2}$ state in CaH lies above the ground state threshold energy, predissociation from the $A^2\Pi_{1/2}$ to $X^2\Sigma^+$ continuum is nominally forbidden due the Von Neumann-Wigner no crossing rule [109]. In the case of diatomic molecules, only states with different symmetries can cross while those with same symmetries form avoided crossings [110, 111]. In other words, the molecular Hamiltonian does not couple states with different symmetries. So the second lowest excited $B^2\Sigma^+$ state is expected to predissociate but the $A^2\Pi_{1/2}$ state is not. However, effects like spin-orbit coupling can lead to mixing of $A^2\Pi_{1/2}$ and $B^2\Sigma^+$ states leading to a small, but finite, P_{pd} for the $A^2\Pi_{1/2}$ state.

5.3 Theoretical Modeling of CaH

The starting point for our calculations is the construction of potential energy surface (PES) for CaH. All calculations were performed using the Molpro program [112, 113, 114]. We adopt a similar basis set and active space as a previous paper [115], where we use cc-pwCVQZ [116] for Ca atom and aug-cc-pVQZ [117] for the H atom. Calculations were performed in C_{2v} sym-

metry, which is the nearest Abelian point group to $C_{\infty v}$. Orbitals were generated with a restricted Hartree-Fock formalism (RHF), then further optimized in a state-averaged complete active space self consistent field (SA-CASSCF) [118] calculation involving three active electrons and 9 active orbitals. For the Σ^+ states, four states were averaged at equal weights in the SA-CASSCF calculation, with (5,2,2,0) closed and (9,4,4,1) occupied orbitals.

For the $A^2\Pi$ state, since only abelian point group symmetries are available, a two-state SA-CASSCF calculation with the same active space was performed in C_{2v} symmetry involving symmetries 2 and 3 of equal weight to represent the $C_{\infty v}$ A state. These wavefunctions were then used in a multireference configuration interaction calculation with Davidson corrections for higher excitations (MRCI+Q) [119, 120, 121]. Here, (3,1,1,0) orbitals made up the core, (5,2,2,0) were closed and (9,4,4,1) were occupied. Electron correlation involving double and single excitations were allowed. Spin-orbit was incorporated at the MRCI level using the Breit-Pauli Hamiltonian [122].

The following three-state Hamiltonian (for the $X^2\Sigma^+$, $B^2\Sigma^+$ and $D^2\Sigma^+$ electronic states) was diagonalized to obtain wavefunctions, FCFs and predissociation estimates:

$$\sum_j^3 H_j = \sum_I \frac{(\hat{p}^I + A_{ij}^I(r))^2}{2\mu} \phi_j(r) + V_j(r) \phi_j(r) \quad (5.1)$$

The first term is the kinetic energy operator, in which \hat{p} is the standard momentum operator, expressed on a grid via the Colbert-Miller derivative. We represent the momentum operator in position space so that we can incorporate our nonadiabatic coupling term directly, which is computed in the position representation. $A_{ij}(r) = \langle \Psi_i | \hat{p} \Psi_j | \Psi_i | \hat{p} \Psi_j \rangle$ is the nonadiabatic coupling term. We obtained $\langle \Psi_i | \frac{\partial}{\partial r} \Psi_j | \Psi_i | \frac{\partial}{\partial r} \Psi_j \rangle$ from a $dr = 0.001 a_0$ potential energy surface scan via Molpro electronic structure calculations, and interpolated this onto a spline to represent $A_{ij}(r)$. μ is the reduced mass of CaH. Finally, $V(r)$ is obtained from the $dr = 0.001 a_0$ scan via the MRCI+Q Davidson energies and interpolated onto a spline before being incorporated into the Hamiltonian.

At 8 a.u., an optical potential of the form $-i(0.2)(r - 8)^2/8^2$ is added only to $X^2\Sigma^+$ state's

$V(r)$ at the PES asymptote with each grid-point to simulate the continuum and create a flux equation. The Hamiltonian is then diagonalized. This optical potential enforces imaginary eigenvalues which are directly related to the non-radiative rates which are then compared to the radiative rates calculated from the MRCI-computed transition dipole moments, to obtain a predissociation probability.

For spin-orbit coupling, the active space for $X^2\Sigma^+$, $A^2\Pi_{1/2}$ and $B^2\Sigma^+$ states must be the same, therefore a compromise was chosen to optimize the $X^2\Sigma^+$ and $B^2\Sigma^+$ FCFs over the $A^2\Pi_{1/2}$ state. Interestingly, we note that using our basis set and active space but shifting the $A^2\Pi_{1/2}$ potential energy surface can also produce FCFs that are equivalent to experimentally measured VBRs, as seen in Table 5.1. This is because the static correlation has converged but important dynamic correlation which is dependent on the original CAS active space and which shifts the equilibrium bond length obtained via MRCI, is missing. We note that previous work, which used a different active space and basis set, predicted $A^2\Pi_{1/2} \rightarrow B^2\Sigma^+$ FCFs which are quite close to experiment, but cannot successfully reproduce the $B^2\Sigma^+$ to $X^2\Sigma^+$ FCFs.[33]

Transition	Vibrational Quanta (v'')	FCF Calculated ($f_{0v''}$)	FCF Measured ($f_{0v''}$)
$A' \rightarrow X$	0	0.9568	0.9572(43)
	1	0.0401	0.0386(32)
	2	2.9×10^{-3}	$4.2(3.2) \times 10^{-3}$
	3	2.5×10^{-4}	-

Table 5.1: Calculated and measured values of FCFs for CaH. We show the experimental FCFs taken from [106] for comparison. A' is the same active space as the $B^2\Sigma^+$ state in this work, shifting the potential to the left by $0.0375 a_0$. Table adopted from Ref. [89].

5.3.1 Calculation of Franck-Condon Factors

Next, we employ the vibrational wavefunctions obtained in Section ?? to calculate the Frank-Condon factors (FCFs) for the CaH transitions of interest. FCFs are calculated using a grid representation of the vibrational wave functions. A spline interpolation was fit to the potential energy surfaces calculated in Molpro to create the potential energy functions, $V(r)$. The real space kinetic energy operator was approximated with the Colbert-Miller derivative [123]. Nonadiabatic

Transition	Vibrational Quanta (v'')	FCF Calculated ($f_{0v''}$)	FCF Measured ($f_{0v''}$)
$A \rightarrow X$	0	0.9788	0.9572(43)
	1	0.0205	0.0386(32)
	2	6.8×10^{-4}	$4.2(3.2) \times 10^{-3}$
	3	4.1×10^{-5}	-
$B \rightarrow X$	0	0.9789	0.9807(13)
	1	0.0192	0.0173(13)
	2	1.8×10^{-3}	$2.0(0.3) \times 10^{-3}$
	3	1.4×10^{-4}	-

Table 5.2: Calculated and measured values of FCFs for CaH. We show the experimental FCFs taken from [106] for comparison. Note that the active space was optimized for the B state for this work, which leads to a disagreement for the A state. Table adopted from Ref. [89].

coupling vectors were computed analytically with the CP-MCSCF program [124] in Molpro and fit to a spline interpolation. They were incorporated into the Hamiltonian by directly adding the nonadiabatic coupling to the momentum operator [125]. The Hamiltonian was diagonalized to obtain eigenvalues and eigenvectors. Our calculations converged with a grid-spacing (dr) of 0.007 a_0 and a box size of 16.5 a_0 . Details are discussed in Appendix ??.

We compare our calculated FCFs to previous experimental measurements taken from [106] in Table 6.1. We chose the active space which matched $B^2\Sigma^+$ and $X^2\Sigma^+$ state FCFs and vibrational energies in all calculations, since MRCl spin-orbit coupling (SOC) requires the same active space for all involved states. Therefore, the FCFs for $A^2\Pi$ could be improved with varied active space, but a compromise was made to estimate SOC splittings. Despite this compromise, we find the $A^2\Pi_{1/2}$ potential is still the correct shape but slightly incorrect equilibrium bond length. More details are in Table 5.1 in the SI.

5.3.2 $B^2\Sigma^+$ Predissociation Estimate

Predissociation estimates were computed using an optical absorbing potential, which has previously predicted scattering cross sections close to experiment [126, 127, 128, 129]. An absorbing, optical potential of the form $-i(0.2)(r - 8)^2/8^2$ was added to the $X^2\Sigma^+$ potential energy starting and centered at 8 a_0 with a height of 0.2 a_0 to resemble a decaying half-parabola. Results are insen-

sitive to absorber placement so long as it is placed along the potential energy surface's asymptote and has a width larger than the typical de Broglie wavelength [126]. This creates a channeled flux equation which imposes a boundary condition on the wavefunction and eigenvalues now have an imaginary component.

This component, for example, the imaginary eigenvalue of $B(v' = 0)$, is directly related to the nonadiabatic coupling between that vibrational wavefunction and the X continuum (where we placed our absorber), as the nonradiative transition rate A_{NR} . Due to limitations in time-resolved measurements, we estimate predissociation as the ratio of our calculated nonradiative (A_{NR}) and radiative (A_R) decay rates, via $A_{NR}/(A_{NR} + A_R)$.

5.4 $B^2\Sigma^+$ Predissociation Measurement

5.4.1 Experimental Setup

The experimental setup has been described in our previous publication [106]. Briefly, CaH is generated through ablation of a CaH_2 target by a pulsed Nd:YAG laser at around 1 Hz. CaH is buffer gas cooled by helium at 6 K and ejected from the cell aperture to form a beam. The molecules are predominately in the $X^2\Sigma^+$ ($v'' = 0$) state. The beam of CaH then enters a high vacuum chamber which, in this measurement, is divided into four regions: state-preparation, interaction, clean-up, and detection region, as shown in Fig 5.1(b). In the first three regions, the molecular beam intersects with transverse lasers that address $X \rightarrow A$ or $X \rightarrow B$ transitions. These lasers can be switched on and off by independent optical shutters. The laser beams are multipassed to increase the interaction time with the molecular beam. In the detection region, we apply a single pass $X \rightarrow A$ or $X \rightarrow B$ light and use an iXon888 EMCCD and Hamamatsu R13456 PMT to collect the laser-induced fluorescence (LIF) signals for spatial and temporal detection. Typically every molecule scatters around 20 photons in the detection region, which implies that we are not sensitive to the initial spin-rotation and hyper-fine distribution. All transitions addressed are from the $X^2\Sigma^+$ ($N'' = 1$) state (N is the rotational quantum number) to $A^2\Pi_{1/2}$ ($J' = 1/2$) (J is the total angular momentum quantum number) or $B^2\Sigma^+$ ($N' = 0$) states in order to obtain rotational

closure [105]. We use electro-optic modulators (EOM) to generate sidebands on all lasers to cover all hyperfine states (HFS) as well as to address spin-rotation manifolds. All transitions used here were first measured experimentally with HFS resolution.

To concisely describe the lasers used in this study, we adopt the notation $M_{v'-v''}^N$, which denotes the transitions addressed and the spatial positions of the lasers. M can be either A or B , representing the electronic state of the excited manifold. N can either be S , I , C , or D , meaning state preparation region, interaction region, cleanup region, and detection region, respectively. In addition, we use $F_{M_{v'v''}}$ notation to describe the vibrational branching ratios (VBR) from either $A^2\Pi_{1/2}$ or $B^2\Sigma^+$ states (represented by M) to $X^2\Sigma^+$ states. For example, F_{B01} is VBR from $B^2\Sigma^+$ ($v' = 0$) to $X^2\Sigma^+$ ($v'' = 1$). We also use similar notations, F_{B0a} and F_{B1a} to represent the predissociation probabilities from $B^2\Sigma^+$ ($v' = 0$) and ($v' = 1$) states.

Next we describe the important properties of the lasers that we use in this experiment, and the transition frequencies for reference. All laser beams eventually pass through an EOM to generate all the sidebands needed to address HFS.

- In the state preparation region, we use A_{1-0}^S (637 nm) light that is generated from two sets of injection-locking amplifiers (ILAs) to address the spin-rotation states, with 95 mW of power.
- In the interaction region, multiple lasers are applied. A_{0-0}^I (695 nm) or A_{1-1}^I (693 nm) is from two ILAs that provide 60 mW in total. B_{0-0}^I (635 nm) or B_{1-1}^I (636 nm) is from two ECDLs with 52 mW in total.
- In the cleanup region, B_{0-1}^C (690 nm) is from two sets of ILAs with 90 mW of power, A_{1-0}^C (637 nm) is from two sets of ILAs at 88 mW, A_{1-2}^C (758 nm) or A_{0-1}^C (762 nm) is from SolsTiS continuous-wave Ti:Sapphire laser, with a 1 GHz EOM to address the spin-rotation states. The total power is 93 mW.
- In the detection region, B_{0-0}^D (635 nm) is from two ECDLs with 60 mW of power, A_{0-0}^D (695 nm) or A_{1-1}^D (693 nm) is from two ILAs with 96 mW of power.

The frequencies of all the transitions that we used can be found in Table 5.4.1. All frequencies are measured transverse to the molecular beam, with ≤ 10 MHz statistical uncertainties and ≤ 60 MHz systematic uncertainties from the wavemeter. HFS in the ground states is clearly resolved in all spectra, while HFS in the excited states is not resolved in our measurements. Our measurements are consistent with the data presented in previous work [27] with less than 60 MHz discrepancy.

5.4.2 $B^2\Sigma^+$ ($v' = 0$) Measurement Method

In order to measure the predissociation probability of $B^2\Sigma^+$ ($v' = 0$) state, we need to scatter as many photons as we can in our system via $B^2\Sigma^+$ ($v' = 0$) state, and detect population loss that cannot be explained by known effects, predominantly rovibrational losses. To characterize the loss in our system, we design several stages, each utilizing different lasers to interact with the molecular beam. We monitor the population of the $v'' = 0$ ground state in the detection region by detecting laser-induced fluorescence (LIF) signals from the B_{0-0}^D laser. For this measurement, we employ a total of six stages. By defining temporally stable parameters that describe the properties of our system, we can express the molecular population distribution at different stages.

For example, in the *Unperturbed* stage we detect $X(v'' = 0)$ population. The population is denoted as N . This is also the calibration stage so the signals of every other stage will be referenced to the signal of this stage. In the *Cleanup* stage we apply B_{0-1}^C laser, and the $X(v'' = 0)$ population is $N + n_1 N \kappa F_{B00} / \mathcal{F}_{B0}$, where n_1 is normalized $X(v'' = 1)$ state natural population, κ is the cleanup efficiency of laser B_{0-1}^C , and $\mathcal{F}_{B0} \equiv F_{B0a} + \sum_{i \in Z^*, i \neq 1} F_{B0i}$ is the VBR normalization factor. This factor accounts for the discrete probability distribution of decay processes based on the VBRs and P_{pd} . By taking the ratio of the integrated signal of $X(v'' = 0)$ population from *Cleanup* stage with signal from *Unperturbed* stage, we get the parameterized ratio $R_1 = 1 + n_1 \kappa F_{B00} / \mathcal{F}_{B0}$. In addition to the *Unperturbed* and *Cleanup* stages, we have four more stages in this measurement, resulting in a total of five ratios and five parameters (including P_{pd}). The details of all the stages, such as the laser configuration and expression for the normalized signal in each stage, can be found

Ground	v''	N''	J''	F''	Excited	v'	N'	J'	Frequency (THz)
X	0	1	3/2	2	A	0	-	1/2	431.274552
				1					431.274653
				1					431.276565
				0					431.276512
X	0	1	3/2	2	B	0	0	1/2	472.026689
				1					472.026790
				1					472.028702
				0					472.028649
X	1	1	3/2	2	A	1	-	1/2	432.342011
				1					432.342120
				1					432.343958
				0					432.343902
X	1	1	3/2	2	B	1	0	1/2	471.557078
				1					471.557178
				1					471.559025
				0					471.558969
X	0	1	3/2	2	A	1	-	1/2	470.113870
				1					470.113971
				1					470.115873
				0					470.115819
X	2	1	3/2	2	A	1	-	1/2	395.717108
				1					395.717218
				1					395.718978
				0					395.718928
X	1	1	3/2	2	B	0	0	1/2	434.254840
				1					434.254949
				1					434.256787
				0					434.256731
X	1	1	3/2	2	A	0	-	1/2	393.502723
				1					393.502832
				1					393.504670
				0					393.504614

Table 5.3: Here we present the frequencies of all the transitions we used in this experiment. The $A^2\Pi_{1/2}$ and $B^2\Sigma^+$ states that we used have unresolved hyperfine splittings. All frequencies presented here have 10 MHz statistical uncertainty and 60 MHz systematic uncertainty due to the wavemeter used for measurement. Table adopted from Ref. [89].

in Table 5.4 and Table 5.5.2. By designing the experiment in this way, we acquire five equations (ratios equal to parameterized expressions) and five variables. Consequently, we can solve the set of equations and express F_{B0a} with R_i s. By measuring R_i precisely, we can estimate the $B^2\Sigma^+$ ($v' = 0$) state predissociation probability.

Table 5.4 provides the necessary details regarding the configurations and expressions of the stages used to measure the $B^2\Sigma^+$ ($v = 0$) state predissociation probability. On the other hand, Table 5.5.2 presents a more comprehensive overview of the parameterized population in various vibrational states.

Purpose	Upstream Laser Config	Downstream Normalized $v = 0$ State Pop	Averaged Signal Ratio
Unperturbed	-	1	-
Cleanup	B_{0-1}^C	$1 + n_1 \kappa F_{B00} / \mathcal{F}_{B_0}$	1.05(2)
X-A Depletion	A_{0-0}^I	d_A	0.018(6)
X-A Depletion + Cleanup	$A_{0-0}^I + B_{0-1}^C$	$d_A + [(1 - d_A) F_{A01} / \mathcal{F}_{A_0} + n_1] \kappa F_{B00} / \mathcal{F}_{B_0}$	0.94(2)
X-B depletion	B_{0-0}^I	d_B	0.086(8)
X-B Depletion + Cleanup	$B_{0-0}^I + B_{0-1}^C$	$d_B + [(1 - d_B) F_{B01} / \mathcal{F}_{B_1} + n_1] \kappa F_{B00} / \mathcal{F}_{B_0}$	0.87(2)

Table 5.4: Experimental stages for $B(v' = 0)$ state predissociation measurement. In the second column, we use $M_{v'-v''}^N$ notation to describe the laser information. M can be either A or B , representing the electronic excited state. N can be S , I , or C , representing state preparation region, interaction region, and cleanup region, respectively. In the third column, we express the normalized ground state molecule population at different stages with respect to that of the unperturbed stage using unknown variables and calculated VBRs. We use five variables here, including n_1 , κ , F_{B0a} , d_A and d_B , representing $X(v'' = 1)$ state natural population, cleanup efficiency of laser B_{1-0}^C , $B(v' = 0)$ state predissociation probability, depletion efficiency of laser A_{0-0}^I and depletion efficiency of laser B_{0-0}^I , respectively. We denote the VBR normalization factors as $\mathcal{F}_{A_0} \equiv \sum_{i \in Z^+} F_{A0i}$, $\mathcal{F}_{B_0} \equiv F_{B0a} + \sum_{i \in Z^*, i \neq 1} F_{B0i}$, and $\mathcal{F}_{B_1} \equiv F_{B0a} + \sum_{i \in Z^+} F_{B0i}$. A more complete table of vibrational population distribution can be found in appendix Table 5.5.2. Table adopted from Ref. [89].

5.4.3 $B^2\Sigma^+$ ($v' = 1$) Measurement Method

For $B(v' = 1)$ state, similar to $v' = 0$, predissociation is measured within the same framework of stages. We design two different methods, each consisting of multiple laser configurations and detection regions, to measure the same quantity. In method I, we use six stages, where we always monitor the $X(v'' = 0)$ population downstream using laser A_{0-0}^D . The aim is to populate $X(v'' = 1)$ state via an off-diagonal pumping laser A_{1-0}^S and perform photon cycling between $X(v'' = 1)$ and $B(v' = 1)$ states. We expect to see an increase of $X(v'' = 0)$ population due to optical cycling. We

can repump the molecules that remain in $X(v'' = 1)$ state back to $v'' = 0$. Given the knowledge of the VBRs and after adding up the fractions, population that comes back might not add up to the number that we expect from vibrational loss. By ruling out other effects that might cause this difference, we can attribute the loss to $B(v' = 1)$ predissociation. The details of the six stages can be found in Table 5.5.

Method II is different from the previous two cases in a few ways. We monitor the $X(v'' = 1)$ population instead of $v'' = 0$ such that we can account for the loss to both $v'' = 0$ and $v'' = 2$ states with high enough signal-noise ratio (SNR) using laser B_{1-1}^D . We use ten stages in this method, leading to nine measurable ratios. And we use seven parameters in total, which means we have more equations than variables. To find the optimal solution set in this over-constrained system, we define a least-squared objective function, and use Levenberg-Marquardt algorithm to search for the local minimum in the parameter space with reasonable initial guesses.

Purpose	Upstream Laser Config	Downstream Ground State Pop Norm	Averaged Signal Ratio
Unperturbed	-	1	-
State Prep	A_{1-0}^S	$1 - a$	0.22(2)
Cleanup	A_{0-1}^C	$1 + n_1 \kappa F_{A00} / \mathcal{F}_{A_1}$	1.10(3)
State Prep + Cleanup	$A_{1-0}^S + A_{0-1}^C$	$1 - a + (n_1 + a F_{A11} / \mathcal{F}_{A_2}) \kappa F_{A00} / \mathcal{F}_{A_1}$	1.01(3)
State Prep + X-B 1-1 Cycling	$A_{1-0}^S + B_{1-1}^I$	$1 - a + (n_1 + a F_{A11} / \mathcal{F}_{A_2}) d_B F_{B10} / \mathcal{F}_{B_2}$	0.39(2)
State Prep + X-B 1-1 Cycling + Cleanup	$A_{1-0}^S + B_{1-1}^I + A_{0-1}^C$	$1 - a + (n_1 + a F_{A11} / \mathcal{F}_{A_2}) (d_B F_{B10} / \mathcal{F}_{B_2}) + (1 - d_B) \kappa F_{A00} / \mathcal{F}_{A_1}$	0.40(2)

Table 5.5: Method I of $B^2\Sigma^+$ ($v' = 1$) state predissociation measurement. Notations are the similar with what are used in table 5.4, so here we will only discuss the differences. In the third column, the variables include a , n_1 , κ , F_{B1a} and d_B , representing state preparation (from $X(v'' = 0)$ to $X(v'' = 1)$) efficiency, $X(v'' = 1)$ state natural population, cleanup efficiency of laser A_{1-0}^C , $B(v' = 1)$ state predissociation probability, depletion efficiency of laser B_{1-1}^I , respectively. We denote the VBR normalization factors as $\mathcal{F}_{A_1} \equiv \sum_{i \in Z^*, i \neq 1} F_{A0i}$, $\mathcal{F}_{A_2} \equiv \sum_{i \in Z^+} F_{A1i}$ and $\mathcal{F}_{B_2} \equiv F_{B1a} + \sum_{i \in Z^*, i \neq 1} F_{B1i}$. A more complete table of vibrational population distribution downstream can be found in appendix Table 5.5.2. Table adopted from Ref. [89].

5.4.4 Predissociation Measurement Analysis

The yield of our CBGB source is relatively stable short term while showing significant drift long term. In order to reduce the systematic error due to number fluctuations, we put a reference stage before and after every other stages within a group when taking the data. For example, in $B(v' = 0)$ predissociation measurement, data was taken in the following order: *Unperturbed* →

Purpose	Upstream Laser Config	Downstream $X^2\Sigma^+$ $v = 1$ State Pop Norm	Ave Ratio
State Prep + Cleanup v0	$A_{1-0}^S + A_{1-0}^C$	$n_1 + (a + \kappa_1 - a\kappa_1)F_{A11}/\mathcal{F}_{A_2}$	-
Unperturbed	-	n_1	0.13(3)
State Prep	A_{1-0}^S	$n_1 + aF_{A11}/\mathcal{F}_{A_2} \equiv \mathcal{Z}$	0.89(4)
Cleanup v0	A_{1-0}^C	$n_1 + \kappa_1 F_{A11}/\mathcal{F}_{A_2}$	0.93(4)
State Prep + X-A 1-1 Cycling	$A_{1-0}^S + A_{1-1}^I$	$\mathcal{Z}(1 - d_A)$	0.03(3)
State Prep + X-A 1-1 Cycling + Cleanup v0	$A_{1-0}^S + A_{1-1}^I + A_{1-0}^C$	$\mathcal{Z}(1 - d_A) + (1 - a + \mathcal{Z}d_A F_{A10}/\mathcal{F}_{A_3})\kappa_1 F_{A11}/\mathcal{F}_{A_2}$	0.33(3)
State Prep + X-A 1-1 Cycling + Cleanup v2	$A_{1-0}^S + A_{1-1}^I + A_{1-2}^C$	$\mathcal{Z}(1 - d_A) + (aF_{A12}/\mathcal{F}_{A_2} + \mathcal{Z}d_A F_{A12}/\mathcal{F}_{A_3})\kappa_2 F_{A11}/\mathcal{F}_{A_4}$	0.57(4)
State Prep + X-B 1-1 Cycling	$A_{1-0}^S + B_{1-1}^I$	$\mathcal{Z}(1 - d_B)$	0.12(3)
State Prep + X-B 1-1 Cycling + Cleanup v0	$A_{1-0}^S + B_{1-1}^I + A_{1-0}^C$	$\mathcal{Z}(1 - d_B) + (1 - a + \mathcal{Z}d_B F_{B10}/\mathcal{F}_{B_2})\kappa_1 F_{A11}/\mathcal{F}_{A_2}$	0.35(3)
State Prep + X-B 1-1 Cycling + Cleanup v2	$A_{1-0}^S + B_{1-1}^I + A_{1-2}^C$	$\mathcal{Z}(1 - d_B) + (aF_{A12}/\mathcal{F}_{A_2} + \mathcal{Z}d_B F_{B12}/\mathcal{F}_{B_2})\kappa_2 F_{A11}/\mathcal{F}_{A_4}$	0.42(3)

Table 5.6: Method II of $B^2\Sigma^+$ ($v' = 1$) state predissociation measurement. In the third column, we introduce seven variables, that include a , n_1 , κ_1 , κ_2 , F_{B1a} , d_A and d_B , representing state preparation (from $X(v'' = 0)$ to $X(v'' = 1)$) efficiency, $X(v'' = 1)$ state natural population, cleanup efficiency of laser A_{1-0}^C , cleanup efficiency of laser A_{1-2}^C , $B(v' = 1)$ state predissociation probability, depletion efficiency of laser A_{1-1}^I , depletion efficiency of laser B_{1-1}^I , respectively. We denote the VBR normalization factors as $\mathcal{F}_{A_2} \equiv \sum_{i \in Z^+} F_{A1i}$, $\mathcal{F}_{A_3} \equiv \sum_{i \in Z^*, i \neq 1} F_{A1i}$, $\mathcal{F}_{A_4} \equiv \sum_{i \in Z^*, i \neq 2} F_{A1i}$, and $\mathcal{F}_{B_2} \equiv F_{B1a} + \sum_{i \in Z^*, i \neq 1} F_{B1i}$. A more complete table of vibrational population distribution downstream can be found in appendix Table 5.5.2. Table adopted from Ref. [89].

Cleanup → Unperturbed → X-A Depletion → Unperturbed ... X-B Depletion + Cleanup → Unperturbed. The reference stage of $B(v' = 1)$ method I is *Unperturbed*, while for method II it is *State Prep + Cleanup v0*. To calculate the ratios, we divide the signal by the average signal from the calibration shots before and after. We repeat the sequence of measurements multiple times and collect all the ratios. The averaged ratios can be found in Tables 5.4, 5.5, and 5.6. The values in parenthesis denote the $2 - \sigma$ statistical error. A graphical representation of the analysis process and a histogram of all five ratios can be found in Figure 5.2.

With the ratios measured, we use a Bootstrapping method [130, 131, 132] to derive the mean value and build confidence interval of the predissociation probabilities depicted in Fig. 5.3. This method is particularly useful as it does not require any additional assumptions about the data, such as the independence assumptions typically made for standard error calculations. We considered several other analysis methods, such as bootstrapping pair-wise and regular error propagation, but the outcomes were all within error of each other. Details of bootstrapping method can be found in Appendix ??.

To demonstrate the robustness of our measurement to small variations in FCFs, we calculate P_{pd} using different values of FCFs obtained from various *ab initio* calculations [33, 34] and show that for a range of theoretical FCFs, our measurement consistently produce a non-zero predissoci-

ation probability (Fig.5.3 triangles). Moreover, we consider other potential loss channels, which are discussed in Section 5.5.1.

After carefully considering all systematic effects and analyzing statistical errors, we obtain the predissociation probability for the $B^2\Sigma^+$ ($v' = 0$) state to be $0.00097^{+0.00059}_{-0.00057}$ and for the $B^2\Sigma^+$ ($v' = 1$) state to be $0.056^{+0.044}_{-0.034}$. The reported value for $B(v' = 1)$ is the average of the two methods (method I yields $0.079^{+0.021}_{-0.017}$ and method II yields $0.033^{+0.013}_{-0.011}$), and the 95% confidence interval is the largest of the two methods combined. These values are consistent with the probability calculated in Sec. 5.3.2 within the order of magnitude. In addition, we perform a comparative analysis by utilizing the FCFs obtained from previous theoretical work on CaH [33, 34], and the results are within errorbars of each other. The rapid and monotonic increase in P_{pd} seen in Fig. 5.3 can be understood in the context of a bound molecular state quantum tunneling through the $B^2\Sigma^+$ potential barrier into an $X^2\Sigma^+$ continuum state at the same energy. As the energy of the incident quantum state increases, the transmission probability also increases.

	$A^2\Pi_x$ ($v = 0, m_s = 1/2$)	$A^2\Pi_y$ ($v = 0, m_s = 1/2$)	$B^2\Sigma^+$ ($v = 0, m_s = -1/2$)
$A^2\Pi_x$ ($v = 0, m_s = 1/2$)	0	-35.5 <i>i</i>	21.5
$A^2\Pi_y$ ($v = 0, m_s = 1/2$)	35.5 <i>i</i>	0	-21.5 <i>i</i>
$B^2\Sigma^+$ ($v = 0, m_s = -1/2$)	21.5	21.5 <i>i</i>	1400

	$A^2\Pi_x$ ($v = 1, m_s = 1/2$)	$A^2\Pi_y$ ($v = 1, m_s = 1/2$)	$B^2\Sigma^+$ ($v = 0, m_s = -1/2$)	$B^2\Sigma^+$ ($v = 1, m_s = -1/2$)
$A^2\Pi_x$ ($v = 1, m_s = 1/2$)	0	-35.5 <i>i</i>	21.5 <i>f</i>	21.5
$A^2\Pi_y$ ($v = 1, m_s = 1/2$)	35.5 <i>i</i>	0	-(21.5 <i>f</i>) <i>i</i>	-21.5 <i>i</i>
$B^2\Sigma^+$ ($v = 0, m_s = -1/2$)	21.5 <i>f</i>	(21.5 <i>f</i>) <i>i</i>	64	0
$B^2\Sigma^+$ ($v = 1, m_s = -1/2$)	21.5	21.5 <i>i</i>	0	1310

Table 5.7: Spin-orbit matrices accounting for mixing of vibrational states of the A and B states. The Π_x and Π_y basis states split under SOC to produce $\Pi_{1/2}$ and $\Pi_{3/2}$ states. Bottom, mixing between $A^2\Pi_{1/2}$ ($v' = 1$), $B^2\Sigma^+$ ($v' = 1$) and $B^2\Sigma^+$ ($v' = 0$). The Franck-Condon factor f is introduced to account for the off-diagonal vibrational wavefunction overlap. The diagonal terms represent the energies of the unperturbed states in units of cm^{-1} . Table adopted from Ref. [89].

5.4.5 $A^2\Pi_{1/2}$ Predissociation Estimate

The $A^2\Pi_{1/2}$ state in the diatomic molecule CaH does not undergo predissociation via the process described for the $B^2\Sigma^+$ state in the previous sections. However, spin-orbit coupling (SOC) can induce mixing between the A and B states, leading to predissociation of the $A^2\Pi_{1/2}$ spin-orbit state. For a linear molecule, the z-component of total angular momentum (J_z) is a good quantum number. So the spin-orbit component $A^2\Pi_{1/2}$ has the same J_z as $B^2\Sigma^+(J_z = 1/2)$ and can hence interact. It is important to note that a similar interaction exists between the $A^2\Pi_{1/2}$ and $X^2\Sigma^+(J_z = 1/2)$ ground state but the energy separation is much larger ($\sim 14,000 \text{ cm}^{-1}$) compared to that between the A and B state ($\sim 1,400 \text{ cm}^{-1}$). Higher vibrational states of the X manifold will be closer in energy to the A state but the effective coupling to the states relevant for laser cooling is expected to be weaker due to a poor vibrational wavefunction overlap.

We estimate the mixing between the $A(v' = 0)$ and the $B(v' = 0)$ states separated by 1400 cm^{-1} . The spin-orbit parameters were obtained with the Breit-Pauli Hamiltonian at the MRCI level [122] and are given in Table 5.7. Diagonalization of this Hamiltonian matrix leads to a 0.05% $B(v' = 0)$ character into the $A(v' = 0)$ state. Similarly, we can compute the mixing between $A(v' = 1)$, $B(v' = 0)$ and $B(v' = 1)$ states. The coupling between $A(v' = 1)$ and $B(v' = 1)$ states is expected to be similar to the case of $v' = 0$ since the energy difference of 1310 cm^{-1} is similar to that in the case of $v' = 0$. However, the $A(v' = 1)$ and $B(v' = 0)$ states are only 64 cm^{-1} apart; hence a small Franck-Condon factor may still lead to significant mixing. Note that the measured FCF for the $A(v' = 0) \rightarrow X(v'' = 1)$ transition is 4% (Table 6.1) and that the $A - B$ bond length difference is smaller than the $X - A$ bond length. We use a value of $f = 5\%$ as an upper limit for the $A(v' = 1) \rightarrow B(v' = 0)$ FCF. Diagonalization of the corresponding Hamiltonian matrix in Table 5.7 gives a 8.4% $B(v' = 0)$ character in $A(v' = 1)$. Combining them with the measured P_{pd} for $B(v' = 0, 1)$, we estimate that the $A(v' = 0)$ state will very weakly predissociate with a probability of $\approx 5 \times 10^{-7}$ while the $A(v' = 1)$ state has a higher probability of $\approx 3 \times 10^{-5}$. The Franck-Condon factor used here is an upper-bound value. Therefore, these estimated probabilities serve as upper bounds for the actual probabilities.

5.5 Discussion

5.5.1 Other Possible Loss Channels

Other dark states that have not been considered for the molecules to exit the cycling states would also appear as molecule loss, leading to overestimating the predissociation probability. We estimate all possible loss channels that may contribute to the population loss. We consider the following processes in our system:

- Off-resonant excitation to $B^2\Sigma^+$ ($v' = 0, N' = 2$) state. The nearest parity allowed transition from the $X(v'' = 0, N'' = 1)$ state is with $B(v' = 0, N' = 2)$ state which is ≈ 768 GHz away from the $B(v' = 0, N' = 1)$ state. The transition linewidth is $\approx 2\pi \times 3$ MHz. Assuming two level system excitation, the scattering rate is given by [94]:

$$R = \frac{s\Gamma/2}{1 + s + (2\Delta/\Gamma)^2}$$

In our system, the saturation parameter s is estimated to be less than 1000. Due to that, the maximum possible off-resonant excitation happens at a rate of ≈ 2 s $^{-1}$. This rate is too low compared to estimated non-radiative decay rate of 10^5 s $^{-1}$, hence, off-resonant excitation will not affect the result.

- The existence of external electric fields can induce mixing between $B^2\Sigma^+$ ($v' = 0, N' = 0$) and $N' = 1$ states (for details, see [44] Sec 8.4.2.1). For the $A^2\Pi_{1/2}$ state, the matrix elements of the dipole operator $T_p^1(d)$ in Hund's case a basis is $-\frac{1}{3}\epsilon d$. For the $B^2\Sigma^+$ state expressed in Hund's case b basis, we need to project the states to Hund case a basis first, then calculate the matrix elements. We then calculate the matrix element to be $-\frac{1}{2}\epsilon d$. The rotational spacing of $B^2\Sigma^+$ states is approximately 250 GHz. For $A^2\Pi_{1/2}$ state, lambda doubling is approximately 26 GHz [27], The decay rate is given by

$$\frac{1}{\tau^{N=0,2}} = R_{sc} \frac{(d\epsilon/2)^2}{4\omega^2 + \Gamma^2/4}$$

where $d = 3.1$ D for B and 2.57 D for A state. $\omega = 2\pi \times 125$ GHz for B and $2\pi \times 13$ GHz for A state. $\Gamma = 2\pi \times 3$ MHz for B and $2\pi \times 5$ MHz for A state. A reasonable guess of R_{sc} is approximately 1 MHz. Since we electrically ground the entire vacuum chamber, the electric field amplitude inside the chamber should be less than 100 V/m. Eventually, the possible remixing rate is 9.7×10^{-6} s⁻¹ for $B^2\Sigma^+$ states and 6.2×10^{-4} s⁻¹ for $A^2\Pi_{1/2}$ states. These numbers are several orders of magnitude smaller than non-radiative decay rates. As a result, it will not change the measured value at a significant level.

- Photon scattering along the beam propagation direction can cause acceleration or deceleration and affect signal strength. In the interaction region, we scatter less than 100 photons per molecule. The laser beams are reflected in a zig-zag fashion, meaning the interaction is not exactly 90 degree, and there will be a nonzero projection toward beam traveling direction. The actual interaction angle is estimated to be $\arctan(1/15) \approx 4$ deg. It means there will be less than 10 photon worth of momentum is added to the molecular beam, and that would only bring 15 cm/s velocity change. The velocity of the beam is around 200 m/s, implying that the change of signal will be only around 8×10^{-4} , which is too small compared to the measured signal fluctuation.
- Off-diagonal vibrational loss due to spin-orbit mixing. As discussed in Sec. ??, the $B^2\Sigma^+$ ($v' = 0$) state mixes with the $A^2\Pi_{1/2}$ ($v' = 1$) state at the 0.06% level. This implies that population from the $B(v' = 0)$ state can decay to $X(v'' = 1)$ state via the $A(v' = 0)$ state at the rate of $6 \times 10^{-4} \times F_{A10} \approx 5 \times 10^{-4}$. This value is 40 times smaller than the FCF of $B(v' = 0) \rightarrow X(v'' = 1)$ decay (1.92×10^{-2}) and hence is a negligible correction to our model. A similar argument holds for the off-diagonal vibrational loss induced by spin-orbit mixing for the $B(v' = 1)$ state with either the $A(v' = 0)$ or the $A(v' = 2)$ states.

5.5.2 Examples of Measurement Stages

In general, a key principle in designing the stages is to have at least as many independent equations as the number of parameters, which includes the B state predissociation probability. If the number of equations and parameters are equal, as in the cases of $B(v' = 0)$ and $B(v' = 1)$ using method I, we can directly express P_{pd} using the measured ratios. Other parameters used in the experiment will also be determined and analyzed, but only serve as consistency checks. When there are more equations than parameters, we define a cost function to minimize the difference between the left and right hand sides of all equations. Further details on data analysis can be found in Section ???. Here we present a detailed illustration of how the stages are used for predissociation measurements. We first discuss the simplest $v = 0$ probability measurement, where the stages include:

- *Unperturbed.* After ablation, only $X(v'' = 0) \rightarrow B(v' = 0)$ detection lasers are turned on. This stage serves as molecule number calibration. By taking ratios of other stages with this stage, we can eliminate molecule number N from the expressions
- *Cleanup.* B_{0-1}^C vibrational repumpers are turned on. This stage can be thought of as method of estimating the $X(v'' = 1)$ natural population
- *X-A Depletion.* A_{0-0}^I cycling lasers are turned on. This stage can be used to estimate the vibrational population distribution after $X - A$ cycling, and measure the depletion efficiency
- *X-A Depletion + Cleanup.* A_{0-0}^I cycling lasers and B_{0-1}^C repumps are turned on. This stage can be used to know the repump efficiency, knowing the $X(v'' = 1)$ state natural population
- *X-B Depletion.* B_{0-0}^I cycling lasers are turned on. This stage can be used to know vibrational population distribution after $X - B$ cycling
- *X-B Depletion + Cleanup.* B_{0-0}^I cycling lasers and B_{0-1}^C repumpers are turned on. Combined with previous stages, this stage can be used to know the $B^2\Sigma^+$ state predissociation probability

To understand the parameterization of stages better, let's take an example when N ground state molecules interact with the $X(v'' = 0) \rightarrow A(v' = 0)$ laser. Due to photon cycling, the downstream ground state population will decrease to $d_A N$ (where $d_A < 1$ and is measurable simply by taking the ratios of signals). In this process, we can describe the depletion efficiency as $1 - d_A$. We can also describe how d_A is distributed amongst the different vibrational levels of $X^2\Sigma^+$ states using the known VBRs. For example, the population in $X(v'' = 1)$ state is $N(1 - d_A)F_{A01}/\mathcal{F}_{A0} + n_1 N$, where F_{A01} , \mathcal{F}_{A0} and n_1 represent the VBR from $A(v' = 0) \rightarrow X(v'' = 1)$, the sum of VBRs from $A(v' = 0) \rightarrow X(v'' = 1, 2, 3\dots)$, and normalized $X(v'' = 1)$ natural population. Because when one molecule gets excited to the $B(v' = 0)$ state, it will eventually decay to a vibrational level or break apart. This process follows a discrete probability distribution based on the VBRs and predissociation probability. In the case discussed above, $(1 - d_A)N$ molecules leave $B(v' = 0)$ state, and based on the law of large numbers we would expect the population that goes to $X(v'' = 1)$ state is $N(1 - d_A)F_{A01}/\mathcal{F}_{A0}$.

Note that in this picture, it is not recommended to describe things with number of photons scattered, since d_A is a more direct description to population transfer, whereas number of photons is not well defined. It is also worth mentioning that, the measurement protocol presented here does not rely on the lasers having good overlap with molecular beam or with each other, because as long as molecules all travel in the same spatial / velocity distribution shot by shot, the parameters (e.g. cleanup efficiency) will be constant values and will not change the mathematical ground of the measurement.

Here we briefly introduce the idea of stages in method I of $B^2\Sigma^+ (v' = 1)$ rate measurement.

- *Unperturbed.* We always monitor the $X(v'' = 0)$ population in the downstream, this serves as a signal calibration.
- *Cleanup.* With A_{0-1}^C laser, we can pump the natural population in the $X(v'' = 1)$ to $X(v'' = 0)$ state. This is to check cleanup efficiency
- *State Prep.* With A_{0-1}^S laser, we can pump the natural population in $X(v'' = 0)$ to $X(v'' = 1)$

state. This is to check state preparation efficiency. Only by pumping molecules to $X(v'' = 1)$ state efficiently, can we perform high SNR photon cycling on $X(v'' = 1) \rightarrow B(v' = 1)$ transition. Otherwise, the loss due to predissociation will be too low to be measured

- *State Prep + Cleanup.* We first populate $X(v'' = 1)$ state with A_{1-0}^S laser, then move the $X(v'' = 1)$ population back to $X(v'' = 0)$ state. Signal should be comparable to the unperturbed case. This step is to solve for κ , a and n_1 , which are cleanup efficiency, state preparation efficiency and $X(v'' = 1)$ natural population
- *State Prep + X-B 1-1 Cycling.* With most molecules in $X(v'' = 1)$ state, we can perform optical cycling via $B(v' = 1)$ state. We should see signal increment compared to *State Prep* due to photon cycling and a distribution of population based on VBR and predissociation probability
- *State Prep + X-B 1-1 Cycling + Cleanup.* By cleaning up the population left in $X(v'' = 1)$ state, we know exactly how many molecules are left in $X(v'' = 1)$ state after photon cycling. Combined with previous stages, this provides us with five equations and five variables, and we can solve for the variables including P_{pd} .

The idea behind the design of method II is as follows. We first perform state preparation to populate $X(v'' = 1)$ state for the same reason as method I. By repumping the population that leaks to $X(v'' = 0)$ and $X(v'' = 2)$ states individually, we can have a measure of unwanted loss. This also serves as a direct comparison of $A^2\Pi_{1/2}$ state and $B^2\Sigma^+$ state in terms of the loss distribution. Useful information of the ten stages can be found in Table 5.6. The fact that method II accounts for the loss to $X(v'' = 0)$ and $X(v'' = 2)$ states has both pros and cons. On the one hand, method II provides additional level of sanity checks with more equations than variables. Our approach of solving the over-constrained equation sets can be found in Appendix ???. On the other hand, it relies on detection on the $X(v'' = 1)$ state, which means that the signal will be lower than detection on $X(v'' = 0)$ state, and more sensitive to drifts in the system. Hence the eventual SNR of outcome from method II is not significantly better than method I.

It is worthwhile to note that measuring the predissociation probability for $B^2\Sigma^+$ ($v' = 2$) and higher vibrational levels would require pumping the population to $X^2\Sigma^+$ ($v'' = 2$) state and higher and performing optical cycling there, with repump light recovering the population, and monitoring unexplained loss. However, due to limitations in available space and number of lasers, as well as the increased complexity of the required stages, we have decided not to pursue these measurements at this time.

5.5.3 Bootstrap Method in Data Analysis

Bootstrapping is a statistical technique that involves generating multiple samples from a dataset by sampling with replacement [130]. It is a useful tool for constructing confidence intervals for a population parameter, and in our case, it is the expectation values of predissociation probabilities.

One of the main benefits of bootstrapping is that it allows one to make inferences about a population based on a sample, without making any assumptions about the underlying distribution of the population. Given the complexity of the functional form of predissociation probability with respect to experimentally measured ratios, utilizing bootstrapping method can avoid making any assumptions of normal distribution when determining the confidence interval of predissociation probabilities.

One way to bootstrap a set of data d with size n is to use this array of d datapoints to generate n "bootstrapped" samples by sampling with replacement. We can then compute a statistic of interest, such as the mean, from n "bootstrapped" samples, and save that to a new array. We repeatedly generate n "bootstrapped" samples, calculate the mean and save it to the storage array. The resulting distribution of the statistic can then be used to make inferences about the population. In our case, this method needs more attention regarding the dataset to be resampled.

Let's take the $B(v' = 0)$ predissociation probability as an example. The experimental procedure to acquire ratios is shown in Fig. 5.2 and explained in Sec. ???. All the ratios (r_1, r_2, r_3, r_4, r_5) are expressed using the variables given in Table 5.4, including $n_1, \kappa, F_{B0a}, d_A$ and d_B . Five equations can be explicitly written as:

Purpose	Laser Config	$v = 0$ State Pop Norm	$v = 1$ State Pop Norm	$v = 2$ State Pop Norm
Unperturbed	-	1	n_1	≈ 0
Cleanup	B_{0-1}^C	$1 + n_1 \kappa F_{B00}/\mathcal{F}_{B0}$	$n_1(1 - \kappa)$	$n_1 \kappa F_{B02}/\mathcal{F}_{B0}$
X-A Depletion	A_{0-0}^I	d_A	$(1 - d_A)F_{A01}/\mathcal{F}_{A0} + n_1$	$(1 - d_A)F_{A02}/\mathcal{F}_{A0}$
X-A Depletion + Cleanup	$A_{0-0}^I + B_{0-1}^C$	$d_A + [(1 - d_A)F_{A01}/\mathcal{F}_{A0} + n_1] \kappa F_{B00}/\mathcal{F}_{B0}$	$[(1 - d_A)F_{A01}/\mathcal{F}_{A0} + n_1](1 - \kappa)$	$[(1 - d_A)F_{A01}/\mathcal{F}_{A0} + n_1] \kappa F_{B02}/\mathcal{F}_{B0} + (1 - d_A)F_{A02}/\mathcal{F}_{A0}$
X-B depletion	B_{0-0}^I	d_B	$(1 - d_B)F_{B01}/\mathcal{F}_{B1} + n_1$	$(1 - d_B)F_{B02}/\mathcal{F}_{B1}$
X-B Depletion + Cleanup	$B_{0-0}^I + B_{0-1}^C$	$d_B + [(1 - d_B)F_{B01}/\mathcal{F}_{B1} + n_1] \kappa F_{B00}/\mathcal{F}_{B0}$	$[(1 - d_B)F_{B01}/\mathcal{F}_{B1} + n_1](1 - \kappa)$	$[(1 - d_B)F_{B01}/\mathcal{F}_{B1} + n_1] \kappa F_{B02}/\mathcal{F}_{B0} + (1 - d_B)F_{B02}/\mathcal{F}_{B1}$
Unperturbed	-	1	n_1	≈ 0
State Prep	A_{1-0}^S	$1 - a$	$n_1 + aF_{A11}/\mathcal{F}_{A2}$	$aF_{A12}/\mathcal{F}_{A2}$
Cleanup	A_{1-0}^C	$1 + n_1 \kappa F_{A00}/\mathcal{F}_{A1}$	$n_1(1 - \kappa)$	$n_1 \kappa F_{A02}/\mathcal{F}_{A1}$
State Prep + Cleanup	$A_{1-0}^S + A_{0-1}^C$	$1 - a + (n_1 + aF_{A11}/\mathcal{F}_{A2}) \kappa F_{A00}/\mathcal{F}_{A1}$	$(n_1 + aF_{A11}/\mathcal{F}_{A2})(1 - \kappa)$	$aF_{A12}/\mathcal{F}_{A2} + (n_1 + aF_{A11}/\mathcal{F}_{A2}) \kappa F_{A02}/\mathcal{F}_{A1}$
State Prep + X-A 1-1 Cycling	$A_{1-0}^S + B_{1-1}^I$	$1 - a + (n_1 + aF_{A11}/\mathcal{F}_{A2}) d_B F_{B10}/\mathcal{F}_{B2}$	$(n_1 + aF_{A11}/\mathcal{F}_{A2})(1 - d_B)$	$aF_{A12}/\mathcal{F}_{A2} + (n_1 + aF_{A11}/\mathcal{F}_{A2}) d_B F_{A02}/\mathcal{F}_{A1}$
State Prep + X-B 1-1 Cycling + Cleanup	$A_{1-0}^S + B_{1-1}^I + A_{1-1}^C$	$1 - a + (n_1 + aF_{A11}/\mathcal{F}_{A2}) [d_B F_{B10}/\mathcal{F}_{B2} + (1 - d_B) \kappa F_{A00}/\mathcal{F}_{A1}]$	$(n_1 + aF_{A11}/\mathcal{F}_{A2})(1 - \kappa)(1 - d_B)$	$aF_{A12}/\mathcal{F}_{A2} + (n_1 + aF_{A11}/\mathcal{F}_{A2}) [d_B F_{B10}/\mathcal{F}_{B2} + (1 - d_B) \kappa F_{A02}/\mathcal{F}_{A1}]$
State Prep + Cleanup v0	$A_{1-0}^S + A_{1-0}^C$	$(1 - a)(1 - \kappa_1)$	$n_1 + (a + \kappa_1 - d\kappa_1) F_{A11}/\mathcal{F}_{A2}$	$(a + \kappa_1 - d\kappa_1) F_{A12}/\mathcal{F}_{A2}$
Unperturbed	-	1	n_1	≈ 0
State Prep	A_{1-0}^S	$1 - a$	$n_1 + aF_{A11}/\mathcal{F}_{A2} \equiv \mathcal{Z}$	$aF_{A12}/\mathcal{F}_{A2}$
Cleanup v0	A_{1-0}^C	$1 - \kappa_1$	$n_1 + \kappa_1 F_{A11}/\mathcal{F}_{A2}$	$\kappa_1 F_{A12}/\mathcal{F}_{A2}$
State Prep + X-A 1-1 Cycling	$A_{1-0}^S + A_{1-1}^I$	$1 - a + \mathcal{Z} d_A F_{A10}/\mathcal{F}_{A3}$	$\mathcal{Z}(1 - d_A)$	$aF_{A12}/\mathcal{F}_{A2} + \mathcal{Z} d_A F_{A12}/\mathcal{F}_{A3}$
State Prep + X-A 1-1 Cycling + Cleanup v0	$A_{1-0}^S + A_{1-1}^I + A_{1-0}^C$	$(1 - a + \mathcal{Z} d_A F_{A10}/\mathcal{F}_{A3})(1 - \kappa_1)$	$\mathcal{Z}(1 - d_A) + (1 - a + \mathcal{Z} d_A F_{A10}/\mathcal{F}_{A3})$	$aF_{A12}/\mathcal{F}_{A2} + \mathcal{Z} d_A F_{A12}/\mathcal{F}_{A3}$
State Prep + X-A 1-1 Cycling + Cleanup v2	$A_{1-0}^S + A_{1-1}^I + A_{1-2}^C$	$1 - a + \mathcal{Z} d_A F_{A10}/\mathcal{F}_{A3} + (aF_{A12}/\mathcal{F}_{A2} + \mathcal{Z} d_A F_{A12}/\mathcal{F}_{A3}) \kappa_2 F_{A10}/\mathcal{F}_{A4}$	$\mathcal{Z}(1 - d_A) + (aF_{A12}/\mathcal{F}_{A2} + \mathcal{Z} d_A F_{A12}/\mathcal{F}_{A3}) \kappa_2 F_{A11}/\mathcal{F}_{A4}$	$(aF_{A12}/\mathcal{F}_{A2} + \mathcal{Z} d_A F_{A12}/\mathcal{F}_{A3})(1 - \kappa_2)$
State Prep + X-B 1-1 Cycling	$A_{1-0}^S + B_{1-1}^I$	$1 - a + \mathcal{Z} d_B F_{B10}/\mathcal{F}_{B2}$	$\mathcal{Z}(1 - d_B)$	$aF_{A12}/\mathcal{F}_{A2} + \mathcal{Z} d_A F_{B10}/\mathcal{F}_{B2}$
State Prep + X-B 1-1 Cycling + Cleanup v0	$A_{1-0}^S + B_{1-1}^I + A_{1-0}^C$	$(1 - a + \mathcal{Z} d_B F_{B10}/\mathcal{F}_{B2})(1 - \kappa_1)$	$\mathcal{Z}(1 - d_B) + (1 - a + \mathcal{Z} d_B F_{B10}/\mathcal{F}_{B2})$	$aF_{A12}/\mathcal{F}_{A2} + \mathcal{Z} d_B F_{B10}/\mathcal{F}_{B2}$
State Prep + X-B 1-1 Cycling + Cleanup v2	$A_{1-0}^S + B_{1-1}^I + A_{1-2}^C$	$1 - a + \mathcal{Z} d_B F_{B10}/\mathcal{F}_{B2} + (aF_{A12}/\mathcal{F}_{A2} + \mathcal{Z} d_B F_{B10}/\mathcal{F}_{B2}) \kappa_2 F_{A10}/\mathcal{F}_{A4}$	$\mathcal{Z}(1 - d_B) + (aF_{A12}/\mathcal{F}_{A2} + \mathcal{Z} d_B F_{B10}/\mathcal{F}_{B2}) \kappa_2 F_{A11}/\mathcal{F}_{A4}$	$(aF_{A12}/\mathcal{F}_{A2} + \mathcal{Z} d_B F_{B10}/\mathcal{F}_{B2})(1 - \kappa_2)$

Table 5.8: Complete stage information for $B^2\Sigma^+$ state predissociation measurement. Key information is presented in the main text and in Tables 5.4 5.5 and 5.6. For $B(v' = 0)$, we use five variables, including n_1 , κ , F_{B0a} , d_A and d_B , representing $X(v'' = 1)$ state natural population, cleanup efficiency of laser B_{1-0}^C , $B(v' = 0)$ state predissociation probability, depletion efficiency of laser A_{0-0}^I and depletion efficiency of laser B_{0-0}^I , respectively. For $B(v' = 1)$ method I, five variables are used, including a , n_1 , κ , F_{B1a} and d_B , representing state preparation (from $X(v'' = 0)$ to $X(v'' = 1)$) efficiency, $X(v'' = 1)$ state natural population, cleanup efficiency of laser A_{1-0}^C , $B(v' = 1)$ state predissociation probability, depletion efficiency of laser B_{1-1}^I , respectively. For $B(v' = 1)$ method II we use seven variables, that include a , n_1 , κ_1 , κ_2 , F_{B1a} , d_A and d_B , representing state preparation (from $X(v'' = 0)$ to $X(v'' = 1)$) efficiency, $X(v'' = 1)$ state natural population, cleanup efficiency of laser A_{1-0}^C , depletion efficiency of laser B_{1-1}^I , cleanup efficiency of laser B_{1-2}^I , respectively. We denote the VBR normalization factors as $\mathcal{F}_{A_0} \equiv \sum_{i \in Z^+} F_{A0i}$, $\mathcal{F}_{A_1} \equiv \sum_{i \in Z^*, i \neq 1} F_{A1i}$, $\mathcal{F}_{A_3} \equiv \sum_{i \in Z^*, i \neq 1} F_{A3i}$, $\mathcal{F}_{B_0} \equiv F_{B0a} + \sum_{i \in Z^*} F_{B0i}$, $\mathcal{F}_{B_1} \equiv F_{B1a} + \sum_{i \in Z^*} F_{B1i}$, and $\mathcal{F}_{B_2} \equiv F_{B1a} + \sum_{i \in Z^*} F_{B2i}$.

$$r_1 = 1 + n_1 \kappa F_{B00} / \mathcal{F}_{B_0}$$

$$r_2 = d_A$$

$$r_3 = d_A + [(1 - d_A) F_{A01} / \mathcal{F}_{A_0} + n_1] \kappa F_{B00} / \mathcal{F}_{B_0} \quad (5.2)$$

$$r_4 = d_B$$

$$r_5 = d_B + [(1 - d_B) F_{B01} / \mathcal{F}_{B_1} + n_1] \kappa F_{B00} / \mathcal{F}_{B_0}$$

By solving these five equations and five variables, we are able to express F_{B0a} as a function of r_i ($i \in \{1, 2, 3, 4, 5\}$) with known VBRs. Therefore, we have a function f_{B0a} that takes in r_i ($i \in \{1, 2, 3, 4, 5\}$) and outputs predissociation probability F_{B0a} . Here we describe the procedure of performing bootstrapping analysis to the data. The data we have are n (≈ 200) sets of ratios $\{r_1, r_2, r_3, r_4, r_5\}$, with r_i ($i \in \{1, 2, 3, 4, 5\}$) being an array of length n .

1. Randomly sample n elements from the original r_1 array with replacement, which means the elements from original r_1 array can appear more than once in the new array r_1^{bt} . This step mimics the situation where the same measurement is performed again. We then perform independent random sampling with replacement to r_2 , r_3 , r_4 and r_5 as well, and get r_i^{bt} ($i \in \{1, 2, 3, 4, 5\}$) arrays
2. Calculate the mean of the newly generated r_i^{bt} arrays individually, which can be denoted as $\overline{r_i^{bt}}$. We can feed these $\overline{r_i^{bt}}$ s to the function f_{B0a} and store the output to an array F
3. Repeat step 1 to 2 for, typically, a million times, until the statistical properties such as mean and standard deviation of the normalized distribution of array F converges
4. Analyze the distribution of F . For the expectation value, we use the mean of array F . To determine the 95% confidence interval, we take the 2.5% quantile from the distribution of F as the lower bound, and 97.5% quantile as the upper bound.

A few comments are necessary about the bootstrapping method used here. For step 1, we

sample n elements many times. One can think of it as that we are trying to mimic the situation where we perform the same measurement once again. For step 2, we do not need to make any assumptions of the data array r_i s, and this step remains legitimate. For step 3, one needs to monitor the statistical properties such as mean and std of the distribution as it varies with bootstrapping times, in order to claim the distribution has reached equilibrium. The data presented here are all done with one million times of bootstrapping resampling. For step 4, 2.5% quantile means the value that meets the following criteria: the number of elements that are smaller than it is 2.5% of the total number of elements in the array.

The data analysis of $B(v' = 1)$ method I is almost identical to that for $B(v' = 0)$. The procedures of doing bootstrapping are the same, so we won't elaborate here. The analysis code can be found online¹.

The data analysis of $B(v' = 1)$ method II is slightly different from the previous two cases. We no longer have a deterministic function of F_{B1a} because we have nine equations and seven variables. In order to solve this over-constrained system, what we can do is perform a least-square fit. We first write down these nine equations, move all terms to the right hand side of the equations, leaving left hand side to be zeros. We define the cost function as the sum of squares of all the right hand side of the equations, and use Levenberg-Marquardt algorithm to search for the local minimum with a reasonable initial guess. We do the same set of procedure every time we receive nine ratios, and treat this as the function that express F_{B10} with R_i s.

Other analysis methods such as regular error propagation are attempted and they perform similarly in terms of mean value and confidence interval. Bootstrapping, however, relies on minimum number of assumptions to the data, and was chosen to be presented here.

¹[github.com/QiSun97/CaH_Predissociation/bootstrapping_v6_final.github.ipynb](https://github.com/QiSun97/CaH_Predissociation/blob/main/bootstrapping_v6_final.github.ipynb)

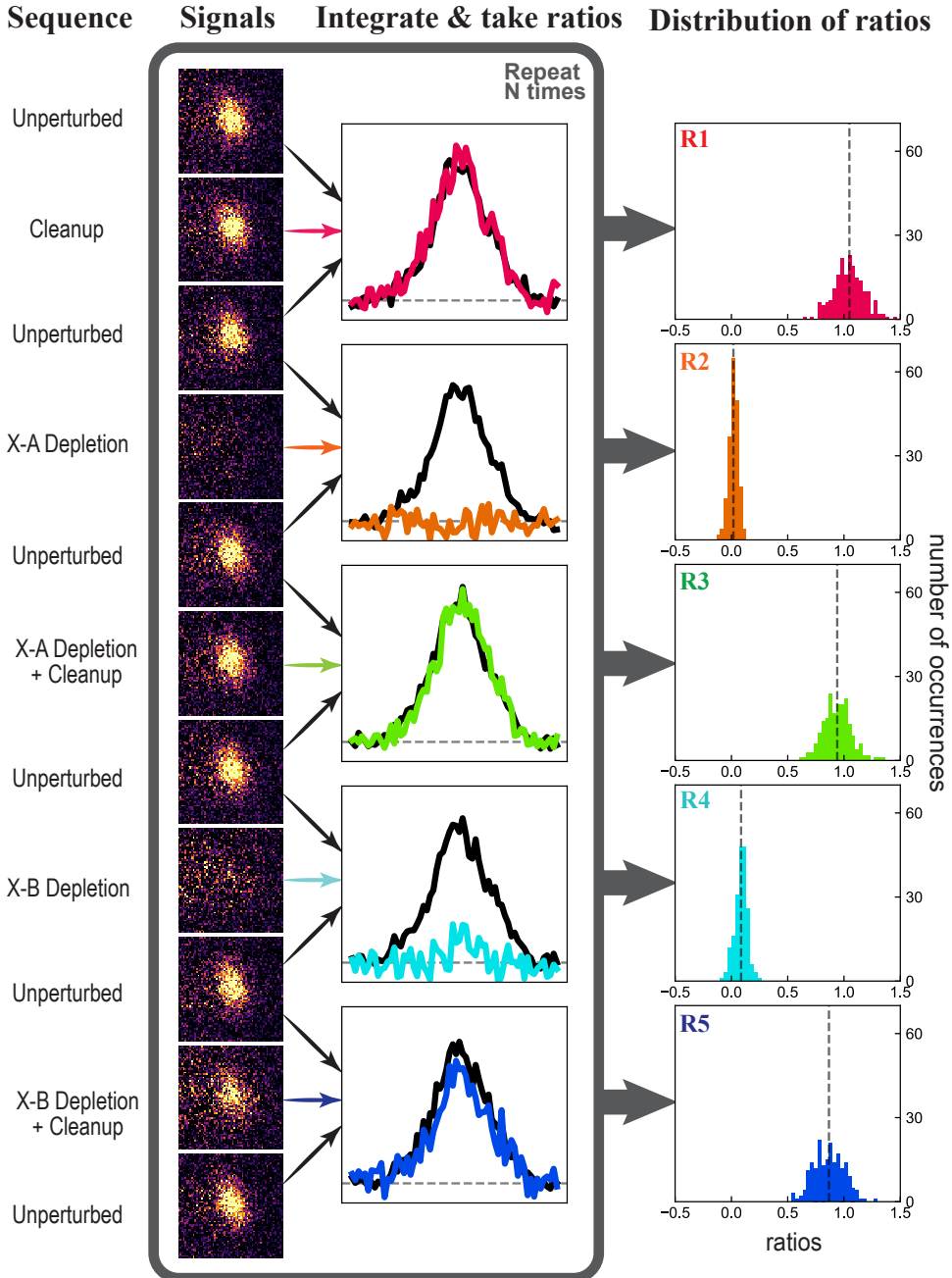


Figure 5.2: Graphical illustration of ratio extractions process of $B^2\Sigma^+$ ($v' = 0$) predissociation measurement. We run the group of stages sequentially with a reference stage interlaced between other stages, and collect LIF with EMCCD. We integrate the images along both axes to obtain the signals, which we then used to calculate ratios. By repeating the whole sequence N times, we collect N sets of five ratios. In this figure, we first show an example sequence of one-shot camera images of the stages. We present the integrated signal along one axis, and use colored traces for science stages and black traces for reference stages. The horizontal lines represent the baseline in the plots. Lastly, we show the histograms of the five ratios individually. The vertical dashed line represents the mean of the ratios. The difference in distribution widths indicates that we are dominated by source fluctuation and detection noise. Figure adopted from Ref. [89].

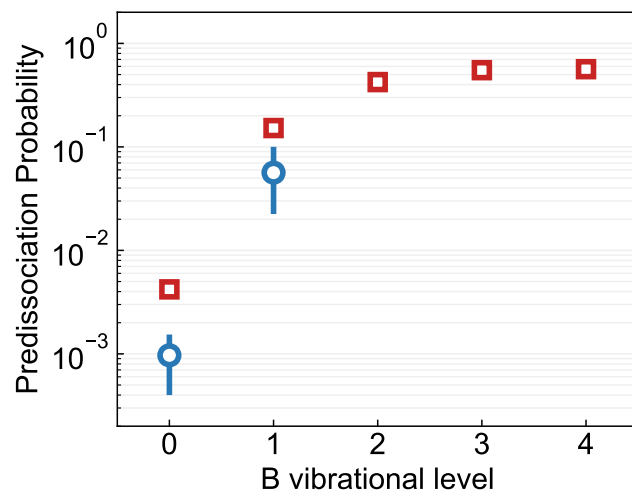


Figure 5.3: Predissociation measurement results. Red squares are the theoretical calculation results from the non-radiative decay rates for different vibrational states of $B^2\Sigma^+$. The blue circles are the experimental results, where errorbars represent 95% confidence interval. Figure adopted from Ref. [89].

Chapter 6: Laser Cooling and Slowing

6.1 Fun Fact: An Experimentalist Should Be Brave

Before I start to discuss cooling and slowing, I have to mention this at the forefront. This project might be the one that cost me most time during my PhD, partially because this was during COVID, but more importantly, I was too junior to dare making decisions about vacuum system. Looking back, the reason why we got much better sub-Doppler cooling signal with CaD than CaH, was from removing an inhomogeneous external magnetic field source - an Edwards Active Wide Range Gauge. This gauge has a permanent magnet inside and is capable of creating thousands of gauss of B field within 1 cm and a few gauss within 30 cm. It was installed near the differential pumping region and was \approx 30 cm away from cooling center. We knew it might disturb the B field in the interaction region so we wounded coils to try to compensate for it. In the end, the data with CaH was not too ideal and we could not improve it with the two sets of compensation coils we had. A change of vacuum chamber happened during our attempt with laser cooling CaD, and we removed this gauge and replaced it with a low field gauge. The benefit was obvious. A great lesson that I learned from it was, to make an experiment work, we should be brave enough to make changes to those that may potentially harm the experiment. Another important lesson is, our system is not that sensitive to vacuum quality, BaF can get a MOT with 4E-6torr pressure, we do not need to worry about it until we hit that level. *So be brave, future hydride team!*

6.2 Summary of CaH Laser Cooling Experiment

We demonstrate optical cycling and laser cooling of a cryogenic buffer-gas beam of calcium monohydride (CaH) molecules. We measure vibrational branching ratios for laser cooling transitions for both excited electronic states *A* and *B*. Furthermore, we measure that repeated photon

scattering via the $A \leftarrow X$ transition is achievable at a rate of $\sim 1.6 \times 10^6$ photons/s and demonstrate interaction-time limited scattering of ~ 200 photons by repumping the largest vibrational decay channel. We also demonstrate a sub-Doppler cooling technique, namely the magnetically assisted Sisyphus effect, and use it to cool the transverse temperature of a molecular beam of CaH. Using a standing wave of light, we lower the transverse temperature from 12.2(1.2) mK to 5.7(1.1) mK. We compare these results to a model that uses optical Bloch equations and Monte Carlo simulations of the molecular beam trajectories. This work establishes a clear pathway for creating a magneto-optical trap (MOT) of CaH molecules. Such a MOT could serve as a starting point for production of ultracold hydrogen gas via dissociation of a trapped CaH cloud.

6.2.1 Introduction

The development of robust techniques for laser cooling of atoms [133, 134] has led to major advancements in the fields of quantum simulation, quantum computation, and frequency metrology, and has enabled precise tests of fundamental physics [135, 136, 137, 138]. Cooling and trapping of molecules represents the next level in experimental complexity because of the additional internal degrees of freedom and the lack of perfect two-level structure that can be used for sustained photon cycling [139]. In exchange for this increase in complexity, molecules provide enhanced sensitivity for fundamental precision measurements [140, 141, 142], long coherence times for quantum information [143, 144, 145], and tunable long-range interactions for quantum simulators [146, 144]. The technique of buffer gas cooling [68, 147] has enabled direct laser cooling of molecules, including several diatomic [148, 149, 73, 150, 151], triatomic [79, 142, 152], and symmetric top [80] species. We add the alkaline-earth-metal monohydride CaH to this growing list.

A cold and trapped cloud of hydrogen atoms promises to be an ideal system for testing quantum electrodynamics (QED) and precise measurements of fundamental constants [153, 154]. More than two decades ago, a BEC of atomic hydrogen was prepared in a magnetic trap [155]. The measurement of the $1S - 2S$ transition has been performed in a magnetic trap of hydrogen [156] and antihydrogen [157] and also in a beam [158]. More recently, experiments measured the $1S - 3S$

[159] and the $2S_{1/2} - 8D_{5/2}$ [160] transitions of hydrogen with unprecedented precision. Furthermore, magnetic slowing of paramagnetic hydrogen has been proposed [161]. While extremely successful, these experiments are often limited by motional effects. Performing measurements with dilute ultracold samples of hydrogen tightly trapped in an optical potential could improve the precision.

A possible pathway to such samples is via fragmentation of hydride molecules [162] and ions [163]. Diatomic hydride radicals can be efficiently cooled using direct laser cooling techniques. Additionally, if the controlled fragmentation process does not heat the sample, the resulting hydrogen atoms can populate a Boltzmann distribution at a lower temperature than the parent molecules. This presents barium monohydride as an ideal candidate where the large mass difference between the barium atom and the hydrogen atom could result in an ultracold cloud of hydrogen atoms after fragmentation [162]. Although BaH was successfully laser cooled [151], its low recoil momentum and a relatively weak radiation pressure force make it challenging to load into a magneto-optical trap.

In this work, we explore an alternative molecule for laser cooling and trapping, calcium monohydride. Due to its diode-laser accessible transitions and short excited state lifetimes, CaH is a promising candidate for optical cycling. Indeed CaH was among the earliest molecules proposed for laser cooling [105]. In addition, buffer gas cooling [164], magnetic trapping and evaporative cooling [165] of CaH have been demonstrated. Here we show direct laser cooling of CaH. In Sec. 6.2.2 we describe the electronic structure and relevant optical transitions for this molecule. We also characterize our cryogenic buffer gas beam source. In Sec. 6.2.3 we summarize the measurement of the vibrational branching ratios for this molecule and establish a photon budget for laser cooling. In Sec. 6.2.4 we present the measurement of the photon scattering rate and show that we can achieve rates over 10^6 photons/s. In Sec. 6.2.5 we demonstrate an ability to cool a beam of CaH via a sub-Doppler technique by a factor of ~ 2 in one dimension while only scattering ~ 140 photons. Finally, in Sec. 6.2.6 we conclude that these results establish CaH as a promising candidate for laser cooling and trapping.

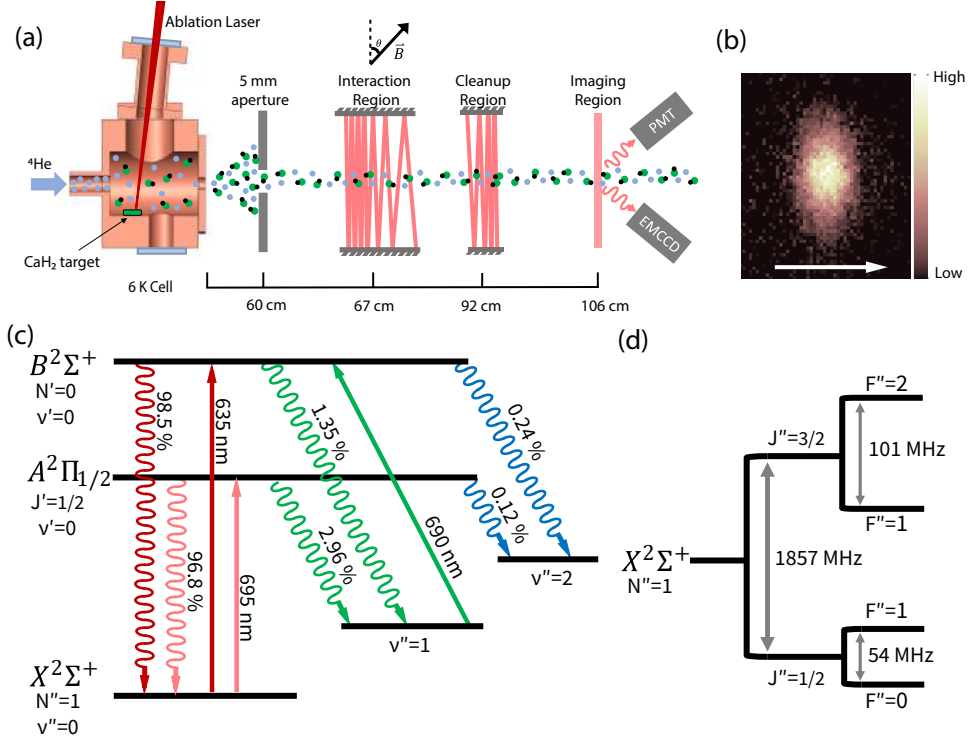


Figure 6.1: Experimental setup and molecular structure. (a) Experiment diagram (not to scale). CaH molecules and Ca atoms are produced via ablation of a solid target of CaH₂. The ejected molecules thermalize to the ~ 6 K ${}^4\text{He}$ buffer gas and are extracted through a 3 mm diameter aperture. An additional 5 mm aperture is placed just before the molecular beam enters the interaction region to limit the transverse velocity distribution. The cooling chamber consists of 12 cm of optical access followed by a cleanup region and a detection region. (b) A sample image of molecules in the beam taken with the EMCCD camera. Photons are collected for 7 ms during imaging. Arrow indicates the direction of the molecular beam. (c) The main cooling line used in this work is the $A^2\Pi_{1/2}(v' = 0, J' = 1/2) \leftarrow X^2\Sigma^+(v'' = 0, N'' = 1)$ transition at 695 nm. We detect the molecular beam using the $B^2\Sigma^+(v' = 0, N' = 0) \leftarrow X^2\Sigma^+(v'' = 0, N'' = 1)$ transition using 2.6 W/cm² of 635 nm light. We employ laser light at 690 nm to repump molecules that decay to the $v'' = 1$ vibrational state in X by addressing the $B^2\Sigma^+(v' = 0, N' = 0) \leftarrow X^2\Sigma^+(v'' = 1, N'' = 1)$ transition. By closing this leak, we create a quasi-closed transition capable of cycling ~ 200 photons sufficient to exert a measurable Sisyphus force. (d) The 1.86 GHz spin-rotation splitting and the 54 MHz (101 MHz) hyperfine structure of the $J = 1/2$ ($J = 3/2$) states in the ground X manifold. The details of the laser setup can be found in Appendix 6.2.7.

6.2.2 Experimental Setup

The experiment consists of a cryogenic buffer gas beam source operating at ~ 6 K [68, 147, 151]. We employ ${}^4\text{He}$ as a buffer gas that is flowed into the cell at a rate of ~ 6 sccm (standard cubic centimeter per minute) via a capillary on the back of the cell (Fig. 6.1(a)). The target is

composed of pieces of CaH₂ (Sigma-Aldrich, 95% purity) held on a copper stub using epoxy. To ablate the target, we use the fundamental output of an Nd:YAG pulsed laser operating at 1064 nm and at a 2 Hz repetition rate. We run the ablation laser at a maximum pulse energy of 30 mJ and focus the beam to a diameter of 1.5 mm. We observe the highest molecular yield when the ablation energy is deposited over a large target surface area. The CaH radicals produced due to ablation subsequently thermalize their internal rotational and vibrational degrees of freedom via collisions with the buffer gas. These molecules are then hydrodynamically entrained in the buffer gas flow out of the cell. The molecules leaving the cell are predominantly in the lowest two rotational states ($N'' = 0$ and 1) and the ground vibrational state ($\nu'' = 0$).

After leaving the cryostat, the molecules enter a high vacuum chamber equipped with a beam aperture of 5 mm diameter to filter out the $1/e^2$ transverse velocity range to $\sim \pm 3$ m/s (Fig. 6.1(a)). We keep the aperture in place for all data shown in this work. Subsequently, the molecules enter an interaction region with rectangular, antireflection coated windows enabling a 12 cm long interaction length. Next, the molecules enter a “cleanup” region, where population accumulated in the $X(\nu'' = 1)$ state is pumped back to the $X(\nu'' = 0)$ state via the $B(\nu' = 0)$ state, and are then detected in the imaging region by scattering photons on the $B(\nu' = 0) \leftarrow X(\nu'' = 0)$ transition. The scattered photons are simultaneously collected on a photon counting photo-multiplier tube (PMT) and an electron-multiplying charge-coupled device (EMCCD) camera. An example of the average camera images collected is shown in Fig. 6.1(b).

The relevant energy level structure for CaH is depicted in Fig. 6.1(c). We start in the ground electronic manifold ($X^2\Sigma^+$) and excite to the two lowest excited electronic states ($A^2\Pi_{1/2}$ and $B^2\Sigma^+$). A rotationally closed optical cycling transition can be guaranteed by selection rules if we address the $N'' = 1$, $J'' = 1/2, 3/2$ ground states to the opposite parity $J' = 1/2$ excited state in the A manifold or the $N' = 0$ state in the B manifold [166]. The ground $X(N = 1)$ state is split into two components separated by 1.86 GHz due to the spin-rotation interaction (Fig.6.1(d)). Each sublevel is further split into two hyperfine sublevels ($J = 1/2$, $F = 0, 1$ and $J = 3/2$, $F = 1, 2$) separated by 54 MHz and 101 MHz respectively. Each hyperfine sublevel is composed of $2F + 1$ m_F states

that remain unresolved for the purpose of this study. The hyperfine splitting of the excited A and B states of interest ($J = 1/2$) is not resolved. The primary vibrational decay from both A and B excited states is to the $v'' = 1$ state ($\sim 1\text{-}3\%$) and subsequently to the $v'' = 2$ state ($< 0.3\%$). For this work, we only repump the population out of the $v'' = 1$ state. The details of the laser setup can be found in Appendix 6.2.7.

We estimate the longitudinal velocity of our molecular beam as follows. Every ablation pulse produces Ca atoms that get buffer gas cooled and extracted from the cell alongside the CaH molecules. We measure the longitudinal velocity profile of these Ca atoms within the cleanup region, 92 cm from the cell aperture, by addressing the $^1S_0 \rightarrow ^1P_1$ transition in calcium at 423 nm in a velocity sensitive configuration (laser \vec{k} is at 70° relative to the beam's forward velocity vector). The high density of calcium in the beam allows us to measure the Doppler-shifted atomic resonance with a high signal-to-noise ratio. We find that the longitudinal velocity is peaked at ~ 250 m/s with a full width at half maximum of ~ 200 m/s. Since the masses of CaH and Ca are nearly identical and they experience identical buffer-gas cooling, we assign the same longitudinal velocity profile to both species. We also estimate the molecular beam flux in our system via the total camera counts and the estimated collection efficiency of the imaging system (see Appendix 6.2.8 for details). We obtain a typical beam flux of $\sim 1 \times 10^{10}$ molecules/steradian/pulse.

6.2.3 Vibrational Branching Ratio Measurement

Although the cycling transition in CaH is rotationally closed, no selection rules prevent vibrational decay. The probability of decay from the excited electronic state to vibrationally excited X states is quantified by the vibrational branching ratio (VBR).

To reduce the number of repumping lasers required to scatter $\sim 10^5$ photons, it is essential that the off-diagonal VBRs are highly suppressed [105, 166]. The directly laser cooled diatomic molecules to date, including CaF [149, 73], SrF [167], YbF [168] and YO [150], all possess highly diagonal transitions. The Franck-Condon factor (FCF) is defined as the square of the wavefunction overlap for two different vibrational states which is typically obtained from *ab initio* calculations.

The conversion between VBRs (denoted as q) and FCFs (denoted as f) can be derived from the Einstein A coefficient [169] and is given by

$$q_{\nu'\nu''} = \frac{f_{\nu'\nu''} \times \omega_{\nu'\nu''}^3}{\sum_{n=0}^{\infty} f_{\nu'n} \times \omega_{\nu'n}^3} \quad (6.1)$$

where $\omega_{\nu'\nu''}$ is the positive energy difference between the states ν' and ν'' . Alkaline-earth monohydrides have been extensively studied and FCFs have been calculated or measured for BeH, MgH, SrH and BaH [33, 170, 171, 34]. Calculated values for CaH [33, 172, 34] are summarized in Table 6.1. In this section we report our measurement of VBRs for the $A(\nu' = 0)$ and $B(\nu' = 0)$ states of CaH, denoted by $q_{0,\nu''}$ where ν'' is 0, 1 and 2.

We perform the VBR measurement with our molecular beam using a process similar to the one described in Ref. [173]. A pump laser beam intersects the CaH beam orthogonally in the imaging region, and resonantly excites the molecules from $X^2\Sigma^+(\nu'' = 0)$ ground states to the $A^2\Pi_{1/2}(\nu' = 0)$ or $B^2\Sigma^+(\nu' = 0)$ excited states. Once excited, two PMTs in photon-counting mode with different dichroic filters are used to collect the photons simultaneously emitted from the various decay pathways of the excited state. The narrow bandpass dichroic filters are strategically chosen to isolate photons with a frequency resonant with vibrational decay to a single excited vibrational state ($\lambda_{0\nu''}$) while simultaneously detecting the molecules that return to the ground state (λ_{00})¹.

We first compare the time traces of two PMTs when their filters allow transmission at the same λ_{00} frequency. The ratio of integrated signals, R_0 , can be expressed with systematic parameters and VBRs as

$$R_0 = \frac{Nq_{00}\Omega_{P_2}T_{F_2,\lambda_{00}}Q_{P_2,\lambda_{00}}}{Nq_{00}\Omega_{P_1}T_{F_1,\lambda_{00}}Q_{P_1,\lambda_{00}}}, \quad (6.2)$$

where the subscripts P_1/P_2 stand for two PMTs used in this experiment², subscripts F_1/F_2 stand

¹A complete list of filters used in this experiment and their measured transmission efficiencies at certain wavelengths can be found in Sec. 6.2.9.

²PMTs used: Hamamatsu R13456 and SensTech P30PC-01.

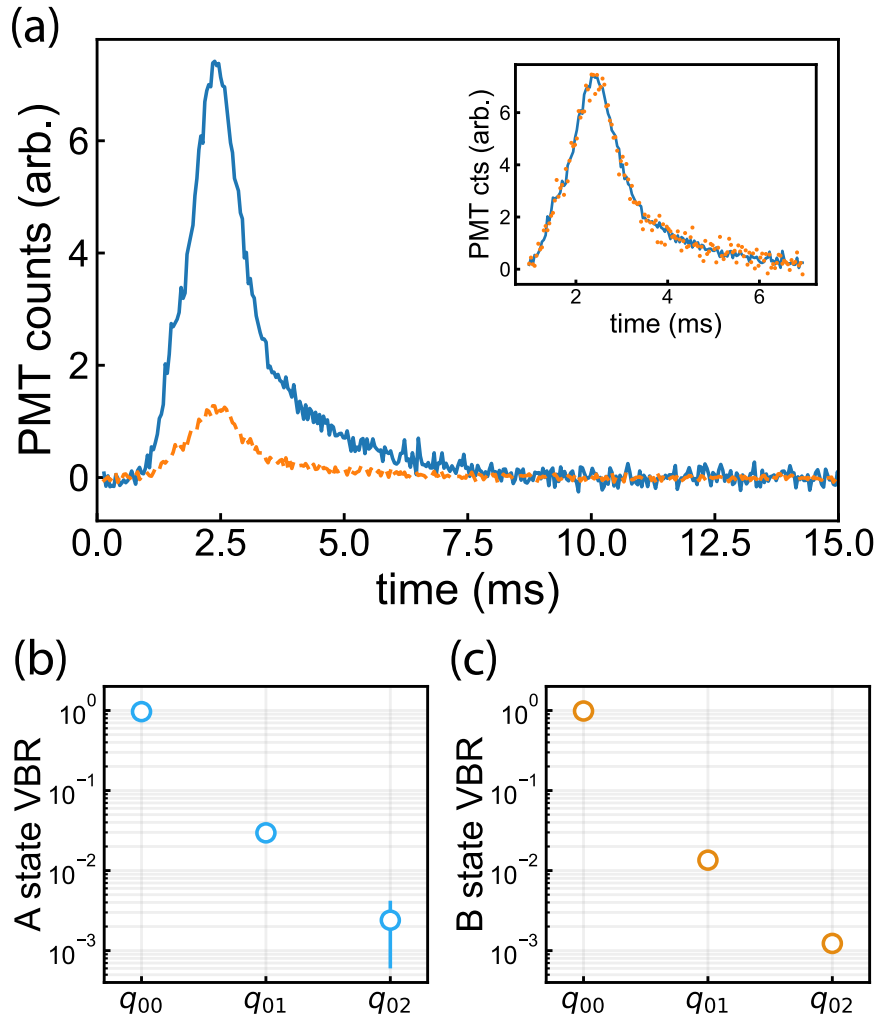


Figure 6.2: Measurement of the VBRs for CaH molecules. (a) An example of PMT traces used to calculate the VBRs. These two time traces correspond to background-subtracted fluorescence from the decay to $X(\nu'' = 0)$ for PMTs P_1 (orange, dashed) and P_2 (blue, solid) while the $B^2\Sigma^+(\nu' = 0) \leftarrow X^2\Sigma^+(\nu'' = 0)$ transition is excited. Due to a different operating configuration, the molecular beam velocity is ~ 400 m/s for this data. The inset denotes how the ratio of integrated signals, R_0 , is computed. We perform a one-parameter fit of the dashed trace to the solid trace. The result of the fit produces the orange points that can be seen to overlap temporally with the blue trace. (b,c) The resulting VBRs from the measured ratio $R_{\nu''}$, obtained by evaluating Eq. (6.4), for the A and B states. Each point represents an average of at least 200 shots with background subtraction, while the higher vibrational decays require ~ 700 shots for an appreciable signal-to-noise ratio due to the low probability of decaying to these excited states. Error bars are statistical standard errors. Figure adopted from Ref. [30].

Transition	Lifetime τ (ns)	Vibrational Quanta (v'')	Transition wavelength (nm)	FCF Theory ($f_{0v''}$)	FCF measured ($f_{0v''}$)	VBR measured ($q_{0v''}$)
$A \rightarrow X$	33(3)	0	695.13	0.953	0.9572(43)	0.9680(29)
		1	761.87	0.0439	0.0386(32)	0.0296(24)
		2	840.07	2.74×10^{-3}	$4.2(3.2) \times 10^{-3}$	$2.4(1.8) \times 10^{-3}$
		3	932.80	2.3×10^{-4}	-	-
$B \rightarrow X$	58(2)	0	635.12	0.9856	0.9807(13)	0.9853(11)
		1	690.37	0.0132	0.0173(13)	0.0135(11)
		2	753.97	1.1×10^{-3}	$2.0(0.3) \times 10^{-3}$	$1.2(0.2) \times 10^{-3}$
		3	827.84	1×10^{-4}	-	-

Table 6.1: FCFs and VBRs for the measured transitions of CaH. The experimental radiative lifetime for the A state was obtained from Ref. [31] and for the B state from Ref. [32]. The excited state vibrational quantum number is always $v' = 0$. The $A(v' = 0) \leftarrow X(v'' = 0)$ excitation wavelength at 695.13 nm, the $B(v' = 0) \leftarrow X(v'' = 0)$ excitation wavelength at 635.12 nm, and the $B(v' = 0) \leftarrow X(v'' = 1)$ excitation wavelength at 690.37 nm were determined experimentally. The other transition wavelengths are derived using measured vibrational energies given in Ref. [27]. The calculated FCFs are obtained from [33] for the $A \rightarrow X$ decay and from [34] for the $B \rightarrow X$ decay. Error bars for the measured FCFs and VBRs are statistical standard errors. Table adopted from Ref. [30].

for the two bandpass filters used, N is the number of scattering events, q_{00} is the diagonal VBR, Ω_P is the geometrical collection efficiency for a given PMT, $T_{F,\lambda}$ is the transmission efficiency for a given bandpass filter at a wavelength λ , and $Q_{P,\lambda}$ is the quantum efficiency for a given PMT at a wavelength λ .

Next, we replace filter F_2 with another filter F_3 which blocks transmission at λ_{00} and allows transmission at $\lambda_{0v''}$, where v'' is 1 or 2. The ratio of integrated signals, $R_{v''}$, can then be written as

$$R_{v''} = \frac{N' q_{0v''} \Omega_{P_2} T_{F_3, \lambda_{0v''}} Q_{P_2, \lambda_{0v''}}}{N' q_{00} \Omega_{P_1} T_{F_1, \lambda_{00}} Q_{P_1, \lambda_{00}}} \quad (6.3)$$

An example of the measured signals is shown in Fig. 6.2(a). For each measurement we simultaneously collect the time traces from the two PMTs. In order to obtain the ratio $R_{v''}$, we perform a one-parameter least square fit of all points in one time trace to the other (Fig. 6.2(a) inset). Since the PMTs are stationary throughout the experiment, any variation in Ω is negligible. By measuring the transmission efficiency of the filters F_2/F_3 at $\lambda_{00}/\lambda_{0v''}$, as well as the quantum efficiency of P_2

at $\lambda_{00}/\lambda_{0\nu''}$, and combining Eqs. (6.2) and (6.3), we estimate the ratio of VBRs as

$$\frac{q_{0\nu''}}{q_{00}} = \frac{R_{\nu''} Q_{P_2, \lambda_{00}} T_{F_2, \lambda_{00}}}{R_0 Q_{P_2, \lambda_{0\nu''}} T_{F_3, \lambda_{0\nu''}}}. \quad (6.4)$$

We calculate the individual VBRs by assuming that the sum is $\sum_{\nu''=0}^2 q_{0\nu''} = 1$. This is a reasonable approximation since the calculated value of f_{03} is smaller than the statistical uncertainty in the measured FCFs for both *A* and *B* states (Table 6.1). The resulting VBRs are plotted in Figs. 6.2(b,c). The measured FCFs were calculated using the inverted form of Eq. (6.1).

6.2.4 Scattering Rate Measurement

Efficient cooling and slowing of molecules require rapid scattering of photons while simultaneously minimizing the loss to unaddressed vibrationally excited states. From the measured VBRs for the primary decay pathways for CaH as described in Sec. 6.2.3, we obtain the average number of photons per molecule, $\langle N_{\text{ph}} \rangle$, that we expect to scatter while addressing N_ν vibrational channels before only $1/e$ of the ground state population remains available for optical cycling as

$$\langle N_{\text{ph}} \rangle \simeq \frac{1}{1 - \sum_{\nu''=0}^{N_\nu} q_{0\nu''}}. \quad (6.5)$$

Thus we expect to scatter 31(3) photons for $A \leftarrow X(\nu'' = 0)$ and 68(5) photons for $B \leftarrow X(\nu'' = 0)$ before losing 63% of molecules to the $X(\nu'' = 1)$ state. Next, if the $X(\nu'' = 1)$ state is repumped, this photon number increases to around 400 for the *A* state and 800 for the *B* state cycling schemes. In order to slow a CaH molecule travelling at 250 m/s to within the capture velocity of a MOT [73, 151], we would need to scatter $\sim 2 \times 10^4$ photons. Although the loss to excited vibrational modes can be minimized by using repumping lasers for higher vibrational states, it is essential to scatter photons at a high rate so that the slowing distance can be minimized. The maximum scattering rate for a multilevel system with n_g ground states and n_e excited states is given by [174]

$$R_{\text{sc,max}} = \Gamma_{\text{eff}} = \frac{1}{\tau} \frac{n_e}{n_e + n_g} \quad (6.6)$$

where τ is the excited state lifetime given in Table 6.1. The rotationally closed transition employed here is $N' = 0 \leftarrow N'' = 1$, i.e., $n_e = 4$ and $n_g = 12$ (see Fig. 6.1(d)). Here we assume that the repumping lasers couple to different excited states. We obtain the maximum scattering rate $\sim 7.6 \times 10^6 \text{ s}^{-1}$ for the A state and $\sim 4.3 \times 10^6 \text{ s}^{-1}$ for the B state. In practice, however, it is difficult to achieve these maximum values and most experiments with diatomic, triatomic, and polyatomic molecules to date achieve scattering rates up to $\sim 2 \times 10^6 \text{ s}^{-1}$.

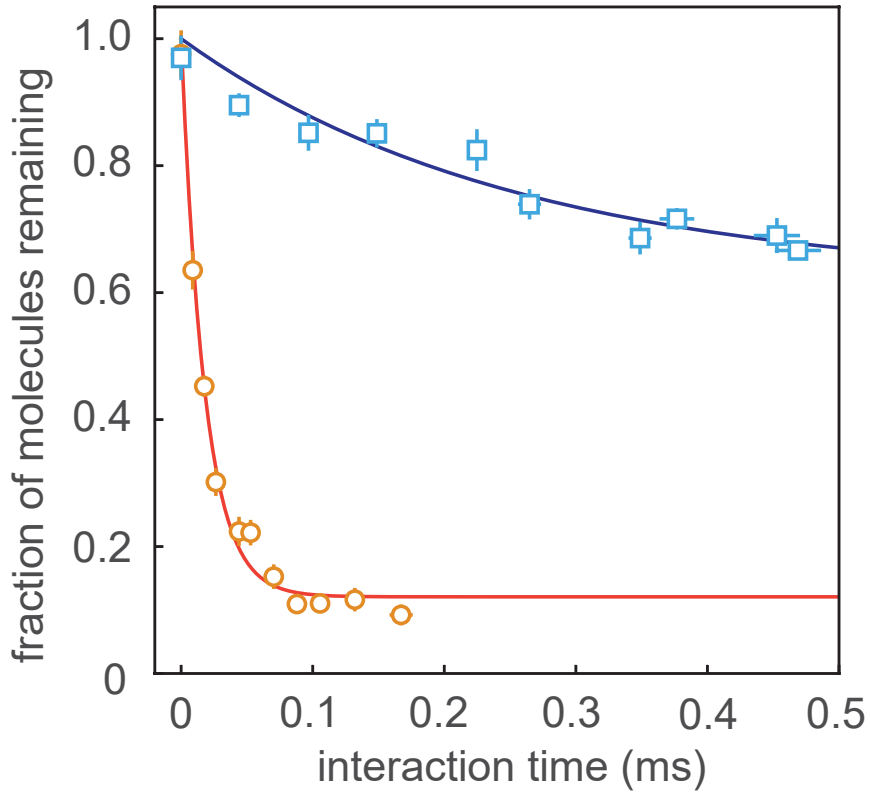


Figure 6.3: Scattering rate measurement. The fraction of molecules remaining in the $X(v'' = 0)$ state when cycling on the $A(v' = 0) \leftarrow X(v'' = 0)$ transition (orange circles) and the fraction remaining in $X(v'' = 0) + X(v'' = 1)$ states when cycling simultaneously on the $A(v' = 0) \leftarrow X(v'' = 0)$ and the $B(v' = 0) \leftarrow X(v'' = 1)$ transitions (blue squares) are measured as a function of the interaction time. Lines are fits to exponential decay curves with finite offsets. The offset is due to detected molecules that are only weakly addressed in the interaction region. The exponential decay time constant τ from the fit is $5.5(3) \times 10^4 \text{ s}^{-1}$ for the orange curve and $3.92(13) \times 10^3 \text{ s}^{-1}$ for the blue curve. Figure adopted from Ref. [30].

In order to determine the maximum scattering rate achievable in our setup, we measure the fraction of molecules that are pumped to dark vibrationally excited states as a function of interac-

tion time. First, we apply only the $A \leftarrow X(\nu'' = 0)$ linearly polarized, resonant light (~ 80 mW per spin-rotation component) in the interaction region in a multi-pass configuration (Fig.6.1(a)). Each pass of the laser beam is spatially resolved so that the effective interaction length can be varied and quantified by counting the number of passes. We detect the population remaining in $X(\nu'' = 0)$, and we convert the interaction length to time by measuring the laser beam waist ($1/e^2$ radius of 0.55 mm in the direction parallel to the molecular beam and 0.84 mm in the orthogonal direction) and estimating the average velocity weighted by the relative population within the velocity distribution (251 m/s). We also apply a 3 G magnetic field in the interaction region to destabilize the dark magnetic sublevels that become populated during optical cycling. Magnetic field strength and laser polarization angle with respect to the magnetic field are scanned to maximize the scattering rate. The angle between the magnetic field and the polarization of the laser that addresses $A \leftarrow X|J = 3/2, F = 2\rangle$ was ultimately chosen to be $\sim 13^\circ$.

As the molecules propagate through the interaction region and scatter photons, some of the excited state molecules decay to unaddressed higher vibrational states at a rate given by the sum of addressed state VBRs as

$$f_{\text{rem}}(t) = \frac{N_{\text{mol}}(t)}{N_{\text{mol}}(t=0)} = \left(\sum_{\nu''=0}^{v_a} q_{0\nu''} \right)^{N_p(t)} \quad (6.7)$$

where f_{rem} is the fraction of molecules that remain in all the addressed states combined. The number of scattered photons is $N_p(t) = R_{\text{sc}}t$, and v_a is the highest addressed vibrational level. The experimental data is shown in Fig. 6.3 (orange circles). We fit the decay in f_{rem} to an exponential decay with a finite offset. We note that in the limit of infinite interaction time, $f_{\text{rem}} \rightarrow 0$. However, in our setup we have a small fraction of the molecules that only weakly interact with the laser beam but are still detected in the imaging region. These molecules are accounted for by adding a constant offset to f_{rem} . From the exponential decay constant τ_d , we can obtain the scattering rate

$$R_{\text{sc}} \simeq \frac{1}{\tau_d \left(1 - \sum_{\nu''=0}^{v_a} q_{0\nu''} \right)}. \quad (6.8)$$

Using our measured values of the VBRs and τ_d from the orange curve of Fig. 6.3, we estimate an average scattering rate of $1.67(15) \times 10^6 \text{ s}^{-1}$. Here we make a simplifying assumption that the local variation in light intensity does not affect our estimate. We justify this assumption by noting that the laser intensity far exceeds the predicted saturation intensity ($I_{\text{sat}} \approx 1.9 \text{ mW/cm}^2$) after accounting for the Gaussian laser beam profile, beam propagation, and power loss per pass.

Next, we measure R_{sc} after adding $\sim 110 \text{ mW}$ of repumping light addressing the $B(\nu' = 0) \leftarrow X(\nu'' = 1)$ transition, co-propagating with the main cooling light. In this case, we also add $\sim 40 \text{ mW}$ of the same repumping light to the cleanup region. Within this multi-pass cleanup region, we are able to transfer the $X(\nu'' = 1)$ population to $X(\nu'' = 0)$ with $> 90\%$ efficiency. The resulting data is plotted in Fig. 6.3 (blue squares). In this case the decay time is much longer, since it takes 33 photons for a $1/e$ decay in ground state population when only the $A(\nu' = 0) \leftarrow X(\nu'' = 0)$ is addressed, while it takes ~ 400 photons when the repump is added. However, the precision of this experiment is limited by the measured VBR values from Sec. 6.2.3. From the decay constant of the exponential fit, we obtain an average scattering rate $1.6(1.2) \times 10^6 \text{ s}^{-1}$. The uncertainty mostly comes from the VBR value q_{02} . Nevertheless, the two independent measurements provide an order-of-magnitude estimate of the scattering rate. The relatively high values of R_{sc} indicate that we can achieve sufficiently high scattering rates for CaH molecules. Finally, at the longest interaction time, we estimate that 170^{+500}_{-70} photons per molecule are scattered.

6.2.5 Magnetically Assisted Sisyphus Cooling

The techniques of radiative slowing and magneto-optical trapping rely on the Doppler mechanism, where the scattering rate is optimized when the laser detuning matches the Doppler shift of the molecular transition ($\delta = \vec{k} \cdot \vec{v}$). However, Doppler cooling is fundamentally limited by the excited state lifetime to a temperature of $T_D = \hbar/(2k_B\tau)$, which is known as the Doppler temperature. For CaH cooled on the $A \leftarrow X$ transition, we estimate $T_D = 116 \mu\text{K}$. Hence in order to achieve temperatures below this limit, sub-Doppler cooling techniques must be implemented [149, 175, 176, 177]. Here we demonstrate the ability to perform a type of sub-Doppler cooling known

as magnetically assisted Sisyphus cooling in one dimension.

The technique of Sisyphus cooling was first demonstrated with atoms [178, 179]. It was subsequently demonstrated with diatomic [148, 168], triatomic [79], and symmetric top [80] molecules. Alternative methods such as optoelectric Sisyphus cooling [102] and Zeeman-Sisyphus deceleration [104] of polyatomic molecules have also been demonstrated. Briefly, in a Type-II cycling scheme with more ground than excited sublevels, dark states exist. Molecules travelling at a velocity v through a standing wave formed by counter-propagating, near-resonant laser beams lose kinetic energy as they travel up potential hills that arise from spatially varying AC Stark shifts. At the top of the hill where the intensity is highest, molecules absorb the near-resonant photons and rapidly decay to a dark state, finding themselves at the bottom of the hill. If the magnetic field induced remixing rate is matched to the propagation time along the standing wave, $\lambda/(4v)$, the molecules return to the bright state and can climb up the potential hill again. This process repeats multiple times, leading to cooling. The opposite effect of Sisyphus heating can be generated by using a red-detuned laser (see Fig. 6.5 in the Appendix and Ref. [180] for details).

We perform Sisyphus cooling and heating by allowing the laser beam in a multi-pass configuration to overlap between adjacent passes. In order to achieve higher intensities, we keep the laser beam waist relatively small. This leads to substantial beam expansion as the beam propagates. We rely on this expansion after ~ 16 passes to create sufficient overlap for a standing wave. We estimate a peak intensity of $\sim 200 \text{ mW/cm}^2$ for one beam within a 5 cm long interaction region (see Appendix 6.2.10). We apply a magnetic field \vec{B} perpendicular to both the molecular beam and the laser wave vector \vec{k} , and tune the linear laser polarization to maximize R_{sc} . When optimized, we observe Sisyphus cooling at a detuning of +20 MHz as a visible compression of the width of the molecular distribution and also a slight enhancement in the on-axis molecule number (Fig. 6.4(a)). When the detuning is switched to -20 MHz, we instead see an increase in the molecular width and the emergence of bimodality near the center, a tell-tale sign of Sisyphus heating. We fit each trace to a 1D Gaussian function to obtain the $1/e$ cloud radius σ (see Appendix 6.2.10).

We perform optical Bloch equation (OBE) simulations of the internal states of the molecule

in order to estimate the Sisyphus force. Details of the simulation can be found in Refs. [180, 181] and in Appendix 6.2.10. Briefly, we account for 12 ground states and 4 excited states. We let these molecular states evolve under the OBEs. The force is calculated once the excited state population has reached steady state. Next, we perform Monte Carlo (MC) simulations of individual trajectories as the molecules travel through the interaction region and arrive in the detection region. The spatial distribution from the MC simulation can be compared to the measured camera images. In addition, the associated velocity distribution gives us access to the beam transverse temperature. Furthermore, we consider the full possible range of the standing wave intensity which determines the magnitude of the Sisyphus effect, and use this range to estimate the simulation uncertainty.

We characterize the Sisyphus effect in our experiment as a function of three parameters: detuning δ , intensity I , and magnetic field strength B (Figs. 6.4(b-d)). To quantify the cooling effect, we plot the change in cloud radius, $\Delta\sigma$, measured in mm. To minimize systematic effects, we take one molecule image with the Sisyphus laser beams on in one ablation pulse, followed by one molecule image with them off in the subsequent ablation pulse. This allows us to account for drifts in the ablation yield and beam velocity. We repeat this process for 200 shots to obtain the signal-to-noise ratio depicted in Fig. 6.4. We observe the expected Sisyphus behavior with detuning that is opposite of the Doppler effect: red-detuned heating and blue-detuned cooling. We additionally observe that the Sisyphus effect persists for detunings up to ± 50 MHz (Fig. 6.4(b)). We next measure the dependence on the laser intensity by varying the laser power while keeping the detuning fixed at $\delta = +20$ MHz. We note that we do not reach saturation of Sisyphus cooling at our maximum available laser intensity, although we expect to be in the saturated regime for photon scattering. This is due to the fact that the depth of the potential hill that quantifies the energy loss per cycle during Sisyphus cooling has a stronger dependence on the degree of overlap between adjacent beams than on the peak laser intensity. From the simulations, we predict that saturation can be expected for intensities above 600 mW/cm² (Fig. 6.4(c)). At the intensity where we see the largest cooling effect, we estimate that the transverse temperature of the molecular beam is reduced from $12.2(1.2)$ mK to $5.7(1.1)$ mK while scattering 140^{+400}_{-60} photons. Lastly, we measure the dependence on magnetic

field strength at a fixed detuning ($\delta = +20$ MHz) and intensity (200 mW/cm²). The magnetically assisted Sisyphus effect should operate at non-zero magnetic fields, and at our low laser intensities the peak is expected at ~ 1 G as corroborated by simulations (Fig. 6.4(d)). Since the Earth's field is not cancelled in the experiment, we do not detect a clear dip around $B = 0$. Nevertheless, we can be certain that Sisyphus cooling is observed here, since maximum photon scattering occurs at $B \sim 3$ G.

6.2.6 CaH Laser Cooling Experiment Conclusion

In conclusion, we have characterized the dynamics of a cryogenic beam of CaH and experimentally measured the vibrational branching ratios to the first three vibrational levels. We estimate that repumping the $v'' = 1$ and 2 vibrational states should allow us to scatter the $\sim 2 \times 10^4$ photons needed to slow the molecular beam to within the MOT capture velocity. We have demonstrated an ability to scatter ~ 200 photos at a rate of $\sim 1.6 \times 10^6$ photons/s on the $A \leftarrow X$ transition while repumping the first excited vibrational state through the $B \leftarrow X(v'' = 1)$ transition. This scattering rate implies that, with an additional $v'' = 2$ repumping laser, we should be capable of slowing the molecular beam to within the MOT capture range in ~ 20 ms. Finally we have demonstrated a sub-Doppler cooling mechanism on a CaH beam, reducing the transverse temperature from 12.2(1.2) mK to 5.7(1.1) mK while only scattering 140 photons via the magnetically assisted Sisyphus effect. Thus we have established that CaH molecules are amenable to further laser cooling. Once these molecules are cooled and trapped in a MOT, they could be used as a precursor for producing dilute ultracold hydrogen via photodissociation, for high-precision fundamental measurements.

6.2.7 Laser Configuration

For the $A \leftarrow X(v'' = 0)$ transition at 695 nm, we use two home-built external cavity diode lasers (ECDLs) separated by ~ 2 GHz to address the $J = 1/2$ and $J = 3/2$ manifolds. Each ECDL is then passed through an acousto-optic modulator to generate two frequencies separated by the hy-

perfine splitting of the corresponding J -manifold (54 MHz for $J = 1/2$ and 101 MHz for $J = 3/2$, Fig. 6.1(d)). The resulting four frequencies are used to individually seed four injection-locked amplifiers (ILAs). Laser beams from the ILAs corresponding to a single J -manifold are first combined with orthogonal linear polarizations on a polarizing beam splitter, and then the two J -manifolds are combined on a 50:50 beam splitter. Hence a single $\lambda/2$ -waveplate is sufficient to determine the polarization of each frequency component. The combined beam is spatially overlapped with light addressing the $B \leftarrow X(v'' = 1)$ repump transition at 690 nm using a narrow-band dichroic filter (FF01-690/8-25). Each repump transition is addressed with light produced by two ECDLs, each seeding one ILA and addressing a J -manifold. The hyperfine sidebands are added to the seed light via electro-optic modulators (EOMs), resonant at ~ 50 MHz and using different order Bessel functions. In total, this laser setup is capable of providing 150 mW of $A \leftarrow X(v'' = 0)$ cooling light and 110 mW of $B \leftarrow X(v'' = 1)$ repumping light propagating from the same fiber. To achieve the maximum intensity for Sisyphus experiments, an additional 150 mW of cooling light was added to the system through a separate fiber. This additional cooling light is derived from the same laser source and results from the combination of different frequency components using beam splitters (Fig. 6.5(c)). After cooling we repump any leftover $v'' = 1$ population to $v'' = 0$ using 40 mW of repump light in the cleanup region. Detection is performed on the $B \leftarrow X(v'' = 0)$ transition by using two ECDLs at 635 nm addressing the two J -manifolds, with the hyperfine sidebands added via EOMs. Since 60 mW of light with 1.2 mm $1/e^2$ radius is sufficient for detection, no ILAs are used. EMCCD in the detection region is triggered at 0.5 ms after ablation, and exposure time is set to 7 ms.

6.2.8 Molecular Beam Flux Estimation

Here we discuss the estimation of the molecular beam flux. In the experiment, we detect the molecules using the $B(v' = 0) \leftarrow X(v'' = 0)$ transition at 635 nm and collect the scattered photons with an EMCCD camera (Andor iXon Ultra 888). We use the following equation to convert the

camera counts to the total energy of the collected photons per manufacturer:

$$E_{\text{ph}} = \frac{\text{Cts}}{g} \times \frac{S}{Q} \times 3.65 \text{ eV} \quad (6.9)$$

where Cts , g , S and Q denote total camera counts, EM gain, CCD sensitivity and quantum efficiency, respectively. We can then estimate the molecule number as

$$N_{\text{mol}} = \frac{E_{\text{ph}}/\hbar\nu}{\eta \times R_{\text{sct}}} \quad (6.10)$$

The collection efficiency of our imaging system η is around 1% and constitutes the highest source of uncertainty due to our inability to directly measure it. The interaction time t is determined using the laser beam waist and a ~ 250 m/s peak velocity.

Molecular beam flux is defined as the number of molecules detected per unit solid angle with respect to the cell aperture. With an estimation of the solid angle given the molecular beam size on the camera and the distance from the cell, we estimate our molecular beam flux to be $\sim 1 \times 10^{10}$ molecules/steradian/pulse.

6.2.9 VBR Measurement

Here we present the details that factor into the calculation of A and B state VBRs (Sec. 6.2.3). In general, $R_{\nu''}$, where $\nu'' = 0, 1, 2$, is the fitted ratio of two PMT time traces. The fitting time window is from 1 ms to 7 ms, and we use the data between 35 ms and 90 ms for background subtraction. We use the same fitting protocol for all $R_{\nu''}$ measurements. The ratio $R_{\nu''}$ is stable during data collection and only varies if the position of either PMT is altered.

The quantum efficiencies of PMTs are either experimentally measured or obtained from factory calibration results. We use the following expression to measure the quantum efficiency:

$$Q = \frac{\text{Cts}}{P/\hbar\omega}, \quad (6.11)$$

where Cts is the total number of PMT counts per second, P is the laser power incident into the PMT, and $\hbar\omega$ is the photon energy. Each PMT is placed into a black box, and an optical fiber carrying light directly points at the PMT active surface. To prevent saturation of the PMT, we insert calibrated neutral-density filters between the fiber and the PMT head. We measure Q at several different laser powers and fit to a line to obtain the PMT linear response. Eventually we measured Q at 635 nm, 690 nm and 695 nm, and find that our measured Q is within 5% of the manufacturer's specifications. However, due to the lack of available laser sources at the other fluorescence wavelengths, we employ the factory calibrated values for Q provided by the manufacturer, and assign a 5% error to them. We also directly measure the transmission efficiencies of all dichroic filters used for the experiment if a laser source is available, otherwise we use the manufacturer's specifications.

Table 6.2 shows all the measured values that are used in calculating VBRs and their errors, and Table 6.3 lists the dichroic filters used for the measurement of VBRs.

$A^2\Pi_{1/2}$ q_{01}	value	error
R_0	1.575	0.013
R_1	0.0410	0.0017
$Q_{P_2,\lambda_{01}}/Q_{P_2,\lambda_{00}}$	0.73	0.04
$T_{F_3,\lambda_{01}}/T_{F_2,\lambda_{00}}$	1.17	0.06
q_{01}/q_{00}	0.0306	0.0025

$A^2\Pi_{1/2}$ q_{02}	value	error
R_0	1.363	0.015
R_2	0.0007	0.0005
$Q_{P_2,\lambda_{02}}/Q_{P_2,\lambda_{00}}$	0.167	0.008
$T_{F_3,\lambda_{02}}/T_{F_2,\lambda_{00}}$	1.15	0.06
q_{02}/q_{00}	0.0025	0.0019

$B^2\Sigma^+$ q_{01}	value	error
R_0	5.83	0.05
R_1	0.0696	0.0021
$Q_{P_2,\lambda_{01}}/Q_{P_2,\lambda_{00}}$	0.86	0.05
$T_{F_3,\lambda_{01}}/T_{F_2,\lambda_{00}}$	1.01	0.04
q_{01}/q_{00}	0.0137	0.0011

$B^2\Sigma^+$ q_{02}	value	error
R_0	5.83	0.03
R_2	0.0040	0.0005
$Q_{P_2,\lambda_{02}}/Q_{P_2,\lambda_{00}}$	0.56	0.03
$T_{F_3,\lambda_{02}}/T_{F_2,\lambda_{00}}$	1.00	0.05
q_{02}/q_{00}	0.00125	0.00019

Table 6.2: Measured parameter values that are used to calculate VBRs and FCFs for CaH given in Sec. 6.2.3. Table adopted from Ref. [30].

	F_1	F_2	F_3
$A^2\Pi_{1/2} q_{01}$	FF01-692/40-25	FF02-684/24-25	FF01-760/12-25
$A^2\Pi_{1/2} q_{02}$	FF01-692/40-25	FF02-684/24-25	FF01-840/12-25
$B^2\Sigma^+ q_{01}$	FL635-10	FF01-630/20-25	FF01-690/8-25
$B^2\Sigma^+ q_{02}$	FL635-10	FF01-630/20-25	FF01-760/12-25

Table 6.3: List of all dichroic filters used in the VBR and FCF measurements for CaH given in Sec. 6.2.3. All filters are purchased from Semrock, except FL635-10 which is purchased from Thorlabs. Table adopted from Ref. [30].

6.2.10 OBE and MC Simulations

We developed the optical Bloch equation solver [180, 181, 182, 183] using Python and Julia (via PyJulia). The source code can be found online³. We include 12 ground states of $|X^2\Sigma^+, \nu'' = 0, N'' = 1\rangle$ in Hund's case (b) and 4 excited states of $|A^2\Pi_{1/2}, \nu' = 0, J' = 1/2\rangle$ in Hund's case (a). We ignore another 12 states in the $|X^2\Sigma^+, \nu'' = 1, N'' = 1\rangle$ level, because the population in the vibrationally excited state is not significant in our experiment. The transition dipole moments are calculated with the help of a Matlab package⁴ where a Hund's case (b) basis is projected onto a case (a) basis. We perform Monte-Carlo simulation of the classical trajectories of the cryogenic molecular beam⁵. We initialize 10^4 molecules at the exit of the 5 mm beam aperture described in Sec. 6.2.2, and propagate them through the interaction region where they experience Sisyphus forces as described in Sec. 6.2.5.

We combine the OBE and MC simulations as follows: at a given laser polarization and other experimental parameters, we perform a two-dimensional parameter sweep of velocity and laser intensity using the OBE simulation of the optical force. Then within the MC simulation, for each particle with a position and velocity, we perform a 2D interpolation to obtain the instantaneous force on the particle. In order to accurately model the spatial variation of intensity, we assume Gaussian beam propagation along with loss per pass due to imperfections. We measure the beam width before it enters the interaction region, and use the number of passes to estimate the traveling

³github.com/QiSun97/OBE-Solver

⁴github.com/QiSun97/Rabi_Matrix_Elements_Calculator

⁵github.com/QiSun97/Cryogenic_Beam_Sisyphus_MC_Simulation

distance and calculate the laser beam waist. The beam waist $w(z)$ at a distance z is calculated as

$$w(z) = w(0)\sqrt{1 + (z/z_R)^2} \quad (6.12)$$

where $z_R = \pi w(0)^2 n / \lambda$ is the Rayleigh range. We measure the spacing of the laser beams to convert from the spatial coordinate to the number of passes. We also observe a moderate power loss every time a laser beam passes through the chamber ($\sim 1.8\%$). Together, these provide us with a conversion from spatial position to local laser intensity. Molecules propagate through the interaction region and eventually exit to reach the detection region. We then plot the spatial distribution of molecules and perform a one-dimensional Gaussian fit to extract the width information. The fit function used for all experimental data as well as simulations is

$$y(r) = y(0) + A \exp\left\{(-(r - r_0)^2/(2\sigma^2))\right\} \quad (6.13)$$

where σ is the $1/e$ radius of the cloud (Fig. 6.4(a)).

Assignment of Simulation Uncertainty

The main source of uncertainty in the simulations stems from our inability to measure the position and amplitude of the standing wave that gives rise to the Sisyphus effect. Although the multi-pass laser beams are distinguishable initially (i.e. do not overlap), after 16 passes they overlap significantly. This overlap region, where the standing wave is formed and Sisyphus forces act, covers ~ 5 cm of the interaction length (Fig. 6.5(b)). In addition, it is challenging to estimate the beam waist within this region. We quantify this uncertainty by considering two situations: (1) the laser beams are tightly spaced and the effective overlap is long, and (2) the beams are loosely spaced and their overlap is small. For example, in Fig. 6.4(c), the simulation band ranges from a 5 cm overlap with 1 mm beam spacing, or a 4 cm overlap with 2 mm beam spacing. The same strategy is used in generating the simulation bands in Figs. 6.4(b,d) as well.

Laser Intensity Estimation

The intensity of a Gaussian laser beam is defined as $I = 2P/(\pi w^2)$ where I is the peak intensity, P is the total power, and w is the $1/e^2$ waist. We measure the laser beam power and waist before it enters the interaction region. The beam focus lies outside the interaction region. Then we estimate the peak intensity after the beam undergoes N passes using Eq. 6.12. Furthermore, since the beam overlap that can lead to a Sisyphus effect is between the beam aperture and ~ 5 cm downstream, we denote the average intensity between 7 cm and 12 cm from the first pass of the laser beam that is coupled from the downstream side of the 12 cm long interaction region (Fig. 6.1(a)). This is how the x -axis of the experimental data in Fig. 6.4(c) is generated.

For the MC simulation, we define the average intensity from the local intensities experienced by each molecule as the molecular beam traverses the interaction region. We tabulate the local intensities experienced by all detected particles at the end of the simulation and calculate the median of the distribution to obtain the average intensity.

Transverse Temperature Estimation

We estimate the transverse temperature of the molecular beam as follows. Within the MC simulation, the only free parameter that allows us to match the detected spatial distribution is the transverse temperature that governs the transverse velocity distribution. The spatial distribution is assumed to be uniform at the 5 mm aperture, and the forward velocity is experimentally determined. Thus, we obtain a one-to-one correspondence of the molecular beam width to the transverse temperature of the beam. The unperturbed beam has a width of 3.11(14) mm, which corresponds to 12.2(1.2) mK, and the coldest beam has a width of 2.34(13) mm, which corresponds to 5.7(1.1) mK.

6.3 Summary of CaD Laser Cooling Experiment

If I dream about having ultracold hydrogen, why not include deuterium in the dream as well?

Fun fact is, only bosonic molecular species have been directly laser cooled to date, primarily due to an abundance of bosonic isotopes in nature and to their simpler hyperfine structure. Fermionic molecules provide new opportunities for ultracold chemistry, quantum simulation, and precision measurements. This section I will describe direct laser cooling of a fermionic molecular isotopologue, calcium monodeuteride (CaD). With a nuclear spin $I = 1$, only 5 hyperfine states need to be addressed for rotational closure in optical cycling. These hyperfine states are unresolved for typical experimental linewidths. We present a method for efficiently producing alkaline-earth metal hydrides and deuterides. We demonstrate rotational closure and show magnetically assisted Sisyphus cooling in one dimension for a beam of CaD molecules. Our results indicate that the experimental complexity for laser cooling CaD is similar to that of calcium monohydride (CaH). Laser cooling of CaD is a promising first step for production of ultracold and trapped atomic deuterium. This section will be mainly based on our publication [88].

6.3.1 Introduction

Recent achievements in quantum-state control of molecules have demonstrated their potential for ultracold chemistry [64, 184], quantum simulation [185, 186], quantum computation [187, 188], and precision measurements [140, 189, 190]. While fermionic molecules have been assembled from ultracold atoms [191, 192, 193], to date all directly laser cooled molecules have been exclusively bosonic. This stems partly from the fact that most abundant isotopes of neutral atoms in nature that constitute these molecules are bosonic, with the notable exceptions of beryllium and nitrogen. Additionally, a guiding principle for laser cooling candidate molecules is the simplicity of the hyperfine structure [148]. Most laser cooled molecules are of the type MX , where M is an optical cycling center with nuclear spin $I_M = 0$ and X is an electronegative ligand with $I_X = 1/2$. The resulting hyperfine structure consists of only four states that need to be optically addressed for rotational closure of the optical cycling process [190]. $I_M \neq 0$ for a fermionic species can significantly complicate the laser cooling scheme [194].

Fermionic molecules possess many favorable properties for quantum science applications. Be-

ing less prone to collisional loss than their bosonic counterparts due to the *p*-wave barrier [195], fermionic molecules are an important ingredient in ultracold chemistry experiments. The combination of Fermi-Dirac statistics and long-range interactions of polar molecules can enable the realization of topological superfluid phases [196] and lattice-spin models [197]. A fermionic cycling center *M* can be employed for precision measurements of nuclear-spin-dependent parity violation (NSD-PV) [198, 199] and axion-like dark matter searches [138]. This has motivated recent studies with fermionic ^{137}BaF [194] and $^{171,173}\text{YbOH}$ [200], with the demonstration of rotational closure for the latter. In order to overcome the hyperfine complexity that plagues the molecules listed above, we turn our attention to calcium monodeuteride (CaD) - the easiest fermionic molecule to laser-cool in the near term.

Cold CaH and CaD isotopologues have astrophysical significance as they have been observed in stellar and interstellar media [201, 202, 203]. Studying their ultracold chemical reactions in the laboratory would improve our understanding of fundamental chemical processes [204]. Moreover, CaD is a promising precursor for producing ultracold atomic deuterium, in analogy to the proposals for CaH dissociation [162, 89]. High-precision measurements with hydrogen and deuterium allow testing quantum electrodynamics [205], determining fundamental constants such as the proton charge radius [206, 207], and probing new physical forces and particles [208]. In addition, a degenerate Fermi gas of ultracold deuterium atoms would enable a new paradigm in quantum simulation with the simplest Fermi liquid [209]. Even without dissociation, the fermionic nature of CaD could allow it to reach lower temperatures and achieve better shielding from collisional losses in a conservative trap, creating a promising playground for quantum simulation experiments. The existence of an electron spin in the ground state of CaD provides an additional degree of freedom compared to bi-alkali molecules. The relative simplicity and extensive applications make CaD an interesting laser cooling candidate. In this work, we demonstrate the production and one-dimensional (1D) laser cooling of CaD, which, to our knowledge, is the only fermionic molecule to have been directly cooled.

6.3.2 Methods

6.3.3 Experimental setup

In this work, we demonstrate the production and one-dimensional (1D) laser cooling of CaD, which, to our knowledge, is the only fermionic molecule to have been directly cooled. Fig. 6.6(a) illustrates the experimental setup. The experiment starts with a cryogenic buffer gas beam (CBGB) source. An Nd:YAG pulsed laser at 1064 nm is used to ablate a solid rock sample of CaD₂, creating a hot cloud of CaD radicals. The molecules are buffer gas cooled to ~6 K using ⁴He and then ejected from the cell. This creates a CaD molecular beam pulse with peak forward velocity of ~250 m/s. The molecules are collimated with a 2.5-mm diameter aperture to 16(1) mK transverse temperature (Appendix 6.3.10) before entering the interaction region where we perform laser cooling. The molecules then enter the clean-up region and are detected through laser induced fluorescence (LIF) with an electron-multiplying charge-coupled device (EMCCD) camera. The setup has been described in detail in the context of CaH experiments [106, 89] with some modifications. Our ultrahigh-vacuum chamber is set up in a 3D radio-frequency magneto-optical trap (RF-MOT) configuration, with the MOT chamber here serving as the interaction region. We apply magnetic field using the in-vacuum MOT coils in the Helmholtz configuration.

Although some deuterated compounds are commercially available, CaD₂ is not. We produce the molecules by following a procedure outlined in Ref. [210] and detailed in Appendix 6.3.6. The flux of the CaD molecules in the $X^2\Sigma^+(\nu'' = 0, N'' = 1, -)$ state out of the CBGB source is $\sim 10^{11}$ molecules/steradian/pulse. Compared to CaH, we find an overall $\sim 5\times$ higher yield under a full range of experimental parameters such as helium flow rate, ablation laser energy, and ablation laser beam waist. This could be attributed to differences in collisional cross section with ⁴He and in crystalline chemistry between the species (Appendix 6.3.7).

Relevant Level Structure for Laser Cooling

Fig. 6.6(b) shows the level structure of the main cycling transition $A^2\Pi_{1/2}(\nu' = 0, J' = 1/2, +) \leftarrow X^2\Sigma^+(\nu'' = 0, N'' = 1, -)$ used for laser cooling. We are able to locate the transition in Fig. 6.6(c) within ~ 200 MHz of available spectroscopic data [202, 203]. The hyperfine splittings of the $J = 1/2$ and $J = 3/2$ states are adapted from Ref. [201], which we are unable to resolve due to Doppler broadening of the beam. This is of particular advantage compared to CaH where the spacings are ~ 50 -100 MHz [106]. We show our ability to rotationally close the transition by adding the two spin-rotation components $J = 1/2$ and $J = 3/2$ in the inset of Fig. 6.6(c). The LIF is normalized to that of $J = 3/2$ only and we observe a $\sim 15\times$ higher fluorescence when both components are present. This also confirms that the $A^2\Pi_{1/2}(\nu' = 0, J' = 1/2, +)$ excited state hyperfine levels are unresolved.

A key requirement to directly laser cool a molecule is the ability to continuously scatter photons at a relatively fast rate ($\sim 10^6$ s $^{-1}$). The vibrational branching ratios (VBRs) of the molecule should be diagonal so that a practical number of lasers can mitigate loss to higher vibrational states. The VBRs for CaD have been calculated [203] and are shown in Table 6.4 of Appendix 6.3.8. Since the electronic potential energy surface does not depend on the mass of the nuclei, we do not expect large isotope shifts in the VBRs. However, the mass change leads to a significant shift of fundamental vibrational frequencies, from 37 THz in CaH to 27 THz in CaD. Overall, we assume the VBRs for CaD to be the same as our measured VBRs for CaH in order to calculate the number of scattered photons.

We perform laser cooling on the $A^2\Pi_{1/2}(\nu' = 0, J' = 1/2, +) \leftarrow X^2\Sigma^+(\nu'' = 0, N'' = 1, -)$ transition, together with a ($\nu = 1$) repump laser addressing the $A^2\Pi_{1/2}(\nu' = 0, J' = 1/2, +) \leftarrow X^2\Sigma^+(\nu'' = 1, N'' = 1, -)$ transition. This allows us to scatter $\sim 1/(1 - \text{VBR}_{\nu=0, 1}) \approx 400$ photons before populating higher vibrational states. We add frequency sidebands for the ground state spin-rotation and hyperfine splittings using electro-optic modulators (EOMs) (see Appendix 6.3.9 for details). The main cooling laser and the repump laser are combined with a polarizing beam splitter and coupled to a single-mode polarization-maintaining optical fiber. They are expanded to $(2w_1 \times$

$2w_2)=(10.8 \text{ mm} \times 5.4 \text{ mm})$ $1/e^2$ diameter and retro-reflected in the interaction region to form a standing wave. The polarization of the main cooling laser ($\nu = 0$) is set to 45° with respect to the applied magnetic field along the y -axis for efficient dark state remixing. In the clean-up region, only the ($\nu = 1$) repump laser is applied in a multipass configuration. Finally we detect the molecules that remain in the ($\nu = 0$) state using the main cycling transition. The total power of the lasers shown in the schematic are 475 mW, 180 mW, 180 mW, and 45 mW, corresponding to the main cooling laser, ($\nu = 1$) repump laser in the interaction region, ($\nu = 1$) repump laser in the clean-up region, and the detection laser, respectively.

6.3.4 Results

We demonstrate 1D cooling in a beam of CaD molecules using the magnetically assisted Sisyphus effect [178]. This technique has served as a barometer for the feasibility of laser cooling for molecules such as SrF [148], YbF [168], SrOH [79], YbOH [78], and CaOCH₃ [80]. Fig. 6.7(a-c) shows the molecular beam profile detected on the EMCCD camera, with a magnetic field $|\vec{B}| = 1.7 \text{ G}$ applied along the y -axis in the interaction region. The image in Fig. 6.7(a) is taken when the main cooling laser is absent, representing the unperturbed molecular beam profile in the ($\nu = 0, 1$) states. The fluorescence along the x -axis indicates the size of the molecular beam in the detection region, while the z -axis width is determined by the detection laser beam. In Fig. 6.7(b) the main cooling laser is applied at +40 MHz detuning from resonance and we observe an accumulation of molecules near the center of the beam due to Sisyphus cooling. In Fig. 6.7(c) the laser is detuned by -40 MHz and we observe an expulsion of molecules from the center due to Sisyphus heating. We integrate the images along the z -axis and obtain the 1D profile shown in Fig. 6.7(d). We note that because of the limited interaction time of $\sim 40 \mu\text{s}$, we only deplete the population to 93(3)% even when the main cooling laser is set on resonance. This corresponds to 30(13) photons scattered at a rate of $0.7(3) \times 10^6 \text{ s}^{-1}$. This number further decreases in Sisyphus cooling and heating configurations due to the laser detuning. With the limited number of scattered photons, the integrated LIF signals under Sisyphus cooling and heating configurations are essentially unchanged from an

unperturbed beam, as in Fig. 6.7(d). We note that the estimated scattering rate is roughly half of the maximum scattering rate due to the fact that both ($\nu = 0$) and ($\nu = 1$) lasers address the same excited state $A^2\Pi_{1/2}(\nu' = 0, J' = 1/2, +)$.

Fitting Protocol

We fit the 1D profile with a phenomenological model capable of describing both Sisyphus cooling and heating. The model combines a Gaussian and a second derivative of a Gaussian, the latter serving as a modulation of the amplitude. The function is given by

$$f(x) = A \times g_{x_0, \sigma_0}(x) \times (1 - \Delta h \times g''_{x_0, \sigma_S}(x)), \quad (6.14)$$

where $g_{x_0, \sigma_0}(x) = \exp(-(x - x_0)^2/(2\sigma_0^2))$ and $g''_{x_0, \sigma_S}(x) = ((x - x_0)^2/\sigma_S^2 - 1) \times \exp(-(x - x_0)^2/(2\sigma_S^2))$. The parameters A , x_0 , and σ_0 represent the amplitude, center position, and width of an unperturbed beam, while Δh and σ_S represent the fractional peak height change and the width of the region where Sisyphus cooling or heating is effective. The shape of the second derivative of a Gaussian qualitatively reproduces how Sisyphus cooling or heating affects the central part of the molecular beam. The fits are shown as solid lines in Fig. 6.7(d).

The characteristic feature of the Sisyphus effect arises from the finite capture velocity v_c of the Sisyphus force. In the Sisyphus cooling configuration, only molecules with $v < v_c$ can experience the Sisyphus force and get cooled. The molecules are cooled from 16(1) mK to 2.7(2) mK, which we infer from the width of the peak. The Sisyphus cooled molecules reach a transverse temperature of 2.7(2) mK. In the Sisyphus heating configuration, on the contrary, slower molecules are heated and pushed away from the center. From the position of the two peaks in the Sisyphus heating profile, we determine a capture velocity of ~ 1 m/s.

Characterization of the Sisyphus Effect

The Sisyphus mechanism in a Type-II system with more ground states than excited states relies

on dark state remixing. In the cooling configuration, for example, molecules lose kinetic energy as they climb to the intensity maxima of the standing wave produced by the retro-reflected laser beam. At the maxima they are optically pumped into dark states at a lower energy [178]. Dark state remixing allows the molecules to return to a bright state and repeat the cycle, thus reducing the beam temperature. We characterize the Sisyphus effect for the following experimental parameters: laser detuning, intensity, and magnetic field. The Sisyphus effect as a function of laser detuning is shown in Fig. 6.8(a), taken at $|\vec{B}|=1.7$ G. Here we use peak height change, Δh in Eq. (6.14), as a proxy for the strength, its sign representing cooling (positive) or heating (negative). The Sisyphus effect is antisymmetric around zero detuning, and the optimal detuning for cooling and heating are found to be at $\sim \pm 40$ MHz, respectively, which corresponds to $\sim \pm 10\Gamma$. Here $\Gamma \approx (2\pi) \times 3.8$ MHz represents the natural linewidth of the main cycling transition and is estimated from Ref. [203]. The relatively large optimal detunings primarily result from the small hyperfine splittings, since at small detunings all the sidebands introduced to address the hyperfine structure of the ground state compete with each other. Fig. 6.8(b) shows the laser intensity dependence of Sisyphus cooling (blue circles) and heating (red squares). Laser intensity here is defined as the mean intensity of the Gaussian beam in a $1/e^2$ -diameter area ($P_{\text{tot}}/\pi w_1 w_2$), with only the effective laser sidebands accounted (Appendix 6.3.9). We are not able to saturate the Sisyphus effect primarily due to the limited interaction time, and the scattering rate increases linearly with laser intensity in this regime.

The Sisyphus mechanism in a Type-II system with more ground states than excited states relies on dark state remixing. In the cooling configuration, for example, molecules lose kinetic energy as they climb to the intensity maxima of the standing wave produced by the retro-reflected laser beam. At the maxima they are optically pumped into dark states at a lower energy [178]. Dark state remixing allows the molecules to return to a bright state and repeat the cycle, thus reducing the beam temperature. This is achieved through Larmor precession in the hyperfine sublevels in the presence of an external magnetic field. Fig. 6.8(c) shows the magnetic field response of the Sisyphus effect, taken at maximum laser intensity and ± 40 MHz detuning for cooling (blue circles) and heating (red squares). We observe a sharp decrease of strength in both cooling and heating at

$|\vec{B}| \approx 0$, when dark state remixing is the least efficient. At higher magnetic fields, Sisyphus effect is again suppressed due to large Zeeman shifts. We also note that the Sisyphus effect cannot be completely eliminated by tuning the magnetic field in the standing wave configuration for two reasons. First, the magnetic field cannot be perfectly cancelled throughout the entire interaction region due to the presence of the Earth’s magnetic field. Second, polarization gradient cooling could occur due to imperfect linear polarizations.

6.3.5 Conclusion of CaD Laser Cooling Experiment

In conclusion, we have demonstrated laser cooling of a fermionic molecule, CaD. The complexity introduced by the larger nuclear spin $I_D = 1$ is comparable to that of other bosonic molecules that have been laser cooled and trapped. This is a key first step towards a MOT of a fermionic molecule, opening the door to a variety of quantum science applications such as the realization of the dipolar Fermi-Hubbard model [211] and topological superfluids [196]. With a fermionic molecule added to the list of directly laser-coolable molecular species, qudit platforms with high-fidelity readout become possible [145]. Due to a small isotope shift between CaD and CaH, we expect the deuterated isotopologue to suffer from similar rates of predissociation for the A and B excited states as CaH [89]. However, the same predissociative nature can be leveraged to engineer dissociation pathways for the generation of ultracold and trapped atomic deuterium [162]. This will enable a novel precision measurement platform with trapped hydrogen and deuterium [208]. Finally, the efficient hydrogenation and deuteration method described in this work can be extended to produce chiral molecular isomers such as the chiral methyl group [212] in order to study parity violation effects predicted to be the source of biomolecular homochirality [213].

6.3.6 Synthesis of CaD₂

We produce CaD₂ samples by following a procedure outlined in Ref. [210] for the production of CaH₂. We build a high pressure, high temperature reactor using readily available components (Fig. 6.9(a)). The body of the reactor is composed of a standard CF 2.75" stainless steel nipple.

The bottom of the nipple is blanked off using a nickel gasket and constitutes the main reaction area wrapped with an electrical heating coil and a thermocouple connected to a temperature controller. The top is a CF to 1/4" VCR adapter and the subsequent connections are all made with standard stainless steel VCR connectors. Such connections are rated for pressures > 5,000 psi and temperatures > 500 °C. However, CF flanges are only rated for pressures below atmospheric pressure and temperatures up to 450 °C.

Once assembled, we stress test the reactor using inert helium gas. We confirm that the system is leak-tight first at atmospheric pressure and 450 °C, then up to 80 psi at room temperature, and finally up to 80 psi at 450 °C. With no leaks appearing at any point during these tests, we deem our reactor safe for operation with deuterium gas. We use calcium pieces of >99% purity from Millipore Sigma (327387-25G) and 99.8% pure deuterium gas from Cambridge Isotope Labs (DLM-408-100).

We charge our reactor with 3 g of Ca metal pieces measuring a few millimeters in size. Powderizing the Ca target is expected to improve reaction yield due to larger surface area but this is avoided since it would require pressing to form a target. The reactor is charged and sealed in an inert nitrogen environment to avoid contamination. Then we gradually heat the sample under vacuum to 450 °C over 2 hours. Care is taken to avoid large thermal gradients in the system that could lead to a formation of leaks. Since Ca melts at 840 °C, this temperature only enhances the rate of deuterating the Ca pieces. We then charge the hot reactor instantly with D₂ gas to 88 psi. With the D₂ reservoir valved off, the pressure in the reactor starts decreasing immediately, signaling that the reaction is underway. The pressure decreases to 62 psi after 40 min and the rate of change stagnates. This implies that the first phase of the reaction, surface deuteration, is complete (Fig. 6.9(b)). The measured reaction rate is $k = 0.11 \text{ min}^{-1}$. We leave the reactor charged and hot overnight, and after 9 hours the pressure decreases to ~50 psi. During this time, D₂ molecules diffuse through the Ca surface and penetrate into the bulk.

Once the system has cooled down to room temperature, we open the reactor in a nitrogen environment. Since the temperature is not high enough to melt calcium, the pieces do not change

their shape or size. However, they turn from a dark silvery gray to a light powdery gray. We perform a powder X-ray diffraction (PXRD) analysis of the sample and find that it predominantly consists of CaD₂ (Fig. 6.9(c)). This confirms our assumption that D₂ molecules can easily diffuse through the metal surface and cause deuteration in the bulk of the Ca pieces with high efficiency.

6.3.7 Characterization of Molecular Yield

We employ a CBGB source described in detail in Ref. [106]. The steady-state in-cell density of the He buffer gas is given by Eq. (6.15), where f_{He} is the flow rate of the buffer gas and v_{He} is its average thermal velocity at 6 K [68]:

$$n_{\text{He}} = \frac{4f_{\text{He}}}{A_{\text{aperture}}v_{\text{He}}}. \quad (6.15)$$

For the measurements taken in this work a buffer gas flow rate of ~20 standard cubic centimeters per minute (sccm) is used, giving a steady-state buffer gas density of $1.4 \times 10^{16} \text{ cm}^{-3}$, similar to other buffer gas experiments. Although the higher He flow rate leads to higher beam velocities, we obtain a higher molecular yield and signal-to-noise ratio (SNR). Interestingly, we measure a $\sim 5\times$ higher CaD yield both inside the buffer gas cell and also in the extracted beam compared to CaH measured under identical conditions.

This difference in production of the two isotopologues can give insight into the dynamics of our CBGB source, allowing for further improvements in molecule production and molecular beam flux. Differences in thermalization resulting from different collisional cross sections is one possible explanation for our observations. As the hot molecules diffuse away from the target, they collide with the cold buffer gas. The rate of these collisions affects the time it takes the molecules to diffuse through the cell. Assuming the molecular species instantly freezes (or is "lost") once it reaches the cell walls, and the molecules are much lower density than the buffer gas, the decay in absorption is a good representation of the time it takes for the molecules to diffuse out. This characteristic time τ can be found by fitting a simple exponential to the tails of absorption traces.

Transition	Vibrational Quanta (ν'')	CaH VBR Measured ($q_{0\nu''}$)	CaH VBR Calculated ($q_{0\nu''}$)	CaD VBR Calculated ($q_{0\nu''}$)
$A \rightarrow X$	0	0.9680(29)	0.9820	0.9758
	1	0.0296(24)	0.0175	0.0235
	2	$2.4(1.8) \times 10^{-3}$	4.61×10^{-4}	7.18×10^{-4}
	3	-	2.0×10^{-5}	3.2×10^{-5}
$B \rightarrow X$	0	0.9853(11)	0.9790	0.9688
	1	0.0135(11)	0.0202	0.0295
	2	$1.2(0.2) \times 10^{-3}$	7.5×10^{-4}	1.5×10^{-3}
	3	-	6.7×10^{-5}	1.5×10^{-4}

Table 6.4: Measured CaH VBRs [106] and calculated CaH and CaD VBRs [203]. The calculated VBRs for CaH are in good agreement with our own calculations [89]. Table adopted from Ref. [88].

Then, using the method employed in Ref. [68], the collisional cross section can be calculated via the expression

$$\sigma_{\text{He-m}} = \tau \frac{9\pi v_{\text{He}}}{16A_{\text{cell}} n_{\text{He}}}, \quad (6.16)$$

where A_{cell} is the cross-sectional area of the cell, n_{He} is the steady-state density from Eq. (6.15), and v_{He} is the thermal velocity of the buffer gas. We find the cross sections to be $\sigma_{\text{He-CaH}} = 2.0(8) \times 10^{-14} \text{ cm}^2$ and $\sigma_{\text{He-CaD}} = 3.0(3) \times 10^{-14} \text{ cm}^2$. These calculated cross sections are consistent with previous work [214]. However, given the large errors of these values and their relative closeness, we cannot definitively attribute the difference in the production between the two species to He thermalization. We also cannot rule out other factors such as crystalline chemistry of the substrates.

6.3.8 Vibrational Branching Ratios

The VBRs for CaD calculated from Ref. [203] are shown in Table 6.4. We also show the calculated CaH VBRs and find a small isotope shift between CaH and CaD. We make the assumption that the VBRs for CaD are approximately the same as those for CaH.

6.3.9 Laser Configuration

The frequencies of the lasers used in this work are presented in Table 6.5. The spectroscopy of the $A^2\Pi_{1/2}(\nu' = 0, J' = 1/2, +) \leftarrow X^2\Sigma^+(\nu'' = 0, N'' = 1, -)$ main cycling transition is done in a quasi-rotationally-closed configuration. We scan the frequency of one spin-rotation component while holding the other on resonance. This provides higher SNR because of the enhancement in LIF due to optical cycling. With the hyperfine levels unresolved (Fig. 6.6(c)), we fit the spectra to Gaussians with fixed spacing and relative amplitude, according to the hyperfine splittings obtained from Ref. [201] and state degeneracies. However, there are no previously measured hyperfine splittings for the $X^2\Sigma^+(\nu'' = 1, N'' = 1, -)$ state. We instead fit the ($\nu = 1$) repump transition with a single Gaussian for each spin-rotation component. All the frequencies are measured using a HighFinesse WS7-60 wavemeter, which is calibrated using the ${}^1S_0 \rightarrow {}^3P_1$ transition in Sr.

Ground	ν''	N''	J''	F''	Excited	ν'	N'	J'	Frequency (THz)
X	0	1	3/2	5/2	A	0	-	1/2	431.140421
				3/2					431.140441
				1/2					431.140453
				3/2					431.141437
				1/2					431.141425
	1	1	3/2	5/2, 3/2, 1/2	A	0	-	1/2	403.852444
			1/2	3/2, 1/2					403.853423

Table 6.5: CaD transition frequencies used in this work. The uncertainties are ~ 10 MHz statistical and ~ 60 MHz systematic from the wavemeter. Table adopted from Ref. [88].

In order to generate the sidebands for the ground-state spin-rotation and hyperfine splittings of the main cycling transition, we use two EOMs operating at 980 MHz and 11 MHz in series. Specifically, we use the -1^{st} and 0^{th} order of the 980 MHz EOM for the $J = 3/2$ and $J = 1/2$ spin-rotation components, respectively, and the 0^{th} , $\pm 1^{\text{st}}$, $\pm 2^{\text{nd}}$ orders of the 11 MHz EOM for the hyperfine levels. We note that the $+1^{\text{st}}$ order of the 980 MHz EOM is unused in the cooling experiment because it is far-off-resonant, resulting in a $\sim 30\%$ decrease in the effective laser intensity. For the ($\nu = 1$) repump, we use a 978 MHz EOM and a high-Q 4.185 MHz EOM. The 4.185 MHz EOM generates an array of sidebands (± 5 orders) to cover the hyperfine levels in the ($\nu = 1$) manifold.

6.3.10 Beam Temperature Estimation

We estimate the transverse temperature of the molecular beam using Monte-Carlo beam propagation. We generate a uniform spatial distribution of 10^5 particles at the location of the aperture with a Boltzmann-distributed forward velocity of 250 m/s with 40 m/s as standard deviation and a transverse velocity v_{\perp} . We vary v_{\perp} and calculate the molecular beam width at the position of the detector. Matching this value to our measured unperturbed beam width ($\sigma \approx 5.4$ mm) gives us an estimate of $T_{\perp} \approx 16(1)$ mK. Next, we perform the same computation but now compare the calculated beam width to the measured width of the central peak of the Sisyphus cooled profile (Fig. 6.7(d)), $\sigma \approx 2.3$ mm. This provides a rough estimate of the Sisyphus-cooled beam temperature of 2.7(2) mK. We note that this temperature estimate is approximate and only serves as an indicator of cooling efficiency.

6.3.11 Doppler Cooling

In addition to sub-Doppler Sisyphus cooling, we also perform 1D Doppler cooling of the CaD molecular beam. The measured Doppler cooling and heating curve as a function of laser detuning is shown in Fig. 6.10. Because of the large capture velocity of the Doppler force, cooling and heating manifest as a change in Gaussian width ($\Delta\sigma$) of the molecular beam. We can switch from a Sisyphus to a Doppler configuration by multipassing the interaction laser and ensuring little overlap between neighboring passes.

6.4 Recent Progress with Laser Slowing CaH

Chemical production of CaH results in a $\sim 5\times$ greater yield and $\sim 20\times$ better stability (signal decay time constant) than the traditional ablation method [83, 30]. These improvements directly lead to a better signal-to-noise ratio (SNR) and make possible the detection of laser slowing. Figure 6.11(a) shows our background-free detection scheme of the CaH beam's forward velocity. The $A \leftarrow X$ laser at 695 nm is applied transversely to the molecular beam, while the $E \leftarrow A$ laser

is applied at 45° with respect to the molecular beam as the velocity-sensitive probe. The decay light from E to X at 490 nm is background-free and can be detected with a photomultiplier tube (PMT). Figure 6.11(b) shows the spectral line of the $E^2\Pi_{1/2}(J' = 3/2, -) \leftarrow A^2\Pi_{1/2}(J = 3/2, +)$ transition used for the detection. The velocity-sensitive detection method combined with a 1-watt 1668 nm laser source (with determining the line, we obtain a VECSEL system from VEXLUM that could deliver a Watt of laser power at 1668 nm) improves the SNR and enables a robust velocity detection of CaH with a reasonable amount of averaging. A sample measurement is shown in Fig. 6.11(c).

We perform white-light (WL) laser slowing on CaH, and successfully slow the molecules below the MOT capture velocity of ~ 10 m/s. Figure 6.12(a) shows the slowing result. By varying the velocity-dependent $E \leftarrow A$ laser frequency, we measure the molecular signal as a function of time with and without slowing light. The subtracted signal shows an accumulation of lower velocities (highlighted red region). The time-integrated signal in Fig. 6.12(b) demonstrates the appearance of molecules at $\sim 0\text{-}10$ m/s velocities with laser slowing.

We estimate up to a few hundred molecules in this lowest velocity range. This number will be further improved with finer adjustments of the slowing parameters and laser spectral properties, slowing time, and additional repump lasers (currently we repump only the $v = 1, 2$ vibrational levels). In parallel, we are implementing several improvements to the SNR, to help accelerate the optimization process. We are also set up to directly probe molecule capture into a 3D MOT, which is the ultimate goal of this part of the effort.

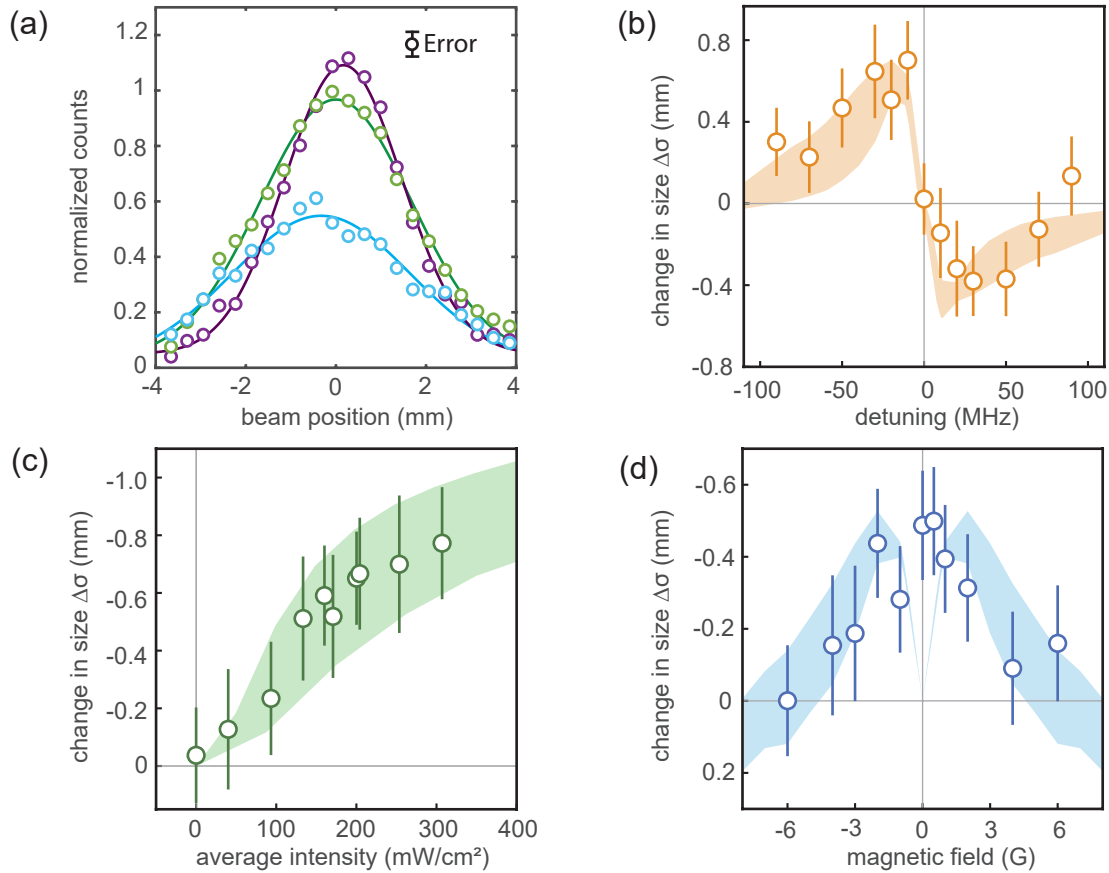


Figure 6.4: Magnetically assisted Sisyphus effect in CaH. (a) Molecular beam profiles obtained for an unperturbed beam (green), Sisyphus cooled beam (purple) at $\delta = +20$ MHz, and Sisyphus heated beam (blue) at $\delta = -20$ MHz. The y-axis is normalized to the unperturbed beam maximum and no other scale factors are used. Lines are fits to a 1D Gaussian function to obtain the $1/e$ cloud radius σ . The increase in on-axis molecule number seen in the cooling configuration is a clear signature of Sisyphus cooling. Statistical error for each point is represented by the bar on top right and is depicted separately for clarity. (b) Change in σ as a function of detuning, where $\Delta\sigma > 0$ implies heating and vice versa. The detuning is applied globally to each spin-rotation and hyperfine addressing lasers. The data was taken at an intensity of 200 mW/cm^2 . The band represents the result of OBE and MC simulations for our experimental system. (c) Change in beam size $\Delta\sigma$ as a function of laser intensity. Detuning has been fixed at $\delta = +20$ MHz. We do not saturate the Sisyphus cooling effect even at the largest available laser intensity ($\sim 300 \text{ mW/cm}^2$). The simulations shown as a band suggest that an intensity of $>600 \text{ mW/cm}^2$ is required for saturation. (d) Change in beam size $\Delta\sigma$ as a function of magnetic field strength. Detuning is $\delta = +20$ MHz and intensity is 200 mW/cm^2 . Maximum cooling is seen for $B \approx 1 \text{ G}$. Note that the scattering rate is maximized at $B \approx 3 \text{ G}$. The Sisyphus effect is expected to be nulled at $B = 0$, but due to the presence of the Earth's magnetic field and the low laser intensity we do not resolve the dip. The simulation shows the same behavior. The bands shown in simulations encompass the spatial variation in laser intensity we expect in the experiment. Each point is a result of 200 repetitions of the experiment, and the experimental error bars are standard errors of Gaussian fitting. Figure adopted from Ref. [30].

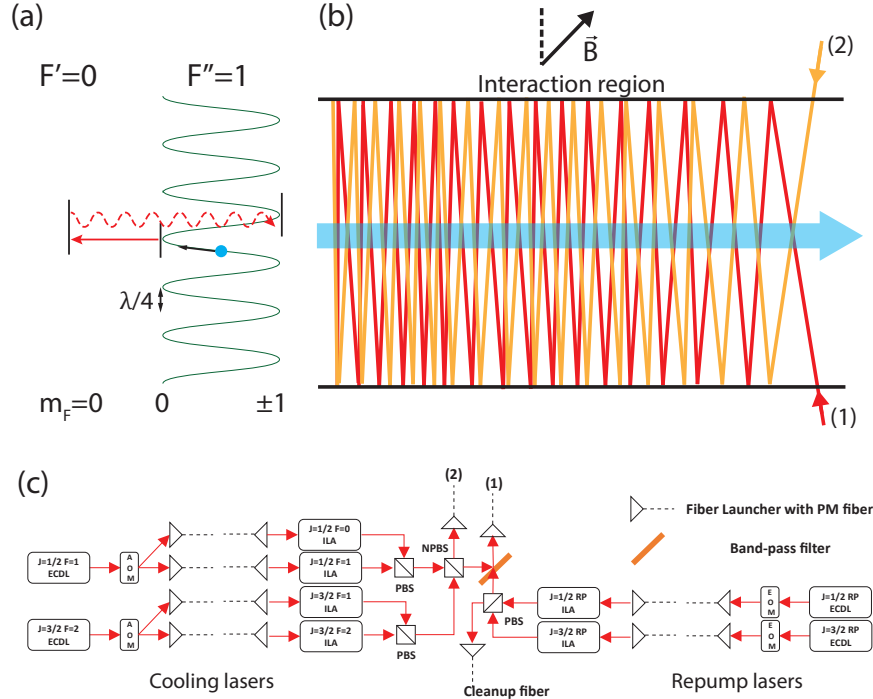


Figure 6.5: Laser configuration for Sisyphus cooling. (a) schematic of the Sisyphus cooling process in the $F' = 0 \leftarrow F'' = 1$ configuration. The standing wave formed by the overlap of the blue detuned, linearly polarized laser beam leads to a Stark-shifted potential hill. As a molecule (blue sphere) travels up this potential hill, it loses energy and is optically pumped to the excited state at the top of the hill. The spontaneous decay brings the molecule back to the dark ground state. Precession around an external magnetic field (\vec{B}) mixes the ground sublevels and brings the molecule back into the bright state to continue the process. (b) schematic of the interaction region. Blue arrow denotes molecular beam direction. Two separate laser beams are used to form independent standing waves. The first laser beam (1) containing both $A \leftarrow X(v'' = 0)$ and $B \leftarrow X(v'' = 1)$ frequencies enters the interaction region near the end and is retroreflected such that the spacing between adjacent passes gradually decreases. After 16 passes, the adjacent passes have sufficient overlap to form a standing wave. The second laser beam (2) only addresses $A \leftarrow X(v'' = 0)$ and can be added to obtain higher average intensities. (c) arrangement of ECDLs and ILAs used to generate the cooling and repump light and their combination. Some components such as mirrors and waveplates are omitted for simplicity. Note that the method of combination leads to an equal split of the cooling light into two fibers (1) and (2). Figure adopted from Ref. [30].

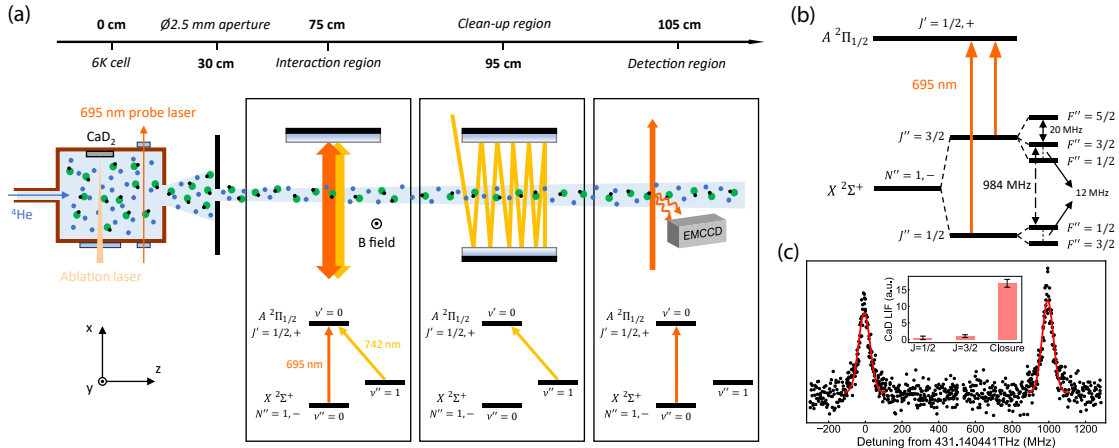


Figure 6.6: (a) Schematic of the experiment viewed from above. CaD molecules are generated in a $\sim 6 \text{ K}$ CBGB source. The molecular beam is collimated by a 2.5-mm diameter aperture and enters the interaction region where it is addressed by the main cooling laser, copropagating with the ($v = 1$) repump laser. The laser beam is expanded to $(10.8 \text{ mm} \times 5.4 \text{ mm}) 1/e^2$ diameter and retro-reflected to form a standing wave. The molecules then enter the clean-up region where only the ($v = 1$) repump laser is applied in a multipass configuration and are finally detected in the ($v = 0$) state. (b) Level structure of the main cycling transition $A^2\Pi_{1/2}(\nu' = 0, J' = 1/2, +) \leftarrow X^2\Sigma^+(\nu'' = 0, N'' = 1, -)$. The hyperfine splittings are adapted from Ref. [201]. (c) In-beam spectroscopy of the transition. The inset shows signal enhancement with rotational closure. Figure adopted from Ref. [88].

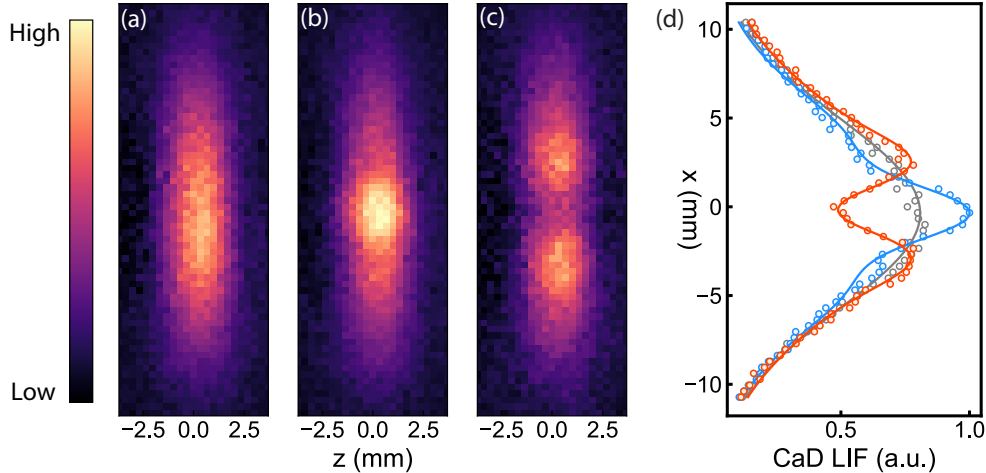


Figure 6.7: Molecular beam profile with Sisyphus cooling and heating. (a-c) Beam images under unperturbed, Sisyphus cooling at $+40 \text{ MHz}$, and Sisyphus heating at -40 MHz configurations, respectively. (d) Integrated 1D profile. Sisyphus cooling narrows the width of the center of the molecular beam (blue), while Sisyphus heating expels molecules away from the center (red). Unperturbed beam is shown as gray. Solid lines show the fits to the beam profile. Figure adopted from Ref. [88].

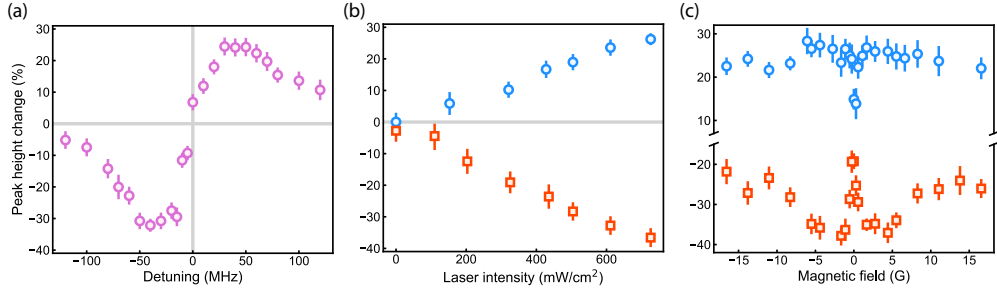


Figure 6.8: Parameter scans of the Sisyphus effect. (a) Peak height change as a function of the main laser detuning, taken with magnetic field $|\vec{B}| = 1.7$ G and at 45° with respect to laser polarization. (b) Sisyphus cooling (blue circles) and heating (red squares) as a function of the main laser intensity, taken at ± 40 MHz detuning and the same magnetic field configuration as in (a). Saturation is not observed. The gray lines are guides to the eye for the unperturbed scenario (horizontal) and zero detuning (vertical in (a)). (c) Sisyphus cooling (blue circles) and heating (red squares) as a function of applied magnetic field, taken at ± 40 MHz detuning and maximum laser intensity. A sharp decrease in the strength of Sisyphus effect is observed when $|\vec{B}| \approx 0$. Error bars represent the 95% confidence intervals. Figure adopted from Ref. [88].

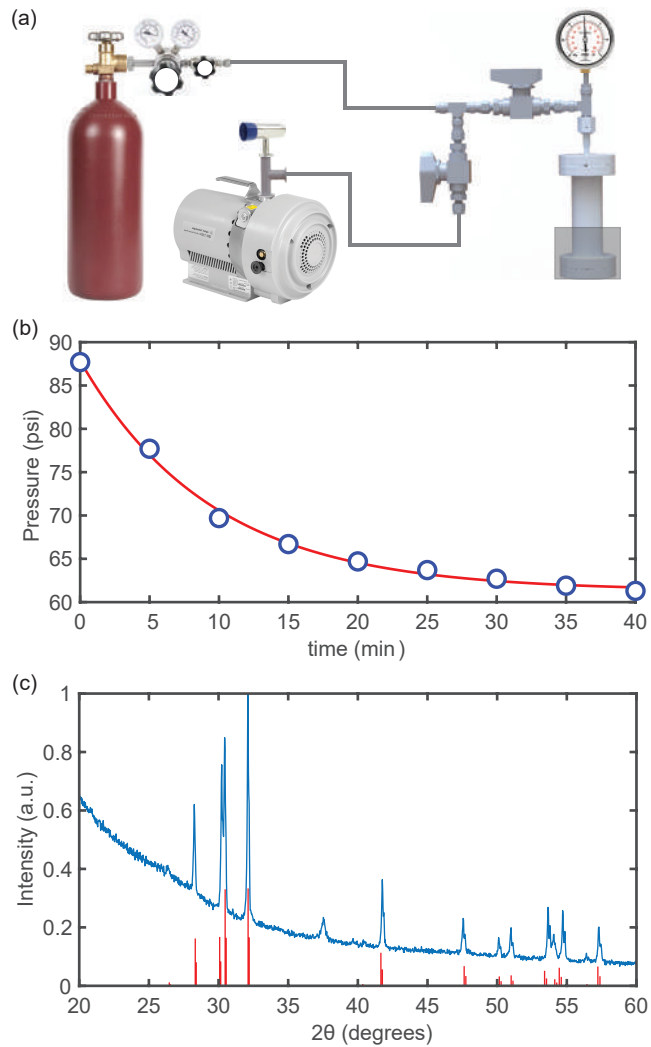


Figure 6.9: Synthesis of CaD_2 . (a) Illustration of the home-built setup used for the synthesis. The main reactor is a standard CF 2.75", 5" long 304 stainless steel nipple. The base is wrapped with heating tape connected to a variac via a temperature controller (Extech 48VFL). A standard J-type thermocouple attached to the base is used for temperature stabilization. A high-pressure gauge (MG1-100-A-9V-R) is placed close to the top of the reactor. All connections henceforth are VCR type. The reactor connects to a scroll pump and a Convectron gauge (MKS 275) via a tee. The other end of the tee connects to a D_2 cylinder using a long flexible hose. The regulator on the cylinder allows for control of the charging pressure, while the valves shown are used to direct the flow. (b) Pressure measured on the high-pressure gauge as a function of time at 450°C . The reactor contains 3 g of Ca pieces. From an exponential fit, we obtain a reaction rate of $k = 0.11 \text{ min}^{-1}$. (c) Powder X-ray diffraction study of the resulting sample. Red lines are the known CaD_2 peaks. Almost all measured peaks match with the known CaD_2 values except for the peak at $2\theta = 37^\circ$. This peak could be attributed to CaO or $\text{Ca}(\text{OH})_2$, possibly resulting from short contact with air. The results suggest very high conversion efficiency from Ca to CaD_2 . Figure adopted from Ref. [88].

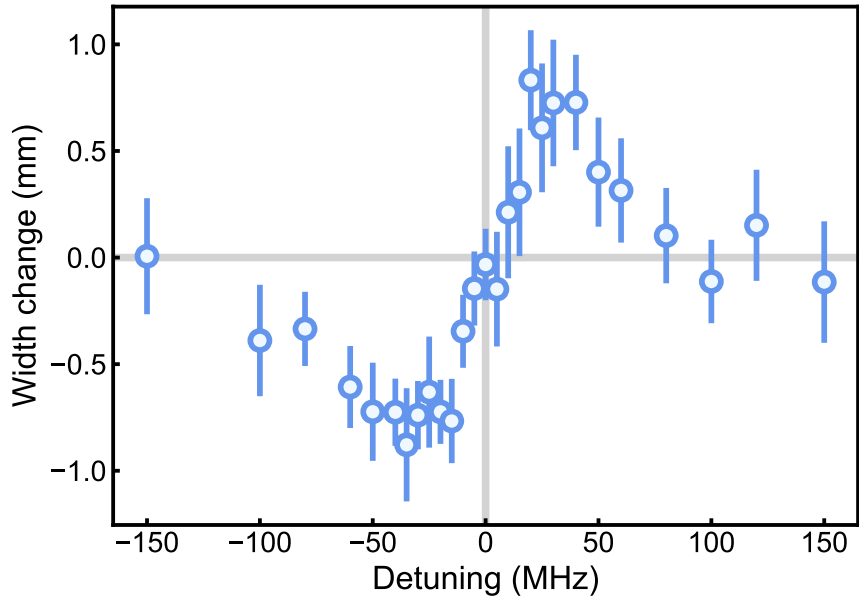


Figure 6.10: Doppler cooling and heating as a function of laser detuning. A change in the molecular beam width demonstrate Doppler cooling (negative) and heating (positive). Error bars represent the 95% confidence intervals. Figure adopted from Ref. [88].

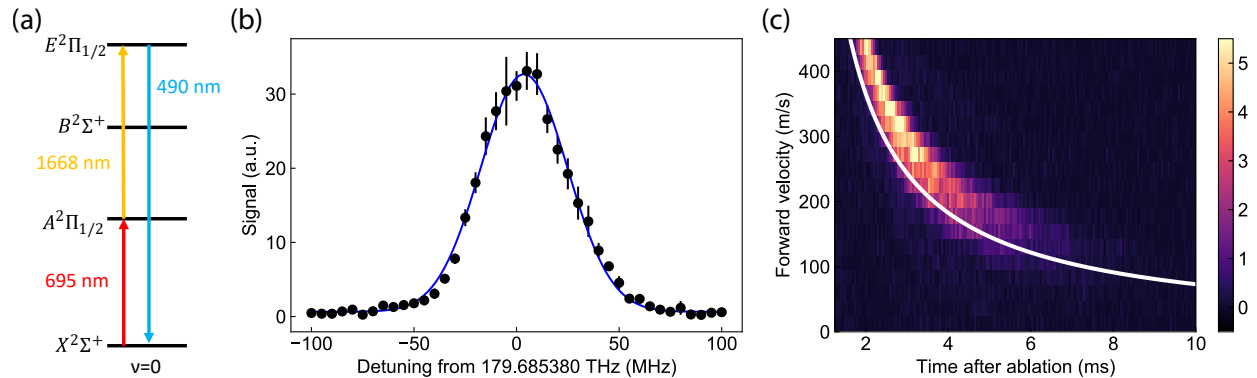


Figure 6.11: Two-photon background-free velocity detection of CaH. (a) Relevant level structure. CaH molecules are excited on the $A \leftarrow X$ transition at 695 nm and subsequently the $E \leftarrow A$ transition at 1668 nm. The photons emitted from E to X thus provide background-free detection at 490 nm. (b) Background-free spectroscopy of the $E^2\Pi_{1/2}(J' = 3/2, -) \leftarrow A^2\Pi_{1/2}(J = 3/2, +)$ transition. (c) Sample CaH velocity measurement. The $A \leftarrow X$ is applied transversely while the $E \leftarrow A$ laser is applied 45° relative to the molecular beam as a velocity sensitive probe. A PMT collects the 490 nm photons with temporal information. The white line marks the earliest possible arrival time for each velocity class.

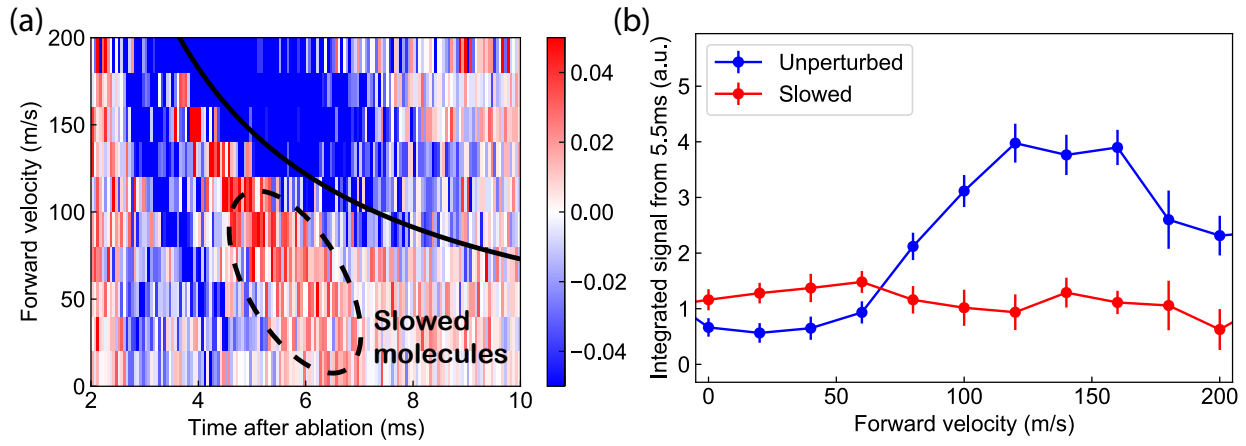


Figure 6.12: White-light slowing of CaH molecules. (a) PMT signal of slowed molecules subtracted from unperturbed molecules at various velocities. An accumulation of lower-velocity molecules (highlighted red region) appears with slowing. (b) Time-integrated signal as a function of molecular velocity. Excess molecules below a typical MOT capture velocity (~ 10 m/s) are observed.

Chapter 7: Optical Bloch Equation (OBE) Solver

7.1 Why Solve OBE

While experiments demonstrate the ability to laser cool molecules, it is equally important to develop a theoretical understanding and compare it with measurements. This is typically done by solving the time evolution of the density matrix, which captures quantum state dynamics, and coupling it with molecular beam simulations. In this section, I focus on the first part: solving optical Bloch equations (OBE). This chapter outlines the basic theoretical framework, illustrates it with simple toy models, extends it to CaH, and briefly introduces how these results are connected to Monte Carlo (MC) simulations of molecular beams.

A few key terms are introduced here to assist readers unfamiliar with this topic. The Hamiltonian describes energy in the system: internal energy of the molecule and its interaction with external fields, such as light. The quantum states are usually chosen as eigenstates of the internal (unperturbed) Hamiltonian. The density matrix is an $n \times n$ matrix, where n is the number of states in the model. Diagonal terms represent population in a given state, and off-diagonal terms represent quantum coherence (superpositions) between states. For example, to calculate the optical force on a molecule from a resonant laser, one can extract the population in the excited state (from relevant diagonal terms of the density matrix) and multiply it by the spontaneous decay rate.

7.2 OBE Theory

The Liouville–von Neumann equation in Lindblad form describes the time evolution of the density matrix. We start from its basic form and explain the reasoning behind each term.

7.2.1 Liouville–von Neumann Master Equation

The Liouville equation for a closed quantum system can be derived from the Schrödinger equation. For a pure state $|\Psi(t)\rangle$ evolving under a time-dependent Hamiltonian $H(t)$, the time evolution is given by a unitary operator $U(t, t_i)$ such that:

$$|\Psi(t)\rangle = U(t, t_i)|\Psi(t_i)\rangle,$$

where U satisfies the equation:

$$i \frac{dU(t, t_i)}{dt} = H(t)U(t, t_i).$$

An ensemble of states is described using the density matrix:

$$\rho(t) = \sum_k c_k |\Psi_k(t)\rangle \langle \Psi_k(t)|,$$

and its time evolution becomes:

$$\rho(t) = U(t, t_i)\rho(t_i)U^\dagger(t, t_i).$$

Taking a time derivative yields the Liouville–von Neumann equation:

$$\frac{d\rho(t)}{dt} = -i[H(t), \rho(t)]. \quad (7.1)$$

To include dissipation and decoherence, we generalize this equation into the Lindblad master equation:

$$\frac{d\rho(t)}{dt} = \mathcal{L}\rho = -i[H, \rho] + \sum_{i=1}^{N^2-1} \gamma_i \left(G_i \rho G_i^\dagger - \frac{1}{2} \{G_i^\dagger G_i, \rho\} \right), \quad (7.2)$$

where G_i are quantum jump operators that describe dissipative processes such as spontaneous emission, and γ_i are the corresponding rates.

The key difference between the unitary Liouville equation (7.1) and the full master equation

(7.2) lies in the second term, the so-called dissipator. This term captures the effects of system-environment interactions that are not included in the Hamiltonian.

7.2.2 Dissipator

The dissipator accounts for non-unitary effects in the system and typically consists of two main components. One includes all dephasing processes, such as collisional broadening and laser linewidth. In typical molecular beam or MOT conditions, these effects are small and often neglected. The second and more important component is spontaneous emission, which we now examine in detail.

The quantum jump operator for spontaneous decay from state $|i\rangle$ to state $|j\rangle$ is given by

$$G_{ij} = \sqrt{\Gamma_{ij}} |j\rangle\langle i|,$$

where Γ_{ij} is the decay rate from $|i\rangle$ to $|j\rangle$. Plugging this into Eq. 7.2 and summing over all decay channels gives a complete description of spontaneous decay. In most practical cases, we set $\gamma_i = 1$ and directly use the physical decay rates Γ_{ij} .

To illustrate this, consider a toy model system with three ground states and one excited state, often referred to as a 3 + 1 system. This simple model captures essential features of more complex systems like CaH (which involves 12+4 states). Label the ground states as $|1\rangle, |2\rangle, |3\rangle$ and the excited state as $|4\rangle$. Suppose $|4\rangle$ decays to each ground state with equal probability, i.e., each decay channel has rate $\Gamma/3$.

Then the jump operators are

$$G_{4j} = \sqrt{\frac{1}{3}\Gamma} |j\rangle\langle 4|, \quad \text{for } j = 1, 2, 3.$$

Substituting these into the Lindblad master equation, the resulting dissipator matrix \mathcal{D} be-

comes:

$$\mathcal{D} = \begin{bmatrix} \frac{1}{3}\Gamma\rho_{44}(t) & 0 & 0 & -\frac{1}{2}\Gamma\rho_{14}(t) \\ 0 & \frac{1}{3}\Gamma\rho_{44}(t) & 0 & -\frac{1}{2}\Gamma\rho_{24}(t) \\ 0 & 0 & \frac{1}{3}\Gamma\rho_{44}(t) & -\frac{1}{2}\Gamma\rho_{34}(t) \\ -\frac{1}{2}\Gamma\rho_{41}(t) & -\frac{1}{2}\Gamma\rho_{42}(t) & -\frac{1}{2}\Gamma\rho_{43}(t) & -\Gamma\rho_{44}(t) \end{bmatrix}$$

The diagonal terms represent population gain into ground states and loss from the excited state.

The off-diagonal terms capture coherence loss between excited and ground states.

7.2.3 Hamiltonian

We now discuss how to construct the Hamiltonian. For molecules, a complete hamiltonian should include the kinetic energy, intramolecular interaction, intermolecular interaction and interaction between particle and environment electromagnetic field. All of these contributions must be considered when constructing the Hamiltonian.

1. To simplify things, we use the eigenstates of kinetic energy plus intramolecular interaction as basis of the density matrix. The energies of those states are therefore well defined, some may be found in Chapter 2 of the thesis in Table 2.2.
2. The intermolecular interaction is weak for CaH due to the relatively low density, so it is not considered here.
3. For the interaction between particle and environment electromagnetic field, one should consider the following situations.
 - A static magnetic field can introduce Zeeman effect. In the low field limit, if the states of study are all M_F states, and we choose the quantization axis to be along the B field direction, the Zeeman effect Hamiltonian is just a diagonal matrix, with the corresponding energy $E_z = g\mu_B B m_F$, where g is Lande g factor, μ_B is Bohr magneton, B is the magnitude of magnetic field, and m_F is the projection of the total angular momentum F to the quantization axis.

- An electromagnetic wave (light or microwave) can introduce electric dipole interaction.

Higher-order interactions are not considered in this discussion. The Hamiltonian typically is written as $H_L = -e\vec{E}(\vec{r}, t) \cdot \vec{r}$. If one uses plane wave traveling in the positive z direction, the electric field operator can be written as $\vec{E}(\vec{r}, t) = E_0\vec{\epsilon}\cos(kz - \omega_l t)$.

This will be discussed in more detail later.

The first term is straightforward and will be demonstrated in a later example. The second term will be neglected. The Zeeman term is also trivial if one uses the B field as the quantization axis (The choice of quantization axis is based on personal preference; here, it is chosen to aid clarity of understanding). The electric dipole interaction term is non-trivial and we should discuss more about it.

7.2.4 Rabi Rate

Rabi rate comes from Rabi cycling, it describes the strength of dipole interaction. Knowing Rabi rate can lead us to the right way of writing the interaction Hamiltonian. As we said the Hamiltonian is $H = -e\vec{E} \cdot \vec{r}$, in the matrix form it is $H_{if} = \langle f | -e\vec{E} \cdot \vec{r} | i \rangle = -\hbar\Omega_R$. The Rabi rate for a transition from state $|i\rangle$ to $|f\rangle$ is defined as:

$$\Omega_R = \frac{eE}{\hbar} \langle f | \vec{\epsilon} \cdot \vec{r} | i \rangle$$

where $\vec{\epsilon}$ is the light polarization vector, E is the electric field amplitude, $e \cdot \vec{r}$ is the transition dipole moment, usually written as \mathbf{d} .

Spherical Basis

To solve for $\langle f | \vec{\epsilon} \cdot \vec{r} | i \rangle$ in 3D space in a way that is consistent with all the quantum numbers of the states, it is important to use the spherical basis as it closely relates to the description of angular momentum in quantum mechanics. The conversion from Cartesian basis to spherical basis is as follows:

$$\mathbf{e}_{+1} = -\frac{1}{\sqrt{2}}\mathbf{e}_x - \frac{i}{\sqrt{2}}\mathbf{e}_y$$

$$\mathbf{e}_{-1} = +\frac{1}{\sqrt{2}}\mathbf{e}_x - \frac{i}{\sqrt{2}}\mathbf{e}_y$$

$$\mathbf{e} = \mathbf{e}_z$$

So if we know the mathematical form of the electric field in Cartesian basis, we can project it into spherical basis with the corresponding amplitude E_p , where $p = 0, -1, +1$ representing the index. We also use a rank 1 spherical tensor $T_p^1(\mathbf{d})$ to represent the cross product, so the Rabi rate can be written as:

$$\Omega_R = \sum_{p=0,-1,+1} (-1)^p \frac{E_{-p}}{\hbar} \langle f | T_p^1(\mathbf{d}) | i \rangle = \mathcal{A} \cdot \mathcal{R} \cdot E$$

From the basic hydrogen model in quantum mechanics, we can guess that $\langle f | T_p^1(\mathbf{d}) | i \rangle$ can be separated into two components: a radial part and an angular part: an angular part and a radial part. The angular part (\mathcal{A}) can be calculated by knowing the quantum numbers of the $|i\rangle$ and $|f\rangle$ states. For molecules, the detailed calculation involves evaluating Wigner 3-j, 6-j, and 9-j symbols, we will not prioritize the calculation here, one can find the packages to calculate them¹. While the radial part (or called electronic part, \mathcal{R}) is determined by the wavefunction overlap, and can be evaluated from other properties of the molecules. Here we can use transition-dipole-moment results from well-established theoretical modeling of the molecules of interest, For example, there are many useful resources related to CaH [215, 216, 217]

Radial Part

Although useful references exist, we can approximate the radial components by another method: experimentally measured decay rate. Because Fermi's golden rule tells us that the decay rate from state $|i\rangle$ to state $|f\rangle$ is:

¹https://github.com/QiSun97/Rabi_Matrix_Elements_Calculator

$$\Gamma_{i \rightarrow f} = \frac{\omega_{if}^3}{3\pi\epsilon_0\hbar c^3} |\langle f | \mathbf{d} | i \rangle|^2 \quad (7.3)$$

We typically can learn the lifetime of certain excited state (for example, the $A\Pi v = 0$ state has a lifetime of 33ns, $B\Sigma v = 0$ state is 56ns), which can be converted into decay rate ($1/\tau$). Therefore, we can sum over the ground states in Eq. 7.3. And a property of the angular components is their squared summation equals 1. This leads to the final expression for the radial part \mathcal{R} :

$$\mathcal{R}^2 = |\langle e | \mathbf{r} | g \rangle|^2 = \frac{3\pi\epsilon\hbar c^3}{e^2\omega^3} \Gamma$$

It should be noted that this equation is not complete because molecules have much more complex internal structures, but in our case it's close to what is predicted by Ref [215]. For CaH, the $A \leftarrow X$ transition has a radial component of $2.24a_0$ (a_0 is the Bohr radius).

Electric Field Strength

We are now close to completing the Hamiltonian construction. The electric field projection to the spherical basis is the only thing left to be calculated. We should first try to write it in the Cartesian basis. There are two cases that are interesting to us.

1. B field is in Z direction (the quantization axis). The light is traveling in X direction. And the linear laser polarization is in the Y-Z plane, having an angle of θ with respect to Z axis. Assume the field strength is E_0 , so the field can written as:

$$\begin{aligned} \vec{E} &= (\cos \theta \vec{z} + \sin \theta \vec{y}) E_0 e^{-i\omega t} \\ &= (\cos \theta \vec{e}_0 - \frac{i}{\sqrt{2}} \sin \theta \vec{e}_{+1} - \frac{i}{\sqrt{2}} \sin \theta \vec{e}_{-1}) E_0 e^{-i\omega t} \end{aligned} \quad (7.4)$$

Without further terms, this interaction Hamiltonian has a rotation symmetry (around Z axis), which means laser can propagate at any direction in the X-Y plane, as long as we keep θ unchanged, then the OBE state population evolution should be the same even though the

Hamiltonian looks different after projection to spherical basis. This can serve as a good sanity check of the system, and user's understanding to writing the hamiltonian. Another way to put it is, the physics is unchanged no matter how we define the basis, which can be used as sanity checks.

2. In the case of two counter-propagating beams that can form a standing wave (used to calculate type II system Sisyphus cooling and MOTing experiment), assume B field is in Z direction, both laser travels along X direction. They have the same polarization direction, which is in the Y-Z plane, having an angle θ with respect to Z axis. The laser field can be written as:

$$\begin{aligned}\vec{E} &= (\cos \theta \vec{z} + \sin \theta \vec{y}) 2E_0 \cos kx \\ &= (\cos \theta \vec{e}_0 - \frac{i}{\sqrt{2}} \sin \theta \vec{e}_{+1} - \frac{i}{\sqrt{2}} \sin \theta \vec{e}_{-1}) 2E_0 \cos kx\end{aligned}\tag{7.5}$$

The time dependence is eliminated with formation of standing wave. Same as case 1, this system also has rotation symmetry around Z axis.

And to acquire E_0 from experimental values, which is intensity I (or power P with beam diameter d). The electric field strength at given experimental parameters can be calculated by

$$E_0 = \sqrt{\frac{2I}{c\epsilon_0}} = \sqrt{\frac{8P}{\pi c \epsilon_0 d^2}}.$$

7.2.5 Unitary Transformation

When introducing high frequency EM wave (laser, typically $\approx 500\text{THz}$) into the Hamiltonian, if we do it without further modification, the minimum time step for calculation becomes too short (<1fs) and it consumes computation efficiency. We can remove this high frequency components by applying a unitary transformation to the quantities. This is also called "rotating frame transformation", or "dressed state picture" in atomic physics classes.

7.2.6 Example: 3+1 System

With the "3+1" system example provided in Dissipator section 7.2.2, we can add more constraints to the system to be more specific. We define the ground states as $F'' = 1$, and excited state as $F' = 0$ system, and assume the radial part is $\mathcal{R} = a_0$ for simplicity. There is only one laser to address all transitions from ground states to excited state, and it has a linear polarization.

We should proceed as follows:

1. Define the basis - the four states used to write the density matrix and Hamiltonian *et. al..*

For example, $|\psi_0\rangle, |\psi_1\rangle, |\psi_2\rangle, |\psi_3\rangle = |1, -1\rangle, |1, 0\rangle, |1, +1\rangle, |0, 0\rangle$ (first number is F , second number is m_F)

2. Write down Hamiltonian.

(a) Assign eigenstate energies. Don't forget the Zeeman term, it's simplest to use B field as quantization axis. Now the hamiltonian looks like

$$\begin{bmatrix} -B \cdot g + E_0 & 0 & 0 & 0 \\ 0 & E_0 & 0 & 0 \\ 0 & 0 & B \cdot g + E_0 & 0 \\ 0 & 0 & 0 & E_e \end{bmatrix}$$

(b) Then add light-atom interaction into the picture. The transition strength between the excited state and different ground states in spherical basis (e_0, e_{+1}, e_{-1}) can be acquired from the code online or from Metcalf book². The Rabi rates for each possible transitions is decorated by a pre-factor, which is based on the polarization of the laser as discussed previously. We use the symbol Ω to represent the overall Rabi rate. Then the

²Laser cooling and trapping, Harold J. Metcalf. Appendix D.

Hamiltonian now will become:

$$\begin{bmatrix} -B \cdot g + E_0 & 0 & 0 & -\frac{1}{6\sqrt{2}}\Omega e^{i\omega t} \sin \theta \\ 0 & E_0 & 0 & \frac{1}{6}\Omega e^{i\omega t} \cos \theta \\ 0 & 0 & B \cdot g + E_0 & \frac{1}{6\sqrt{2}}\Omega e^{i\omega t} \sin \theta \\ -\frac{1}{6\sqrt{2}}\Omega e^{-i\omega t} \sin \theta & \frac{1}{6}\Omega e^{-i\omega t} \cos \theta & \frac{1}{6\sqrt{2}}\Omega e^{-i\omega t} \sin \theta & E_e \end{bmatrix}$$

Till this step, the hamiltonian in the normal basis is done.

3. Perform unitary transformation to the hamiltonian to eliminate the high frequency components and go to the dressed state picture. One thing to notice is, this step does not change the meaning the diagonal terms in the density matrix, which is the state population. The off-diagonal terms will mean differently. But it's critical to remember, unitary transformation is just a transformation, the physics is the same. Eventually the transformed hamiltonian will look like this:

$$\begin{bmatrix} -B \cdot g & 0 & 0 & -\frac{1}{6\sqrt{2}}\Omega \sin \theta \\ 0 & 0 & 0 & \frac{1}{6}\Omega \cos \theta \\ 0 & 0 & B \cdot g & \frac{1}{6\sqrt{2}}\Omega \sin \theta \\ -\frac{1}{6\sqrt{2}}\Omega \sin \theta & \frac{1}{6}\Omega \cos \theta & \frac{1}{6\sqrt{2}}\Omega \sin \theta & \Delta \end{bmatrix}$$

where Δ is the laser detuning with respect to the transition frequency. Note that the Hamiltonian can be always written in frequency unit, such as GHz or $2\pi \cdot GHz$

4. Write down the Dissipator. Since the only dissipation term we want to introduce to our system is spontaneous decay, all we need to know is the branching ratios, and it can be calculated from the Rabi matrix. As discussed before, we can write down the dissipator as following (Γ is the transition linewidth):

$$\begin{bmatrix} \frac{1}{3}\Gamma\rho_{33}(t) & 0 & 0 & -\frac{1}{2}\Gamma\rho_{03}(t) \\ 0 & \frac{1}{3}\Gamma\rho_{33}(t) & 0 & -\frac{1}{2}\Gamma\rho_{13}(t) \\ 0 & 0 & \frac{1}{3}\Gamma\rho_{33}(t) & -\frac{1}{2}\Gamma\rho_{23}(t) \\ -\frac{1}{2}\Gamma\rho_{30}(t) & -\frac{1}{2}\Gamma\rho_{31}(t) & -\frac{1}{2}\Gamma\rho_{32}(t) & -\Gamma\rho_{33}(t) \end{bmatrix}$$

5. Assemble the Bloch Equations from Hamiltonian and Dissipator. In this case, one can acquire 16 equations (4×4) to solve for.
6. Assign numerical values to the symbols, and evolve it with finite range of time. For Rabi rate Ω , it can be written as:

$$\Omega = \mathcal{R} \cdot E = a_0 \sqrt{\frac{2I}{c\epsilon_0}}$$

One may ask why there is only the radial part. The answer is the angular components are already implemented in the Hamiltonian.

7. Special care needs to be taken with units. People might have different preferences with natural units or atomic units. I highly recommend a thorough / complete use of SI units for the eventual calculations to avoid any ambiguity. For instant, I started with using $2\pi MHz$ as time units, but I found it extremely easy to forget correcting for some constants. Eventually I decided to switch everything to SI units, and it became much cleaner.
8. Choice of programming language. It is actually a non-trivial question about what programming language to use for the OBE solver. If you wanna start fresh, there is no doubt that you will benefit a lot from writing it with the language you are good at. But I would strongly recommend using *Julia*³. It supports symbolic language, it can run in parallel, and it is super fast at solving ordinary differential equations. With similar amount of coding, it is almost 300-1000 times faster than Matlab when calculating the same system and evolving for same length of time. As I checked the time cost, in my Matlab code a significant amount of time is used when replacing actual values to symbolic values using its symbolic toolbox. So one

³<https://julialang.org/>

can argue Matlab can be faster. But there is no doubt that Julia can still solve the same ODE system faster even without use of symbolic language.

7.3 Dark States in Toy Models

7.3.1 What is a Dark State

To me, the best paper that talks about dark states is Ref. [218] (despite its typo in Table II). For a complete picture, I would guide the interested readers to it. Here I will only talk about my understanding and how it applies to our research.

Naively speaking, a dark state is a pure state that does not allow photon scattering in presence of light. Formally, a dark state originates from a superposition of the ground states, $|d\rangle = \sum_m C_m |m\rangle$. This state will be "dark" if it can satisfy $\langle d|rE|e\rangle = 0$ for every excited state $|e\rangle$ at a given laser field. Mathematically one can use this equation to acquire the expressions of C_m s by projecting the electric field (to spherical basis) and align them. The solutions should then be written to some orthogonal basis.

Regarding how many dark states can exist in a toy model (ground state F'', excited state F', a monochromatic light is present without polarization alternation), it can be understood as follows:

1. when there are more states in excited states than ground states, there is no dark state
2. when the excited state degeneracy is same as ground states ($F' = F''$), there is one dark state
3. when there are more ground states than excited states, there are more than one dark state basis. For example, if $F''=F'+1$, there will be two dark basis.

7.3.2 Examples of Dark States

For a 3+1 system (3 ground states 1 excited state), the dark state basis should be (π pol situation is special and not included in this expression, because the basis will be null):

$$\begin{bmatrix} C_{-1} \\ C_0 \\ C_{+1} \end{bmatrix} = \begin{bmatrix} -E_{-1} \\ 0 \\ E_{+1} \end{bmatrix} \& \begin{bmatrix} E_0 E_{+1} \\ -(E_{-1}^2 + E_{+1}^2) \\ -E_0 E_{-1} \end{bmatrix}$$

Here, C_m is the coefficient of ground state $|m\rangle$ (unnormalized), E_i is the projected light field to spherical basis. Using previous knowledge of the basis, at 0 degree, two dark states will be $| - 1 \rangle$ and $| + 1 \rangle$. at 90 degree, plug in the numbers: $E_{-1} = 1, E_{+1} = -1, E_0 = 0$, so there will be the well-known dark state $|d\rangle = |0\rangle$, and another dark state basis $|d\rangle = | - 1 \rangle + | + 1 \rangle$. One can normalize the coefficients if necessary. Note that it's a bit different from what's written in Ref [218]. I tend to believe it's a typo but one might argue it's equivalent. I would partially agree with it.

For a 3+3 system, the dark state basis should be the following:

$$\begin{bmatrix} C_{-1} \\ C_0 \\ C_{+1} \end{bmatrix} = \begin{bmatrix} E_{-1} \\ -E_0 \\ E_{+1} \end{bmatrix}$$

For a 5+3 system, the basis is written as:

$$\begin{bmatrix} C_{-2} \\ C_{-1} \\ C_0 \\ C_{+1} \\ C_{+2} \end{bmatrix} = \begin{bmatrix} E_{-1}(E_{-1}E_{+1} - 2E_0^2) \\ \sqrt{8}E_{-1}E_0E_{+1} \\ -\sqrt{6}E_{-1}E_{+1}^2 \\ 0 \\ E_{+1}^3 \end{bmatrix} \& \begin{bmatrix} -\sqrt{2}E_0E_{+1}(2E_0^2 + 3E_{-1}^3E_{+1} + E_{-1}E_{+1}^3 - E_0^2E_{+1}^2) \\ E_{-1}E_{+1}(E_{-1}^4 + 6E_{-1}^2E_{+1}^2 + E_{+1}^4) - 2E_0^2(E_{-1}^4 + E_{+1}^4) \\ -\sqrt{3}E_0(-E_{-1}^4E_{+1} + E_{+1}^5 + 2E_{-1}^3(2E_{+1}^2 + E_0^2)) \\ -E_{+1}^2(E_{-1}^4 + 6E_{-1}^2E_{+1}^2 + E_{+1}^4) + 4E_{-1}^2E_0^2E_{+1}^2(E_{-1} - 2E_{+1}) - 4E_{-1}^2E_0^4 \\ \sqrt{2}E_{-1}E_0(E_{+1}^2(E_{-1}^2 - 2E_{-1}E_{+1} + 3E_{+1}^2) + E_0^2E_{+1}(-3E_{-1} + 4E_{+1}) + 2E_0^4) \end{bmatrix}$$

At 0 degree, two darks states will be $| - 2 \rangle$ and $| + 2 \rangle$. At 90 degree, it will be $|d\rangle = | - 2 \rangle - \sqrt{6}|0\rangle + | + 2 \rangle$ and $|d\rangle = | - 1 \rangle + | + 1 \rangle$. At other angles, the readers can plug in the correct numbers and acquire the result using above expressions. The population can evolve to a dark state very fast.

7.3.3 Adding B field to Destabilize Dark States

Why B field Can Destabilize Dark States

When B is non-zero, no matter how small it is, it will always break the degeneracy of the relevant ground states. The reason is as following.

Assume laser field does not change over time. So at time zero, the dark state of a system is still $|d\rangle = \sum_{mi} C_{mi} |mi\rangle$. But actually if you consider time evolution (solution of Schrodinger equations), it should be written as $|d(t)\rangle = \sum_{mi} C_{mi} |mi\rangle e^{-i\omega t} = e^{-i\omega t} \sum_{mi} C_{mi} |mi\rangle$. The prefactor $e^{-i\omega t}$ was neglected because it is a group phase here and it won't change the physical picture. Then, if we apply a B field to the quantization axis (z axis), energies of states will be shifted if g factor is none-zero, such that the dark state is now $|d(t)\rangle = \sum_{mi} C_{mi} |mi\rangle e^{-i\omega_{mi}t} = e^{-i\omega_0 t} \sum_{mi} C_{mi} |mi\rangle e^{-i\delta_{mi}t}$, effectively $|d(t)\rangle = \sum_{mi} C_{mi} |mi\rangle e^{-i\delta_{mi}t}$, where δ_{mi} represents the energy shifts due to magnetic field.

Imagine at $t=0$ the state is in some dark state $|d\rangle$, where the state coefficients $C_{mi} = C0_{mi}$ are calculated using known laser E field. The next moment ($t= \delta_t$), you will notice that you are no longer in dark state, because your state coefficients $C0_{mi} * e^{-i\delta_{mi}\delta_t}$ is not the solution anymore. The actual solution could be $C_{mi} = C0_{mi} * e^{i\delta_{mi}\delta_t}$. That means even if you start with a dark state, you will always precess into a bright state the next moment.

One might understand now, as long as the degeneracy of ground states is broken (either with magnetic field or electric field), dark states are then destabilized, enabling continuous optical cycling. There are also other methods to destabilize dark states, for example, polarization switching (easily achievable through the use of a Pockel's cell), and the expansion of laser linewidth. For detailed calculations, one can read Ref [218].

Extreme Cases with δ_{mi} and Rabi Rates

It can be noticed that if δ_{mi} is too small, the precession will be slow, so that the photon scattering rate will be small, excited state population will be low. If Rabi rate is small, even though you

precess out from a dark state, you won't be able to scatter any photon, so scattering rate is low.

If δ_{mi} is too large instead, Zeeman splitting will be too much such that the photon scattering rate will also drop. If rabi rate is too high compared to B field, that means if you start from a dark state, you will be able to adiabatically follow the evolution of the dark state, such that the population will be trapped in a time-evolving dark state the whole time, and the excited population will cease.

To understand the adiabatically following, one can use this useful picture: rabi rate basically represents the speed of driving a system from a dark state to a bright state. When the Rabi rate is too high, every time the system evolves out from a dark state to a bright state, shortly after that it will be driven back to the nearest dark state. Eventually, your dark state population will be too high to maintain high excited state population. So a match between δ_{mi} and Rabi rate is important to achieve high scattering rate.

Extreme Cases with Angles

Let's consider two cases when the angle between laser polarization and B field is varied.

At 0 degree, there will be no dark state remixing. This can be inferred from previous section (Sec 7.3.2), where we calculated the dark state basis in a given light field at different angle. There we know that, in the system we are interested, at any non-zero degree angle, all dark states will be superposition of some (at least two) ground states (in m_f basis), which means one state can always precess between some (at least two) states. But at zero degree, the dark state basis will be $|m_f = F\rangle$ and $|m_f = -F\rangle$, so they do not have another ground state to connect to, or to precess into.

At 90 degree, for a 3+1 system, there are two dark state basis (when there is no B field), and one of them is $|0\rangle$, which cannot precess out into any other state (even in presence of B field), and will remain dark the whole time as a result. For a 5+3 system, there are two dark states basis, both of them follow our previous logic about dark state destabilization. So at 90degree, there will not be a state that remains dark the whole time for a 5+3 system.

Both cases (0 degree and 90 degree) are, interestingly, observed in CaH system.

1+1 system, 1+3 system, 3+1 system, 3+3 system and 5+3 system are two systems that are particularly interesting in our experiment. The reason is, the ground states of CaH can be viewed as a combination of $F=0$, $F=1$ and $F=2$ states, and excited states as $F=0$ and $F=1$ states. So before we march to the complete picture, it's a good idea to gain insights from these combinations. Some cases are trivial so we won't bother to elaborate here. I'll discuss two cases with dark states: 3+1 model and 5+3 model.

7.4 3+1 Toy Model

As a reminder, 3+1 stands for 3 ground states ($F'=1$) and 1 excited state ($F'=0$). Ground states are degenerate but with different g factors ($g_{-1}, g_0, g_{+1} = -1, 0, +1$). Excited state has spontaneous decay at rate $\Gamma = 1$, evenly to all three states. Transition matrix (angular part) at different spherical basis can be calculated using packages online or acquired from textbook (Ref [94] Appendix D). Assume the laser is resonant with the transition, linear polarized (angle with quantization axis is θ), providing a total Rabi rate Ω . Construction of OBE follows the procedure mentioned above, and here we will discuss the results.

When there is no B field, there will be stable dark states, leading to zero excited state population at equilibrium. When there is B field, we can sweep θ and B field strength (in unit of Γ) together and plot the excited state population as an indicator of optical cycling rate, as shown in Fig 7.1. One can observe the following features.

- at 0 and 90 degree, the system will fall into dark states even in presence of B field. This is predicted in dark state section 7.3.3. $|0\rangle$ will remain dark and cannot precess out.
- it seems maximum excited population usually comes at around $\theta \approx 55\text{-}65$ degree. I believe there is an elegant explanation for this number, and I have a lot of room here. But I'm not a Mathematician so I'll only provide a physical picture. This angle is roughly where the Rabi matrix strength are equal to each other with different ground states, as shown in (d) of Fig

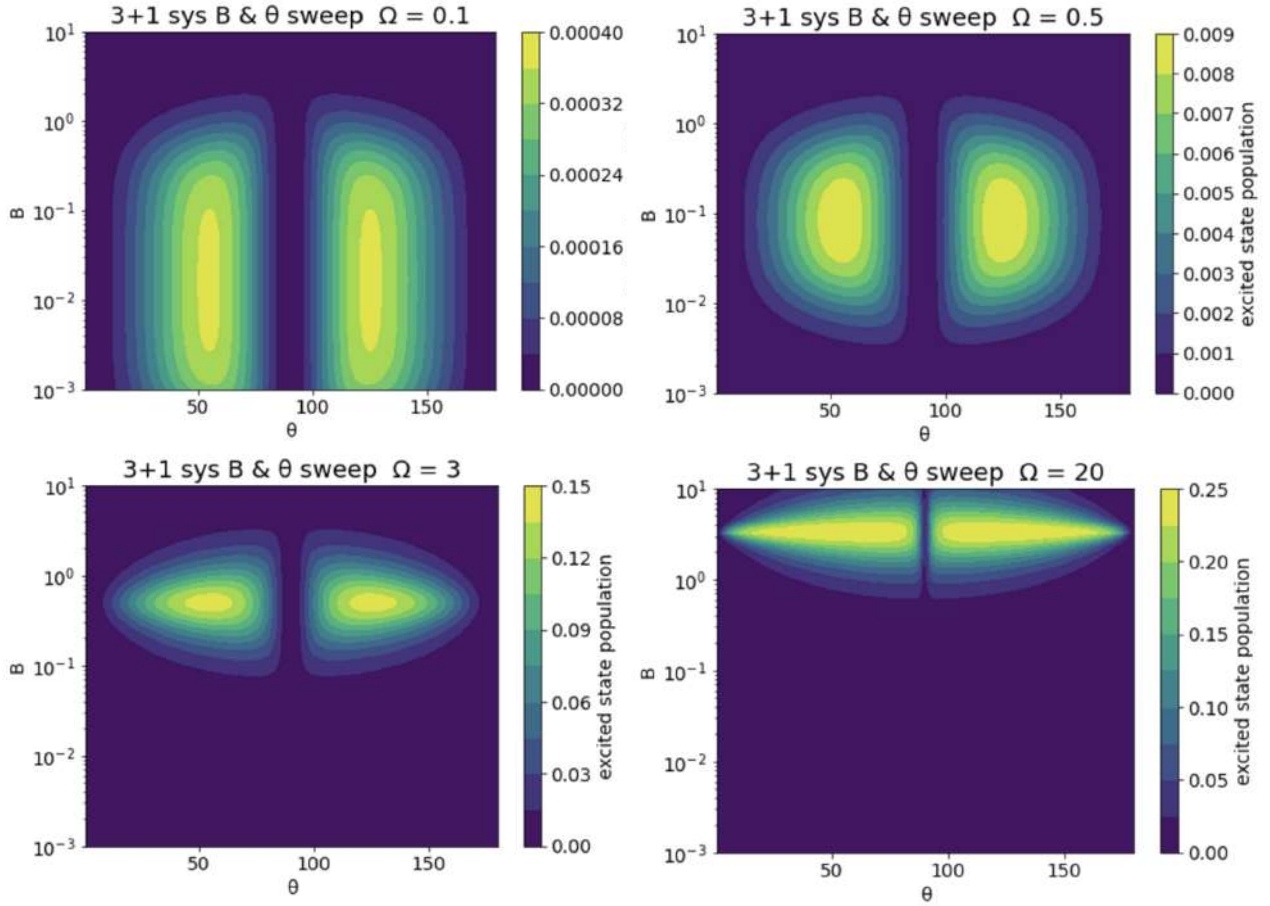


Figure 7.1: Excited state population versus B field, θ and Rabi rate in a 3+1 system. Different figures represent excited state population results at different total Rabi rate (equivalent to laser intensity). B field and Rabi rate are in unit of Γ , θ is in degree.

7.2.

- When stronger light field is applied (higher Ω), a stronger B field is required to mix the state more efficiently, in order to achieve high scattering rate. As explained earlier, if the B field remain the same, it will cause the system to experience adiabatic following and reduce the efficiency.

7.5 3+3 and 5+3 Toy Model

A 3+3 system and 5+3 system has the biggest difference with 3+1 system in their dark state remixing at 90 degree. As mentioned earlier, both 3+3 system and 5+3 system do not have a dark

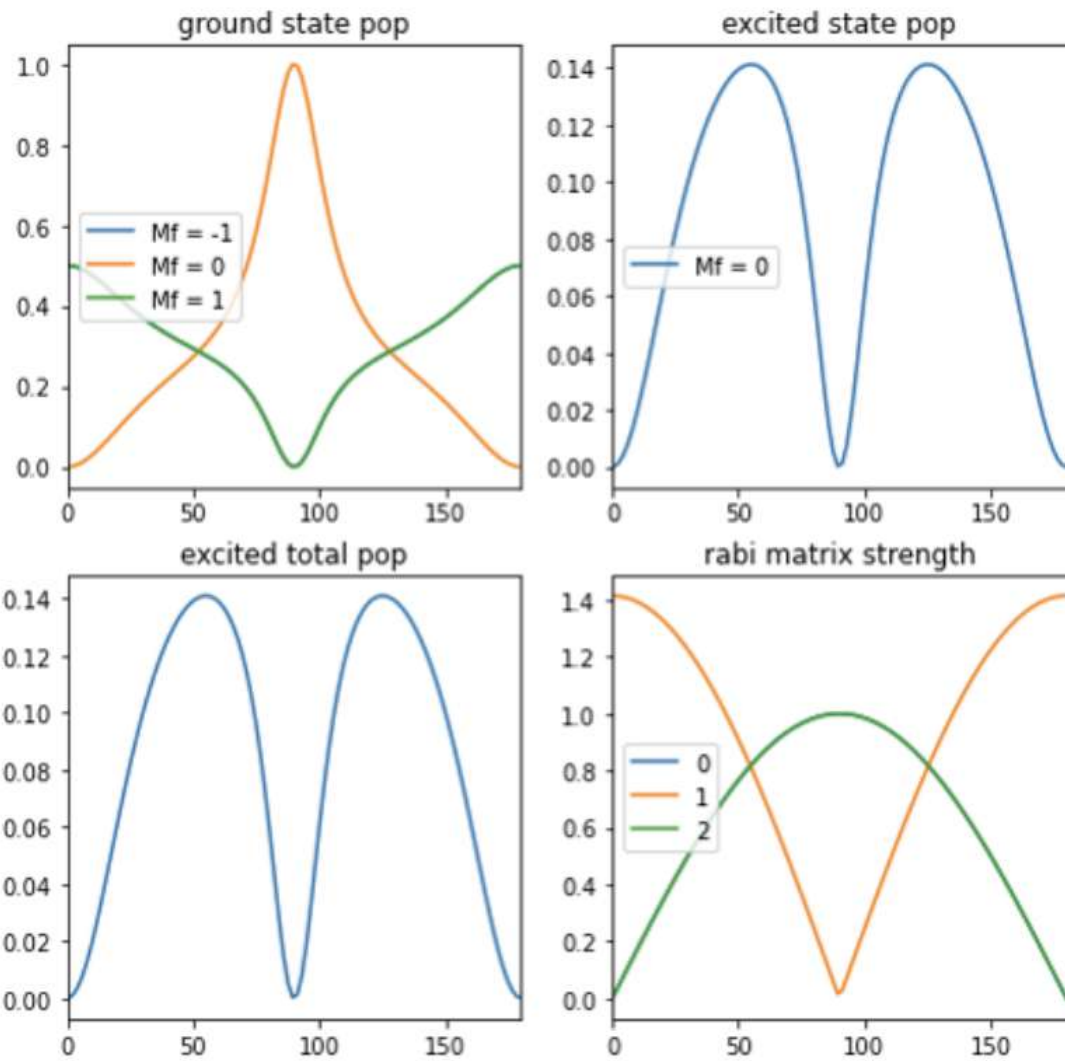


Figure 7.2: An example study of dependence on angle θ in a 3+1 system. This plot is generated for $B=0.45$, $\Omega=3$. Rabi matrix strength is the sum of total excitation to the ground state reflected in the hamiltonian. One can notice at 0 degree and 90 degree there is always some states being in dark, and around 55-65 degree the Rabi matrix is more balanced.

state that cannot be destabilized with B field at 90 degree. But at 0 degree, there will always be some dark state (one should refer to the dark state expression in previous section). As a result, the excited state population distribution will look a bit different from 3+1 case, as shown in Fig 7.3 and Fig 7.4.

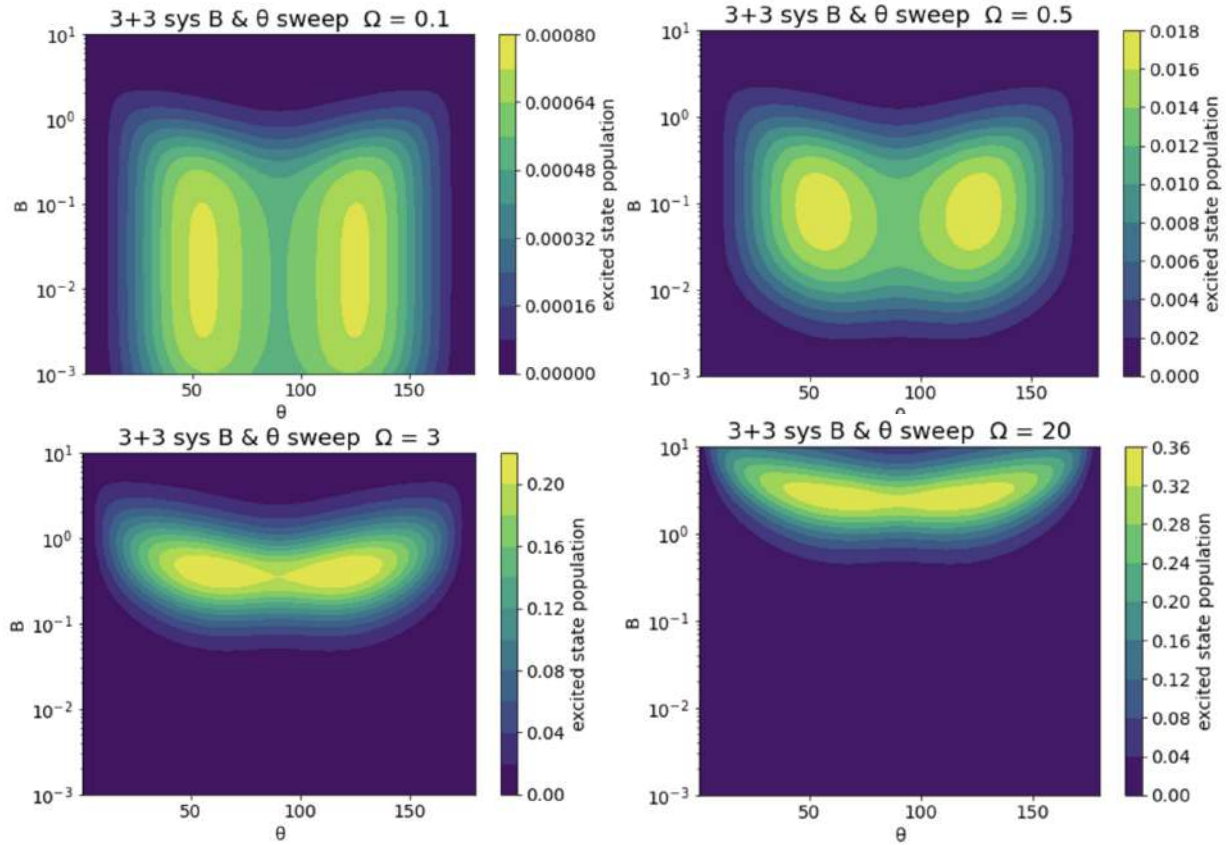


Figure 7.3: Excited state population versus B field, θ and Rabi rate in a 3+3 system. Different figures represent excited state population results at different total Rabi rate (equivalent to laser intensity). B field and Rabi rate are in unit of Γ , θ is in degree.

7.6 CaH System

The study of CaH system is similar to the toy model, but much more complicated. Here I will not elaborate on repetitive work that was done with the toy models, but to emphasize the critical differences with CaH system and the results. I'd like to share two cases of study, with difference emphasizes.

7.6.1 Case 1: X-A Dark State Remmixing Experiment

The reason why we want to study this is as follows: we hope to get as high optical cycling speed as possible experimentally, one of the limitation is dark state remmixing rate. We know B field and polarization angle plays an important role in dark state remmixing, so we measured it experimentally

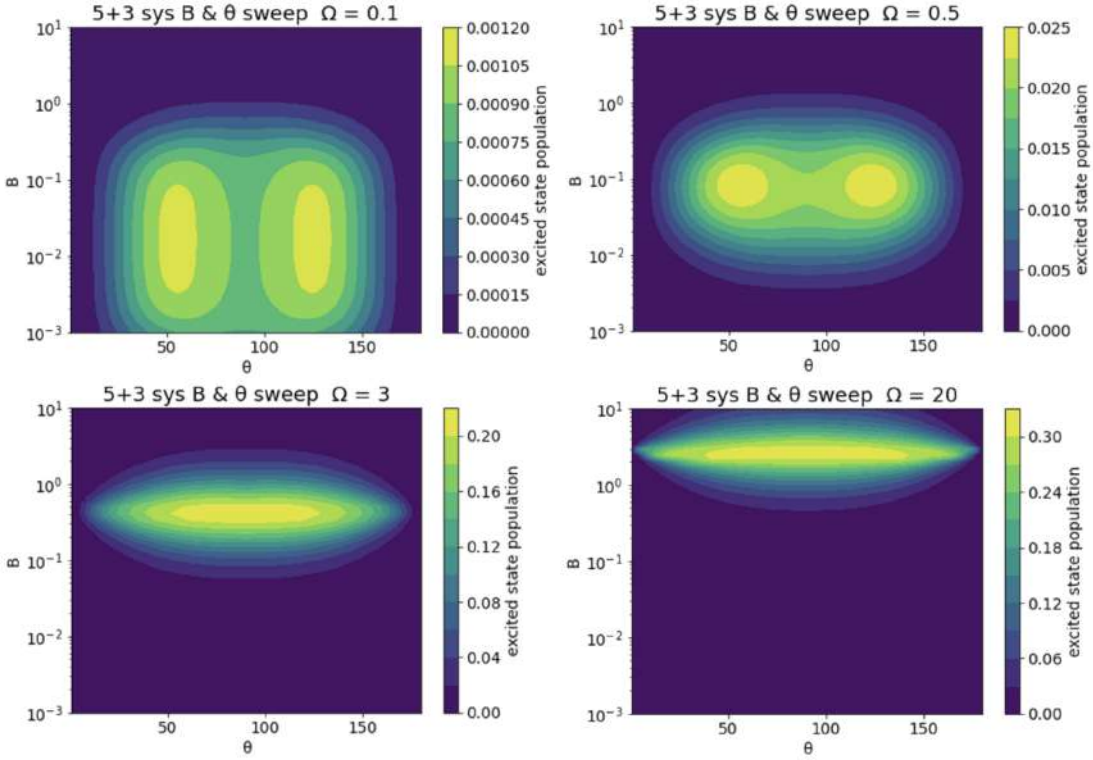


Figure 7.4: Excited state population versus B field, θ and Rabi rate in a 5+3 system. Different figures represent excited state population results at different total Rabi rate (equivalent to laser intensity). B field and Rabi rate are in unit of Γ , θ is in degree.

using the techniques mentioned in previous section and got results as shown in Fig 7.5. The results here show some critical behavior within CaH system: CaH system is just a combination of a few toy models.

1, in Fig 7.5 (a), we saw very high remaining ratio at 0 degree and 90 degree of the waveplate angle, which refers to laser polarization parallel with external B field. Ideally this number should be close to 1 (a high remaining population indicates slow optical cycling, whereas a low population indicates fast cycling) because there should be existence of a perfect dark state, but due to the imperfection of the experimental setup, there is always some leakage of other polarizations, which enables continuous optical cycling. There is also a smaller peak at around 45 degree, which corresponds to laser polarization perpendicular to external B field. This is also observed in 3+3 system and 5+3 system. And 20-30 degree, which corresponds to laser at 40-60 degree angle, maximum photon scattering rate is observed.

2, in Fig 7.5 (b), we saw low B field would lead to slow optical cycling (high remaining ratio) and order of 1 Gs of B field is sufficient to improve the optical cycling rate. It is predicted to show a decrease of optical cycling rate with higher B field applied, but the coils that we added are not capable of creating that strong of field so we could not see it experimentally.

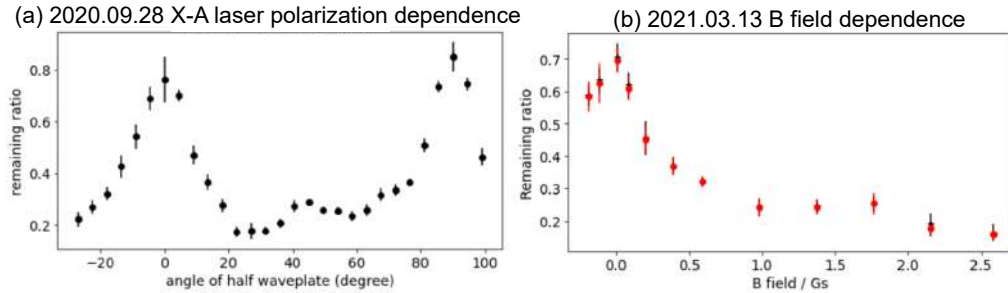


Figure 7.5: CaH optical cycling dependence on laser polarization angle and B field strength. (a) X axis is the angle of the waveplate that controls the X-A laser polarization angle with respect to applied B field. A θ degree change with the waveplate indicates a 2θ degree change with the laser polarization angle. Y axis is the normalized remaining population when we are doing the depletion experiment (deplete CaH from $v=0$ state to higher vibrational states through optical cycling in X-A 0-0 transition). A high remaining population indicates slow optical cycling, whereas a low population indicates fast cycling. (b) X axis is the strength of applied B field in unit of Gauss.

Initially we were amazed by the results and we wanted to use this as a sanity check of the OBE code. Eventually due to the imperfection of experiment, it is difficult to completely benchmark the theory results, so we just show qualitative agreement and proceed.

The definition of density matrix and Hamiltonian, Dissipator etc. are very big, because there is a total of 12+4 states associated with $v=0$ state in CaH (1 for $|X, v = 0, N = 1, J = 1/2, F = 0\rangle$, 3 for $|X, v = 0, N = 1, J = 1/2, F = 1\rangle$, 3 for $|X, v = 0, N = 1, J = 3/2, F = 1\rangle$, 5 for $|X, v = 0, N = 1, J = 3/2, F = 2\rangle$, 1 for $|A, v = 0, J = 1/2, F = 0\rangle$, 3 for $|A, v = 0, J = 1/2, F = 1\rangle$), making all matrices to be 16x16 in size. The readers are directed to the following website for detailed information⁴.

⁴<https://github.com/QiSun97/OBE-Solver/blob/main/Qi%20CaH%20X-A%20perpendicular%20B%20field%20experiment.ipynb>

States and Symbols

Here we have the $12 + 4$ states for X-A scheme. For the 12 ground states, I assign them based on the quantum number.

States are added in following order:

1-4 - $X^2\Sigma^+$ $J=1/2$, $F=0$, $m=0$; $F=1$, $m=-1,0,1$;

5-7 - $X^2\Sigma^+$ $J=3/2$, $F=1$, $m=-1,0,1$;

8-12 - $X^2\Sigma^+$ $J=3/2$, $F=2$, $m=-2,-1,0,1,2$;

13-16 - $B^2\Sigma^+$ $J=1/2$, $F=0$, $m=0$; $F=1$, $m=-1,0,1$

ω_i s are the laser frequencies. Ω_i s are the transition rabi rates (not taking transition dipole moments into account). θ is the polarization angle (we let B field determine quantization axis, z axis). Δ_i is the transition (laser) detuning.

Hamiltonian

The easy part is the state energies. Other than the Zeeman terms, all state energies will be replaced by laser detuning after unitary transformation. The diagonal terms for the Hamiltonian before the unitary transformation and after are shown in Fig.7.6.

In terms of laser coupling, first consider prefactors: a vector (in our case, is E field) that is at angle θ relative to z axis should be projected to spherical tensor basis. So there will be $1/\sqrt{2}$ prefactor. Minus sign is not important here due to the additional degree of freedom (E field is only required to be at angle θ , has one extra DOF) but is taken care of by assuming it is in X-Z plane.

The Hamiltonian before and after transformation can be seen in Fig. 7.7.

I imagined four lasers to address different spin-rotation components of CaH $X^2\Sigma^+$ state to $A^2\Pi_{1/2}$ state, all 4 SR components are parallel to each other. their individual rabi rates (proportional to their laser power), denoted as Ω_i ($i = 1, 2, 3, 4$) might deserve some more illustration.

(a) Before transformation (b) After transformation

```
[E0,
-B*g_x12F1 + E0 - HFS12,
E0 - HFS12,
B*g_x12F1 + E0 - HFS12,
-B*g_x32F1 + E0 + SR,
E0 + SR,
B*g_x32F1 + E0 + SR,
-2*B*g_x32F2 + E0 + HFS32 + SR,
-B*g_x32F2 + E0 + HFS32 + SR,
E0 + HFS32 + SR,
B*g_x32F2 + E0 + HFS32 + SR,
2*B*g_x32F2 + E0 + HFS32 + SR,
Ee,
Ee + HFSB,
Ee + HFSB,
Ee + HFSB]
```

```
[-1.0*\Delta1,
-B*g_x12F1 - 1.0*\Delta2,
-1.0*\Delta2,
B*g_x12F1 - 1.0*\Delta2,
-B*g_x32F1 - 1.0*\Delta3,
-1.0*\Delta3,
B*g_x32F1 - 1.0*\Delta3,
-2*B*g_x32F2 - 1.0*\Delta4,
-B*g_x32F2 - 1.0*\Delta4,
-1.0*\Delta4,
B*g_x32F2 - 1.0*\Delta4,
2*B*g_x32F2 - 1.0*\Delta4,
0,
HFSB,
HFSB,
HFSB]
```

Figure 7.6: CaH system Hamiltonian diagonal terms in sequence. (a) before unitary transformation. (b) after transformation.

(a) Before transformation

	13	14	15	16	
1	0	-0.1666666666666670 ₂ e ^{i 2m\pi sin(0)}	0.2357022643055160 ₂ e ^{i 2m\pi sin(0)}	0.166666666666666670 ₂ e ^{i 2m\pi sin(0)}	
2	-0.1666666666666670 ₂ e ^{i 2m\pi sin(0)}	-0.2357022643055160 ₂ e ^{i 2m\pi sin(0)}	-0.1666666666666670 ₂ e ^{i 2m\pi sin(0)}	-0.166666666666666670 ₂ e ^{i 2m\pi sin(0)}	
3	0.2357022643055160 ₂ e ^{i 2m\pi sin(0)}	-0.1666666666666670 ₂ e ^{i 2m\pi sin(0)}	0	0.2357022643055160 ₂ e ^{i 2m\pi sin(0)}	
4	0.1666666666666670 ₂ e ^{i 2m\pi sin(0)}	-0.1666666666666670 ₂ e ^{i 2m\pi sin(0)}	-0.1666666666666670 ₂ e ^{i 2m\pi sin(0)}	0.2357022643055160 ₂ e ^{i 2m\pi sin(0)}	
5	0.117851301975820 ₂ e ^{i 2m\pi sin(0)}	-0.0813353313333350 ₂ e ^{i 2m\pi sin(0)}	-0.0590255659086870 ₂ e ^{i 2m\pi sin(0)}	0.117851301975820 ₂ e ^{i 2m\pi sin(0)}	
6	-0.1444444444444460 ₂ e ^{i 2m\pi sin(0)}	-0.0590255659086870 ₂ e ^{i 2m\pi sin(0)}	0	-0.0488155659886870 ₂ e ^{i 2m\pi sin(0)}	
7	-0.117851301975820 ₂ e ^{i 2m\pi sin(0)}	-0.0590255659086870 ₂ e ^{i 2m\pi sin(0)}	0.0883333333333350 ₂ e ^{i 2m\pi sin(0)}	-0.117851301975820 ₂ e ^{i 2m\pi sin(0)}	
8	0	0.1444444444444460 ₂ e ^{i 2m\pi sin(0)}	0	0	
9	0	-0.132030726159642 ₂ e ^{i 2m\pi sin(0)}	0	0	
10	0	-0.0590255659086870 ₂ e ^{i 2m\pi sin(0)}	0.117851301975820 ₂ e ^{i 2m\pi sin(0)}	0.0883333333333350 ₂ e ^{i 2m\pi sin(0)}	
11	0	0	-0.1039620726159642 ₂ e ^{i 2m\pi sin(0)}	0.117851301975820 ₂ e ^{i 2m\pi sin(0)}	
12	0	0	0	-0.1443275672974000 ₂ e ^{i 2m\pi sin(0)}	
13	Ee	0	0	0	
14	0	Ee + HFSB	0	0	
15	0	0	Ee + HFSB	0	
16	0	0	Ee + HFSB	0	

(b) After transformation

	13	14	15	16	
1	0	-0.1666666666666670 ₂ e ^{i m\pi sin(0)}	0.2357022660955140 ₂ e ^{i m\pi sin(0)}	0.166666666666666670 ₂ e ^{i m\pi sin(0)}	
2	-0.1666666666666670 ₂ e ^{i m\pi sin(0)}	-0.2357022660955140 ₂ e ^{i m\pi sin(0)}	-0.166666666666666670 ₂ e ^{i m\pi sin(0)}	-0.166666666666666670 ₂ e ^{i m\pi sin(0)}	
3	0.2357022660955140 ₂ e ^{i m\pi sin(0)}	-0.1666666666666670 ₂ e ^{i m\pi sin(0)}	0	0.2357022660955140 ₂ e ^{i m\pi sin(0)}	
4	0.1666666666666670 ₂ e ^{i m\pi sin(0)}	-0.1666666666666670 ₂ e ^{i m\pi sin(0)}	-0.1666666666666670 ₂ e ^{i m\pi sin(0)}	0.2357022660955140 ₂ e ^{i m\pi sin(0)}	
5	0.117851301975820 ₂ e ^{i m\pi sin(0)}	-0.0813353313333350 ₂ e ^{i m\pi sin(0)}	-0.0590255659086870 ₂ e ^{i m\pi sin(0)}	0.117851301975820 ₂ e ^{i m\pi sin(0)}	
6	-0.1444444444444460 ₂ e ^{i m\pi sin(0)}	-0.0590255659086870 ₂ e ^{i m\pi sin(0)}	0	-0.0488155659886870 ₂ e ^{i m\pi sin(0)}	
7	-0.117851301975820 ₂ e ^{i m\pi sin(0)}	-0.0590255659086870 ₂ e ^{i m\pi sin(0)}	0.0883333333333350 ₂ e ^{i m\pi sin(0)}	-0.117851301975820 ₂ e ^{i m\pi sin(0)}	
8	0	0	0	0.1443275672974000 ₂ e ^{i m\pi sin(0)}	
9	0	0	0	-0.132030726159642 ₂ e ^{i m\pi sin(0)}	
10	0	0	0	-0.0590255659086870 ₂ e ^{i m\pi sin(0)}	
11	0	0	0	0.117851301975820 ₂ e ^{i m\pi sin(0)}	
12	0	0	0	-0.1443275672974000 ₂ e ^{i m\pi sin(0)}	
13	Ee	0	0	0	
14	0	Ee + HFSB	0	0	
15	0	0	Ee + HFSB	0	
16	0	0	Ee + HFSB	0	

Figure 7.7: CaH system Hamiltonian off-diagonal terms top right corner part, and the bottom left corner matrix elements are the complex conjugate of the top right corner. There are no coupling between the ground states so the top left corner is mostly zeros. (a) before unitary transformation. (b) after transformation.

Rabi Rate Calculation

To calculate Rabi rate, there are two methods I tried. One is a classical method (I learned from Debayan), and is using saturation intensity.

$$I_s = \frac{2\pi\hbar c\Gamma\pi}{3\lambda^3}$$

$$\Omega = \sqrt{\frac{I}{2I_s}}\Gamma = \sqrt{\frac{3\lambda^3\Gamma}{4\pi^2\hbar c}}$$

The second method is from Konrad's thesis, equation 2.5.6 (pg 37) and equations in page 107-108, where μ_{eff} is given theoretically by $\langle \vec{r} \rangle = \langle A\Pi | r | X\Sigma \rangle$. There might be experimental values

that can be plugged in.

$$\mu_{eff} = \sqrt{\frac{3\pi\epsilon_0\hbar c^3\Gamma}{(2\pi\nu)^3}}$$

$$E_{laser} = \sqrt{\frac{2I}{c\epsilon_0\hbar^2}}$$

$$\Omega = \mu_{eff} E_{laser} = \sqrt{\frac{3\lambda^3\Gamma I}{4\pi^2\hbar c}}$$

If we do not use experimental values, then these two methods are equivalent to each other. We used experimental values, they are still similar to each other. Method one and two results are shown in Fig. 7.8.

```

# r_val = 1/33
# lambda_laser = 695E-9
# c=2997920000
# hbar=1.054e-34
# pi = np.pi
# Int = 2*pi*hbar*c**2*r_val**2*1E9*pi/(3*lambda_laser**3)

power_laser1 = 0.5*30E-3/1
power_laser2 = 0.5*30E-3/3
power_laser3 = 0.5*40E-3/3
power_laser4 = 0.5*40E-3/5

beam_dia = 0.17E-3
Int_laser1 = Power_laser1**4/(pi/beam_dia)**2
Int_laser2 = Power_laser2**4/(pi/beam_dia)**2
Int_laser3 = Power_laser3**4/(pi/beam_dia)**2
Int_laser4 = Power_laser4**4/(pi/beam_dia)**2

Q1_val = np.sqrt(Int_laser1*Int_laser1*r_val)
Q2_val = np.sqrt(Int_laser2*Int_laser2*r_val)
Q3_val = np.sqrt(Int_laser3*Int_laser3*r_val)
Q4_val = np.sqrt(Int_laser4*Int_laser4*r_val)

print('Using method one\n')
print(f'Intensity of all laser legs (W/m^2): {Int_laser1:.5}, {Int_laser2:.5}, {Int_laser3:.5}, {Int_laser4:.5}')
print(f'Saturation intensity (W/m^2): {Int:.5}')
print(f'Rabi rates (GHz): {Q1_val:.5}, {Q2_val:.5}, {Q3_val:.5}, {Q4_val:.5}')
print(f'Normalized Rabi rates (\Gamma): {Q1_val/r_val:.5}, {Q2_val/r_val:.5}, {Q3_val/r_val:.5}, {Q4_val/r_val:.5}')

Using method one
Intensity of all laser legs (W/m^2): 1990.6, 633.52, 844.7, 506.82
Saturation intensity (W/m^2): 18.767
Rabi rates (GHz): 0.21583, 0.12449, 0.14375, 0.11135
Normalized Rabi rates (\Gamma): 7.2158, 4.1083, 4.7439, 3.6746

# print('Using method two\n')
# v = 431.27*1E12
# Gamma = 1/(33E-9)
# Re = np.sqrt(1/d_e**2 * 3*np.pi*eps_0*hbar*c**3/(2*np.pi*v)**3 * Gamma)
# print(f'For A state \nRe is ({Re:.5}) a0, or in meter it is ({Re:.5} m')
# print(f'\mu_eff = ({Re * q_e / (3.33564E-30)}:.5) Debye')

mu_eff = Re * q_e
E_11 = np.sqrt(2 * Int_laser1 / c / eps_0) / hbar
E_12 = np.sqrt(2 * Int_laser2 / c / eps_0) / hbar
E_13 = np.sqrt(2 * Int_laser3 / c / eps_0) / hbar
E_14 = np.sqrt(2 * Int_laser4 / c / eps_0) / hbar

Q1_val = mu_eff * E_11 * 1E-9
Q2_val = mu_eff * E_12 * 1E-9
Q3_val = mu_eff * E_13 * 1E-9
Q4_val = mu_eff * E_14 * 1E-9

print(f'Rabi rates (GHz): {Q1_val:.5}, {Q2_val:.5}, {Q3_val:.5}, {Q4_val:.5}')

Using method two

For A state
Re is 2.2417 a0, or in meter it is 1.1859e-10 m
mu_eff = 5.6954 Debye
Rabi rates (GHz): 0.2157, 0.12453, 0.1438, 0.11138

```

Figure 7.8: Two methods of calculating Rabi rate from laser power and gaussian beam size.

OBE Result

The simulation conditions are as follows: Laser couplings: two SR components parallel to each other; laser power 30mW + 40mW; detuning =0. Excited state population average method is, let the system run for 15us (about 500×33 ns) and take the average excited state population.

- As shown in Fig 7.9, we see consistent double peak structure when sweeping B field strength and polarization angle. The stronger peak always happens around 60degree, and B field

strength is affected by rabi rate (laser power) and balance. Within 10Gs B field the higher the better.

- $J = 3/2$ rabi rate (laser power) should be taken more care of, our system is not sensitive to $J = 1/2$ leg rabi rate as much as to $J = 3/2$ (Fig 7.9).
- In order to reach max scattering rate, Rabi rates need to balance, and B field strength needs to match rabi rate. Either one becomes too high will also decrease the scattering rate. But the system is not very sensitive to B field change or $J = 1/2$ laser rabi rate after it reaches a certain amount. We have not reached that point for the B field, but for $J = 1/2$ laser we have.
- High laser power plus high B field give best optical cycling speed, as shown in Fig. 7.10.
- In Fig. 7.10 (k-l), detuning is basically disentangled from other parameters in terms of its effect on optical cycling.
- With current power and coils that we have, a reasonably reachable scattering rate is $0.12 / 33\text{ns} = 3.6\text{MHz}$. However, this is some scattering rate that neither we, nor anyone in molecule cooling community, have reached.

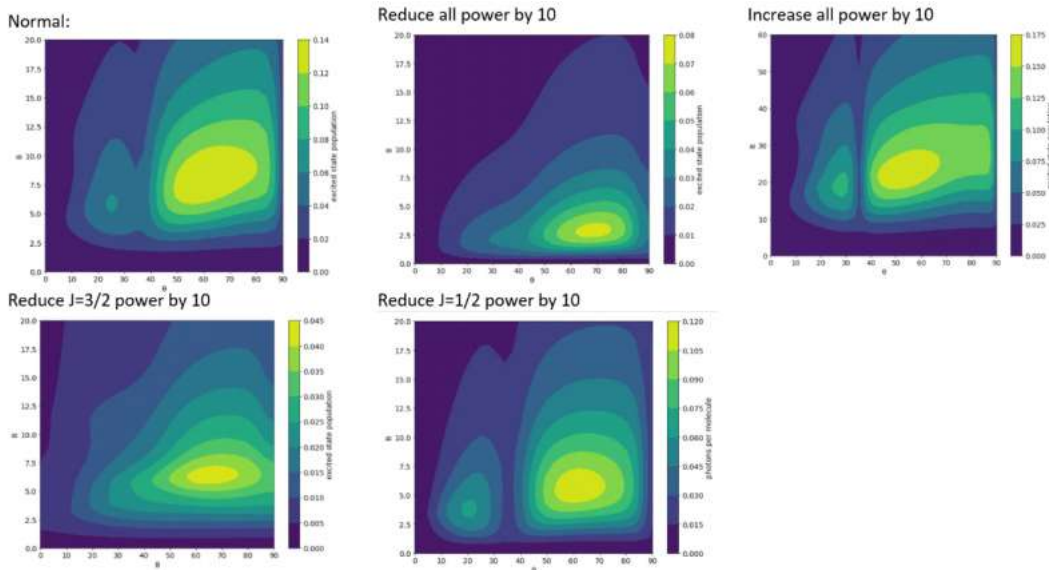


Figure 7.9: OBE result1: sweep B field strength and angle at different laser power conditions.

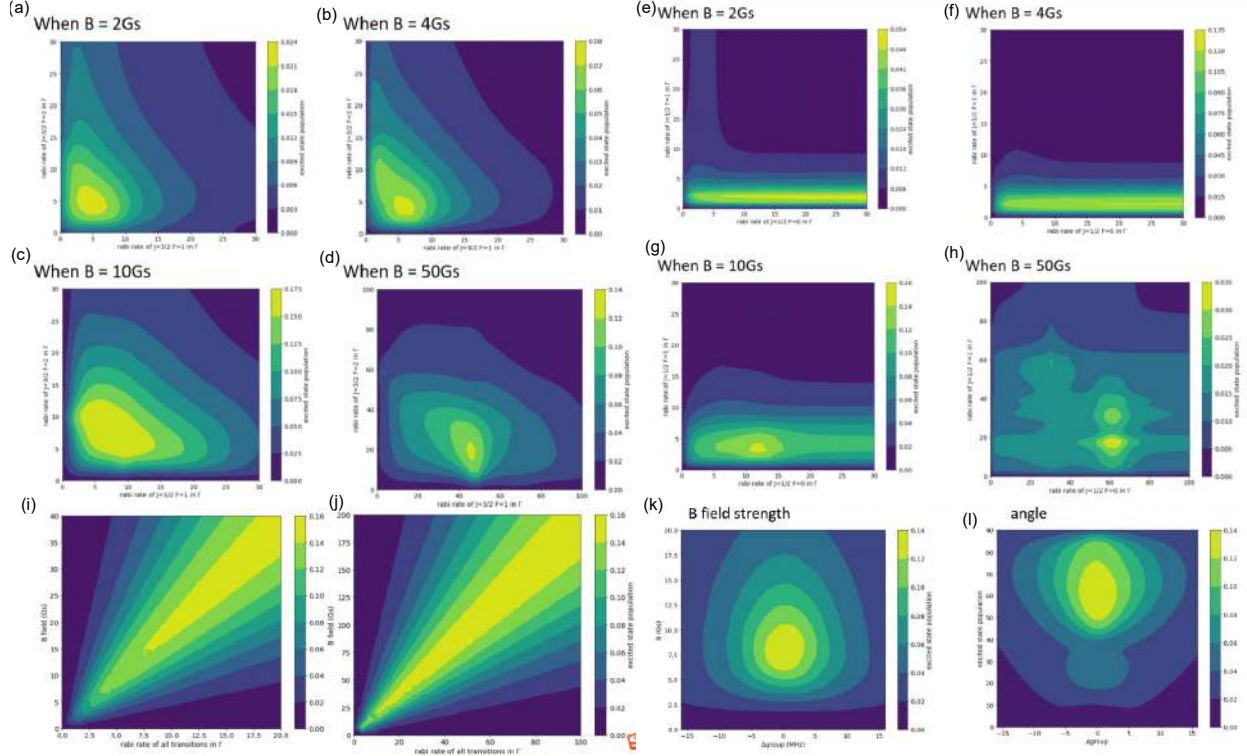


Figure 7.10: OBE result2: (a-d) change different B field strength, while varying $J=3/2$ two hyperfine laser power (Rabi rate) and monitor the excited state population. The conditions are: two SR components parallel to each other, group detuning = 0, $\theta = 60$ degree (since we know this is when we have maximum scattering rate), $J=1/2$ laser power is fixed (30mW, $\Omega \approx 7\Gamma$ for $F=0$ and $\Omega \approx 4\Gamma$ for $F=1$). (e-h) change different B field strength, while varying $J=1/2$ two hyperfine laser power (Rabi rate) and monitor the excited state population. Here, group detuning = 0, $\theta = 60$ degree, $J=3/2$ laser power is fixed (30mW). (i-j) Set all transitions to have the same Rabi rate, we can sweep this Rabi rate with B field strength and see the correspondance. (k-l) Study of how group detuning affects the excited state population with B field and θ .

7.6.2 Case 2: Sisyphus Cooling Experiment

Sisyphus cooling in type-II systems (where $F' \leq F$) operates differently from the well-established mechanism in type-I systems. In a typical type-I system (e.g., alkali atoms on the D_2 transition), sub-Doppler cooling occurs due to polarization gradients leading to optical pumping between Zeeman sublevels, where atoms climb potential hills and lose kinetic energy. However, in type-II systems like CaH, dark states naturally form due to optical pumping. These dark states hinder standard Doppler and sub-Doppler cooling mechanisms. Instead, an alternative Sisyphus-like mechanism can occur, which relies on the following process:

- Non-adiabatic transitions: Atoms or molecules undergo motion-induced transitions between bright and dark states.
- Optical pumping: The atoms are optically pumped back into the dark state at regions of high intensity, effectively converting kinetic energy into internal state population changes.
- Intensity gradients: These help maintain the required conditions for non-adiabatic transitions.

Unlike type-I systems, where red-detuned light provides cooling, type-II systems require blue-detuned light for efficient Sisyphus cooling because atoms must be pumped out of dark states at the right moments to induce cooling. The readers are directed to Ref. [219] for complete picture of sub-Doppler cooling in a type-II system.

In the context of showing sub-Doppler cooling force in CaH system, I will only focus on one situation: linear polarized lasers are retro-reflected without altering the polarization angle while forming a standing-wave. The reason why I study it is because this is the simplest to achieve experimentally without the need to use $\lambda/4$ waveplates to alter the polarizations of the lasers every run (which we attempted, with a giant $\lambda/4$ waveplate, and the polarization actually cannot remain high purity for more than 20 passes).

Chapter 8: Future Outlook: 3D MOT, Dissociation, and H Detection

Physicists often discuss the future, because physics is about understanding past and present phenomena in order to predict future outcomes. This chapter outlines my perspective on the immediate future of the experiment and our ongoing efforts.

To recap, the goal of my PhD was to construct a quantum machine capable of applying optical forces to CaH molecules. The long-term vision is to trap CaH in a MOT, transfer the molecules into a conservative trap (optical dipole trap, ODT), dissociate them into atomic hydrogen and calcium via STIRAP, load the hydrogen atoms into an optical lattice, and perform high-precision spectroscopy. These components are discussed individually in the following sections.

8.1 3D MOT

To achieve strong MOT forces in a Type II system, where there are more ground states than excited states, remixing of dark states is essential. There are two main approaches:

RF MOT This is the approach currently pursued in our setup. It resembles an atomic MOT in many aspects, but the key difference is that the polarization of the MOT beams must be rapidly flipped at a rate comparable to the optical cycling rate. This ensures that dark states become bright again to sustain optical cycling. However, simply flipping the polarization without changing the magnetic field direction leads to alternating trapping and anti-trapping forces, which cancel each other out. Therefore, the magnetic field direction must also be flipped at the same rate.

DC MOT This method involves adding extra polarizations and relying on molecular motion in the magnetic field for dark state remixing. It is experimentally simpler, since it does not require synchronized flipping of polarization or magnetic field. However, according to a calculation by our

former postdoc Ivan, the DC MOT provides a trapping force about five times weaker than the RF MOT. Because we want to trap as many molecules as possible, we chose to pursue the RF MOT.

Coil Design and Thermal Management Our current design is based on the CaOH MOT setup developed by Doyle’s group at Harvard. We have sent the components for manufacturing and tested the magnetic field gradient in air (not *in situ*). Simulation and test results are shown in Fig. 8.1.

A major challenge is managing the heat generated by the coils. We expect to flow up to 10 A peak current, dissipating tens of watts of power. In air, with peak-to-peak 20 A current at 1 MHz, we observed coil temperatures reaching 70°C. In vacuum, where cooling by air is absent, thermal management becomes critical. The coils are mounted on AlN plates (which have high thermal conductivity) and are thermally connected to four copper posts that extend outside the vacuum chamber. A thermal test of a slightly earlier version of the system is shown in Fig. 8.2.

RF Driving Circuit The RF system is another key component. We acquired two 50 W RF amplifiers from eBay. While they deliver the advertised power, they exhibit noticeable noise and the input impedance is not exactly $50\ \Omega$ as specified. Despite this, the system is capable of delivering 12 A amplitude current to the MOT coils. In practice, we only require about 4 A to generate sufficient trapping force, so this is no longer a bottleneck.

8.2 Ultracold Chemistry

Ultracold molecules present an exceptional platform for the study of quantum chemistry. Unlike atom-atom scattering, atom-molecule and molecule-molecule interactions can result in a variety of complex outcomes. For instance, molecules may form long-lived collision complexes with other atoms or molecules, leading to effective loss from the trap. Such collisional loss is currently the principal barrier to reaching lower temperatures and higher densities in molecular systems, yet the underlying mechanisms remain incompletely understood. Conversely, elastic collisions are essential for evaporative cooling—a widely used technique to achieve the ultracold regime.

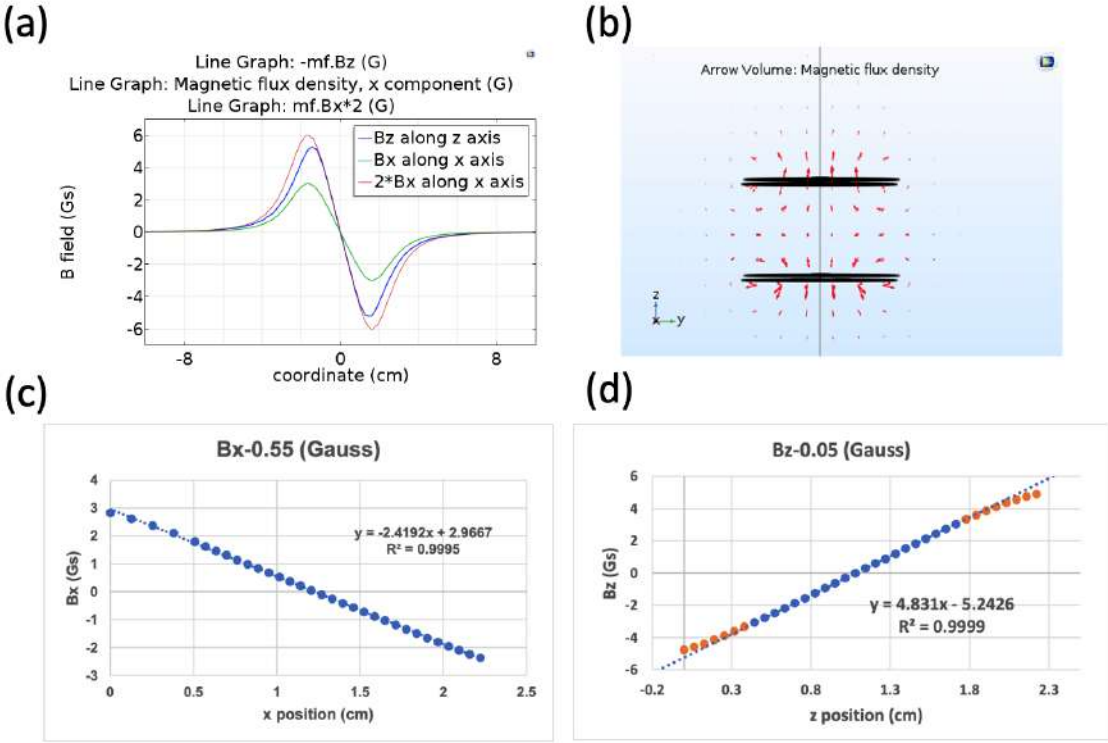


Figure 8.1: Simulation and calibration done for the RF MOT coil in DC configuration. (a) COMSOL simulated B field gradient under 1A of current. (b) the spatial direction of the field. (c) experimentally calibrated x direction (on plane) gradient to be 2.42Gs / cm / A. (d) calibrated z direction (on axis) gradient to be 4.83Gs / cm / A.

Ongoing experiments with cold molecules enable us to probe and characterize these scattering processes in detail. When the loss rate scales quadratically with molecular density, it is typically indicative of two-body, molecule-molecule collisions. Indeed, nearly all ultracold molecule experiments at sufficient densities—whether involving directly laser-cooled molecules or those formed via assembly—observe universal loss at short range. This phenomenon is attributed to “sticky” collisions, wherein molecules form long-lived complexes that are vulnerable to trap loss through mechanisms such as light-assisted scattering [220]. The probability of complex formation and the associated loss dynamics are sensitive to the quantum statistics of the system, particularly distinctions between bosonic and fermionic species.

Beyond molecule-molecule interactions, atom-molecule collisions are also of great interest in the ultracold regime. For example, Ref. [221] reports a rich spectrum of magnetic-field-dependent

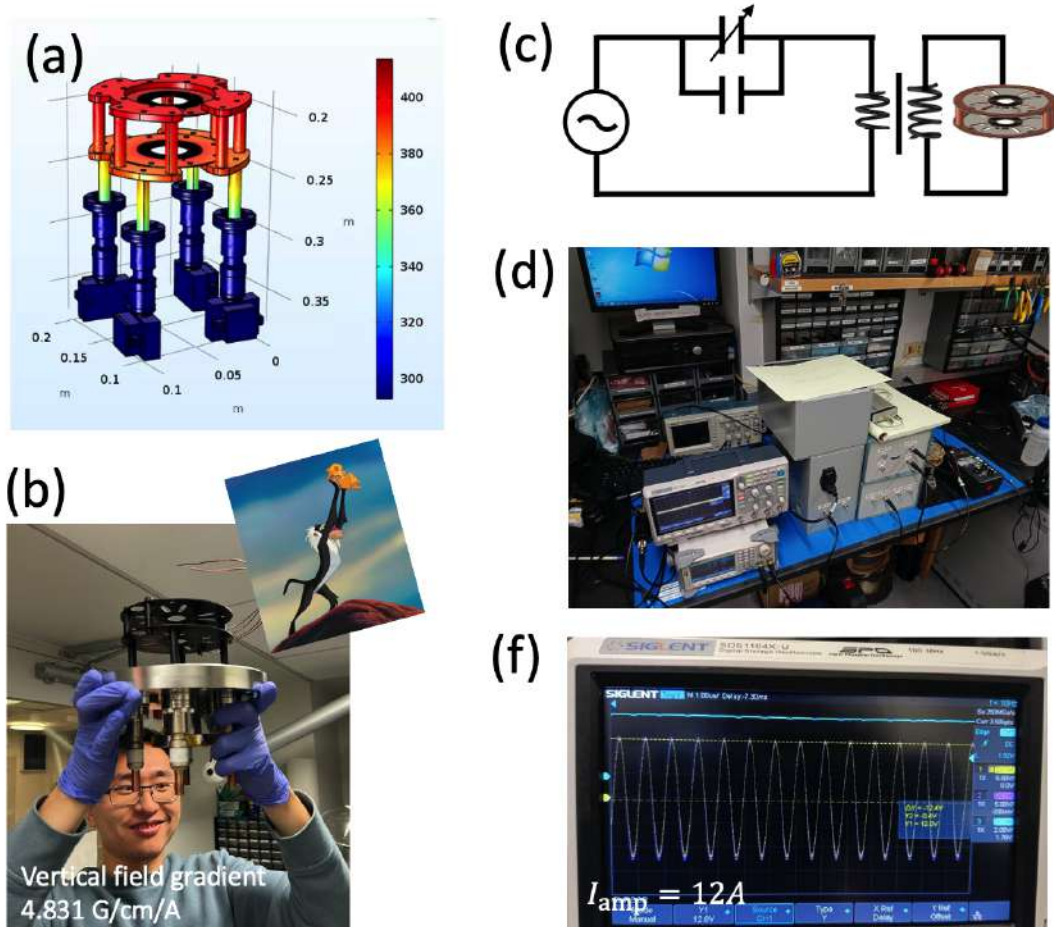


Figure 8.2: Thermal simulation and RF electronic driving circuits. (a) thermo simulation, using console for the initial version of MOT coil. The final version has similar thermal performance. (b) bottom view of the painted MOT coils. (c) RF driving circuits design. The tuneup capacitor is CVUN-1500AC/4-BEAA, and the LC residence circuit is made to be tunable at least 800 kHz to 1200 kHz. For wider frequencies one needs to replace the static capacitor. The impedance matching coils is approximately 5 to 30 rounds ratio, and the event for impedes is approximately 50 ohms. However, the RF amplifiers that we used are purchased from the eBay, and they don't seem to have 50 ohms impedance, leading to a not very ideal energy transfer. However, with a realization in (d), we are able to drive maximum at 12 A amplitude at 1MHz as shown in (e).

Feshbach resonances in collisions between spin-triplet NaLi molecules and Li atoms. These resonances offer a powerful means to control interactions and may enable sympathetic cooling of molecules using ultracold atomic baths. While most chemically assembled molecules such as KRb, NaK, NaCs, and RbCs reside in spin-singlet ground states and hence lack magnetic moments, directly laser-cooled molecules—such as CaF, SrF, CaOH, and CaH—possess magnetic

dipole moments and thus support magnetically tunable Feshbach resonances. This makes them promising candidates for detailed studies of atom-molecule and molecule-molecule scattering.

Among these, CaH stands out due to its light mass and hydrogen content, which allow for relatively precise *ab initio* quantum chemistry calculations. Furthermore, we have demonstrated that the fermionic isotopologue CaD is also amenable to laser cooling. Together, CaH and CaD provide a unique testbed for fundamental studies of ultracold collision processes.

A particularly intriguing system is the CaH + Li reaction, which has been extensively analyzed in theory [222]. The relatively simple internal structures of both CaH and Li render the interaction computationally tractable. Feshbach resonances are predicted to exist in this system, opening the possibility to magnetically tune reaction cross sections. Experimentally, the reactivity of CaH with Li was examined in a cryogenic buffer gas cell at temperatures around 2 K [223]. Even in this relatively warm regime, the reaction rate could be inferred from CaH loss as a function of Li density. Although quantum statistical effects are not expected at these higher temperatures, further cooling would allow us to probe the transition from thermal to quantum-dominated chemical behavior [66].

In parallel, we propose extending this line of research to include **CaH + K** collisions. Potassium offers several experimental advantages: unlike lithium, potassium is significantly easier to cool and trap, both via magneto-optical and optical dipole trapping methods. This experimental accessibility could accelerate progress in studying atom-molecule scattering and facilitate the eventual integration of sympathetic cooling. Furthermore, K has multiple stable isotopes with different quantum statistics, offering a tunable platform for studying spin effects in collisions.

On the other hand, lithium remains compelling for theoretical work due to its exceptionally simple electronic and hyperfine structure, which allows for more accurate quantum chemistry modeling. While the CaH + K system introduces slightly more complexity in *ab initio* calculations, the differences are not prohibitive and can be managed with current computational techniques.

Studying both CaH + Li and CaH + K systems in parallel could provide valuable comparative insights. The Li system enables deep theoretical understanding, while the K system opens doors for more robust and scalable experimental investigations. Together, these pathways will enhance our

ability to control and understand atom-molecule interactions in the ultracold regime, and may pave the way toward new forms of quantum control and sympathetic cooling for molecular systems.

8.3 Controlled Dissociation Pathways for Ultracold Atom Production

Beyond their role in quantum control and cold chemistry, laser-cooled diatomic molecules such as CaH offer exciting possibilities as precursors for generating novel ultracold atomic gases. One particularly compelling application is the controlled dissociation of molecules into fragments that are not directly accessible through laser cooling, such as atomic hydrogen (H) or deuterium (D). These light atoms are among the most fundamental and scientifically important species, yet their lack of closed optical transitions makes direct laser cooling challenging. Harnessing molecules like CaH and CaD as chemically stable, controllable reservoirs for ultracold H and D is therefore a promising direction for the next generation of cold atom experiments.

The basic concept involves preparing a cloud of ultracold CaH molecules in the ground electronic and vibrational state $X^2\Sigma^+(v'' = 0)$ and then coherently dissociating them into Ca and H fragments. If this dissociation process occurs sufficiently close to the zero-energy continuum, the resulting atomic fragments can inherit the ultralow center-of-mass temperature of the parent molecule. This offers a pathway to producing dilute, ultracold hydrogen samples—potentially orders of magnitude colder than what can be achieved via traditional atomic beam or cryogenic methods.

To realize this vision, we have proposed a two-photon stimulated Raman adiabatic passage (STIRAP) pathway that connects the $X(v'' = 0)$ molecular state to the near-threshold $X(v'' = v_{\text{th}})$ continuum via an intermediate excited state $B^2\Sigma^+(v' = 4)$. This vibrational level is particularly well-suited for such a process due to the double-well structure of the B potential, which supports spatially extended vibrational states with strong Franck-Condon overlap with both the ground and continuum states. Our calculations show that $B(v' = 4)$ simultaneously couples strongly to $X(v'' = 0)$ and to the least-bound vibrational state $X(v'' = 15)$, whose energy is only $\sim 500 \text{ cm}^{-1}$ below the dissociation threshold.

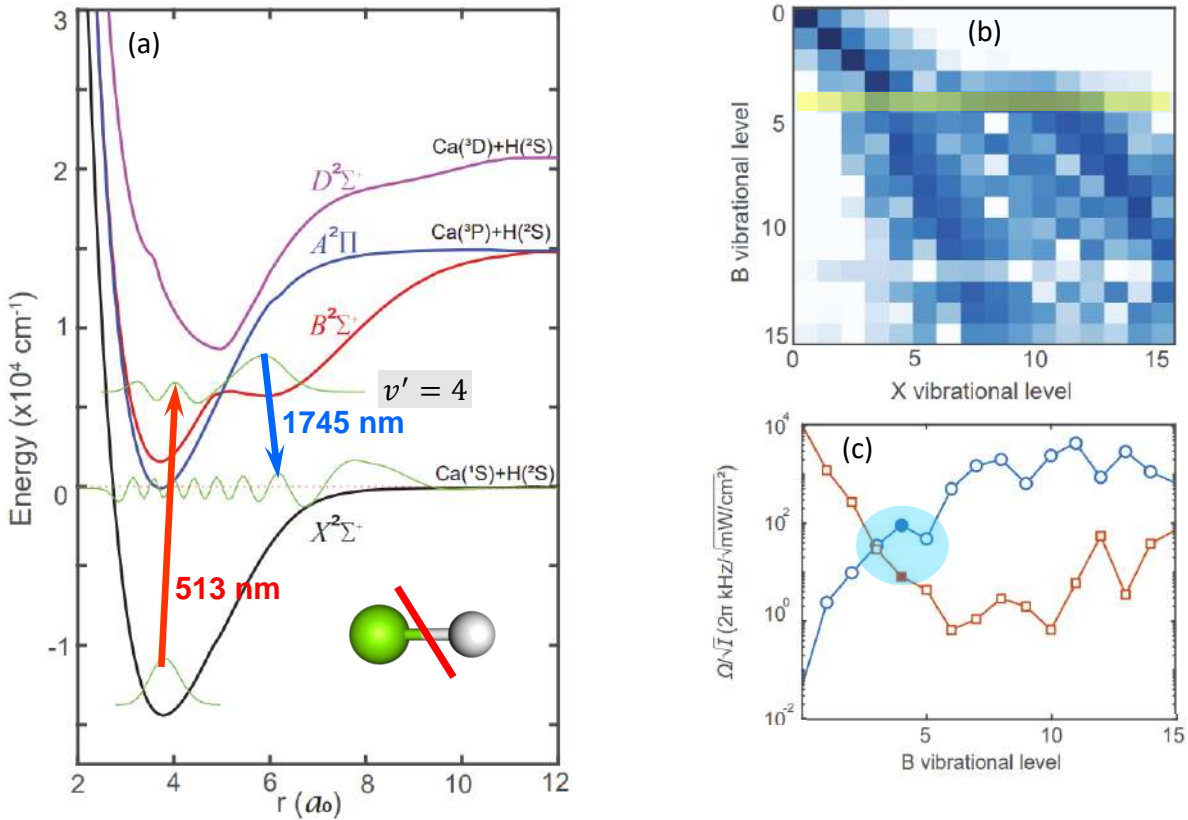


Figure 8.3: Proposed state-controlled photodissociation of CaH molecules [89]. (a) Calculated molecular potentials for CaH in its ground ($X^2\Sigma^+$) and first three excited (A , B and D) states. The lowest bound state of $A^2\Pi$ lies above the Ca+H dissociation continuum placed at 0 cm^{-1} . This implies that a molecule can spontaneously break apart into its constituent atoms when optically excited. The green curves are wavefunctions in the lowest $X(v = 0)$, threshold $X(v = v_{\text{th}})$, and $B(v = 4)$ states. The double-well structure of $B^2\Sigma$ suggests a two-photon molecule dissociation pathway, using laser light at 513 and 1745 nm. (b) Relative transition strengths between $B(v')$ and $X(v)$ vibrational levels, highlighting the ‘diagonal’ nature for low v' and a bifurcation at higher v' . The latter property suggests strong coupling of $v' \sim 4$ to both the absolute ground state of the molecule and the threshold states near dissociation. (c) Expected Rabi frequencies for the controlled dissociation process, with the $v' = 4$ level highlighted as an optimal choice.

The use of STIRAP ensures coherent and efficient population transfer between the molecular and atomic continuum states, minimizing losses and avoiding unwanted heating. This scheme requires two laser wavelengths: the “upleg” transition from $X(v'' = 0)$ to $B(v' = 4)$ at 512.7 nm, and the “downleg” transition from $B(v' = 4)$ to the near-threshold continuum at 1744.7 nm. Both wavelengths are within reach using current technologies such as frequency-doubled dye lasers, diode laser systems, or fiber-based sources. The coherent nature of STIRAP also makes the process

robust against moderate fluctuations in laser intensity and detuning, provided the necessary phase stability is maintained.

In this dissociation process, the kinetic energy of the resulting H atoms is governed by energy and momentum conservation. Because the CaH bond energy is on the order of 20,000 K, dissociation near the threshold results in fragments with extremely low kinetic energies—limited primarily by the mass ratio $m_{\text{H}}/m_{\text{CaH}}$ and the initial temperature T of the molecule. In principle, the hydrogen atoms can emerge with a temperature as low as $T_{\text{H}} \sim T \cdot m_{\text{H}}/m_{\text{CaH}}$, which implies sub-microkelvin temperatures when starting from a buffer-gas-cooled or optically trapped CaH sample [162].

The scientific implications of such ultracold hydrogen sources are far-reaching. Ultracold H and D atoms could be used for high-precision spectroscopy of fundamental transitions, such as the 1S–2S line in hydrogen, which plays a central role in tests of quantum electrodynamics and the determination of fundamental constants. Additionally, access to ultracold H would enable studies of three-body recombination, quantum degenerate Bose gases with extreme interaction strengths, and hybrid molecule-atom quantum systems. These applications are difficult to access with other atomic species, underscoring the transformative potential of molecule-based atomic sources.

This strategy is further strengthened by the flexibility of the CaH molecular system. Its relatively simple electronic structure allows for accurate quantum chemistry calculations, which are essential for designing effective dissociation pathways. Moreover, the experimental control developed for optical cycling and slowing of CaH naturally lays the groundwork for precision manipulation of internal states prior to dissociation.

In future work, the development of a laser cooling and trapping system for CaD will provide access to ultracold deuterium fragments, further extending the range of accessible physical systems. The availability of both H and D at ultracold temperatures would enable side-by-side studies of isotopic effects in atomic physics, chemistry, and metrology.

8.4 Detection of Atomic Fragments after Controlled Dissociation

In order to verify and characterize the coherent dissociation of CaH molecules into ultracold Ca and H fragments, it is essential to develop robust detection techniques for both species. These detection methods serve two purposes: (1) confirming the success and efficiency of the STIRAP transfer to the dissociative continuum, and (2) directly observing and studying the properties of the atomic fragments, especially hydrogen.

8.4.1 Calcium Detection

A straightforward and effective strategy for initial verification of the dissociation process is to monitor the appearance of free calcium atoms in the science region. Since Ca atoms are not present in the system before dissociation, their detection serves as a reliable proxy for successful molecular breakup. We propose using laser-induced fluorescence (LIF) on a strong atomic transition of neutral calcium to detect the Ca fragments. The Ca I $4s^2 \ ^1S_0 \rightarrow 4s4p \ ^1P_1$ transition near 423 nm is particularly suitable due to its strong dipole moment and favored wavelength for efficient detection.

By applying resonant light near this transition and imaging the resulting fluorescence with a PMT or an EMCCD camera, one can achieve high signal-to-noise detection of even modest Ca populations. This method can be implemented in situ, using the same optical access as the dissociation lasers. Furthermore, fluorescence intensity can be calibrated against known atom numbers, enabling a quantitative measure of the STIRAP dissociation efficiency. If no Ca atoms are observed, one can conclude that either the dissociation did not occur or the process was highly inefficient, making LIF a valuable diagnostic tool in the early stages of the experiment.

8.4.2 Hydrogen Detection via Photoionization and Ion Imaging

Detecting the hydrogen (or deuterium) atom is substantially more challenging due to its lack of strong optical transitions and its low mass. Unlike calcium, hydrogen cannot be easily de-

tected using conventional fluorescence methods. To address this, we propose implementing a high-sensitivity detection method based on multiphoton ionization followed by ion imaging.

The general idea is to focus a pulsed high-energy laser beam into the region where the ultracold hydrogen cloud is expected to reside after dissociation. The laser must have sufficient photon energy and intensity to ionize hydrogen atoms through a stepwise or resonant multiphoton ionization process. One possible approach is to use a UV optical parametric oscillator (OPO) laser to drive the two photon 1S–2P transition near 242 nm (Lyman-alpha is 121 nm), with one more photon it can reach the ionization threshold of hydrogen (13.6 eV). The laser pulses can be tightly focused to maximize the intensity and local ionization probability.

Once ionized, the resulting protons (H^+) can be extracted and guided toward an ion detector using a velocity map imaging (VMI) setup. The detector, typically a microchannel plate (MCP) combined with a phosphor screen and CCD camera, can provide both timing and spatial resolution of the ions. The timing signal yields information about the arrival time and thus the energy distribution of the H^+ ions, while the spatial distribution reflects the position and momentum spread of the original hydrogen cloud.

This detection scheme offers several advantages. First, it provides unambiguous identification of hydrogen via its charge-to-mass ratio. Second, it allows for energy resolved measurements, enabling detailed studies of the dissociation dynamics.

8.4.3 Future Outlook and Integration

Developing and integrating both calcium and hydrogen detection into the experimental sequence will be a critical step in establishing controlled dissociation as a tool for ultracold hydrogen production. The Ca LIF method will likely serve as the primary method during the initial optimization phase, helping to align beams, tune laser parameters, and confirm the occurrence of dissociation. Once calcium detection is established, efforts can shift toward the more sophisticated hydrogen ionization and imaging system.

In the end, we plan to load hydrogen atoms in optical lattice to perform high precision spec-

troscopy with them. The calculated hydrogen 1S-2S transition magic wavelength is at 514.646 nm [224]. There is mature laser technology nowadays to create high-power and narrow-linewidth light at this wavelength, indicating a bright future for this experiment.

References

- [1] S. Zhang, W. Yuan, N. Bigagli, C. Warner, I. Stevenson, and S. Will, “Dressed-state spectroscopy and magic trapping of microwave-shielded nacs molecules,” *Physical Review Letters*, vol. 133, no. 26, 2024.
- [2] W. Yuan, S. Zhang, N. Bigagli, C. Warner, I. Stevenson, and S. Will, “A planar cloverleaf antenna for circularly polarized microwave fields in atomic and molecular physics experiments,” *Review of Scientific Instruments*, vol. 94, no. 12, 2023.
- [3] N. Bigagli *et al.*, “Observation of bose–einstein condensation of dipolar molecules,” *Nature*, vol. 631, no. 8020, 289–293, 2024.
- [4] L. Christakis *et al.*, “Probing site-resolved correlations in a spin system of ultracold molecules,” *Nature*, vol. 614, no. 7946, 64–69, 2023.
- [5] L. R. B. Picard *et al.*, “Entanglement and iswap gate between molecular qubits,” *Nature*, 2024.
- [6] Y. Liu and K.-K. Ni, “Bimolecular chemistry in the ultracold regime,” *Annual Review of Physical Chemistry*, vol. 73, no. 1, 73–96, 2022.
- [7] Y.-X. Liu *et al.*, “Quantum interference in atom-exchange reactions,” *Science*, vol. 384, no. 6700, pp. 1117–1121, 2024. eprint: <https://www.science.org/doi/pdf/10.1126/science.adl6570>.
- [8] J. J. Park, Y.-K. Lu, A. O. Jamison, T. V. Tscherbul, and W. Ketterle, “A feshbach resonance in collisions between triplet ground-state molecules,” *Nature*, vol. 614, no. 7946, 54–58, 2023.
- [9] T. S. Roussy *et al.*, “An improved bound on the electron’s electric dipole moment,” *Science*, vol. 381, no. 6653, pp. 46–50, 2023. eprint: <https://www.science.org/doi/pdf/10.1126/science.adg4084>.
- [10] A. Collaboration, “Improved limit on the electric dipole moment of the electron,” *Nature*, vol. 562, no. 7727, 355–360, 2018.
- [11] B. L. Augenbraun *et al.*, “Laser-cooled polyatomic molecules for improved electron electric dipole moment searches,” *New Journal of Physics*, vol. 22, no. 2, p. 022 003, 2020.
- [12] L. Bergström, “Dark matter candidates,” *New Journal of Physics*, vol. 11, no. 10, p. 105 006, Oct. 2009.

- [13] I. Kozyryev, Z. Lasner, and J. M. Doyle, “Enhanced sensitivity to ultralight bosonic dark matter in the spectra of the linear radical sroh,” *Physical Review A*, vol. 103, no. 4, 2021.
- [14] J. J. McClelland, A. V. Steele, B. Knuffman, K. A. Twedt, A. Schwarzkopf, and T. M. Wilson, “Bright focused ion beam sources based on laser-cooled atoms,” *Applied Physics Reviews*, vol. 3, no. 1, p. 011 302, 2016.
- [15] A. Grinin *et al.*, “Two-photon frequency comb spectroscopy of atomic hydrogen,” *Science*, vol. 370, no. 6520, 1061–1066, 2020.
- [16] C. E. Carlson, “The proton radius puzzle,” *Progress in Particle and Nuclear Physics*, vol. 82, pp. 59–77, 2015.
- [17] A. Beyer *et al.*, “The rydberg constant and proton size from atomic hydrogen,” *Science*, vol. 358, no. 6359, pp. 79–85, 2017.
- [18] D. G. Fried *et al.*, “Bose-einstein condensation of atomic hydrogen,” *Phys. Rev. Lett.*, vol. 81, pp. 3811–3814, 18 1998.
- [19] S. F. Cooper, C Rasor, R. G. Bullis, A. D. Brandt, and D. C. Yost, “Optical deceleration of atomic hydrogen,” *New Journal of Physics*, vol. 25, no. 9, p. 093 038, 2023.
- [20] A. Singh, L. Maisenbacher, Z. Lin, J. J. Axelrod, C. D. Panda, and H. Müller, “Dynamics of a buffer-gas-loaded, deep optical trap for molecules,” *Phys. Rev. Res.*, vol. 5, p. 033 008, 3 2023.
- [21] C. Zhang, S. T. Rittenhouse, T. V. Tscherbul, H. R. Sadeghpour, and N. R. Hutzler, “Sympathetic cooling and slowing of molecules with rydberg atoms,” *Phys. Rev. Lett.*, vol. 132, p. 033 001, 3 2024.
- [22] N. V. Vitanov, A. A. Rangelov, B. W. Shore, and K. Bergmann, “Stimulated raman adiabatic passage in physics, chemistry, and beyond,” *Rev. Mod. Phys.*, vol. 89, p. 015 006, 1 2017.
- [23] I. C. Lane, “Production of ultracold hydrogen and deuterium via doppler-cooled feshbach molecules,” *Phys. Rev. A*, vol. 92, p. 022 511, 2 2015.
- [24] J. F. Barry, “Laser cooling and slowing of a diatomic molecule,” Thesis, 2013.
- [25] A. Shayesteh, S. F. Alavi, M. Rahman, and E. Gharib-Nezhad, “Ab initio transition dipole moments and potential energy curves for the low-lying electronic states of cah,” *Chemical Physics Letters*, vol. 667, pp. 345–350, 2017.
- [26] J. Barclay W. L., M. A. Anderson, and L. M. Ziurys, “The millimeter-wave spectrum of cah (x 2sigma(+)),” *The Astrophysical Journal*, vol. 408, no. 9, pp. L65–L65, 1993.

- [27] A. Shayesteh, R. S. Ram, and P. F. Bernath, “Fourier transform emission spectra of the $A^2\Pi$ - $X^2\Sigma^+$ and $B^2\Sigma^+$ - $X^2\Sigma^+$ band systems of CaH,” *J. Mol. Spectrosc.*, vol. 288, pp. 46–51, 2013.
- [28] R. Rama, K. Tereszchuk, I. Gordon, K. Walker, and P. Bernath, “Fourier transform emission spectroscopy of the e2pi-x2sig+ transition of cah and cad,” *Journal of Molecular Spectroscopy*, vol. 266, pp. 86–91, 2011.
- [29] J. Barclay W. L., M. A. Anderson, and L. M. Ziurys, “The millimeter-wave spectrum of cah (x 2sigma(+)),” *The Astrophysical Journal*, vol. 408, no. 9, pp. L65–L65, 1993.
- [30] S. F. Vázquez-Carson, Q Sun, J Dai, D Mitra, and T Zelevinsky, “Direct laser cooling of calcium monohydride molecules,” *New Journal of Physics*, vol. 24, no. 8, p. 083 006, 2022.
- [31] M. Liu, T. Pauchard, M. Sjödin, O. Launila, P. van der Meulen, and L.-E. Berg, “Time-resolved study of the $A^2\Pi$ state of CaH by laser spectroscopy,” *J. Mol. Spectrosc.*, vol. 257, pp. 105–107, 2009.
- [32] L.-E. Berg, K. Ekvall, and S. Kelly, “Radiative lifetime measurement of vibronic levels of the $B^2\Sigma^+$ state of CaH by laser excitation spectroscopy,” *Chem. Phys. Lett.*, vol. 257, pp. 351–355, 1996.
- [33] Y. Gao and T. Gao, “Laser cooling of the alkaline-earth-metal monohydrides: Insights from an ab initio theory study,” *Phys. Rev. A*, vol. 90, 2014.
- [34] M. Ramanaiah and S. Lakshman, “True potential energy curves and Franck-Condon factors of a few alkaline earth hydrides,” *Physica 113C*, vol. 113, pp. 263–270, 1982.
- [35] N. R. Hutzler, H. I. Lu, and J. M. Doyle, “The buffer gas beam: An intense, cold, and slow source for atoms and molecules,” *Chemical Reviews*, vol. 112, no. 9, pp. 4803–4827, 2012.
- [36] J. F. Barry, “Laser cooling and slowing of a diatomic molecule,” Ph.D. dissertation, 2013.
- [37] G. Z. Iwata, “A cryogenic buffer-gas cooled beam of barium monohydride for laser slowing , cooling , and trapping,” Ph.D. dissertation, 2018.
- [38] L. W. Baum, “Laser cooling and 1D magneto-optical trapping of calcium monohydroxide a dissertation presented,” Ph.D. dissertation, 2020.
- [39] W. G. Kaenders, F. Lison, I. Müller, A. Richter, R. Wynands, and D. Meschede, “Refractive components for magnetic atom optics,” *Physical Review A - Atomic, Molecular, and Optical Physics*, vol. 54, no. 6, pp. 5067–5075, 1996.
- [40] H.-I. Lu, “Magnetic trapping of molecules via optical loading and magnetic slowing,” Tech. Rep., 2013.

- [41] R. R. Chaustowski, V. Y. Leung, and K. G. Baldwin, “Magnetic hexapole lens focusing of a metastable helium atomic beam for UV-free lithography,” *Applied Physics B: Lasers and Optics*, vol. 86, no. 3, pp. 491–496, 2007.
- [42] “Velocity-selected magnetic guiding of Zeeman-decelerated hydrogen atoms,” *European Physical Journal D*, vol. 70, no. 1, 2016.
- [43] G. Z. Iwata, R. L. McNally, and T. Zelevinsky, “High-resolution optical spectroscopy with a buffer-gas-cooled beam of BaH molecules,” *Physical Review A*, vol. 96, no. 2, pp. 1–7, 2017. arXiv: 1705.00113.
- [44] E. B. Norrgard, “Magneto-optical trapping of diatomic molecules,” Thesis, 2016.
- [45] A. Dalgarno, “Some problems in interstellar chemistry,” *International Journal of Mass Spectrometry and Ion Processes*, vol. 81, pp. 1–13, 1987.
- [46] I. W. Smith, “Laboratory astrochemistry: Gas-phase processes,” *Annual Review of Astronomy and Astrophysics*, vol. 49, no. Volume 49, 2011, pp. 29–66, 2011.
- [47] Y. Xie *et al.*, “Quantum interference in $\text{H} + \text{HD} \rightarrow \text{H}_2 + \text{D}$ between direct abstraction and roaming insertion pathways,” *Science*, vol. 368, no. 6492, pp. 767–771, 2020.
- [48] H. Son, J. J. Park, Y.-K. Lu, A. O. Jamison, T. Karman, and W. Ketterle, “Control of reactive collisions by quantum interference,” *Science*, vol. 375, no. 6584, pp. 1006–1010, 2022.
- [49] Y.-X. Liu *et al.*, “Quantum interference in atom-exchange reactions,” *Science*, vol. 384, no. 6700, pp. 1117–1121, 2024.
- [50] Y. T. Lee, “Molecular beam studies of elementary chemical processes,” *Science*, vol. 236, no. 4803, pp. 793–798, 1987.
- [51] J. Jankunas and A. Osterwalder, “Cold and controlled molecular beams: Production and applications,” *Annual Review of Physical Chemistry*, vol. 66, no. Volume 66, 2015, pp. 241–262, 2015.
- [52] W. E. Perreault, N. Mukherjee, and R. N. Zare, “Supersonic beams of mixed gases: A method for studying cold collisions,” *Chemical Physics*, vol. 514, pp. 150–153, 2018.
- [53] A. Kilaj, H. Gao, D. Rösch, U. Rivero, J. Küpper, and S. Willitsch, “Observation of different reactivities of *para* and *ortho*-water towards trapped diazenylium ions,” *Nature Communications*, vol. 9, no. 1, p. 2096, 2018.
- [54] S. Y. T. van de Meerakker, H. L. Bethlem, N. Vanhaecke, and G. Meijer, “Manipulation and control of molecular beams,” *Chemical Reviews*, vol. 112, no. 9, pp. 4828–4878, 2012.

- [55] H. L. Bethlem, G. Berden, and G. Meijer, “Decelerating neutral dipolar molecules,” *Phys. Rev. Lett.*, vol. 83, no. 8, pp. 1558–1561, 1999.
- [56] J. Jankunas and A. Osterwalder, “Cold and controlled molecular beams: Production and applications,” *Annual Review of Physical Chemistry*, vol. 66, no. Volume 66, 2015, pp. 241–262, 2015.
- [57] X. Wu, T. Gantner, M. Koller, M. Zeppenfeld, S. Chervenkov, and G. Rempe, “A cryofuge for cold-collision experiments with slow polar molecules,” *Science*, vol. 358, no. 6363, pp. 645–648, 2017.
- [58] F. B. V. Martins, V. Zhelyazkova, A. Osterwalder, and F. Merkt, “Cold ion-molecule chemistry: The very different reactions of He^+ with CO and NO,” *CHIMIA*, vol. 77, no. 4, pp. 221–224, 2023.
- [59] B. Margulis *et al.*, “Tomography of Feshbach resonance states,” *Science*, vol. 380, no. 6640, pp. 77–81, 2023.
- [60] P. F. Staanum, K. Højberre, P. S. Skyt, A. K. Hansen, and M. Drewsen, “Rotational laser cooling of vibrationally and translationally cold molecular ions,” *Nature Physics*, vol. 6, no. 4, pp. 271–274, 2010.
- [61] L. Xu, J. Toscano, and S. Willitsch, “Trapping and sympathetic cooling of conformationally selected molecular ions,” *Phys. Rev. Lett.*, vol. 132, p. 083 001, 8 2024.
- [62] H. Hirzler, R. S. Lous, E. Trimby, J. Pérez-Ríos, A. Safavi-Naini, and R. Gerritsma, “Observation of chemical reactions between a trapped ion and ultracold Feshbach dimers,” *Phys. Rev. Lett.*, vol. 128, p. 103 401, 10 2022.
- [63] M. McDonald *et al.*, “Photodissociation of ultracold diatomic strontium molecules with quantum state control,” vol. 534, pp. 122–126, 2016.
- [64] Y. Liu and K.-K. Ni, “Bimolecular chemistry in the ultracold regime,” *Annual Review of Physical Chemistry*, vol. 73, no. 1, pp. 73–96, 2022.
- [65] J. L. Bohn, A. M. Rey, and J. Ye, “Cold molecules: Progress in quantum engineering of chemistry and quantum matter,” *Science*, vol. 357, no. 6355, pp. 1002–1010, 2017.
- [66] S. S. Kondov *et al.*, “Crossover from the ultracold to the quasiclassical regime in state-selected photodissociation,” *Phys. Rev. Lett.*, vol. 121, p. 143 401, 14 2018.
- [67] S. E. Maxwell *et al.*, “High-flux beam source for cold, slow atoms or molecules,” *Phys. Rev. Lett.*, vol. 95, p. 173 201, 17 2005.

- [68] N. R. Hutzler, H.-I Lu, and J. M. Doyle, “The buffer gas beam: An intense, cold, and slow source for atoms and molecules,” *Chemical Reviews*, vol. 112, pp. 4803–4827, 2012.
- [69] M. G. Tarallo, G. Z. Iwata, and T. Zelevinsky, “BaH molecular spectroscopy with relevance to laser cooling,” *Phys. Rev. A*, vol. 93, p. 032 509, 3 2016.
- [70] J. L. Bohn, “Molecular spin relaxation in cold atom-molecule scattering,” *Phys. Rev. A*, vol. 61, p. 040 702, 4 2000.
- [71] J. Kłos, E. Tiesinga, and S. Kotchigova, “Quantum scattering of icosahedron fullerene C₆₀ with noble-gas atoms,” *Scientific Reports*, vol. 14, no. 1, p. 9267, 2024.
- [72] V. Singh *et al.*, “Chemical reactions of atomic lithium and molecular calcium monohydride at 1 K,” *Phys. Rev. Lett.*, vol. 108, p. 203 201, 20 2012.
- [73] L. Anderegg *et al.*, “Radio frequency magneto-optical trapping of CaF with high density,” *Phys. Rev. Lett.*, vol. 119, p. 103 201, 10 2017.
- [74] J. Lim *et al.*, “Laser cooled YbF molecules for measuring the electron’s electric dipole moment,” *Phys. Rev. Lett.*, vol. 120, p. 123 201, 12 2018.
- [75] S. C. Wright *et al.*, “Cryogenic buffer gas beams of AlF, CaF, MgF, YbF, Al, Ca, Yb and NO - a comparison,” *Molecular Physics*, vol. 121, no. 17-18, e2146541, 2023.
- [76] S. Truppe *et al.*, “Spectroscopic characterization of aluminum monofluoride with relevance to laser cooling and trapping,” *Phys. Rev. A*, vol. 100, p. 052 513, 5 2019.
- [77] N. B. Vilas *et al.*, “Magneto-optical trapping and sub-doppler cooling of a polyatomic molecule,” *Nature*, vol. 606, no. 7912, pp. 70–74, 2022.
- [78] B. L. Augenbraun *et al.*, “Laser-cooled polyatomic molecules for improved electron electric dipole moment searches,” *New Journal of Physics*, vol. 22, no. 2, p. 022 003, 2020.
- [79] I. Kozyryev *et al.*, “Sisyphus laser cooling of a polyatomic molecule,” *Phys. Rev. Lett.*, vol. 118, p. 173 201, 17 2017.
- [80] D. Mitra *et al.*, “Direct laser cooling of a symmetric top molecule,” *Science*, vol. 369, pp. 1366–1369, 2020.
- [81] G.-Z. Zhu *et al.*, “Functionalizing aromatic compounds with optical cycling centres,” *Nature Chemistry*, vol. 14, no. 9, pp. 995–999, 2022.
- [82] X. Liu *et al.*, “The chemistry of AlF and CaF production in buffer gas sources,” *The Journal of Chemical Physics*, vol. 157, no. 7, p. 074 305, Aug. 2022.

- [83] Q. Sun *et al.*, “Chemistry in a cryogenic buffer gas cell,” *arXiv:2501.05613*, 2025.
- [84] R. Koots *et al.*, “Theoretical investigation of CaH production in buffer gas sources,” *manuscript in preparation*, 2024.
- [85] P. C. Souers, C. K. Briggs, J. W. Pyper, and R. T. Tsugawa, “Hydrogen vapor pressures from 4 to 30 k: A review,” Lawrence Livermore Lab, Report, 1977.
- [86] H. J. Hoge and R. D. Arnold, “Vapor pressures of hydrogen, deuterium, and hydrogen deuteride and dew-point pressures of their mixtures,” *J. Research Natl. Bur. Standards*, vol. 47, no. 2, p. 2, Aug. 1951.
- [87] R. McNally, I. Kozyrev, S. Vazquez-Carson, K. Wenz, T. Wang, and T. Zelevinsky, “Optical cycling, radiative deflection and laser cooling of barium monohydride,” *New Journal of Physics*, vol. 22, p. 083 047, 2020.
- [88] J. Dai, Q. Sun, B. C. Riley, D. Mitra, and T. Zelevinsky, “Laser cooling of a fermionic molecule,” *Phys. Rev. Res.*, vol. 6, p. 033 135, 3 2024.
- [89] Q. Sun *et al.*, “Probing the limits of optical cycling in a predissociative diatomic molecule,” *Phys. Rev. Res.*, vol. 5, p. 043 070, 4 2023.
- [90] D. G. Truhlar and J. T. Muckerman, “Reactive scattering cross sections III: Quasiclassical and semiclassical methods,” in *Atom-molecule collision theory: A guide for the experimentalist*, Plenum Press, New York, 1979, pp. 505 –561.
- [91] J. Pérez-Ríos, “Cold chemical reactions between molecular ions and neutral atoms,” in *An introduction to cold and ultracold chemistry: Atoms, molecules, ions and Rydbergs*, Springer International Publishing, 2020, pp. 215 –234, ISBN: 9783030559366.
- [92] R. Koots and J. Pérez-Ríos, “PyQCAMS: Python quasi-classical atom-molecule scattering,” *Atoms*, vol. 12, no. 5, p. 5, 2024.
- [93] S. M. Skoff *et al.*, “Diffusion, thermalization, and optical pumping of YbF molecules in a cold buffer-gas cell,” *Phys. Rev. A*, vol. 83, p. 023 418, 2 2011.
- [94] H. J. Metcalf and P. v. d. Straten, *Laser Cooling and Trapping*. 1999.
- [95] A. H. Myerson *et al.*, “High-fidelity readout of trapped-ion qubits,” *Phys. Rev. Lett.*, vol. 100, p. 200 502, 20 2008.
- [96] R. Blatt and C. F. Roos, “Quantum simulations with trapped ions,” *Nature Physics*, vol. 8, no. 4, pp. 277–284, 2012.

- [97] L. Anderegg *et al.*, “An optical tweezer array of ultracold molecules,” *Science*, vol. 365, no. 6458, pp. 1156–1158, 2019.
- [98] Y. Wu, J. J. Burau, K. Mehling, J. Ye, and S. Ding, “High phase-space density of laser-cooled molecules in an optical lattice,” *Phys. Rev. Lett.*, vol. 127, p. 263201, 26 2021.
- [99] B. Hemmerling *et al.*, “Laser slowing of caf molecules to near the capture velocity of a molecular mot,” *Journal of Physics B: Atomic, Molecular and Optical Physics*, vol. 49, no. 17, p. 174001, 2016.
- [100] H. J. Williams *et al.*, “Characteristics of a magneto-optical trap of molecules,” *New Journal of Physics*, vol. 19, no. 11, p. 113035, 2017.
- [101] P. Aggarwal *et al.*, “Deceleration and trapping of srf molecules,” *Phys. Rev. Lett.*, vol. 127, p. 173201, 17 2021.
- [102] M. Zeppenfeld *et al.*, “Sisyphus cooling of electrically trapped polyatomic molecules,” *Nature*, vol. 491, pp. 570–573, 2012.
- [103] X. Wu, T. Gantner, M. Koller, M. Zeppenfeld, S. Chervenkov, and G. Rempe, “A cryofuge for cold-collision experiments with slow polar molecules,” *Science*, vol. 358, no. 6363, pp. 645–648, 2017.
- [104] B. L. Augenbraun *et al.*, “Zeeman-sisyphus deceleration of molecular beams,” *Phys. Rev. Lett.*, vol. 127, p. 263002, 26 2021.
- [105] M. D. DiRosa, “Laser-cooling molecules: Concept, candidates, and supporting hyperfine-resolved measurements of rotational lines in the $A - X(0, 0)$ band of CaH,” *The European Physical Journal D*, vol. 31, pp. 395–402, 2004.
- [106] S. F. Vázquez-Carson, Q Sun, J Dai, D Mitra, and T Zelevinsky, “Direct laser cooling of calcium monohydride molecules,” *New J. Phys.*, vol. 24, no. 8, p. 083006, 2022.
- [107] G. Herzberg, *Molecular Spectra and Molecular Structure, I. Spectra of Diatomic Molecules*. 1950.
- [108] W. Demtröder, *Molecular Physics*. 2005.
- [109] J. von Neumann and E. Wigner, “Über merkwürdige diskrete eigenwerte. über das verhalten von eigenwerten bei adiabatischen prozessen,” *Phys. Z.*, vol. 30, p. 467, 1929.
- [110] E. Teller, “The crossing of potential surfaces.,” *The Journal of Physical Chemistry*, vol. 41, no. 1, pp. 109–116, 1937.

- [111] C. A. Mead, “The ”noncrossing” rule for electronic potential energy surfaces: The role of time-reversal invariance,” *The Journal of Chemical Physics*, vol. 70, no. 5, pp. 2276–2283, 1979.
- [112] P. K. H-J. Werner *et al.*, “Molpro, version 2022.3, a package of ab initio programs, see <https://www.molpro.net>,” 2022.
- [113] H.-J. Werner, P. J. Knowles, G. Knizia, F. R. Manby, and M. Schütz, “Molpro: A general-purpose quantum chemistry program package,” *Wiley Interdisciplinary Reviews: Computational Molecular Science*, vol. 2, no. 2, pp. 242–253, 2012.
- [114] H.-J. Werner *et al.*, “The molpro quantum chemistry package,” *The Journal of chemical physics*, vol. 152, no. 14, 2020.
- [115] A. Shayesteh, S. F. Alavi, M. Rahman, and E. Gharib-Nezhad, “Ab initio transition dipole moments and potential energy curves for the low-lying electronic states of cah,” *Chemical Physics Letters*, vol. 667, pp. 345–350, 2017.
- [116] J. Koput and K. A. Peterson, “Ab initio potential energy surface and vibrational-rotational energy levels of $x2\Sigma^+$ caoh,” *The Journal of Physical Chemistry A*, vol. 106, no. 41, pp. 9595–9599, 2002.
- [117] T. H. Dunning Jr, “Gaussian basis sets for use in correlated molecular calculations. i. the atoms boron through neon and hydrogen,” *The Journal of chemical physics*, vol. 90, no. 2, pp. 1007–1023, 1989.
- [118] P. J. Knowles and H.-J. Werner, “An efficient second-order mc scf method for long configuration expansions,” *Chemical physics letters*, vol. 115, no. 3, pp. 259–267, 1985.
- [119] H.-J. Werner and P. J. Knowles, “An efficient internally contracted multiconfiguration–reference configuration interaction method,” *The Journal of chemical physics*, vol. 89, no. 9, pp. 5803–5814, 1988.
- [120] P. J. Knowles and H.-J. Werner, “Internally contracted multiconfiguration-reference configuration interaction calculations for excited states,” *Theoretica chimica acta*, vol. 84, pp. 95–103, 1992.
- [121] K. Shamasundar, G. Knizia, and H.-J. Werner, “A new internally contracted multi-reference configuration interaction method,” *The Journal of chemical physics*, vol. 135, no. 5, p. 054 101, 2011.
- [122] A. Berning, M. Schweizer, H.-J. Werner, P. J. Knowles, and P. Palmieri, “Spin-orbit matrix elements for internally contracted multireference configuration interaction wavefunctions,” *Molecular Physics*, vol. 98, no. 21, pp. 1823–1833, 2000.

- [123] D. T. Colbert and W. H. Miller, “A novel discrete variable representation for quantum mechanical reactive scattering via the s-matrix kohn method,” *The Journal of chemical physics*, vol. 96, no. 3, pp. 1982–1991, 1992.
- [124] T. Busch, A. D. Esposti, and H.-J. Werner, “Analytical energy gradients for multiconfiguration self-consistent field wave functions with frozen core orbitals,” *The Journal of chemical physics*, vol. 94, no. 10, pp. 6708–6715, 1991.
- [125] R. Baer, *Electron density functional theory*. Fritz Haber Center for Molecular Dynamics, 2016.
- [126] D. Neuhauser and M. Baer, “The time-dependent schrödinger equation: Application of absorbing boundary conditions,” *The Journal of chemical physics*, vol. 90, no. 8, pp. 4351–4355, 1989.
- [127] D. Neuhauser and M. Baer, “The application of wave packets to reactive atom–diatom systems: A new approach,” *The Journal of chemical physics*, vol. 91, no. 8, pp. 4651–4657, 1989.
- [128] D. Neuhauser, “State-to-state reactive scattering amplitudes from single-arrangement propagation with absorbing potentials,” *The Journal of chemical physics*, vol. 93, no. 11, pp. 7836–7842, 1990.
- [129] D. Neuhauser, “*Molecular Scattering: Very-Short-Range Imaginary Potentials, Absorbing-Potentials, and Flux-Amplitude Expressions*,” *The Journal of Chemical Physics*, vol. 103, no. 19, pp. 8513–8527, 1995.
- [130] B. Efron, “Bootstrap methods: Another look at the jackknife,” *The Annals of Statistics*, vol. 7, no. 1, pp. 1–26, 1979.
- [131] B. Efron and R. J. Tibshirani, *An Introduction to the Bootstrap* (Monographs on Statistics and Applied Probability 57). Boca Raton, Florida, USA: Chapman & Hall/CRC, 1993.
- [132] A. C. Davison and D. V. Hinkley, *Bootstrap Methods and their Application* (Cambridge Series in Statistical and Probabilistic Mathematics). Cambridge University Press, 1997.
- [133] E. L. Raab, M. Prentiss, A. Cable, S. Chu, and D. E. Pritchard, “Trapping of neutral sodium atoms with radiation pressure,” *Phys. Rev. Lett.*, vol. 59, pp. 2631–2634, 23 1987.
- [134] W. D. Phillips, “Nobel lecture: Laser cooling and trapping of neutral atoms,” *Rev. Mod. Phys.*, vol. 70, pp. 721–741, 1998.
- [135] I. Bloch, J. Dalibard, and W. Zwerger, “Many-body physics with ultracold gases,” *Rev. Mod. Phys.*, vol. 80, pp. 885–964, 3 2008.

- [136] M. Morgado and S. Whitlock, “Quantum simulation and computing with Rydberg-interacting qubits,” *AVS Quantum Sci.*, vol. 3, p. 023 501, 2021.
- [137] T. Bothwell *et al.*, “Resolving the gravitational redshift across a millimetre-scale atomic sample,” *Nature*, vol. 602, pp. 420–424, 2022.
- [138] M. S. Safronova, D. Budker, D. DeMille, D. F. J. Kimball, A. Derevianko, and C. W. Clark, “Search for new physics with atoms and molecules,” *Rev. Mod. Phys.*, vol. 90, p. 025 008, 2 2018.
- [139] M. R. Tarbutt, “Laser cooling of molecules,” *Contemp. Phys.*, vol. 59, pp. 356–376, 2018.
- [140] The ACME Collaboration: V. Andreev *et al.*, “Improved limit on the electric dipole moment of the electron,” *Nature*, vol. 562, p. 355, 2018.
- [141] W. B. Cairncross and J. Ye, “Atoms and molecules in the search for time-reversal symmetry violation,” *Nat. Rev. Phys.*, vol. 1, p. 510, 2019.
- [142] B. Augenbraun *et al.*, “Laser-cooled polyatomic molecules for improved electron electric dipole moment searches,” *New Journal of Physics*, vol. 22, p. 022 003, 2020.
- [143] J. W. Park, Z. Z. Yan, H. Loh, S. A. Will, and M. W. Zwierlein, “Second-scale nuclear spin coherence time of ultracold $^{23}\text{Na}^{40}\text{K}$ molecules,” *Science*, vol. 357, pp. 372–375, 2017.
- [144] J. A. Blackmore *et al.*, “Ultracold molecules for quantum simulation: Rotational coherences in CaF and RbCs,” *Quantum Sci. Technol.*, vol. 4, p. 014 010, 2019.
- [145] R. Sawant *et al.*, “Ultracold polar molecules as qudits,” *New J. Phys.*, vol. 22, p. 013 027, 2020.
- [146] K. R. A. Hazzard *et al.*, “Many-body dynamics of dipolar molecules in an optical lattice,” *Phys. Rev. Lett.*, vol. 113, p. 195 302, 19 2014.
- [147] J. F. Barry, E. S. Shuman, and D. DeMille, “A bright, slow cryogenic molecular beam source for free radicals,” *Phys. Chem. Chem. Phys.*, vol. 13, pp. 18 936–18 947, 2011.
- [148] E. S. Shuman, J. Barry, and D. DeMille, “Laser cooling of a diatomic molecule,” *Nature*, vol. 467, pp. 820–823, 7317 2010.
- [149] S. Truppe *et al.*, “Molecules cooled below the Doppler limit,” *Nat. Phys.*, vol. 13, pp. 1173–1176, 2017.
- [150] A. L. Collopy *et al.*, “3D magneto-optical trap of yttrium monoxide,” *Phys. Rev. Lett.*, vol. 121, p. 213 201, 21 2018.

- [151] R. L. McNally, I. Kozryev, S. Vazquez-Carson, K. Wenz, T. Wang, and T. Zelevinsky, “Optical cycling, radiative deflection and laser cooling of barium monohydride ($^{138}\text{Ba}^1\text{H}$),” *New J. Phys.*, vol. 22, p. 083 047, 2020.
- [152] N. B. Vilas *et al.*, “Magneto-optical trapping and sub-doppler cooling of a polyatomic molecule,” *arXiv:2112.08349*, 2021.
- [153] E. Tiesinga, P. J. Mohr, D. B. Newell, and B. N. Taylor, “CODATA recommended values of the fundamental physical constants: 2018,” *Rev. Mod. Phys.*, vol. 93, p. 025 010, 2021.
- [154] F. Biraben, “Spectroscopy of atomic hydrogen,” *The European Physical Journal Special Topics*, vol. 172, pp. 109–119, 2009.
- [155] D. Fried *et al.*, “Bose-Einstein condensation of atomic hydrogen,” *Phys. Rev. Lett.*, vol. 81, p. 8311, 1998.
- [156] C. L. Cesar *et al.*, “Two-photon spectroscopy of trapped atomic hydrogen,” *Phys. Rev. Lett.*, vol. 77, pp. 255–258, 2 1996.
- [157] M. Ahmadi *et al.*, “Observation of the 1S – 2S transition in trapped antihydrogen,” *Nature*, vol. 541, pp. 506–510, 2017.
- [158] C. G. Parthey *et al.*, “Improved measurement of the hydrogen 1S–2S transition frequency,” *Phys. Rev. Lett.*, vol. 107, p. 203 001, 20 2011.
- [159] A. Grinin *et al.*, “Two-photon frequency comb spectroscopy of atomic hydrogen,” *Science*, vol. 370, pp. 1061–1066, 2020. eprint: <https://www.science.org/doi/pdf/10.1126/science.abc7776>.
- [160] A. D. Brandt, S. F. Cooper, C. Rasor, Z. Burkley, A. Matveev, and D. C. Yost, “Measurement of the $2\text{S}_{1/2} – 8\text{D}_{5/2}$ transition in hydrogen,” *Phys. Rev. Lett.*, vol. 128, p. 023 001, 2 2022.
- [161] M. G. Raizen, “Comprehensive control of atomic motion,” *Science*, vol. 324, pp. 1403–1406, 2009.
- [162] I. C. Lane, “Production of ultracold hydrogen and deuterium via Doppler-cooled Feshbach molecules,” *Phys. Rev. A*, vol. 92, p. 022 511, 2 2015.
- [163] S. A. Jones, “An ion trap source of cold atomic hydrogen via photodissociation of the BaH^+ molecular ion,” *New J. Phys.*, vol. 24, p. 023 016, 2022.
- [164] H.-I. Lu, J. Rasmussen, M. J. Wright, D. Patterson, and J. M. Doyle, “A cold and slow molecular beam,” *Phys. Chem. Chem. Phys.*, vol. 13, pp. 18 986–18 990, 2011.

- [165] J. D. Weinstein, R. deCarvalho, T. Guillet, B. Friedrich, and J. M. Doyle, “Magnetic trapping of calcium monohydride molecules at millikelvin temperatures,” *Nature*, vol. 395, pp. 148–150, 1998.
- [166] B. K. Stuhl, B. C. Sawyer, D. Wang, and J. Ye, “Magneto-optical trap for polar molecules,” *Phys. Rev. Lett.*, vol. 101, p. 243 002, 2008.
- [167] J. F. Barry, D. J. McCarron, E. B. Norrgard, M. H. Steinecker, and D. DeMille, “Magneto-optical trapping of a diatomic molecule,” *Nature*, vol. 512, pp. 286–289, 2014.
- [168] J. Lim *et al.*, “Laser cooled YbF molecules for measuring the electron’s electric dipole moment,” *Phys. Rev. Lett.*, vol. 120, p. 123 201, 12 2018.
- [169] I. Kozyryev, T. C. Steimle, P. Yu, D.-T. Nguyen, and J. M. Doyle, “Determination of CaOH and CaOCH₃ vibrational branching ratios for direct laser cooling and trapping,” *New Journal of Physics*, vol. 21, no. 5, p. 052 002, 2019.
- [170] X. Cheng, J. Bai, J.-P. Yin, and H.-L. Wang, “Franck-Condon factors and band origins for MgH in the A²Π – X²Σ⁺ system,” *Chinese J. Chem. Phys.*, vol. 28, pp. 253–256, 2015.
- [171] M. G. Tarallo, G. Z. Iwata, and T. Zelevinsky, “BaH molecular spectroscopy with relevance to laser cooling,” *Phys. Rev. A*, vol. 93, no. 3, 2016.
- [172] A. N. Pathak and P. D. Singh, “Franck-Condon factors and r-centroids of the CaH (B – X) band system,” *Proc. Phys. Soc.*, vol. 87, pp. 1008–1009, 1966.
- [173] R. J. Hendricks, D. A. Holland, S. Truppe, B. E. Sauer, and M. R. Tarbutt, “Vibrational branching ratios and hyperfine structure of ¹¹BH and its suitability for laser cooling,” *Front. Phys.*, vol. 2, 2014.
- [174] E. B. Norrgard, D. J. McCarron, M. H. Steinecker, M. R. Tarbutt, and D. DeMille, “Sub-millikelvin dipolar molecules in a radio-frequency magneto-optical trap,” *Phys. Rev. Lett.*, vol. 116, p. 063 004, 6 2016.
- [175] L. Anderegg *et al.*, “Laser cooling of optically trapped molecules,” *Nat. Phys.*, vol. 14, pp. 890–893, 2018.
- [176] L. Caldwell *et al.*, “Deep laser cooling and efficient magnetic compression of molecules,” *Phys. Rev. Lett.*, vol. 123, p. 033 202, 3 2019.
- [177] S. Ding, Y. Wu, I. A. Finneran, J. J. Burau, and J. Ye, “Sub-Doppler cooling and compressed trapping of YO molecules at μK temperatures,” *Phys. Rev. X*, vol. 10, p. 021 049, 2 2020.

- [178] O. Emile, R. Kaiser, C. Gerz, H. Wallis, A. Aspect, and C. Cohen-Tannoudji, “Magnetically assisted Sisyphus effect,” *J. Phys. II France*, vol. 3, pp. 1709–1733, 1993.
- [179] B. Sheehy, S.-Q. Shang, P. van der Straten, S. Hatamian, and H. Metcalf, “Magnetic-field-induced laser cooling below the Doppler limit,” *Phys. Rev. Lett.*, vol. 64, pp. 858–861, 8 1990.
- [180] J. A. Devlin and M. R. Tarbutt, “Three-dimensional Doppler, polarization-gradient, and magneto-optical forces for atoms and molecules with dark states,” *New J. Phys.*, vol. 18, p. 123 017, 2016.
- [181] J. A. Devlin and M. R. Tarbutt, “Laser cooling and magneto-optical trapping of molecules analyzed using optical Bloch equations and the Fokker-Planck-Kramers equation,” *Phys. Rev. A*, vol. 98, p. 063 415, 6 2018.
- [182] K. Wenz, “*Nuclear Schiff moment search in thallium fluoride molecular beam: Rotational cooling*,” Ph.D. Thesis, Columbia University, 2021.
- [183] K. Wenz, I. Kozyryev, R. L. McNally, L. Aldridge, and T. Zelevinsky, “Large molasses-like cooling forces for molecules using polychromatic optical fields: A theoretical description,” *Phys. Rev. Research*, vol. 2, p. 043 377, 2020.
- [184] S. Ospelkaus *et al.*, “Quantum-state controlled chemical reactions of ultracold potassium-rubidium molecules,” *Science*, vol. 327, no. 5967, pp. 853–857, 2010.
- [185] L. Christakis *et al.*, “Probing site-resolved correlations in a spin system of ultracold molecules,” *Nature*, vol. 614, no. 7946, pp. 64–69, 2023.
- [186] N. Bigagli *et al.*, “Observation of Bose-Einstein condensation of dipolar molecules,” *arXiv:2312.10965*, 2023.
- [187] C. M. Holland, Y. Lu, and L. W. Cheuk, “On-demand entanglement of molecules in a reconfigurable optical tweezer array,” *Science*, vol. 382, no. 6675, pp. 1143–1147, 2023.
- [188] Y. Bao *et al.*, “Dipolar spin-exchange and entanglement between molecules in an optical tweezer array,” *Science*, vol. 382, no. 6675, pp. 1138–1143, 2023.
- [189] T. S. Roussy *et al.*, “An improved bound on the electron’s electric dipole moment,” *Science*, vol. 381, no. 6653, pp. 46–50, 2023.
- [190] D. Mitra, K. H. Leung, and T. Zelevinsky, “Quantum control of molecules for fundamental physics,” *Phys. Rev. A*, vol. 105, p. 040 101, 2022.
- [191] J.-R. Li *et al.*, “Tuning of dipolar interactions and evaporative cooling in a three-dimensional molecular quantum gas,” *Nat. Phys.*, vol. 17, no. 10, pp. 1144–1148, 2021.

- [192] A. Schindewolf *et al.*, “Evaporation of microwave-shielded polar molecules to quantum degeneracy,” *Nature*, vol. 607, no. 7920, pp. 677–681, 2022.
- [193] J. J. Park, Y.-K. Lu, A. O. Jamison, and W. Ketterle, “Magnetic trapping of ultracold molecules at high density,” *Nat. Phys.*, vol. 19, no. 11, pp. 1567–1572, 2023.
- [194] F. Kogel, M. Rockenhäuser, R. Albrecht, and T. Langen, “A laser cooling scheme for precision measurements using fermionic barium monofluoride ($^{137}\text{Ba}^{19}\text{F}$) molecules,” *New J. Phys.*, vol. 23, no. 9, p. 095 003, 2021.
- [195] R. Bause, A. Christianen, A. Schindewolf, I. Bloch, and X.-Y. Luo, “Ultracold sticky collisions: Theoretical and experimental status,” *The Journal of Physical Chemistry A*, vol. 127, no. 3, pp. 729–741, 2023.
- [196] N. R. Cooper and G. V. Shlyapnikov, “Stable topological superfluid phase of ultracold polar fermionic molecules,” *Phys. Rev. Lett.*, vol. 103, p. 155 302, 15 2009.
- [197] A. Micheli, G. K. Brennen, and P. Zoller, “A toolbox for lattice-spin models with polar molecules,” *Nat. Phys.*, vol. 2, no. 5, pp. 341–347, 2006.
- [198] E. B. Norrgard, D. S. Barker, S. Eckel, J. A. Fedchak, N. N. Klimov, and J. Scherschligt, “Nuclear-spin dependent parity violation in optically trapped polyatomic molecules,” *Communications Physics*, vol. 2, no. 1, p. 77, 2019.
- [199] Y. Hao *et al.*, “Nuclear spin-dependent parity-violating effects in light polyatomic molecules,” *Phys. Rev. A*, vol. 102, p. 052 828, 5 2020.
- [200] Y. Zeng, A. Jadbabaie, A. N. Patel, P. Yu, T. C. Steinle, and N. R. Hutzler, “Optical cycling in polyatomic molecules with complex hyperfine structure,” *Phys. Rev. A*, vol. 108, p. 012 813, 1 2023.
- [201] C. I. Frum, J. J. Oh, E. A. Cohen, and H. M. Pickett, “Rotational spectra of the $X^2\Sigma^+$ states of CaH and CaD,” *The Astrophysical Journal*, vol. 408, no. 1, pp. L61–L64, 1993.
- [202] E. GharibNezhad, A. Shayesteh, and P. Bernath, “Fourier transform emission spectra of the $A^2\Pi \rightarrow X^2\Sigma^+$ and $B^2\Sigma^+ \rightarrow X^2\Sigma^+$ transitions of CaD,” *Journal of Molecular Spectroscopy*, vol. 281, pp. 47–50, 2012.
- [203] S. F. Alavi and A. Shayesteh, “Einstein A coefficients for rovibronic lines of the $A^2\Pi \rightarrow X^2\Sigma^+$ and $B^2\Sigma^+ \rightarrow X^2\Sigma^+$ transitions of CaH and CaD,” *Monthly Notices of the Royal Astronomical Society*, vol. 474, no. 1, pp. 2–11, 2018.
- [204] T. V. Tscherbul and J. Kłos, “Magnetic tuning of ultracold barrierless chemical reactions,” *Phys. Rev. Res.*, vol. 2, p. 013 117, 1 2020.

- [205] M. Boshier *et al.*, “Precision spectroscopy of hydrogen and deuterium,” *Nature*, vol. 330, no. 6147, pp. 463–465, 1987.
- [206] A. Grinin *et al.*, “Two-photon frequency comb spectroscopy of atomic hydrogen,” *Science*, vol. 370, no. 6520, pp. 1061–1066, 2020.
- [207] R. Pohl *et al.*, “Laser spectroscopy of muonic deuterium,” *Science*, vol. 353, no. 6300, pp. 669–673, 2016.
- [208] R. M. Potvliege, A. Nicolson, M. P. A. Jones, and M. Spannowsky, “Deuterium spectroscopy for enhanced bounds on physics beyond the standard model,” *Phys. Rev. A*, vol. 108, p. 052 825, 5 2023.
- [209] M. Zaghoo, T. R. Boehly, J. R. Rygg, P. M. Celliers, S. X. Hu, and G. W. Collins, “Breakdown of Fermi degeneracy in the simplest liquid metal,” *Phys. Rev. Lett.*, vol. 122, p. 085 001, 8 2019.
- [210] A. D. Bulanov, O. Y. Troshin, and V. V. Balabanov, “Synthesis of high-purity calcium hydride,” *Russian Journal of Applied Chemistry*, vol. 77, no. 6, pp. 875–877, 2004.
- [211] E. G. C. P. van Loon, M. I. Katsnelson, and M. Lemeshko, “Ultralong-range order in the Fermi-Hubbard model with long-range interactions,” *Phys. Rev. B*, vol. 92, p. 081 106, 8 2015.
- [212] H. G. Floss and S. Lee, “Chiral methyl groups: Small is beautiful,” *Accounts of Chemical Research*, vol. 26, no. 3, pp. 116–122, 1993.
- [213] M. Quack, G. Seyfang, and G. Wichmann, “Parity violation in chiral molecules: From theory towards spectroscopic experiment and the evolution of biomolecular homochirality,” in *Chiral Matter*, pp. 209–268.
- [214] J. D. Weinstein, “Magnetic trapping of atomic chromium and molecular calcium monohydride,” Ph.D. dissertation, Harvard University, 2002.
- [215] A. Shayesteh, S. F. Alavi, M. Rahman, and E. Gharib-Nezhad, “Ab initio transition dipole moments and potential energy curves for the low-lying electronic states of cah,” *Chemical Physics Letters*, vol. 667, pp. 345–350, 2017.
- [216] T. Leininger and G. H. Jeung, “Ab initio calculation of rovibronic transition spectra of cah,” *The Journal of Chemical Physics*, vol. 103, no. 10, pp. 3942–3949, 1995.
- [217] T. C. Steimle, J. Chen, and J. Gengler, “The permanent electric dipole moments of calcium monohydride, cah,” *Journal of Chemical Physics*, vol. 121, no. 2, pp. 829–834, 2004.

- [218] D. J. Berkeland and M. G. Boshier, “Destabilization of dark states and optical spectroscopy in zeeman-degenerate atomic systems,” *Physical Review A*, vol. 65, no. 3, 2002.
- [219] J. A. Devlin and M. R. Tarbutt, “Three-dimensional doppler, polarization-gradient, and magneto-optical forces for atoms and molecules with dark states,” *New Journal of Physics*, vol. 18, 2016.
- [220] R. Bause, A. Christianen, A. Schindewolf, I. Bloch, and X.-Y. Luo, “Ultracold sticky collisions: Theoretical and experimental status,” *J. Phys. Chem. A*, vol. 127, pp. 729–741, 2023.
- [221] J. J. Park *et al.*, “Spectrum of Feshbach resonances in NaLi + Na collisions,” *Phys. Rev. X*, vol. 13, p. 031 018, 2023.
- [222] T. V. Tscherbul and J. Kłos, “Magnetic tuning of ultracold barrierless chemical reactions,” *Phys. Rev. Res.*, vol. 2, p. 013 117, 2020.
- [223] V. Singh *et al.*, “Chemical reactions of atomic lithium and molecular calcium monohydride at 1 K,” vol. 108, p. 203 201, 2012.
- [224] A. Kawasaki, “Magic wavelength for the hydrogen 1S–2S transition,” *Phys. Rev. A*, vol. 92, p. 042 507, 4 2015.

Appendix A: Indirect Measurement of Beam Forward Velocity

For a significant portion of my PhD research (2019–2023), we lacked a crucial experimental tool, the A-E 1668nm laser, which is necessary to perform direct measurements of the molecular beam's forward velocity distribution (FVD). The ability to characterize FVD is of paramount importance for any experimental setup aiming to decelerate and eventually trap molecular beams efficiently. Without this key, it was challenging to optimize our beam slowing and trapping techniques, leading to significant experimental difficulties and uncertainties in our results.

In the case of atomic beams, particularly those consisting of alkali or alkaline earth atoms, measuring the FVD is relatively straightforward (shown in Fig A.1). The fundamental requirement is a laser capable of addressing the primary cycling transition of the atom, which is characterized by a specific wavelength, denoted as λ . The experimental setup typically involves directing this laser at an angle θ (commonly around 45 degrees) with respect to the atomic beam propagation axis. A photon collection system, composed of a lens assembly along with a photodetector such as a photomultiplier tube (PMT), is strategically positioned to detect fluorescence signals. The methodology for extracting the FVD relies on attempting different laser frequencies in different experimental runs, and record the flux of photons as a function of time. The FVD is assumed to be roughly unchanged in neighboring runs. Due to the Doppler effect, atoms moving with a forward velocity v_f experience a frequency shift proportional to $\frac{v_f \cos \theta}{\lambda}$, requiring the laser to be detuned accordingly, either to the red or blue side, depending on the laser's propagation direction. By systematically varying the laser frequency, atoms with different velocity components can be selectively excited, thereby enabling a precise reconstruction of the FVD. For reference, a velocity variation of 1 m/s corresponds approximately to a frequency detuning of 1 MHz in typical experimental conditions.

However, when dealing with molecular beams, the situation becomes significantly more complex due to several inherent challenges. The first major complication arises from the inherently

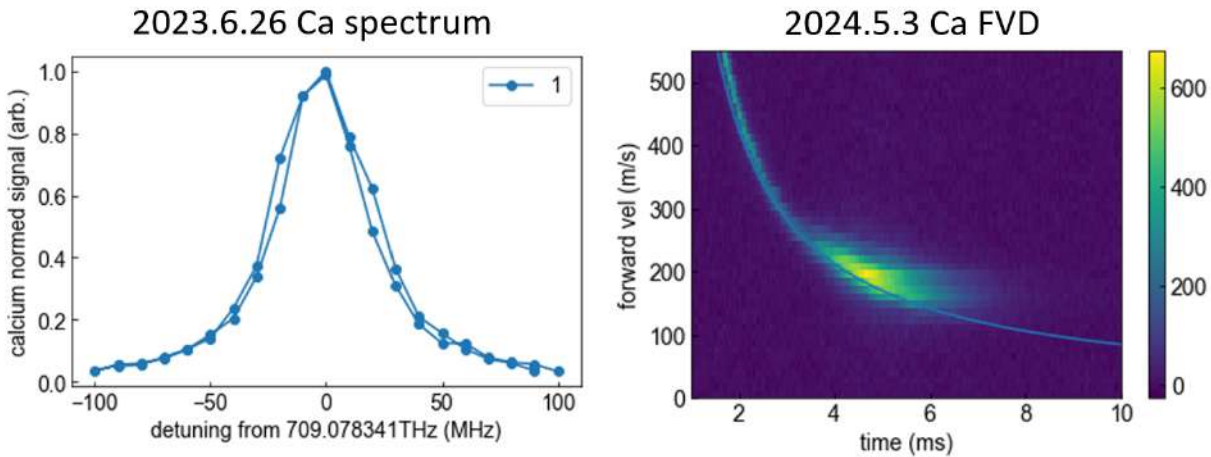


Figure A.1: Left is calcium $^1S_0 \rightarrow ^1P_1$ transition at 423nm in a beam configuration, right is the FVD measurement result using methods in the text.

lower molecular beam yield and slower optical cycling rates compared to atomic systems. This results in the fact that LIF signals are a few orders of magnitude weaker than those observed in atomic experiments, and sometimes in our system, the LIF signals can be significantly weaker than variation of detected background light. Consequently, the signal-to-noise ratio (SNR) becomes a critical limiting factor that requires careful evaluation and optimization. To the best of my knowledge, most diatomic molecule experiments struggle with achieving good SNR via conventional FVD measurement techniques (simply using cycling lasers). Note that even with meticulous experimental efforts—such as blackening the vacuum chamber interior, installing light absorbers and baffles along laser beam paths, and implementing Fourier filtering techniques—the SNR remains insufficient for fast, reliable experimental diagnostics.

The second major challenge stems from the intricate internal energy level structures of molecules. Unlike atoms, which typically exhibit simple cycling transitions, molecules like calcium monohydride (CaH) possess complex hyperfine level structures, with energy spacings on the order of 50 MHz to 100 MHz. As a result, even when employing a single-frequency laser to probe molecules with a forward velocity v_f , there is a substantial likelihood of unintentionally addressing molecules with velocities differing by approximately 50-100 m/s. This unintended excitation introduces significant ambiguities in data interpretation, as the detected fluorescence signal originates from a

broader velocity distribution than intended. While it is theoretically possible to develop sophisticated deconvolution algorithms to mitigate this issue, such solutions introduce additional computational complexity and are beyond the scope of this discussion.

Given these challenges, the most effective method developed in recent years, two-photon background-free (BGF) detection, circumvents both of the aforementioned problems by employing alternative measurement techniques that enhance SNR and mitigate velocity-space ambiguities, as shown in Fig A.2. The core of BGF is about finding a third state that can be E1 connected to both states, and in the case of CaH, $E^2\Pi_{1/2}$ state seems the best option. The idea is as following: we first use a set of lasers with sidebands to excite the molecules from $X^2\Sigma^+$ N=1 state to $A^2\Pi_{1/2}$ J'=3/2 state (695 nm) in a velocity insensitive way (90 degree with molecular beam), while shooting a laser to excite the molecules from $A^2\Pi_{1/2}$ state to $E^2\Pi_{1/2}$ state (1668 nm) in a velocity sensitive way (45 degree with molecular beam), and use a photon detection system (PMT or EMCCD plus bandpass filters) to capture the photons when molecules decay from $E^2\Pi_{1/2}$ state to $X^2\Sigma^+$ state (490 nm). Since there is no longer sources of 490 nm photons other than molecules, the SNR is significantly improved compared to non-background-free scheme by around two orders of magnitude for us, allowing us to detect the FVD of molecules.

Accounting for the fact that the transition matrix element (radial part) is expected to be an order smaller than $X^2\Sigma^+$ to $A^2\Pi_{1/2}$, and the $A^2\Pi_{1/2}$ to $E^2\Pi_{1/2}$ photon needs to be scattered while the molecule is at $A^2\Pi_{1/2}$ state, which lasts only 33 ns, we need a high power laser source, ideally delivering watts of power. The transition wavelength between $A^2\Pi_{1/2}$ and $E^2\Pi_{1/2}$ state is around 1668 nm, which is in an awkward wavelength range where there is barely any mature fiber technology. There are diodes from Seminex (TO0-174-161) that delivers 100mW of light, sufficient for initial studies, but cannot serve the final purpose. We eventually found a Finland company, Vexlum, whose VALO SF VECSEL lasers can do frequency conversion and produce 1668 nm with almost 1W power free space.

My understanding of how a VECSEL laser works is as following: a laser chip, made of multiple quantum wells, generates strong light when excited by a seed laser (or called pump laser). A built-

in mirror, or Distributed Bragg Reflector (DBR), reflects almost all light back into the laser chip direction. An external mirror (etalon) is placed at a distance from the chip to form a long cavity with DBR, which helps amplifying laser power and allows wavelength tuning. Finally, some of the light escapes through the external mirror, passes through BRF and nonlinear crystals with cavities for SHG (only if necessary), producing a high-quality laser beam.

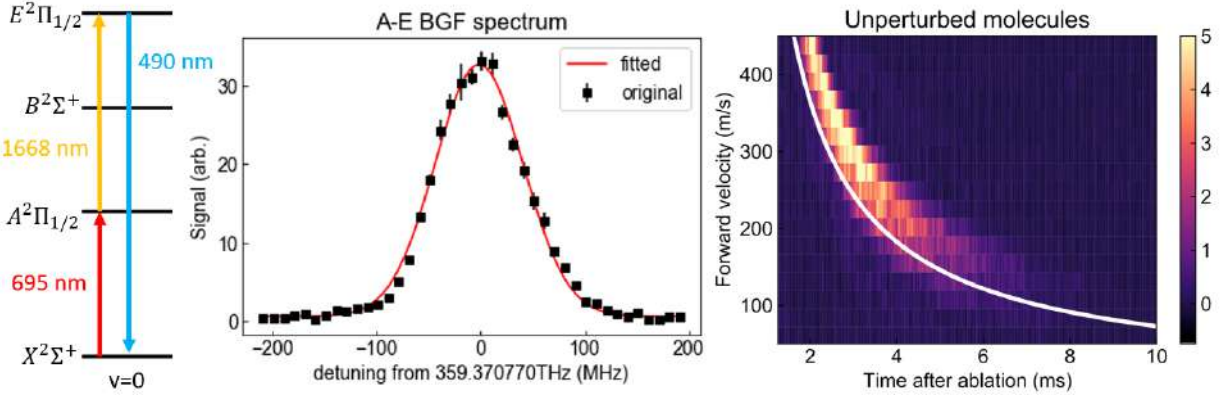


Figure A.2: Left plot is the diagram of CaH two photon background-free detection method. The $E^2\Pi_{1/2}$ to $X^2\Sigma^+$ decay photon is different from all laser sources in this system, leading to high SNR in the spectrum (middle plot) and FVD measurement (right plot).

The $X^2\Sigma^+$ to $A^2\Pi_{1/2}$ laser system, although not emphasized here, actually plays a critical role here, and has significant impact on the forward velocity detection here, much more than what we expected. The goal of this system is to move the ground state population from $|X, v = 0, N = 1\rangle$ to $|A, v = 0, J = 3/2\rangle$. Individual lasers are required to address $|X, v = 0, N = 1, J = 1/2\rangle$, $|X, v = 0, N = 1, J = 3/2\rangle$ and $|X, v = 0, N = 3, J = 5/2\rangle$ (because $|A, v = 0, J = 3/2\rangle$ state can naturally decay to $|X, v = 0, N = 3, J = 5/2\rangle$ state so the last one is basically a repump). This system consists of three ILAs, powered by three ECDLs, each of them passes through an individual EOM to create sidebands.

A.1 Ghosting Effect in BGF

This term that I proposed, ghosting effect, might mean differently in other contexts, but here it refers to the scenario where LIF from molecules at different velocities get detected, and leading to

a double-vision type of effect to the FVD measurement. This can be seen clearly in some recent data we took, as shown in Fig. A.3 (b). This figure shows a standard daily FVD with CaH without exaggeration. The white curve here represents the expected v-t relation for a ballistic traveling particle, calculated using $v = L/t$, where L is measured to be 75cm. Since we know the molecules are boosted after exit from the cell due to the "zone of freezing" (same temperature CaH is slower than He, so CaH gets He collisions to push them forward), we expect molecular signal to be on the right side of the curve. This is always true for Calcium FVD. However, CaH signal sometimes show weird behavior (Fig. A.3 (b)).

There are typically two causes for this behavior. One possibility is the $E^2\Pi_{1/2}$ state or $A^2\Pi_{1/2}$ state have hyperfine splittings, another possibility is we are driving two photon transition even with high detuning from the A state. However, the hyperfine splitting of $A^2\Pi_{1/2}$ state is expected to be very small (less than 2 MHz), similar level of splitting is expected for $E^2\Pi_{1/2}$ state. The reason is the wavefunction symmetry of a Π state indicates a smaller wavefunction overlap with nuclear spin, and thus a smaller HFS than Σ state. As a result, the ghosting is probably coming from $X^2\Sigma^+$ state ground state HFS, which are 54MHz and 101MHz.

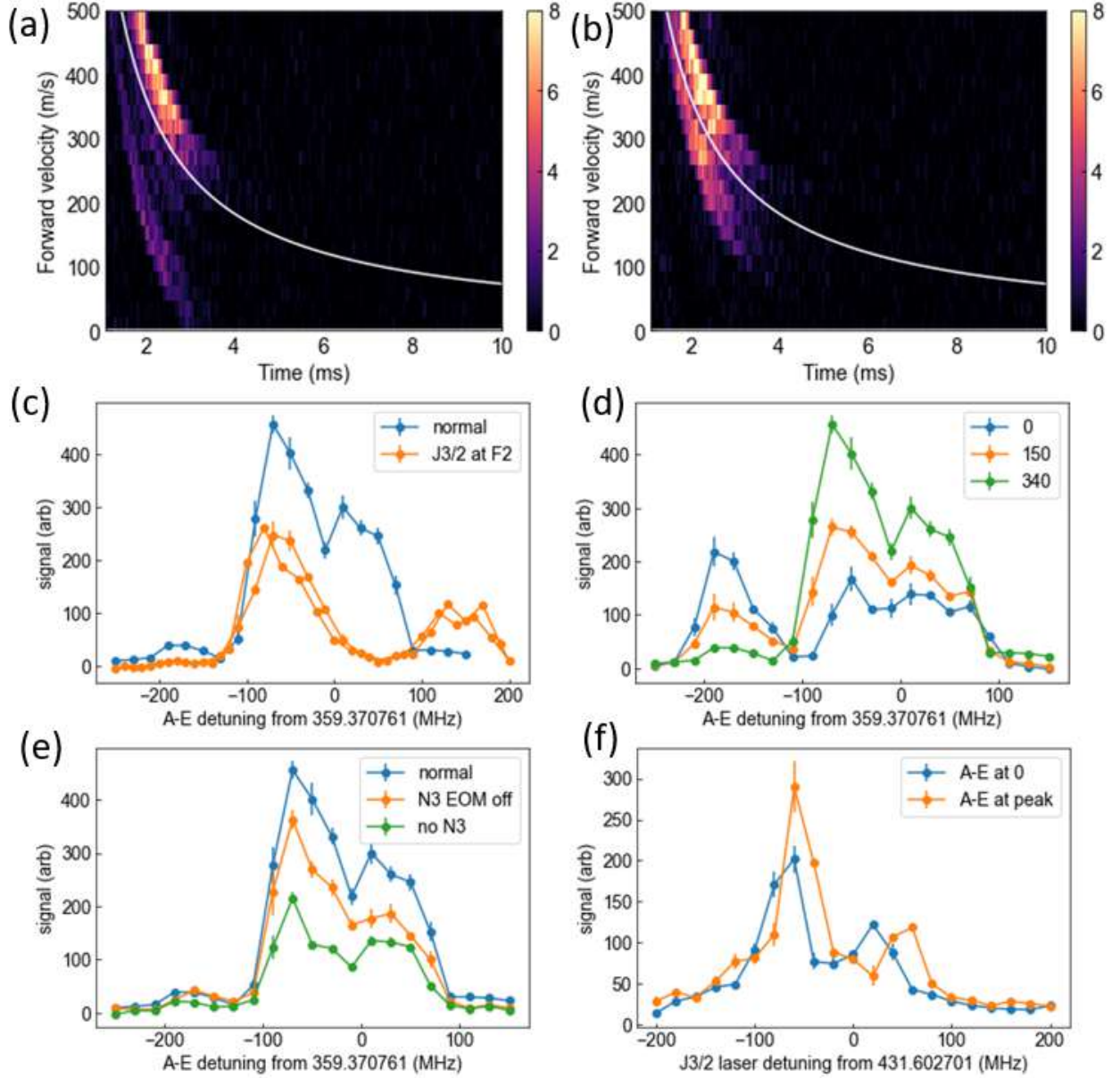


Figure A.3: Study of CaH ghosting effect. (a) For the $|X, N = 1, J = 3/2\rangle$ laser, we turn off EOM and park it at $F=2$ states, and perform FVD measurement. (b) we turn on EOM and park it in between $F=1$ and $F=2$, which is our regular detection method. (c) 1668 nm laser spectrum in velocity insensitive fashion when $|X, N = 1, J = 3/2\rangle$ laser is at different configurations. (d) 1668 nm laser spectrum in velocity insensitive fashion when $|X, N = 1, J = 3/2\rangle$ laser EOM is tuned. The legends 0, 150, 340 is proportional to the EOM modulation depth, where 0 means turned off, 340 means modulation depth is 1. (e) N=3 laser effect on the 1668 nm laser spectrum. (f) $J=3/2$ laser spectrum and its dependence on A-E laser.

ProQuest Number: 32117674

INFORMATION TO ALL USERS

The quality and completeness of this reproduction is dependent on the quality
and completeness of the copy made available to ProQuest.



Distributed by

ProQuest LLC a part of Clarivate (2025).

Copyright of the Dissertation is held by the Author unless otherwise noted.

This work is protected against unauthorized copying under Title 17,
United States Code and other applicable copyright laws.

This work may be used in accordance with the terms of the Creative Commons license
or other rights statement, as indicated in the copyright statement or in the metadata
associated with this work. Unless otherwise specified in the copyright statement
or the metadata, all rights are reserved by the copyright holder.

ProQuest LLC
789 East Eisenhower Parkway
Ann Arbor, MI 48108 USA